Analysing Landslides in the Three Gorges Region (China) Using Frequently Acquired SAR Images

Andrew G. Singleton

B.Sc (dunelm)

Thesis Submitted to the University of Glasgow

for the Degree of Doctor of Philosophy

August 2014

School of Geographical and Earth Sciences

College of Science and Engineering

University of Glasgow

Supervised by

Prof. Zhenhong Li, Prof. Trevor Hoey and Prof. Simon Wheeler

Declaration

The contents of this thesis are the result of my own work, except where material from other sources has been properly and fully acknowledged. The thesis has not been submitted for any other degree at the University of Glasgow or any other institution. The views and opinions expressed herein are mine and not necessarily those of any other person or organisation, unless so attributed.

Selected text and figures within Chapters 4 & 5 are, in part, a reformatted version of material appearing in Singleton, A., Li, Z., Hoey, T., Muller, J-P. (2014) Evaluating sub-pixel offset techniques as an alternative to D-InSAR for monitoring episodic landslide movements in vegetated terrain. *Remote Sensing of Environment 147: 133 – 144.* The thesis author was the principal researcher and author of the paper, whilst the co-authors listed in this publication directed and supervised the research.

This thesis also cites work from Tomás, R., Li, Z., Liu, P., Singleton, A., Hoey, T., and Cheng, X. (2014) Spatiotemporal characteristics of the Huangtupo landslide in the Three Gorges region (China) constrained by radar interferometry. *Geophysical Journal International 197(1): 213 – 232.* The thesis author (and paper co-author) assisted with the data interpretation, but did not take an active role in data processing or analyses.

Andrew Singleton
August 2014

Thesis Citation: Singleton, A.G. (2014) *Analysing landslides in the Three Gorges region (China) using frequently acquired SAR images.* PhD thesis, University of Glasgow, School of Geographical and Earth Sciences, Glasgow, UK.

Abstract

Analysing landslides in the Three Gorges region (China)
using frequently acquired SAR images

Andrew G. Singleton
University of Glasgow

Keywords: Synthetic Aperture Radar (SAR), Differential SAR Interferometry (D-InSAR), SAR Sub-Pixel Offsets, Time-Series Analysis, TerraSAR-X Spotlight, TerraSAR-X Stripmap, ENVISAT Stripmap, Corner Reflectors (CRs), Three Gorges region (China), Slow-Moving Landslides, Landslide Characterisation, 2D Limit Equilibrium Slope Stability Analysis, Reservoir Drawdown.

Spaceborne Synthetic Aperture Radar (SAR) sensors obtain regular and frequent radar images from which ground motion can be precisely detected using a variety of different techniques. The ability to remotely measure slope displacements over large regions has many uses and advantages, although the limitations of an increasingly common technique, Differential SAR Interferometry (D-InSAR), must be considered to avoid the misinterpretation of results. Areas of low coherence and the geometrical effects of mountainous terrain in SAR imagery are known to hinder the exploitation of D-InSAR results. A further major limitation for landslide studies is the assumption that variable rates of movement over a given distance cannot exceed a threshold value, dependent upon the SAR image pixel spacing, the radar sensor wavelength and satellite revisit frequency.

This study evaluates the use of three SAR image modes from TerraSAR-X and ENVISAT satellites for monitoring slow-moving landslides in the densely vegetated Three Gorges region, China. Low coherence and episodically fast movements are shown to exceed the measureable limit for regular D-InSAR analysis even for the highest resolution, 11-day interferograms. Subsequently, sub-pixel offset time-series techniques applied to corner reflectors and natural targets are developed as a robust method of resolving time-variable displacements. Verifiable offsets are generated with the TerraSAR-X imagery and the precise movement history of landslides is obtained over a period of up to four years.

The capability to derive two-dimensional movements from sub-pixel offsets is used to infer a rotational failure mechanism for the most active landslide detected, and a greater understanding of the landslide behaviour is achieved through comparisons with likely triggering factors and 2D limit equilibrium slope stability analysis.

Extended Abstract

Analysing landslides in the Three Gorges region (China)
using frequently acquired SAR images

Andrew G. Singleton
University of Glasgow

Keywords: Synthetic Aperture Radar (SAR), Differential SAR Interferometry (D-InSAR), SAR Sub-Pixel Offsets, Time-Series Analysis, TerraSAR-X Spotlight, TerraSAR-X Stripmap, ENVISAT, Corner Reflectors (CRs), Three Gorges region (China), Slow-Moving Landslides, Landslide Characterisation, 2D Limit Equilibrium Slope Stability Analysis, Reservoir Drawdown.

Landslides have long been the most frequent and widespread geological hazard in the Three Gorges region, China, predominantly because of high slope gradients, geological weaknesses, heavy rainfall and human activities. Over the last decade, the construction and operation of the Three Gorges Project (TGP) dam has created a 600 km long reservoir with a bi-annually fluctuating water level which has been shown to reactivate ancient landslide deposits (Wang *et al.*, 2008a). Communities within the Three Gorges are continuing to relocate due to the residential safety problems associated with slope instabilities. Therefore it is important to identify, measure and understand the mechanisms of landslide movements to help current and future land-use planning.

Probabilistic hazard assessments over large areas are possible using geostatistical methods applied to optical imagery and secondary data, while in-situ methods such as GNSS receivers or extensometers can precisely monitor existing landslides. However, the development of Differential Interferometric Synthetic Aperture Radar (D-InSAR) techniques makes it possible to remotely monitor ground displacement phenomena, such as landslides (reviewed by Colesanti and Wasowski, 2006; Rott, 2009), across the areal coverage of a radar image. This can reduce the cost and complexities of field-based monitoring and offers a potential method for remotely detecting, monitoring and characterising landslides throughout the Three Gorges region.

Extended Abstract

The Three Gorges region is commonly defined as the land bordering a 193 km section of the Yangtze River between Fengjie and Yichang, and this research focuses on a 30 km stretch in Zigui Country between the Wu and Xiling gorge. These "inter-gorge" areas are characterised by less resistant rocks (Fourniadis and Liu, 2007) where slope failures measurable using D-InSAR are likely to be concentrated. However, D-InSAR techniques in the Three Gorges region are potentially limited by steep slopes and temporal decorrelation between SAR image acquisitions caused by dense orange tree vegetation. This has led to previous studies focusing on time-series D-InSAR methods applied to unstable slopes in urban areas (e.g. Liu *et al.*, 2013; Tomás *et al.*, 2014) or the installation of corner reflectors (e.g. Xia *et al.*, 2004). This study therefore aims to develop techniques which can extend the use of frequently acquired SAR data to rural parts of the Three Gorges region. Further analysis of active landslides could then be undertaken (by comparison to data on triggering factors and the use of 2D limit equilibriums models) to determine dominant controls on a slope's factor of safety.

Within the study area, a large amount of Synthetic Aperture Radar (SAR) data are available in three different imaging modes which overlap in time and space. These include: (i) 57 TerraSAR-X (TSX) Spotlight images between February 2009 – February 2013; (ii) 23 TSX Stripmap images between April – December 2009; and, (iii) 14 ENVISAT Stripmap images between December 2008 and May 2010. Given the variability in SAR sensor wavelength and pixel spacing for the different image modes, this study provides one of the most detailed assessments on the capabilities and limitations of SAR data for investigating landslides in such a densely vegetated region as the Three Gorges.

Interferometric coherence (required for reliable D-InSAR analysis) is shown to be low for all image modes over the whole duration of each data set. However, TSX Spotlight and Stripmap data display seasonally higher coherence values compared with the ENVISAT data, attributed to their higher spatial resolution and greater acquisition frequency. The annual variations in coherence are also shown to be related with fluctuations in rainfall (and therefore soil moisture) as well as summer vegetation growth.

In the best circumstances (i.e. short repeat intervals and low perpendicular baselines), TSX Spotlight interferograms can detect, map and measure slope movements in the Three Gorges region. This helps to identify previously unknown instabilities and accurately (re)define the boundary of active landslides. However, the highest SAR resolution also highlights a significant danger of using D-InSAR techniques for landslide monitoring.

Extended Abstract

Fast and episodic movements of the Shuping landslide are shown to exceed the measureable spatial displacement gradient, particularly around the landslide boundary where complete coherence is lost. Any D-InSAR time-series technique spanning this event would erroneously underestimate the landslide displacement. This is believed to cause the disparities between previous D-InSAR studies of the Shuping landslide (Xia, 2010; Liao *et al.*, 2012), and in-situ extensometer data (Wang *et al.*, 2013b).

A robust sub-pixel offset technique is developed and applied to corner reflectors installed across the Shuping landslide, which help recover non-linear vertical displacements of ~0.6 m/yr. Corner reflectors provide a very consistent radar return allowing precise sub-pixel offset measurements to be obtained, with RMSE values of 0.024 m and 0.038 m in range direction for the TSX Spotlight and Stripmap data, respectively. However, the acceptable cross-correlation threshold of 0.78 (required to generate precise sub-pixel offset measurements from natural features in the landscape) is only applicable to the TSX Spotlight imagery. A regional coverage of point-like pixel offsets across the TSX Spotlight image frame helps identify one previously unknown active landslide, although the density of measurements remains relatively sparse.

With precise sub-pixel offset measurements from corner reflectors capable of measuring displacements in the two dimensions of SAR images (in range and azimuth directions), it is possible to estimate vertical and horizontal movements to characterise the likely failure mechanism of the Shuping landslide. Time-series displacement curves can be compared with potential triggering factors and the Shuping landslide is shown to be most influenced by the fastest periods of reservoir drawdown, compared to heavy rainfall or seismic activity. Scenarios of reservoir drawdown are analysed using a 2D limit equilibrium model which shows the factor of safety for the landslide decreases when the reservoir quickly falls, most likely due to high pore water pressures which remain within the slide body.

Combining the regional detection of active landslides with site-specific characterisation of individual slope movements should help develop appropriate remedial measurements to protect the communities and infrastructure within the boundary of active landslides. The developed techniques which employ frequently acquired SAR data are applicable to different types of terrain, and future studies are recommended to use the highest possible spatial and temporal resolution SAR data. Higher resolution SAR data reduces the spatial displacement gradient constraints and helps achieve the greatest sub-pixel offset precision.

This research also helps explore the dynamics of reactivated landslide deposits and consistent displacements in the Three Gorges region are shown to be caused by the annually-occurring trigger of reservoir drawdown. No long-term acceleration or deceleration is detected, although additional acquisitions of TSX Spotlight data would be beneficial for continued monitoring beyond the four year period covered in this study. This work also has significant implications for the monitoring of slopes bordering large reservoirs in other parts of the world.

Acknowledgements

My greatest thanks are owed to my supervisors Zhenhong Li, Trevor Hoey and Simon Wheeler for their considerable expertise, guidance and enthusiasm over the last few years. In addition to their time and efforts that went into regular meetings and reviewing written work, I am very appreciative of their encouragement to attend major conferences and participate in research projects beyond the scope of this PhD. It has broadened my horizons and made me new friends around the world.

I gratefully acknowledge all the colleagues that provided assistance throughout the course of this research, particularly: Jan-Peter Muller for the provision of TerraSAR-X data; Alessio Cantone and Stefano Monaco for solving problems related to data processing; Tao Li, Shilai Cheng and Peng Li for coordinating fieldwork in the Three Gorges region; Roberto Tomás for his useful discussions on landslide mechanisms; and, to all members of the Centre for the Observation and Modelling of Earthquakes and Tectonics (COMET) research group for enjoyable meetings and constructive questioning after my presentations. Special thanks are also owed to Patrice Carbonneau, Alex Densmore and Chris Stokes for their advice during my undergraduate study which undoubtedly influenced my decision to pursue academic research to this level.

The seminars and activities of the Space Geodesy Research Group at the University of Glasgow have always been interesting and useful. I'm particularly thankful for the help and friendship of Peng Liu, Zhiwei Zhou and Wanpeng Feng in tackling technical problems and carefully managing the use of computing resources and data storage!

Being part of the School of Geographical and Earth Sciences at Glasgow University has been an incredible pleasure and I'll never forget all the people (too numerous to mention individually) who have made my time learning, teaching and socialising so enjoyable. The work of administrative and technical staff also needs highlighting – no one was ever too busy to solve any logistical problems.

Acknowledgements

My love and heartfelt thanks go to my parents for their continual support towards my education. They instilled beliefs that almost anything can be achieved when you set your mind to it and how the greatest reward often comes from helping others. These are valuable attitudes for undertaking PhD research and coincidently echo high school and university college mottos respectively...

'Nihil sine labore' *'Sic vos non vobis'*

Finally, I am indescribably grateful and appreciative for the patience, understanding, love and laughs from Mhairi throughout my PhD. Thank You.

This research was jointly funded by an Industrial Studentship from the Engineering and Physical Sciences Research Council (EPSRC – EP/P505534/1) and the College of Science and Engineering at the University of Glasgow. A student award from the Geological Remote Sensing Group (GRSG), mobility scholarship from the University of Glasgow and sponsorship from the European Space Agency (ESA) are also gratefully acknowledged in support of fieldwork and workshop events.

ENVISAT SAR data were supplied through the ESA-MOST Dragon-2 Cooperation Program (ID: 5343) and the TerraSAR-X data were supplied through a DLR proposal (ID: GEO0112). SRTM topographic data were provided by the US Jet Propulsion Laboratory (JPL). The ASTER topographic data were a product of Japan's Ministry of Economy, Trade and Industry (METI) and the US National Aeronautics and Space Administration (NASA).

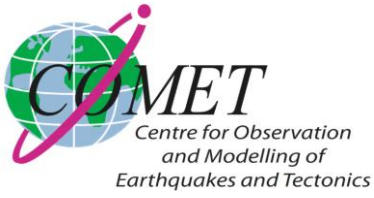

Contents

Declaration i
Abstract ii
Extended Abstract iii
Acknowledgements vii
List of Figures xiii
List of Tables xvii
List of Acronyms xviii
Notation xx
Chapter 1 : Introduction 1
1.1 Global Landslide Hazards 2
1.2 Slow-Moving Landslides 4
1.3 Remote Monitoring of Landslides 6
1.4 Research Motivation 7
1.5 Aim and Research Questions 9
1.5.1 Research Aim 9
1.5.2 Research Questions 10
1.6 Thesis Outline 10
Chapter 2 : Principles of D-InSAR and SAR Sub-Pixel Offsets 12
2.1 Synthetic Aperture Radar 13
2.1.1 Range and Azimuth Resolution 14
2.1.2 Speckle 17
2.1.3 Spotlight Imaging Mode 18
2.1.4 Geometrical Image Distortions 19
2.2 Differential Interferometry (D-InSAR) 20
2.2.1 Processing Overview 21
2.2.2 Decorrelation Sources 23
2.2.2.1 Geometric Decorrelation 23
2.2.2.2 Doppler Centroid Decorrelation 25
2.2.2.3 Temporal Decorrelation 25

2.2.2.4 Spatial Displacement Gradient and Scale Constraints 26
2.2.2.5 InSAR Time-Series Methods 29
2.2.3 D-InSAR Landslide Applications 29
2.3 SAR Sub-Pixel Offset Techniques 31
2.3.1 Overview 31
2.3.2 Early Applications 33
2.3.3 Application to Landslides 34
2.4 Summary 35
Chapter 3 : Landslides in the Three Gorges Region 36
3.1 Geological Background of the Three Gorges 37
3.1.1 Local Geology 39
3.1.2 Tectonic Setting 41
3.2 Hydrological Influences on Landslides 42
3.2.1 Rainfall Patterns in the Three Gorges Region 43
3.2.2 The Three Gorges Project (TGP) 44
3.3 Remote Sensing of Landslides 46
3.3.1 Spaceborne Optical Imagery 47
3.3.2 Spaceborne Radar Imagery 49
3.3.2.1 Shuping Landslide Observations 50
3.4 Large Colluvial Landslides 53
3.4.1 Geological Description of the Shuping Landslide 55
3.5 Slope Stability Modelling 56
3.6 Summary 57
Chapter 4 : Evaluating D-InSAR Use in the Three Gorges Region 58
4.1 Study Area and Data Sets 59
4.1.1 TerraSAR-X Spotlight Data 61
4.1.2 TerraSAR-X Stripmap Data 62
4.1.3 ENVISAT ASAR Stripmap Data 63
4.2 Coherence Analysis 64
4.2.1 Coherence Processing 65
4.2.2 Coherence Results 66
4.3 Identifying Landslides from D-InSAR Analysis 70
4.3.1 DEM Selection 70
4.3.2 TSX Spotlight Interferograms 72
4.3.3 TSX Stripmap Interferograms 80
4.3.4 ENVISAT Stripmap Interferograms 81
4.3.5 Geometrical Distortions 83

4.4 Spatial Displacement Gradient Limitations 84
4.5 Decorrelation from Landslide Movements 87
4.6 Downslope Sliding Velocities 91
4.7 Summary 92
Chapter 5 : SAR Sub-Pixel Offset Time-Series Results 93
5.1 SAR Sub-Pixel Offset Parameter Selection 94
5.2 TerraSAR-X SPOT-CR Results for the Shuping Landslide 98
5.2.1 TerraSAR-X SPOT-CR Results: 2009 - 2010 100
5.2.2 TerraSAR-X SPOT-CR Results: 2009 - 2013 102
5.2.3 TerraSAR-X SPOT-CR Precision 104
5.3 TerraSAR-X SPOT-CR results for other landslides 105
5.3.1 Kaziwan and Chalukou Landslide Complex 106
5.3.2 Xintan Landslide 107
5.4 Measuring Landslides with Point-Like Pixel Offsets 108
5.5 TerraSAR-X Spotlight Regional Point-Like Pixel Offsets 115
5.6 TerraSAR-X Stripmap Limitations 123
5.7 ENVISAT Limitations 123
5.8 Summary 124
Chapter 6 : Investigating the Shuping Landslide 125
6.1 Landslide Triggering Factors 126
6.1.1 Reservoir Drawdown 127
6.1.2 Rainfall 131
6.1.3 Seismicity 132
6.2 Landslide Failure Mechanism 133
6.2.1 Vertical Movement (d_U) 135
6.2.2 Horizontal Movement (d_N) 135
6.2.3 Rotational Failure 136
6.3 2D Limit Equilibrium Slope Stability Analysis 137
6.3.1 Model Parameter Selection 140
6.3.2 Deterministic Analysis 142
6.3.2.1 145 m Water Level 143
6.3.2.2 175 m Water Level 143
6.3.3 Probabilistic Analysis 145
6.3.4 Sensitivity Analysis 147
6.3.5 Rapid Drawdown Scenario 148
6.4 Summary 150

Chapter 7 : Discussion and Conclusions 151
7.1 Discussion 152
7.1.1 D-InSAR use in the Three Gorges Region 152
7.1.2 SPOT use in the Three Gorges Region 154
7.1.3 Landslide Characterisation in the Three Gorges Region 156
7.2 Conclusions 158
7.3 Research Contributions 163
7.4 Future Research Directions 164
Reference List 167
Appendix A – Supplementary Tables & Figures 187
Appendix B – First Author *Remote Sensing of Environment* Paper 190
Appendix C – Co-Author *Geophysical Journal International* Paper 203

List of Figures

Figure 1-1: Global distribution of fatal landslides....3
Figure 1-2: Distribution and elevation of landslides in the eastern part of the Three Gorges region....4
Figure 1-3: Different stages of landslide movement....5
Figure 2-1: The configuration of a regular SAR antenna and its imaging footprint, reproduced from Curlander and McDonough (1991)....13
Figure 2-2: The synthetic aperture (antenna) generated by the platform motion of a SAR sensor....16
Figure 2-3: Single Look Complex (SLC) image matrix, defined by the ground range and azimuth resolution. 17
Figure 2-4: Geometry of the Spotlight SAR imaging mode....18
Figure 2-5: Layover and shadow effects....19
Figure 2-6: A typical D-InSAR processing chain, reproduced from Dong and Huang (2011). 21
Figure 2-7: Interferometric phase difference for the ERS configuration across a flat earth distance of 5 ground range pixels. 24
Figure 2-8(a): Wrapped phase for 1999 Hector Mine earthquake. 27
Figure 2-8(b): Corresponding coherence map showing decorrelation close to the fault in areas of the highest fringe frequency 27
Figure 2-9(a): The range of applications for C-band deformation mapping in terms of the size and the magnitude of movement. 28
Figure 2-9(b): Classification of displacement signals by rate and duration....28
Figure 2-10: SAR pixel offset schematic showing the investigated pixel within the reference template and searching window....32
Figure 3-1: The Three Gorges region from Fengjie in the west to Yichang in the east. 37
Figure 3-2: Typical land cover of orange trees in the Three Gorges region....37
Figure 3-3: First order geophysical contrasts in topography, crustal thickness and lithospheric thickness around the Three Gorges region....39
Figure 3-4: Hypothetical Paleo-Yangtze drainage basin with the original watershed close to the Three Gorges region 39
Figure 3-5: Geological setting of the Three Gorges region along the Yangtze River. 40
Figure 3-6: Relationship between landslide occurrence and precipitation in the Three Gorges reservoir region, 1971 – 2003 44
Figure 3-7: Impact of the Three Gorges reservoir impoundment on the Dragon Gate Bridge 44
Figure 3-8: Annual operations of the Three Gorges reservoir and the associated water level changes 45

Figure 3-9: Susceptibility to block-type landslides between Wushan in the west and Zigui in the east. 47
Figure 3-10: Landslide susceptibility mapping of the Three Gorges from Badong in the west to Zigui in the east 48
Figure 3-11: Mean Line-of-Sight (LOS) velocity of the Huangtupo landslide (right landslide block), between August 2003 and July 2010 50
Figure 3-12: Published boundaries of Block-1 and Block-2 for the Shuping landslide 51
Figure 3-13(a): Noisy mean velocity map over the Shuping landslide for the period January 2008 – January 2010 52
Figure 3-13(b): Noisy time-series curves of displacement, in relation to variation of the Three Gorges reservoir 52
Figure 3-14: Conceptual model for the slow and episodic movement of landslides observed in the Three Gorges region 54
Figure 3-15: Lithological column diagram of the borehole located towards the middle/bottom of Block 1 in the Shuping landslide 56
Figure 4-1: Location map and elevation of the eastern TG region. 60
Figure 4-2(a): Baseline plot of TSX Spotlight data from 2009 – 2010. 62
Figure 4-2(b): Baseline plot of TSX Spotlight data from 2012 – 2013. 62
Figure 4-3: Baseline plot of TSX Stripmap data. 63
Figure 4-4: Baseline plot of ENVISAT Stripmap data. 64
Figure 4-5: Coherence analysis for the three SAR imaging modes from December 2008 – May 2010. 67
Figure 4-6(a): NDVI map of the eastern TG region from the Landsat 8 OLI sensor. 68
Figure 4-6(b): Cumulative distribution of NDVI values in the TG region 68
Figure 4-7: Coherence analysis for TSX Spotlight data from January 2012 – February 2013. 70
Figure 4-8: DEM comparisons between STRM, ASTER and TanDEM-X (TDX) data. 71
Figure 4-9: TSX Spotlight, wrapped winter 11-day interferograms with $B_{\perp} < 30$ m 73
Figure 4-10: TSX Spotlight, wrapped winter 11-day interferograms with $B_{\perp} > 30$ m. 74
28^{th} Apr – 9^{th} May 2009: 75
Figure 4-11: TSX Spotlight, wrapped 11-day interferograms outside the winter months with $B_{\perp} < 30$ m. 75
Figure 4-12: TSX Spotlight, wrapped 11-day interferograms outside the winter months with $B_{\perp} > 30$ m. 76
Figure 4-13: TSX Spotlight, wrapped winter interferograms of different time intervals with $B_{\perp} < 30$ m. 77
Figure 4-14: TSX Spotlight, wrapped interferograms of different time intervals outside the winter months with $B_{\perp} < 30$ m 78
Figure 4-15: TSX Stripmap, wrapped 11-day interferograms with $B_{\perp} < 30$ m showing the difference between summer/winter coherence. 81
Figure 4-16: ENVISAT Stripmap wrapped 35-day interferograms showing the difference between summer/winter coherence 82
Figure 4-17: R-index calculated for the three different satellite imaging modes, showing the degree of image distortion. 85
Figure 4-18: TSX Spotlight wrapped 11-day consecutive interferograms showing the Shuping landslide exceeding the spatial displacement gradient 89
Figure 4-19: TSX Stripmap wrapped 11-day consecutive interferograms showing incoherence over the Shuping landslide over the same period as Figure 4-18 90

List of Figures

Figure 5-1: Cumulative percentage of TSX Spotlight sub-pixel offset values in azimuth direction for different window sizes 96
Figure 5-2: Cumulative percentage of TSX Spotlight sub-pixel offset values in range direction for different window sizes 96
Figure 5-3: Cumulative percentage of TSX Stripmap sub-pixel offset values in azimuth direction for different window sizes 97
Figure 5-4: Cumulative percentage of TSX Stripmap sub-pixel offset values in range direction for different window sizes 97
Figure 5-5(a): The value of peak correlation used for the TSX Spotlight offset measurements. 99
Figure 5-5(b): The numbering of corner reflectors used to extract time-series of displacement, overlain on an interferogram showing the landslide boundary. 99
Figure 5-6: Offset displacements for the corner reflectors labelled in Figure 5-5 from Feb 2009 – April 2010 100
Figure 5-7: Accumulated displacement of all extensometer monitoring points on the Shuping landslide 102
Figure 5-8: TSX Spotlight offset displacements for the corner reflectors labelled in Figure 5-5 from Feb 2009 – Feb 2013 103
Figure 5-9: TSX Stripmap range offsets across the Kaziwan and Chalukou landslide complex showing no significant displacement. 106
Figure 5-10: TSX Stripmap range offsets across the Xintan landslide showing no significant displacement. 107
Figure 5-11: Schematic diagram of significantly overlapping, independent SAR offset pairs 108
Figure 5-12: Mean difference between two independent TSX Spotlight offset maps overlapping in time, classified by offset cross-correlation values. 110
Figure 5-13: Standard deviation of the difference in offset values from independent TSX Spotlight offset maps overlapping in time, in relation to offset correlation values and SAR image time interval. 112
Figure 5-14: Standard deviation of the difference in offset values from independent TSX Spotlight offset maps overlapping in time, in relation to offset correlation values and perpendicular baseline. 113
Figure 5-15: The number of mutual pixels with similar correlation values from independent TSX Spotlight offset maps overlapping in time, in relation to SAR image time interval. 114
Figure 5-16: Regional offset maps for the TSX Spotlight scene from 21st Feb 2009 until 15th April 2010. 117
Figure 5-17: Regional offset maps for the TSX Spotlight scene from 15th April 2010 until 2nd Jan 2012. 118
Figure 5-18: Regional offset maps for the TSX Spotlight scene from 2nd Jan 2012 until 23rd Feb 2013. 119
Figure 5-19: Regional offset maps for the TSX Spotlight scene from 21st Feb 2009 until 23rd Feb 2013. 120
Figure 5-20: Offset displacements for the new riverbank instability identified in Figure 5-17 & Figure 5-19, from Feb 2009 – Feb 2013 121
Figure 5-21: Online photos of the new riverbank instability area in three different years, from Panoramio & Google Maps. 122
Figure 5-22: Mean difference between two independent TSX Stripmap offset maps overlapping in time, in relation to offset correlation values. 123

List of Figures

Figure 6-1: Large boulders found amongst a finer matrix of softer sediments within the boundary of the Shuping landslide. 127
Figure 6-2: Range displacement of the fastest moving corner reflectors (CRs 9 & 10), in relation to water level changes of the Three Gorges reservoir 130
Figure 6-3: Range displacement of the fastest moving corner reflector (CR 10) in relation to the 5-day water level change 130
Figure 6-4: Range displacement of the fastest moving corner reflector (CR 10) in relation to 10-day accumulated rainfall. 131
Figure 6-5: Range displacement of the fastest moving corner reflector (CR 10) in relation to seismicity within a 50 km radius of the Shuping landslide. 133
Figure 6-6: Accumulated displacement in (a) vertical direction and (b) horizontal direction, for three different time periods. 135
Figure 6-7(a): Schematic diagram of a rotational failure mechanism, as inferred from the results in Figure 6-6 136
Figure 6-7(b): Construction of slip surface using ground station movements, relative to the SAR sensor Line-of-Sight (LOS) direction 136
Figure 6-8: Illustration of the method of slices for limit equilibrium analysis. 139
Figure 6-9: Geometry and parameterisation of a 2D profile through the centre of Block 1 of the Shuping landslide. 141
Figure 6-10: Factor of safety calculation using Spencer's method for a reservoir water level of 145 m 143
Figure 6-11: Factor of safety calculation using Spencer's method for a reservoir water level of 175 m 144
Figure 6-12: Comparison of factor of safety values from different methods. 145
Figure 6-13: Upper and lower limits of the water-table for the probabilistic and sensitivity analysis. 146
Figure 6-14(a): Convergence plot of 2000 samples following the random variation in model parameters 147
Figure 6-14(b): Histogram of the minimum FS calculated for each random variation in model parameters 147
Figure 6-15: Sensitivity plot of the factor of safety, across the range of parameters specified in Table 6-2 148
Figure 6-16: Factor of safety following the complete and rapid lowering of the Three Gorges reservoir from 175 m – 145 m 149
Figure 6-17: Factor of safety following a rapid, realistic 5 m drop in the Three Gorges reservoir. 150
Figure A-1: Installed corner reflectors at the toe of the densely vegetated Shuping landslide 187
Figure A-2: Landslide warning sign (displaced!) at the site of the Dujiawu landslide. 187
Figure A-3: Offset displacement of Point 3 measured from TSX Spotlight data 188
Figure A-4: Building damage indicative of land movements and confirmed in communication with residents. 188

List of Tables

Table 1-1: Landslide classification based on the displacement velocity 2
Table 2-1: List of SAR satellite missions and the viewing/orbit parameters. 14
Table 4-1: Basic information about previously known (i.e. published) landslides in the study area. 60
Table 4-2: Parameter selection to assess the impact of seasonality, perpendicular baseline and time interval on interferogram quality 72
Table 4-3: Metadata for the available stacks of SAR images used in this study. 86
Table 4-4: Displacement gradients for the three image modes used in this study. 87
Table 4-5: Parameters and unit vectors of the satellite look direction and the downslope sliding direction 91
Table 5-1: Time taken to process TSX Spotlight offsets (HH:MM) using different parameter settings for a reference area assumed to be stable, adjacent to Shuping landslide 98
Table 5-2: Comparison of all CR offset measurements between two independent offset calculations from two image pairs significantly overlapping in time. 105
Table 6-1: Published geotechnical parameters for the Shuping landslide and from other landslides close to the Shuping landslide. 142
Table 6-2: The range of parameters, varied randomly and following a uniform distribution, for both the probabilistic and sensitivity slope stability analysis. 146
Table 7-1: Summary table for factor of safety results for different hydrological scenarios affecting the Shuping landslide 162
Table A-1: Individual estimates of the vertical (d_U) and horizontal (d_N) components of landslide movement for the numbered corner reflectors shown in Figure 5-5. 189

List of Acronyms

ALOS	Advanced Land Observing Satellite
ASAR	Advanced Synthetic Aperture Radar
ASTER	Advanced Spaceborne Thermal Emission and Reflection Radiometer
B_{PERP}	Perpendicular Baseline
CR	Corner Reflector
CSN	China Seismic Network
DEM	Digital Elevation Model
D-InSAR	Differential Interferometric Synthetic Aperture Radar
DLR	German Aerospace Centre
DORIS	Delft Object-orientated Radar Interferomtric Software
E	Easting
ENVISAT	Environmental Satellite
EO	Earth Observation
ERS	European Remote-Sensing Satellite
ETM+	Enhanced Thematic Mapper Plus
EWS	Early Warning Systems
FEM	Finite Element Methods
FFT	Fast Fourier Transform
GDEM	Global Digital Elevation Model
GMTSAR	Generic Mapping Tools SAR
GNSS	Global Navigation Satellite System
GPS	Global Positioning System
HH	Horizontal transmit, Horizontal receive polarisation
HH:MM	Hour : Minutes
HS	High Resolution Spotlight Image Mode
IS	Image Swath
JERS	Japanese Earth Resources Satellite
JPL	Jet Propulsion Laboratory
LiDAR	Light Detection and Ranging

LOS	Line-of-Sight
M_L	Local (Richter) Earthquake Magnitude
M_S	Surface-Wave Earthquake Magnitude
M_W	Moment Earthquake Magnitude
MAI	Multiple Aperture InSAR
METI	Ministry of Economy Trade and Industry in Japan
N	Northing
NASA	National Aeronautics and Space Administration of America
NCC	Normalised Cross-Correlation
NDVI	Normalised Difference Vegetation Index
NEST	Next ESA SAR Toolbox
OLI	Operational Land Imager
PALSAR	Phased Array type L-band Synthetic Aperture Radar
PS	Permanent/Persistent Scatterer
ROI_PAC	Repeat Orbit Interferometry Package
RMSE	Root Mean Square Error
SAR	Synthetic Aperture Radar
SBAS	Small BAseline Subset
SLC	Single Look Complex
SM	Stripmap Image Mode
SNR	Signal-to-Noise Ratio
SPOT	Sub-Pixel Offset Time-series
SPOT-CR	Sub-Pixel Offset Time-series applied to Corner Reflectors
SRTM	Shuttle Radar Topography Mission
TG	Three Gorges
TGP	Three Gorges Project (i.e. Three Gorges Dam)
TM	Thematic Mapper
TDX	TanDEM-X
TSX	TerraSAR-X
VV	Vertical-transmit, Vertical-receive SAR polarisation

d_R	3D Range Displacement	$d_R = 1$ (unit vector)
u_D	3D Downslope Sliding Direction	$u_D = 1$ (unit vector)
S	Amplification Scaling Factor	Dimensionless
β	Antenna Beamwidth	Degrees (°)
l_a	Antenna Length	Metres (m)
W_a	Antenna Width	Metres (m)
B_R	Chirp Bandwidth	Megahertz (MHz)
r^2	Coefficient of Determination	-1 ≤ r^2 ≤ 1 (dimensionless)
r	Correlation Coefficient	-1 ≤ r ≤ 1 (dimensionless)
A	DEM-derived aspect, corrected with the difference between north and the satellite heading	Degrees (°)
Sl	DEM-derived Slope	Degrees (°)
d_E	Displacement Vector: East	0 ≤ d_E ≤ 1 (dimensionless)
d_N	Displacement Vector: North	0 ≤ d_N ≤ 1 (dimensionless)
d_U	Displacement Vector: Up	0 ≤ d_U ≤ 1 (dimensionless)
d	Distance of slice central axis from rotation centre	Metres (m)
B_D	Doppler Bandwidth	Hertz (Hz)
D_C	Doppler Centroid	Hertz (Hz)
u_E	Downslope Sliding Vector: East	0 ≤ u_E ≤ 1 (dimensionless)
u_N	Downslope Sliding Vector: North	0 ≤ u_N ≤ 1 (dimensionless)
u_U	Downslope Sliding Vector: Up	0 ≤ u_U ≤ 1 (dimensionless)
c'	Effective Cohesion	Kilopascal (kPa)
φ'	Effective Internal Angle of Friction	Degrees (°)
σ'	Effective Normal Stress	Pascal (Pa)
F_S	Factor of Safety	0 ≤ F_S (dimensionless)
Azi_g	Ground Azimuth Resolution	Metres (m)
r_g	Ground Range Resolution	Metres (m)
E_L E_R	Horizontal lateral forces between slices	Newtons (N)
γ	Interferometric Coherence	0 ≤ γ ≤ 1 (dimensionless)

Φ	Landslide Model Slice Inclination	Degrees (°)
l	Length of Landslide Model Slice Base	Metres (m)
θ	Local Incidence Angle	Degrees (°)
Ω	Maximum spatial displacement gradient	Metres per metre (m/m)
ρ	Normalised Cross-Correlation Coefficient	$0 \leq \rho \leq 1$ (dimensionless)
N	Number of samples in the moving window	Dimensionless
χ	Oversampling Factor	Dimensionless
$B_{\perp}$	Perpendicular Baseline	Metres (m)
u	Pore Pressure	Pascal (Pa)
R	Radius of Landslide Failure Surface	Metres (m)
R_0	Range to Target	Kilometres (km)
$\Delta\phi$	Residual Interferometric Phase	Radians (rad.)
R	R-index (from Notti *et al.*, 2010)	$-1 \leq R \leq 1$ (dimensionless)
α	Satellite Azimuth Heading	Degrees (°)
v	Satellite Orbital Velocity	Kilometres / second (km/s)
γ_S	Saturated Unit Weight	Kilonewton per cubic metre (kN/m^3)
τ_f	Shear Strength	Pascals (Pa)
τ_s	Shear Stress	Pascals (Pa)
r_s	Slant Range Resolution	Metres (m)
η	Smallest Pixel Spacing	Metres (m)
c	Speed of Light	~3,000,000 m/s
σ	Standard Deviation	Variable units
W_g	Swath Width	Metres (m)
L_a	Synthetic Aperture (Antenna) Length	Metres (m)
σ^T	Total Normal Stress	Pascal (Pa)
τ_P	Transmitted Pulse Duration	Microseconds (μs)
γ_U	Unsaturated Unit Weight	Kilonewton per cubic metre (kN/m^3)
$X_L\ X_R$	Vertical Shear Forces Between Slice	Newtons (N)
λ	SAR Wavelength	Metres (m)
W	Weight of Landslide Model Slice	Kilonewtons (kN)
b	Width of Landslide Model Slice	Metres (m)

Chapter 1 : Introduction

A simple and widely accepted definition of landsliding was given by Cruden (1991) and Cruden and Varnes (1996), referring to a landslide as the downslope movement of rock, earth or debris. Despite being used interchangeably, the term 'landslide' belongs to a much broader group of slope processes referred to as mass movement – defined as "the outward and downward gravitational displacement of slope forming materials" (Gutiérrez *et al.*, 2010 p. 95).

Landslides are the failure of a slope which occurs when forces and stresses acting upon it exceed the strength of the ground materials. Processes influencing landslide occurrence can be separated into two categories, conditioning factors and triggers, based on the timescale over which the process operates. Over longer time-periods, landslides are conditioned by a variety of factors (e.g. relief, lithology, weathering, deforestation, tectonic movements, environmental change, and human activity) and initiated by short-term effects (such as heavy rainfall, earthquake shaking and slope undercutting) (Glade and Crozier, 2005). The combination of these factors determines the behaviour of the unstable mass and therefore dictates the duration, form and run out distance of slope failure (Thiebes, 2012).

Various classifications exist which commonly divide landslides based upon the slope material (e.g. rock, debris, earth) and the process type (e.g. fall, topple, slide, flow, creep) (e.g. Cruden and Varnes, 1996; Dikau *et al.*, 1996). Soil is distinguished from rock, being subdivided into earth and debris depending on the grain size, and landslides which exhibit multiple failure modes are described as complex movements (Lu and Godt, 2013).

Given the large range of potential landslide magnitudes, slope failures can also be ranked in terms of their velocity (Table 1-1). The impact of a landslide is often considered proportional to its volume and velocity (Lee and Jones, 2004) and appropriate management strategies are dependent upon the magnitude of movement. Even for slow-moving landslides, the effects are related to the amount of displacement per unit time given the destructive nature of earth pressure and differential surface shearing, as opposed to the collision impact of faster moving failures (Glade and Crozier, 2005).

Table 1-1: Landslide classification based on the displacement velocity (adapted from Australian-Geomechanics-Society, 2002 p. 76).

Class	Description	Typical Velocity	Physical Damage	Human Losses
1	Extremely Rapid	> 5 m/sec	Catastrophic and violent disaster, buildings destroyed by landslide impact.	Population killed by impact of displaced material or disaggregation of the displaced mass.
2	Very Rapid	> 5 m/min	Major destruction of buildings.	Some lives lost since landslide velocity does not permit all persons to escape.
3	Rapid	> 1 m/hour	Structures and equipment destroyed.	Escape and evacuation is possible.
4	Moderate	> 10 m/month	Temporary structures in front of the landslide can be maintained in the short term. Extensive damage for structures located on the landslide.	Full escape and evacuation is likely. Injury or death would only be attributable to secondary effects such as building collapse.
5	Slow	> 1 m/year	Remedial construction possible and temporary structures can be maintained with frequent work if episodic movements are not too great.	
6	Very Slow	> 10 mm/year	Some permanent structures undamaged by movement.	
7	Extremely Slow	< 10 mm/year	Imperceptible without instruments, construction possible with precautions.	

Landsliding is one of many natural processes that shape the landscape, noted for its prevalence and effectiveness in all parts of the world (Lu and Godt, 2013). Not only are landslides an important control on local hillslope evolution, the interplay of rock uplift and heterogeneous landslide erosion (particularly from coseismic failures) can affect the evolution of whole orogens (Densmore *et al.*, 1997; Korup *et al.*, 2010; Parker *et al.*, 2011). Variations in the mechanisms and hillslope location of landslides are also dependent upon tectonic and climatic regimes (Densmore and Hovius, 2000; Meunier *et al.*, 2007). The risk from landslides is significantly increased for populated areas and when indirect impacts occur, such as tsunamis, soil depletion or river channel blocking.

1.1 Global Landslide Hazards

Catastrophic and low-frequency landslides often receive the greatest media attention, although the cumulative effects of smaller and more frequent landslides have significant social and economic implications. Recognised as the most widespread natural hazard on

Earth (McGuire *et al.*, 2002; Bryant, 2004), landslides cause billions of dollars worth of damage and thousands of deaths each year (Hong *et al.*, 2006). The significance and documentation associated with landslide hazards is also often undervalued given their common association with other triggering events such as earthquakes, typhoons or volcanic eruptions. It should be noted that landslides are becoming increasingly 'quasi-natural' or 'hybrid' in origin given the effects of human activity on slope instability (Lee and Jones, 2004).

Despite the global distribution of landslide-prone slopes, the pattern of fatal landslides is strongly heterogeneous (Figure 1-1). Fatal landslides (recorded for the 7-year period from January 2004 – December 2010) show significant clusters in areas such as the southern edge of the Himalayan Arc, in the mountain chains of Indonesia and the Philippines (with 21% of global landslide fatalities combined), and in the coastal/central parts of China (also with 21% of global fatalities). The reasons for such clustering is driven by the availability of significant relief in which a landslide can occur, the availability of precipitation to trigger landslides and the density of potential victims (Petley, 2012).

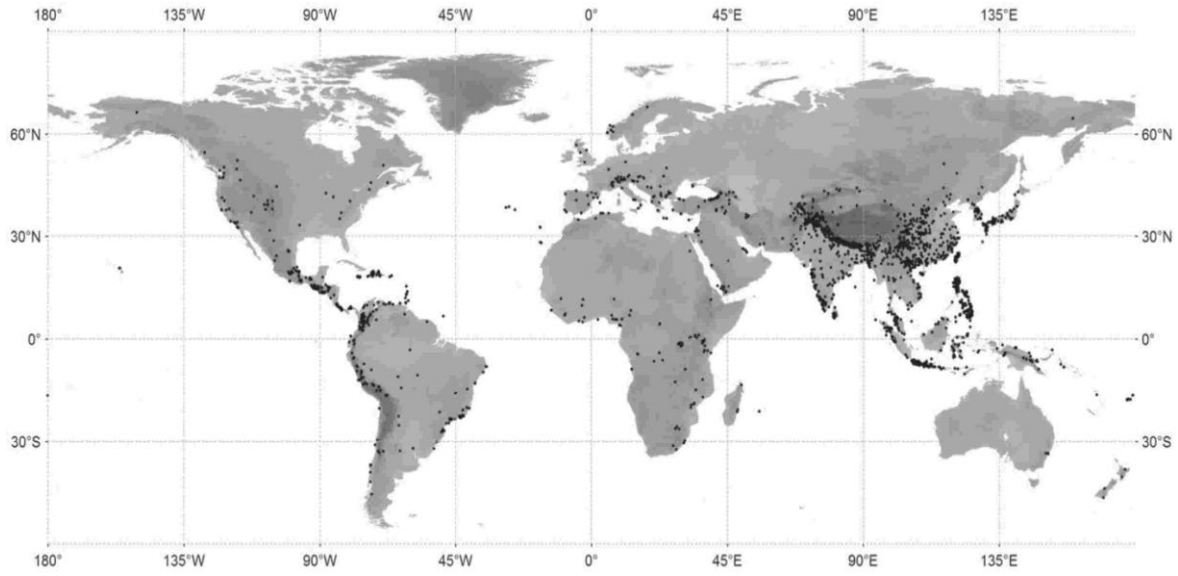

Figure 1-1: Global distribution of fatal landslides. Each dot represents a single fatal landslide. Clustering of fatal landslides is attributed to areas of high relief, heavy precipitation and population density. Note this database explicitly excludes coseismic landslides due to the high levels of uncertainty associated with these events (Petley, 2012).

The impact of these geohazards is highly dependent upon the economic development of the affected country. The vast majority of landslide-related casualties occur in less developed countries whereas economic losses are concentrated in more developed nations (Gutiérrez *et al.*, 2010). Using economic losses as an indicator of landslide impact would

significantly alter the spatial pattern shown in Figure 1-1, although economic losses are also relatively higher in less developed countries given the cost constitutes a higher proportion of a country's national income.

This study focuses on the Three Gorges region, central-eastern China, in an area shown to have a high landslide concentration (Figure 1-2) as well as a history of fatal landslides (e.g. Wang *et al.*, 2004). The less developed nature of the inhabited, yet rural study area means that many other economic and social factors can outweigh the risk of living on or close to unstable slopes. Additionally, the displacement of entire village/town populations to higher ground following inundation of the Three Gorges reservoir has already triggered several large landslides (Liu *et al.*, 2004). Improving understanding on the location and activity state of landslides in this region is therefore an important aim.

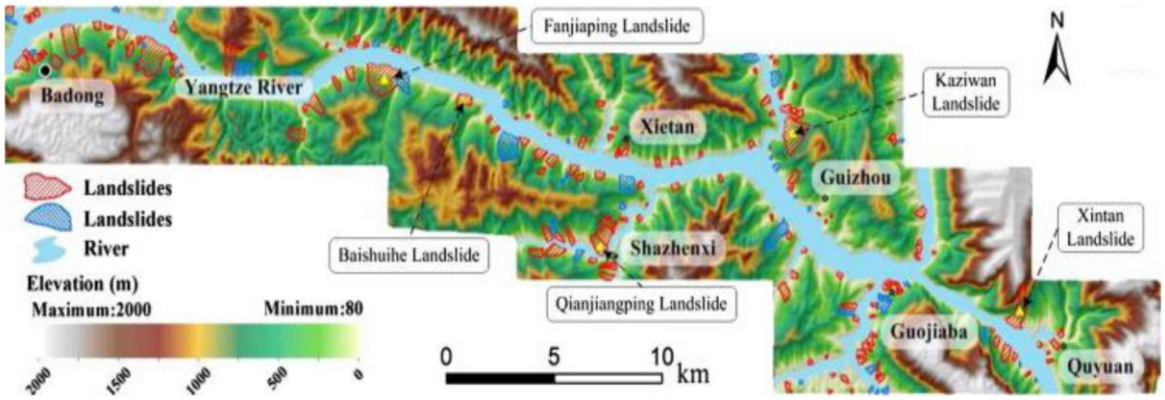

Figure 1-2: Distribution and elevation of landslides in the eastern part of the Three Gorges region (Peng *et al.*, 2014 p. 290).

1.2 Slow-Moving Landslides

While rapid landslides are the most dangerous, deep-seated and slow-moving landslides are capable of destroying buildings and infrastructure particularly on reactivated ancient landslide deposits (Sassa *et al.*, 2009). A comprehensive review of more than 50 slow- and very slow-moving landslides with varying velocities (Mansour *et al.*, 2011) shows that movement as low as 100 mm/yr can still have significant impacts through the disruption of service utilities, buckling house walls and human losses caused by building collapse.

Slow-moving landslides present many problems in the prediction of their future behaviour and are also scientifically interesting phenomena which require important consideration. Deformation within the landslide body can affect the hydrological and mechanical

properties of the sliding mass and slow-moving landslides commonly have complex and episodic responses to hydrological influences (van Asch *et al.*, 2007).

If the lifetime of a landslide follows four distinct phases (Figure 1-3), a good understanding of its current activity state is important to understand the likelihood and character of any future movements. A pre-failure stage is associated with changing stresses and internal deformation which reflect an accelerating progressive failure. This is followed by complete failure when a continuous shear surface develops through the entire landslide mass, often generating rapid displacements. Post failure relates to movement from the onset of failure until it ceases and a final reactivation stage can be observed over significant time periods when soil or rock masses slide along pre-existing shear surfaces (Leroueil *et al.*, 2001). Such reactivation is usually episodic, with limited displacements associated with each phase of movement (Lee and Jones, 2004).

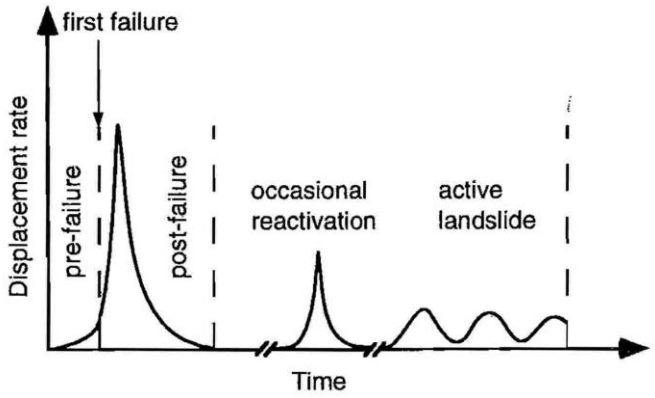

Figure 1-3: Different stages of landslide movement (Leroueil *et al.*, 1996).

This model of landslide movement matches observed movements of various landslides in the Three Gorges region. Accelerated movements of the Xintan landslide were detected as a pre-failure warning, allowing the town to be evacuated before its catastrophic failure in 1985 (Xue, 2009). The ancient deposits of the Shuping landslide have also been reactivated and experience episodic displacements of relatively small magnitudes (Wang *et al.*, 2013b).

Landslides, mainly deep and slow-moving, are the most frequent and widespread geohazard in the Three Gorges region, predominantly caused by high slope gradients, geological weaknesses, heavy summer rainfall and human activities (Liu *et al.*, 2004). Over the last decade, construction of the Three Gorges Project (TGP) has created a 600 km long reservoir with a bi-annually fluctuating water level (range ≈ 30 m) which has been shown to reactivate ancient landslides (Wang *et al.*, 2008a).

Even prior to the construction of the TGP, slow-moving landslides had been identified and monitored in the region. In the case of the Xintan landslide, a 7-year ground-monitoring campaign documented the gradual and step-wise increase in very slow landslide behaviour before its catastrophic failure on 12th June 1985 (Du *et al.*, 2013). The long-term prior monitoring and subsequent awareness of the landslide prevented any loss of life during its sudden failure due to adequate understanding, warning and evacuation.

Reactivated landslides can be triggered much more readily than first-time failures (Lee and Jones, 2004) and ancient landslides with the potential for reactivation have been identified in the Three Gorges region. Knowledge of reactivated landslide behaviour is limited and could be improved if regular high precision measurements were available over time periods of years rather than the most published timescales of days – months (Massey *et al.*, 2013). An improved understanding of the behaviour of currently deforming slopes should help inform and protect communities living on these landslides.

1.3 Remote Monitoring of Landslides

In the best cases of landslide management, Early Warning Systems (EWS) have been developed and employed to minimise harm and loss. The nature of EWS and the landslide risk is strongly dependent upon landslide type, classified by the initial mechanism of motion and the associated velocity. Whilst an EWS is composed of several social and technical components, one aspect involves the detailed monitoring of potential hazard(s).

This thesis uses the term 'landslide monitoring' in reference to numerous steps which can improve knowledge of local landslide risks. Landslide monitoring therefore involves the: (i) detection; (ii) rapid mapping; (iii) characterisation; and (iv) long-term monitoring of landslides (Tofani *et al.*, 2010). Each of these four stages must be achieved for landslide monitoring to be deemed successful and this thesis aims to evaluate the use of remotely-acquired Synthetic Aperture Radar (SAR) data in monitoring slow-moving landslides.

Real-time in-situ monitoring systems can observe individual landslides (e.g. Malet *et al.*, 2002; Li *et al.*, 2010) but are costly to operate over large areas and require prior knowledge on landslide locations. Regional hazard susceptibility maps are increasingly available (e.g. Bai *et al.*, 2010), although the results are strongly dependent upon the included causal factor maps. The generic benefits of using remote sensing data are well known, and a sub-report from the European SAFELAND Project (Stumpf *et al.*, 2010)

compares the merits of numerous remote sensing techniques for monitoring different types of landslides. Airborne LiDAR surveys can provide useful data in terms of spatial resolution, precision and the capacity to measure a variety of displacement rates, although the cost and logistics required for regular repeat acquisitions are barriers for its routine use.

Satellite radar imagery has been recognised as a powerful tool for measuring surface motions over large regions and offers the capability to remotely monitor unstable slopes (Rott, 2009; Tofani *et al.*, 2010). Synthetic Aperture Radar (SAR) images from the most recent generation of SAR satellite sensors (e.g. TerraSAR-X and COSMO SkyMed) can acquire regular data (up to every four days), over regional areas (e.g. 10 – 1000 km^2), at a high resolution (up to 1 m ground resolution) and in the case of slow-moving landslides, can potentially meet the four requirements of landslide monitoring mentioned above. The relatively short repeat interval and the ability to collect data over many years may also help reveal patterns of slow-moving landslide displacement which has previously been difficult because of limitations with data recording facilities (Mansour *et al.*, 2011). Whilst the repeat interval may not be short enough to provide timely warnings to vulnerable populations, it is possible to detect individual landslide accelerations over large regions and then direct monitoring equipment and warning systems to areas at risk.

More detailed information on the development of remote sensing data for landslide studies is presented in Sections 2.2.3, 2.3.3, and 3.3.

1.4 Research Motivation

The measurement of superficial displacement induced by slope failure is often the most useful information to define its behaviour, particularly when observations can be compared with likely triggering factors in the region (Tofani *et al.*, 2013). Rapid advances in the capability of satellite sensors and available processing algorithms have led to an exponential growth in the number of landslide studies using SAR imagery although the application of Differential Interferometry (D-InSAR) techniques for the monitoring of slow-moving landslides is still a relatively new and challenging topic.

Many limitations either related to the specification of the SAR missions (e.g. incidence angle, revisit frequency, spatial resolution) or the properties of the landslides (e.g. densely vegetated, in areas of high rainfall, exhibiting relatively large non-linear movements) make the application of such techniques difficult (Farina *et al.*, 2006). An insufficient

appreciation of the theoretical constraints associated with SAR data, coupled with the complexities of landslide movements can result in significant misinterpretations of D-InSAR results (Colesanti and Wasowski, 2006; Peduto *et al.*, 2010). In the Three Gorges region, previous studies using SAR data to monitor the Shuping landslide over the same time period display conflicting results (Xia, 2010; Liao *et al.*, 2012; Wang *et al.*, 2013b) and this promotes further investigation into the cause of these discrepancies.

D-InSAR analyses are also limited by the amount of spatially-variable movement that can be measured over the time interval of repeated SAR acquisitions, particularly in densely vegetated regions. This might be wrongly interpreted to result from temporal decorrelation between radar signals when the real reason was a landslide movement exceeding the spatial displacement gradient. Subsequently, any D-InSAR time-series technique spanning this fast event would erroneously underestimate the landslide displacement. Such a scenario is shown to occur in the Three Gorges and motivates this research to find a complimentary technique capable of extracting verifiable landslide measurements from frequently acquired SAR images.

This study also aims to advance the use of SAR data throughout the Three Gorges region. Major technical limitations in this area include steep slopes, heavy rainfall and temporal decorrelation between SAR image acquisitions caused by rapid changes in the surface properties of very dense vegetation. Previous studies have therefore focused on installing corner reflectors around unstable slopes (e.g. Xia *et al.*, 2004) or the use of time-series D-InSAR techniques in urban areas (e.g. Wang *et al.*, 2008e). This study develops appropriate techniques and evaluates the use of remote landslide monitoring in non-urban areas resulting in greater exploitation of SAR imagery within the Three Gorges region.

Finally, the high availability of data over the Three Gorges region provides the ideal circumstances to further understand slow-moving landslides. The relationship of (potentially reactivated) landslide movements to changes in the Yangzte River water level can be assessed using archived SAR data that have been collected over the same time period as the development of the Three Gorges reservoir. The relative effects of different hydrological conditions on landslides can also be quantified through the use of 2D limit equilibrium slope stability analyses, to help further understand landslide mechanisms.

The results of this work can be divided into two categories. The first part involves significant application and evaluation of both D-InSAR and sub-pixel offset methods to monitor landslides in the Three Gorges region using a variety of SAR data modes. The

second part concentrates on the most active landslide detected (the Shuping landslide), investigating its most likely triggering mechanism(s) and failure mode.

1.5 Aim and Research Questions

It is interesting to note an increase in the scientific literature on landslides and risk mitigation has been accompanied by an increase in the number of damaging landslide events throughout the world (Gutiérrez *et al.*, 2010). The thesis focuses on various recommended aspects aimed at helping to address this coincidence: (1) Where are landslides and their exact limits? (2) What is the kinematic history of landslides? (3) Are landslides currently active? (4) What is the relevant contribution of the factors that influence landslide development? and, (5) How will landslides behave in the future? (Gutiérrez *et al.*, 2010).

This thesis focuses on evaluating various SAR data sets for the purpose of remotely investigating landslides in the Three Gorges region, China. The overall aim of this research and the associated research questions (in the order they were investigated) are outlined below.

1.5.1 Research Aim

> *To evaluate the use of frequently acquired SAR imagery for detecting, mapping, monitoring and understanding the mechanisms of slow-moving landslide hazards in the Three Gorges region.*

It is important to note this aim does not solely focus upon the use of D-InSAR techniques for landslide monitoring. D-InSAR methods are evaluated, but an alternative method using frequently acquired SAR imagery is also developed and assessed. Numerous SAR data sets with overlapping spatial extents are available over the same time period which permits detailed comparisons to be made. For each employed technique, the different data characteristics associated with the SAR imaging modes are considered, in order to determine the optimal data for the requirements of investigating landslides.

1.5.2 Research Questions

(1) To what extent can Differential InSAR (D-InSAR) methods monitor landslides in the Three Gorges region?

(2) To what extent can Sub-Pixel Offset Time-series (SPOT) techniques monitor landslides in the Three Gorges region?

(3) Can regularly-acquired SAR data be used to characterise active landslide mechanisms and determine the associated triggering factors?

(4) What are the dominant geotechnical parameters controlling slope instability?

1.6 Thesis Outline

This thesis is divided into two background information chapters which summarise the employed techniques and the study area. Three result chapters answer the above research questions in order and this is followed by a discussion/conclusion chapter which evaluates this research and provides recommendations for future work. Each chapter is briefly summarised below.

Chapter 2 reviews the theory behind SAR image formation and the general processing steps for D-InSAR methods. The associated limitations of SAR images and D-InSAR processing are outlined with a particular focus on landslide applications. Secondly, sub-pixel offset methods are explained. The historical developments specifically applied to landslide hazards are reviewed for both techniques which highlights how this research is the first study to develop pixel offset time-series methods to measure landslide movements over a period of up to four years.

Chapter 3 provides a general background to the Three Gorges region as well as documenting the hydrological triggering factors of landslides in the study area. A review of the most important remote sensing studies investigating landslides in the Three Gorges is carried out as well as presenting conflicting results which employ D-InSAR techniques for landslide monitoring. For the first time, sub-pixel offset measurements from SAR images are shown to be capable of measuring annual landslide displacements in the order of metres.

Chapter 4 focuses on answering the first research question and evaluates three different SAR data sets regarding their ability to monitor landslides within the Three Gorges region using D-InSAR techniques. Interferometric coherence is assessed, along with geometric distortions and decorrelation from episodically large landslide movements.

Chapter 5 presents the results of Sub-Pixel Offset Time-series (SPOT) techniques to answer the second research question. The three different SAR data sets are evaluated again, as well as determining the optimal sub-pixel offset processing parameters. The quality of results is also compared in relation to offsets derived from installed corner reflectors and natural point-like targets.

Chapter 6 answers both the third and fourth research questions. The ability of SPOT techniques to monitor spatially large, two-dimensional movements can help identify the possible failure mechanisms of active landslides. Comparison of displacement time-series curves with external data relating to triggering factors also helps determine the initiating factors of instability. This is further investigated with 2D limit equilibrium analysis.

Chapter 7 summarises the original findings of this research and critically evaluates the techniques used in answering the research questions. The limitations and wider implications of this study are outlined, along with recommendations on future research directions following the outcomes of this work.

Chapter 2 : Principles of D-InSAR and SAR Sub-Pixel Offsets

Advances in spaceborne geodesy over the last three decades can be characterised by three major trends. The first relates to the definition of global reference systems which enables substantial areas on Earth to be mapped from satellites acquiring data over increasingly large areas. Secondly, technological developments of the sensors onboard satellite platforms have made geodetic measurements more accurate, reduced the repeat measurement interval and increased the spatial resolution. As a result, geodetic observations have become a crucial source of information for geophysical interpretation leading to a better understanding of surface deformation processes such as those associated with earthquakes, volcanoes, landslides and glaciers (Hanssen, 2001).

Characteristics of radar remote sensing are significantly different to those of optical images. Operating at microwave frequencies in the electromagnetic spectrum, Synthetic Aperture Radar (SAR) images reflect the electrical and geometrical properties of the surface, providing all-weather imaging capabilities independent of solar illumination (Massonnet and Feigl, 1998; Fletcher, 2005). As the number of published studies using SAR data continue to grow exponentially, Differential Interferometric techniques applied to SAR images (D-InSAR) have been transformed from a largely interpretive science to a quantitative tool (Rosen *et al.*, 2000). This enables surface deformation to be measured with increasing levels of precision and has revolutionised a range of earth science fields (Bürgmann *et al.*, 2000).

Given the wealth of currently available literature on D-InSAR and its applications, this chapter specifically outlines elements of SAR image formation and D-InSAR processing most relevant to landslide studies. A review of significant developments in landslide-related applications using radar remote sensing is also provided. Finally, SAR sub-pixel offset techniques are introduced and evaluated, followed by a review of major developments in this field. These are shown to be associated with seismic and volcanic case studies, although such techniques have only been applied to landslides very recently.

2.1 Synthetic Aperture Radar

Synthetic Aperture Radar is a pulsed radar system that alternates between transmitting a pulse and receiving echoes of electromagnetic frequency. Images are produced by actively illuminating the ground and receiving the reflected energy from targets, the amplitude of which depends on the local incidence angle, roughness and dielectric properties of the surface. A SAR system uses a side-looking configuration to avoid ambiguous returns from either side of the satellite flight path (Figure 2-1), whereby the timing of the returned echoes relates to the range (i.e. distance) of the target from the sensor.

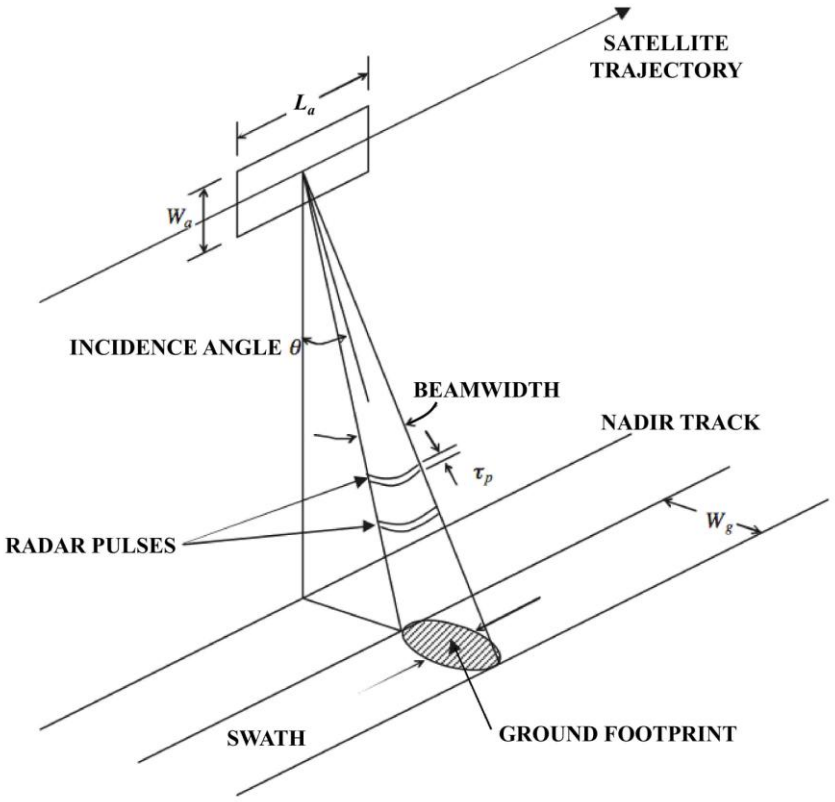

Figure 2-1: The configuration of a regular SAR antenna and its imaging footprint, reproduced from Curlander and McDonough (1991). L_a = antenna length, W_a = antenna width, θ = incidence angle, τ_P = transmitted pulse duration, W_g = swath width.

Common radar frequencies and wavelengths include X band (~0.03 m or ~10 GHz), C band (~0.06 m or ~5.3 GHz) and L band (~0.24 m or ~1.25 GHz). Backscatter is strongly dependent upon the SAR wavelength (λ) as this determines the relative roughness of the imaged surface, and when combined with the different satellite platform orbital cycles, can influence the choice of SAR data used for a particular application (Table 2-1).

Table 2-1: List of SAR satellite missions and the viewing/orbit parameters.

Frequency Band	SAR Satellite	Lifetime	Ground Range Resolution (m)	Incidence Angle (°)	Swath Width (km)	Repeat Cycle (days)
L	JERS-1	1992 – 1998	18	35	75	44
	ALOS PALSAR-1	2006 – 2011	10 - 100	8 – 60	30 – 350	46
	ALOS PALSAR-2	2014 -	3 - 100	8 – 70	25 – 490	14
S	HJ-1C	2012 -	20	25 – 47	100	4 – 31
C	ERS-1	1991 – 2000	20	23	100	3/35/336
	ERS-2	1995 – 2011	20	23	100	35
	RadarSat-1	1995 – 2013	8 – 100	20 – 49	45 – 500	24
	ENVISAT ASAR	2002 – 2010	20 – 150	15 – 45	100 – 400	35
	RadarSat-2	2007 -	3 – 100	20 – 49	10 – 100	24
	Sentinel-1A	2014 -	5 – 40	20 – 45	20 – 400	12
X	TerraSAR-X	2007 -	1 – 18	20 – 55	10 – 100	11
	COSMO SkyMed	2007 -	1 – 100	25 – 50	10 – 200	1 – 16
	TanDEM-X	2010 -	1 – 18	20 – 55	10 - 100	11
	KOMPSAT-5	2013 -	1 – 20	20 – 45	5 – 100	28

More detailed information can be found in comprehensive reviews of SAR image processing by Curlander and McDonough (1991), Bamler and Hartl (1998), Massonnet and Feigl, (1998), Bürgmann *et al.* (2000), Rosen *et al.* (2000), Hanssen (2001) and Richards (2009).

2.1.1 Range and Azimuth Resolution

Resolution in range direction (r_g) from a single radar pulse is dependent upon the transmitted pulse duration (τ_P) as the ability to separate targets from the received signal will be impossible if echoes overlap (Equation 2-1):

$$r_g = \frac{c\,\tau_P}{2\,\sin\theta}$$

Equation 2-1: Ground range resolution for real aperture radar without the use of chirp pulses.

where c is the speed of light and θ is the local incidence angle.

Whilst very short pulse durations would increase range resolution, the transmitted energy would be below the radar's sensitivity. Using linearly frequency modulated (FM) pulses (i.e. chirps), shorter effective pulse lengths are achieved, inversely proportional to the chirp bandwidth ($1 / B_R$). Therefore the ground resolution (r_g) can be improved without reducing transmission power (Equation 2-2):

$$r_g = \frac{c}{2\, B_R\, \sin\theta}$$

Equation 2-2: Ground range resolution for synthetic aperture radar which employs chirp pulses.

where B_R is the bandwidth of the chirp pulses.

With the ENVISAT ASAR sensor, a chirp bandwidth of 16.5 MHz and scene-centre incidence angle of 23° results in a ground range resolution of ~23 m. For the TerraSAR-X satellite, the high-resolution Spotlight mode has a chirp bandwidth of 300 MHz and a scene-centre incidence angle of 44°. This generates a ground range resolution of ~0.70 m.

Azimuth resolution (Azi_g) (spatial resolution in the direction parallel to the satellite motion) in real aperture radar systems is calculated by Equation 2-3:

$$Azi_g = \beta\, R_0$$

Equation 2-3: Real aperture radar azimuth resolution, determined by the beamwidth ($\beta = \lambda / l_a$) and range distance.

where β is the azimuth beamwidth and R_0 is the target distance in range.

Therefore azimuth resolution deteriorates across the swath width from near to far range. Due to the dependence upon range and antenna length, the achievable resolution from real aperture radar is only satisfactory for airborne platforms rather than satellite sensors.

Using the Doppler frequency shift of the received pulses, induced from the satellite along-track motion illuminating a target for longer (Figure 2-2), the azimuth resolution limit is equal to half the antenna length (Equation 2-4):

$$Azi_g = l_a / 2$$

Equation 2-4: Azimuth resolution, determined by half the length of the antenna (l_a).

However, to unambiguously sample the Doppler spectrum, the Doppler bandwidth must not exceed the pulse repetition frequency (Hanssen, 2001). The maximum Doppler bandwidth (B_D) is calculated as (Equation 2-5):

$$B_D = 2v\beta / \lambda = 2v / l_a$$

Equation 2-5: The maximum variation of Doppler frequency during illumination from the SAR antenna.

where v is the satellite orbiting velocity, β is the azimuth beamwidth, λ is the radar wavelength and l_a is the length of the real antenna. Given B_D is dependent upon the beamwidth, the antenna length cannot be reduced beyond a threshold limit.

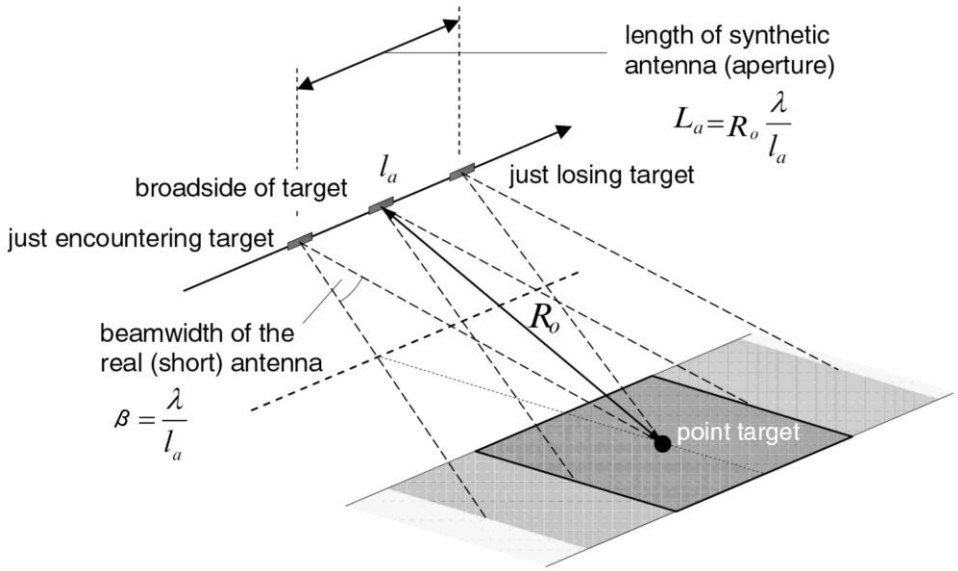

Figure 2-2: The synthetic aperture (antenna) generated by the platform motion of a SAR sensor. The antenna footprint is shown as rectangular for simplicity (Richards, 2009 p. 62).

For the ENVISAT ASAR sensor with an antenna length of ~10 m, the maximum achievable azimuth resolution is ~5 m. With an orbiting velocity of 7.45 km/s, the Doppler bandwidth is therefore 1500 Hz, below the typical pulse repetition frequency of 1650 Hz for the Image Swath 2 (IS2) imaging mode.

After SAR focusing, the radar image is a two-dimensional matrix carrying amplitude and phase information associated with each pixel, the spacing defined by the ground range and azimuth resolution. The coherent imaging property of the radar means both the amplitude of the returned signal and its phase component are recorded as complex numbers in Single Look Complex arrays (Figure 2-3). Since the range resolution cell is very large relative to the SAR wavelength, a single pixel is likely to contain thousands – millions of individual targets resulting in random phase values throughout an SLC image. A modulo 2π ambiguity also prohibits exact distance measurements from sensor to target. Interferometric SAR (InSAR) differences two SAR images with the intention of cancelling

this unpredictable phase response, assuming coherent behaviour of the ground pixel over the time period of image acquisitions.

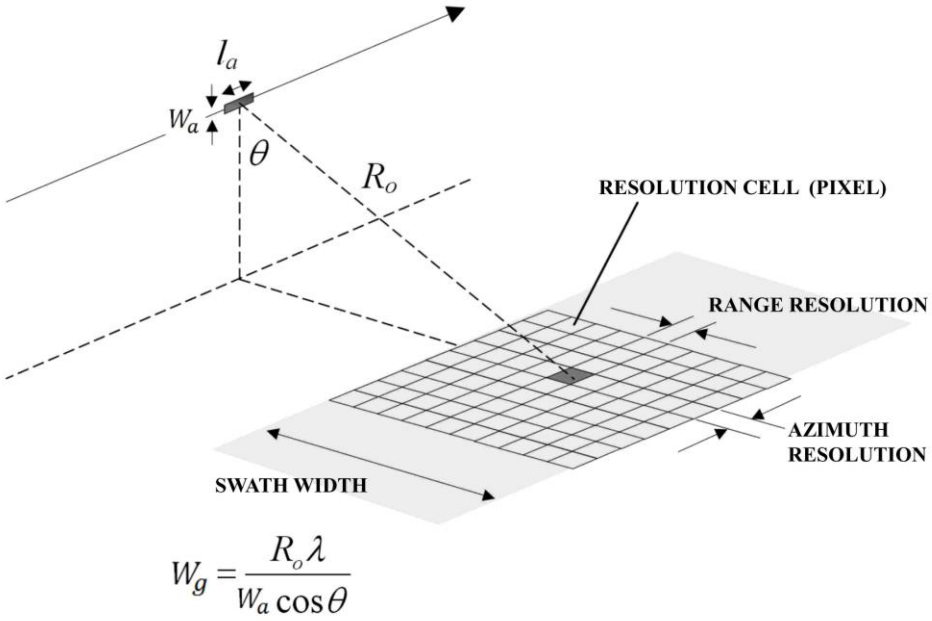

Figure 2-3: Single Look Complex (SLC) image matrix, defined by the ground range and azimuth resolution. Adapted from Richards (2009 p. 69).

2.1.2 Speckle

The amplitude of a SAR image is also dependent upon the relationship between target size, image resolution and SAR wavelength. When a large reflective surface exists within the resolution cell, its amplitude appears very bright compared to objects that restrict the reflected energy and appear dark. Such dominating objects relative to the image resolution are known as point-like targets and may consist of passive objects (e.g. buildings, bridges) or specifically installed devices (e.g. corner reflectors or transponders).

However, natural terrain targets such as grass, forest trees and loose debris are typically smaller than the resolution cell. In such cases, the echo from one pixel is therefore the superposition of multiple individual echoes and in the same way phase values can vary randomly throughout an image, the amplitude may also be highly varied leading to 'speckle'. Whilst methods exist to reduce speckle in amplitude images, the accuracy of SAR sub-pixel offset measurements can be improved when coherence is retained and the speckle pattern of two images is correlated due to the increased contrast in backscatter (Strozzi *et al.*, 2002). For incoherent image pairs, sub-pixel offset measurements are still feasible, but require larger image matching patches (explored further in Section 2.3).

2.1.3 Spotlight Imaging Mode

Generally landslides are small features in comparison to the length and width of SAR image frames. For such small features where strong spatial filtering would obscure landslides, the highest resolution images are optimal to increase interferometric coherence, raise the spatial displacement gradient threshold and improve the precision of SAR sub-pixel offset measurements. Spotlight SAR operational modes can achieve a higher resolution in the azimuth direction compared with Stripmap imaging modes (Figure 2-4).

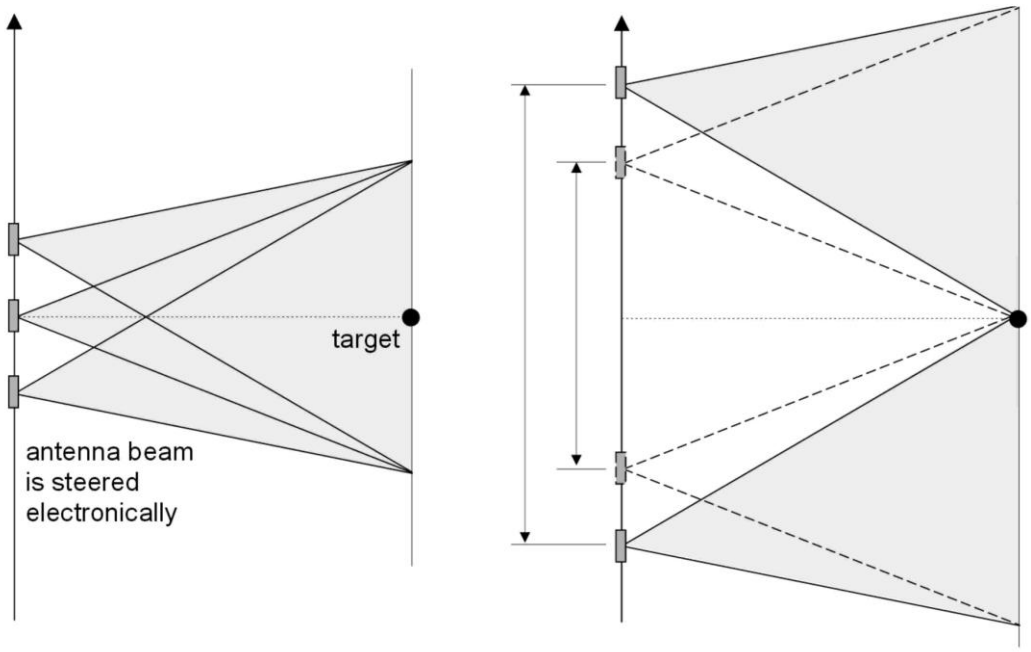

Figure 2-4: Geometry of the Spotlight SAR imaging mode. A larger synthetic aperture length is created by steering the sensor to focus on a small footprint for a longer period of time, increasing the azimuth resolution. The right-hand diagram indicates the increased synthetic antenna length which results from antenna steering in Spotlight mode, compared with a static antenna in Stripmap mode (Richards, 2009 p. 74).

The antenna is steered throughout the image acquisition from forward to backward as the satellite platform moves along track. A larger synthetic aperture length is achieved which therefore improves resolution of the azimuth pixel spacing (Eineder *et al.*, 2009; Ren *et al.*, 2012). For example TerraSAR-X Spotlight data have an azimuth resolution of ~1 m, compared to the Stripmap data equivalent of ~3 m. Greater detail can be achieved for landslide studies with the use of a Spotlight imaging mode, although the high resolution of the target region is only possible at the expense of resolution (i.e. areal coverage) in the remainder of the imaged domain. As such, this mode is most beneficial to target known landslide areas rather than identifying landslides over a wider region.

2.1.4 Geometrical Image Distortions

For all image modes, the side-looking configuration of the SAR sensor has implications for image distortions. As range measurements reflect the sensor – target distance, significant topography causes various geometrical problems limiting the use of SAR imagery. The main distortions are termed the layover effect and shadowing (Figure 2-5).

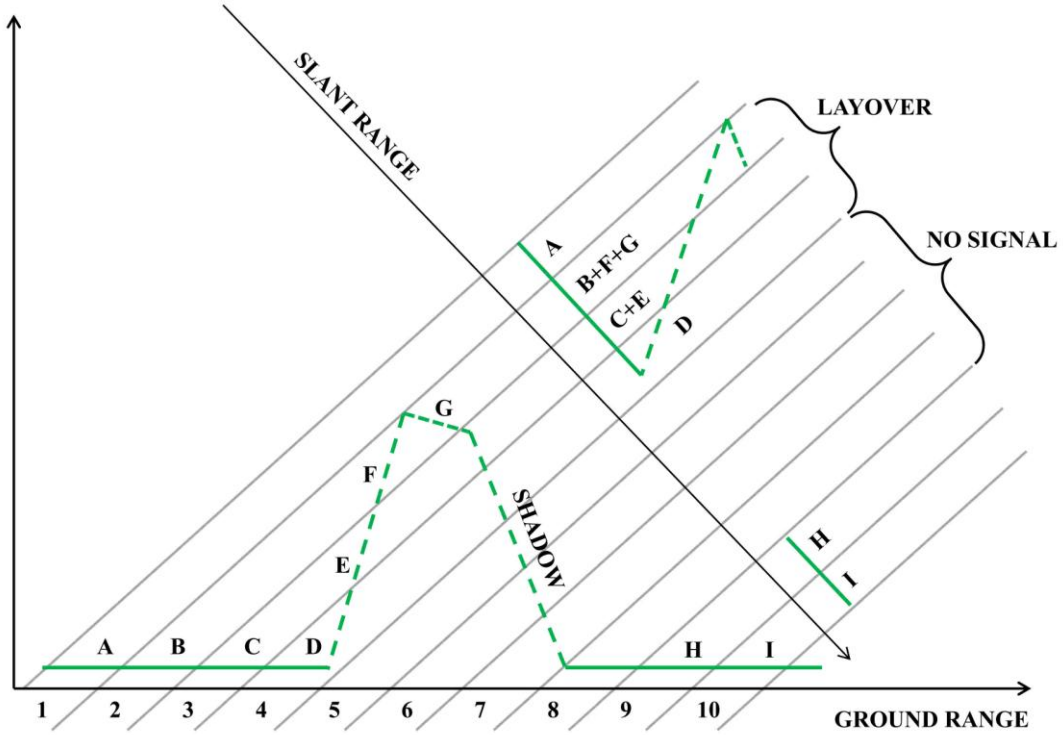

Figure 2-5: Layover and shadow effects. Depending on the terrain slope and the viewing geometry, layover exists when targets at increasing ground range positions are imaged in reverse order by the SAR system (e.g. points D, E and F). Targets not illuminated by the radar (i.e. in shadow) lead to dark gaps in the radar image. Reproduced from Ferretti *et al.* (2007 p. A-12).

Layover is caused by different ground targets having the same range distance/time, resulting in multiple targets being mapped into the same resolution cell in the slant range SLC image. Layover is dependent upon the local incidence angle and range resolution of the SAR sensor. It can be further divided into active layover (points producing layover effects) and passive layover (points upon which active layover is imposed) (Kropatsch and Strobl, 1990). Often layover areas appear bright in amplitude images whereas shadows are markedly dark regions where targets are not illuminated by any radar beam (either due to the local incidence angle exceeding 90° or being blocked by another object). Foreshortening exists when the terrain slope is towards the sensor line-of-sight which

increases the ground range cell dimension. Layover is an extreme form of foreshortening when the terrain slope exceeds the look angle of the sensor.

Areas of foreshortening, layover and shadow display unreliable pixel values, reducing the likelihood of successful D-InSAR and SAR sub-pixel offset results (Gelautz *et al.*, 1998; Colesanti and Wasowski, 2006; Plank *et al.*, 2012). Given the majority of landslide sites are in steep terrain, the imaging mode and SAR satellite configuration is an important consideration prior to ordering data. In contrast to these problems, slopes facing away from the SAR sensor (at inclinations less than the incidence angle) are imaged at higher resolutions and are often best suited for monitoring landslides (Strozzi *et al.*, 2010).

2.2 Differential Interferometry (D-InSAR)

SAR interferometry is based upon the differencing of phase components between two SAR images acquired at different times or from slightly different viewing positions to generate an interferogram (for more information, see Bamler and Hartl, 1998; Massonnet and Feigl, 1998; Bürgmann *et al.*, 2000; Rosen *et al.*, 2000; Hanssen, 2001). If the satellite orbit and imaging geometries of two SAR images are identical, any phase difference in the interferogram is caused by changes over the time of the SAR system clock, variable propagation delay or surface motion in the radar line-of-sight (LOS) (Rosen *et al.*, 2000). However, because orbit positions are rarely this precise, interferograms commonly contain both topographic information as well as surface motion. Removal of topographic fringes using an external digital elevation model (DEM) (Massonnet *et al.*, 1993b) is now commonplace, with the aim of generating a differential interferogram principally containing ground displacement information. This is the basis of differential interferometry (D-InSAR).

The residual phase ($\Delta\phi_{total}$) in an interferogram is proportional to the SAR wavelength (λ) and the difference in the range distance between satellite passes. This range difference is made up of numerous components (Equation 2-6):

$$\Delta\phi_{total} = \Delta\phi_{pos} + \Delta\phi_{topo} + \Delta\phi_{disp} + \Delta\phi_{atm} + \Delta\phi_{noise}$$

Equation 2-6: The components of residual phase (Wasowski and Bovenga, 2014).

where $\Delta\phi_{pos}$ is the sensor position, $\Delta\phi_{topo}$ is the ground elevation, $\Delta\phi_{disp}$ refers to displacement, $\Delta\phi_{atm}$ is path changes in atmospheric refractivity and $\Delta\phi_{noise}$ are decorrelation sources.

Through the use of satellite orbit data and independent elevation models, the first two terms of Equation 2-6 can be minimised leaving contributions from displacement, atmospheric differences and decorrelation. Whilst decorrelation sources remain significant (outlined in Section 2.2.2), atmospheric effects are likely to be smaller than displacement signals for individual landslide studies given the localised nature of landslides relative to the scale of long-wavelength atmospheric effects (Liu *et al.*, 2013).

2.2.1 Processing Overview

Many open source and commercial software packages exist to generate a differential interferogram from two SAR images (e.g. ROI_PAC, DORIS, GMTSAR, NEST, GAMMA, SARscape), which all follow a similar general procedure (Figure 2-6).

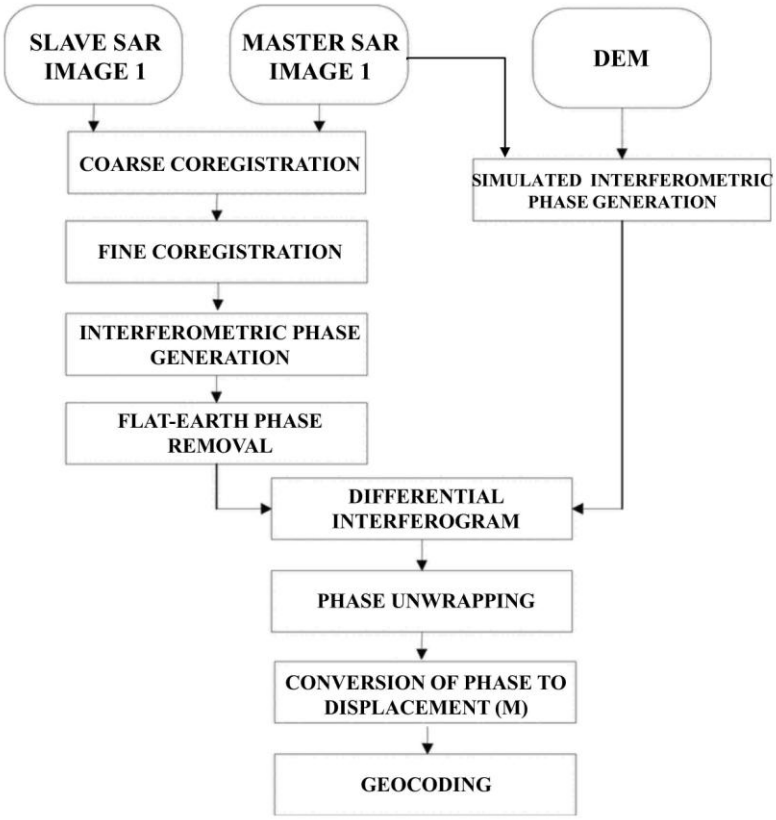

Figure 2-6: A typical D-InSAR processing chain, reproduced from Dong and Huang (2011).

After generating SLC images acquired at different times, the first step of coregistration requires alignment of these images with sub-pixel accuracy such that phase interference is related to the same ground target. In the ideal case of parallel orbits and aligned acquisitions, coregistration would only need to compensate for the differing geometry due

to the different view angle, however in practice coregistration should account for orbital crossing and shifts in attitude and/or velocity (Ferretti *et al.*, 2007). Coregistration is usually achieved using a gross shift estimate from the image acquisition times and orbital information, followed by a coarse coregistration calculated from windowed cross-correlation results from numerous points throughout an image. Once the relative shifts between two SAR images have been determined within tens of pixels in azimuth and a few pixels in range, fine coregistration is performed to obtain an accurate transformation to resample the slave image onto the master geometry.

To generate the interferogram, each complex pixel of the master image is multiplied by the complex conjugate of the same pixel in the slave image, differencing the phase and making it possible to measure accumulated displacement between observation times (Bürgmann *et al.*, 2000). Phase contributions from the Earth's curvature and topography must also be subtracted to generate the differential interferogram.

At this stage it is also recommended to apply filtering to reduce the noise in the interferogram and to enhance the signal prior to phase unwrapping. Goldstein and Werner (1998) proposed a filter which adapts to the local phase gradient, enhancing the components with the highest power. However, a stronger filter reduces the resolution of interferometric phase. This has been modified to incorporate interferometric coherence (Baran *et al.*, 2003), ensuring low coherence areas are filtered more and the maximum resolution in high coherence areas is maintained.

An important condition of interferometry assumes the complex reflectivity of the pixel as a whole (i.e. the reflectivity of all targets and their sensor-target distance) does not change in the time between image acquisitions, therefore cancelling out in the interferometric phase (Colesanti and Wasowski, 2006). In such circumstances the process would not suffer any decorrelation, otherwise known as full coherence.

The degree of coherence within an interferogram is measured as the magnitude of the complex cross-correlation between radar signals (Equation 2-7):

$$\gamma = \frac{|\langle s_1 s_2{}^* \rangle|}{\sqrt{\langle s_1 s_1{}^* \rangle \langle s_2 s_2{}^* \rangle}}$$

Equation 2-7: Interferometric coherence (γ) calculated from time-separated radar signals (s_1 and s_2).

Ideally, the coherence should be obtained using an ensemble average from a record of simultaneous observations for each pixel, requiring a large number of interferograms acquired in identical circumstances. However this procedure is not feasible as every full-

resolution element is observed only once during each SAR acquisition (Hanssen, 2001). Therefore, spatial averaging is used (shown by $\langle \quad \rangle$ in Equation 2-7), typically using small windows (e.g. 5 x 5 pixels). Point-like stable targets have a coherence $\gamma \rightarrow 1$ whereas independent and uncorrelated signals result in incoherent areas $\gamma \rightarrow 0$. Pixels may become incoherent for a variety of reasons, as described in the following section.

2.2.2 Decorrelation Sources

In reality, a residual differential reflectivity term always affects the interferometric phase, referred to as decorrelation noise (Equation 2-6). Defining decorrelation as the noise caused by error sources with a correlation length smaller than the coherence estimation window (Hanssen, 2001), the main contributions reducing coherence include large differences between SAR acquisitions in terms of viewing geometry, Doppler centroid, volume scattering or rates of surface movement (Equation 2-8):

$$\gamma = \gamma_{spatial} * \gamma_{temporal} * \gamma_{thermal}$$

Equation 2-8: Components of coherence include spatial terms (geometric γ_{geom} and Doppler centroid γ_{DC} coherence), temporal coherence and thermal noise (Zebker and Villasenor, 1992).

Spatial ($\gamma_{spatial}$) and temporal ($\gamma_{temporal}$) decorrelation sources are explored below, whereas thermal noise ($\gamma_{thermal}$) is assumed negligible and insignificant (Bürgmann *et al.*, 2000). Determining the dominant cause of decorrelation is often difficult and whilst time-series D-InSAR techniques have been developed to identify slowly decorrelating pixels (e.g. Hooper *et al.*, 2007; Hooper, 2008), resolving episodic and time-varying landslide displacements remains a difficult task.

2.2.2.1 Geometric Decorrelation

The cross-track orbital separation is referred to as the interferometric baseline and a critical parameter is the perpendicular baseline ($B_{\perp}$), defined as the baseline component perpendicular to the SAR slant range direction. Complete decorrelation across an interferogram will occur if the perpendicular baseline exceeds a maximum threshold. The perpendicular baseline controls the phase change associated with changing incidence angles and therefore larger baselines result in a more sensitive interferometer and increasing topographic fringe frequency. However, if the phase change across a resolution element is greater than 2π (due to an excessively large antenna baseline), the interferometric signal decorrelates and prohibits the use of the interferogram (Gatelli *et al.*, 1994; Bürgmann *et al.*, 2000). This becomes clear from a plot of theoretical phase difference across a flat earth

in relation to a range of perpendicular baselines (Figure 2-7), using the physical parameters of the ERS satellite (altitude = 785 km, incidence angle = 23°, ground range resolution = 25 m and wavelength = 0.056 m). Whilst the theoretical limit is reached when a 2π change occurs within a single resolution cell, the reconstruction task gets increasingly difficult up to the point when it becomes impossible.

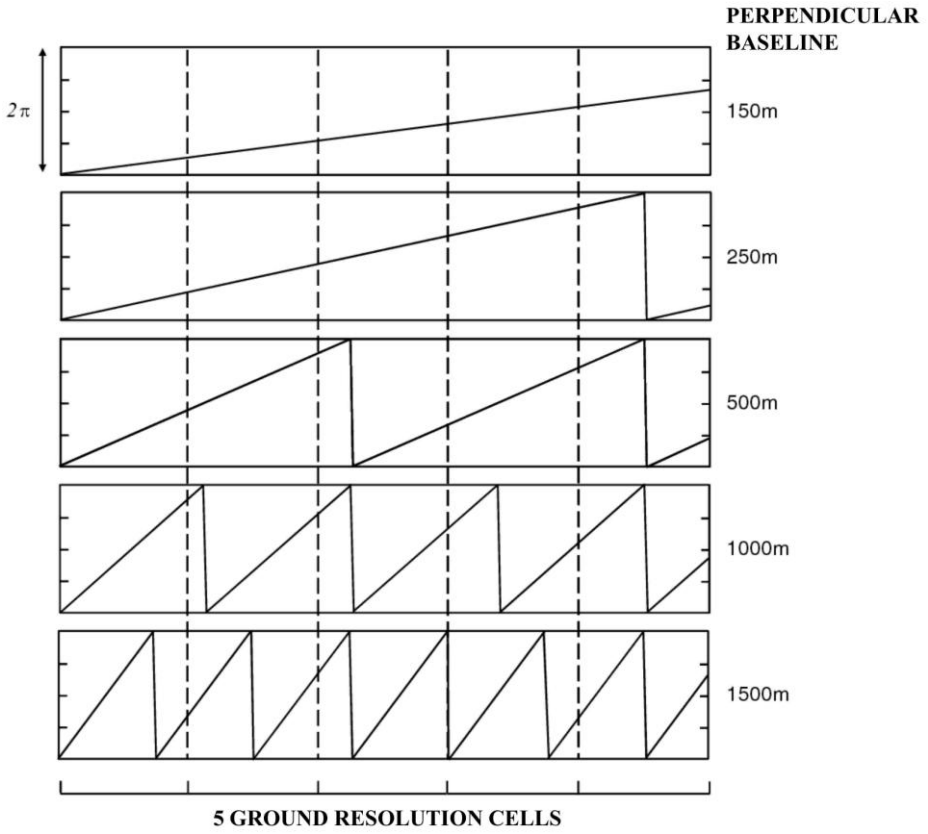

Figure 2-7: Interferometric phase difference for the ERS configuration across a flat earth distance of 5 ground range pixels. 2π jumps can be compensated for with small baselines. However, for baselines exceeding 1000 m, at least one phase jump exists within each ground resolution cell (Richards, 2009 p. 194).

The critical baseline (above which the change in look angle between the two satellite passes is large enough to cause the pixel backscatter to be completely uncorrelated) is dependent upon the wavelength and incidence angle of the SAR sensor and topographic slope of the imaged ground features (Equation 2-9):

$$B_{critical} = \frac{\lambda R_0}{2 r_g \cos(\theta - Sl)}$$

Equation 2-9: Critical baseline, dependent upon the wavelength (λ), range (R_0), ground range resolution (r_g), incidence angle (θ) and topographic slope (Sl).

Subsequently, geometrical decorrelation can be simply defined as in Equation 2-10:

$$\gamma_{geom} = \begin{cases} \frac{B_{critical} - B_{\perp}}{B_{critical}} & for\ B_{\perp} \leq B_{critical} \\ 0, & for\ B_{\perp} > B_{critical} \end{cases}$$

Equation 2-10: Geometrical coherence loss as a function of perpendicular baseline (Hanssen, 2001 p. 102).

For deformation studies, the lowest perpendicular baseline is optimal to minimise geometrical decorrelation and topographic errors.

2.2.2.2 Doppler Centroid Decorrelation

With geometrical decorrelation a purely range geometry phenomenon, large differences in the Doppler centroid frequencies between two SAR acquisitions can also lead to complete decorrelation. A difference in the Doppler frequencies could be caused by non-parallel satellite orbits and the coherence factor (γ_{DC}) associated with Doppler centroid differences (ΔD_C) decreases at a linear rate (Equation 2-11):

$$\gamma_{DC} = \begin{cases} 1 - \frac{\Delta D_C}{B_D} & for\ \Delta D_C \leq B_D \\ 0, & for\ \Delta D_C > B_D \end{cases}$$

Equation 2-11: Doppler centroid coherence loss as a function of Doppler centroid difference and Doppler bandwidth (Hanssen, 2001 p. 103)

The critical value is reached when the Doppler centroid is equivalent to the Doppler bandwidth. However, this is rarely a limiting factor of coherence when generating interferograms using SAR data acquired in the same mode and from the same sensor.

2.2.2.3 Temporal Decorrelation

One of the most frequent and significant limitations in repeat-pass D-InSAR used for landslide monitoring is the loss of coherence through temporal decorrelation (Herrera *et al.*, 2011; Perissin and Teng, 2012). Temporal decorrelation results from significant changes in the distribution or electrical properties of wavelength-scale scatterers within a resolution cell, between SAR image acquisitions (Hanssen, 2001). Processes such as vegetation growth, vegetation movement, erosion and cultivation can cause scatterers to become rearranged in an effectively random manner over time, resulting in the decorrelation of images (Rosen *et al.*, 2000).

Choice of sampling interval should be tuned to the deformation phenomena under investigation as coherence can be lost incredibly quickly (e.g. over hours-days for glacier flow) although this is dictated by the orbit cycle of the various SAR sensors. Consequently, areas of exposed bedrock and urban areas have been the focus of most D-InSAR studies as these features often maintain interferometric coherence over long time-spans.

Variation in the SAR wavelength is also a factor determining the levels of temporal decorrelation. C-band interferograms display higher fringe rates and decorrelate relatively easily in lightly vegetated areas whereas L-band interferograms are commonly reported as providing more coherent results as the longer wavelength can penetrate further through vegetation (Zebker *et al.*, 1997; Strozzi *et al.*, 2003; Metternicht *et al.*, 2005; Bovenga *et al.*, 2006). However, the choice of a longer wavelength decreases the sensitivity to ground movements and shorter revisiting times makes the detection of low velocity displacements more difficult (Colesanti *et al.*, 2003; Bovenga *et al.*, 2006; Herrera *et al.*, 2013).

Additionally, wavelength is not independent from the satellite revisit frequency and resolution of the SAR images. L-band sensors such as ALOS PALSAR can acquire images every 46 days and has been shown to generate better results compared with the ENVISAT sensor with a repeat cycle of 35 days. However, despite more recent sensors (e.g. TerraSAR-X) operating at shorter X-band wavelengths, the higher resolution and lower repeat interval may be beneficial for both vegetated and faster moving landslides.

Temporal decorrelation is difficult to estimate within a single interferogram, although it is possible if other decorrelation components can be isolated and subtracted from the total coherence equation (Equation 2-8) (Ahmed *et al.*, 2011). Using a stack of SAR images, amplitude and phase characteristics can be observed over time providing an estimate of the phase stability of a pixel and hence its degree of temporal decorrelation. This provides the basis upon which most persistent scatterer time-series D-InSAR algorithms operate.

2.2.2.4 Spatial Displacement Gradient and Scale Constraints

A very significant factor leading to complete decorrelation is the spatial displacement gradient measureable by interferometry. To reliably observe interferometric fringe patterns without ambiguity, the maximum displacement between two neighbouring pixels in a wrapped interferogram must not exceed $\lambda / 2$ (Massonnet and Feigl, 1998), with

wavelengths (λ) typically in the order of 30 – 300 mm. D-InSAR can therefore only map displacements at the temporal and spatial scales dictated by the sensor resolution and repeat imaging interval (Massonnet and Feigl, 1998; Metternicht *et al.*, 2005). Subsequently, D-InSAR is not capable of measuring rapid slope movements, being most commonly applied to deformation phenomena within the spatial gradient limits such as very slow-moving landslides, city subsidence and earthquake deformation patterns. With the original ERS C-band sensors, the best achievable measurements were in the order of less than 0.02 m per month in areas of sparse vegetation (Canuti *et al.*, 2004). Subsequently, it is practically impossible to derive measurements of fast moving phenomena with sharp velocity boundaries such as glaciers or co-seismic deformation along faults, resulting in complete decorrelation (e.g. Figure 2-8).

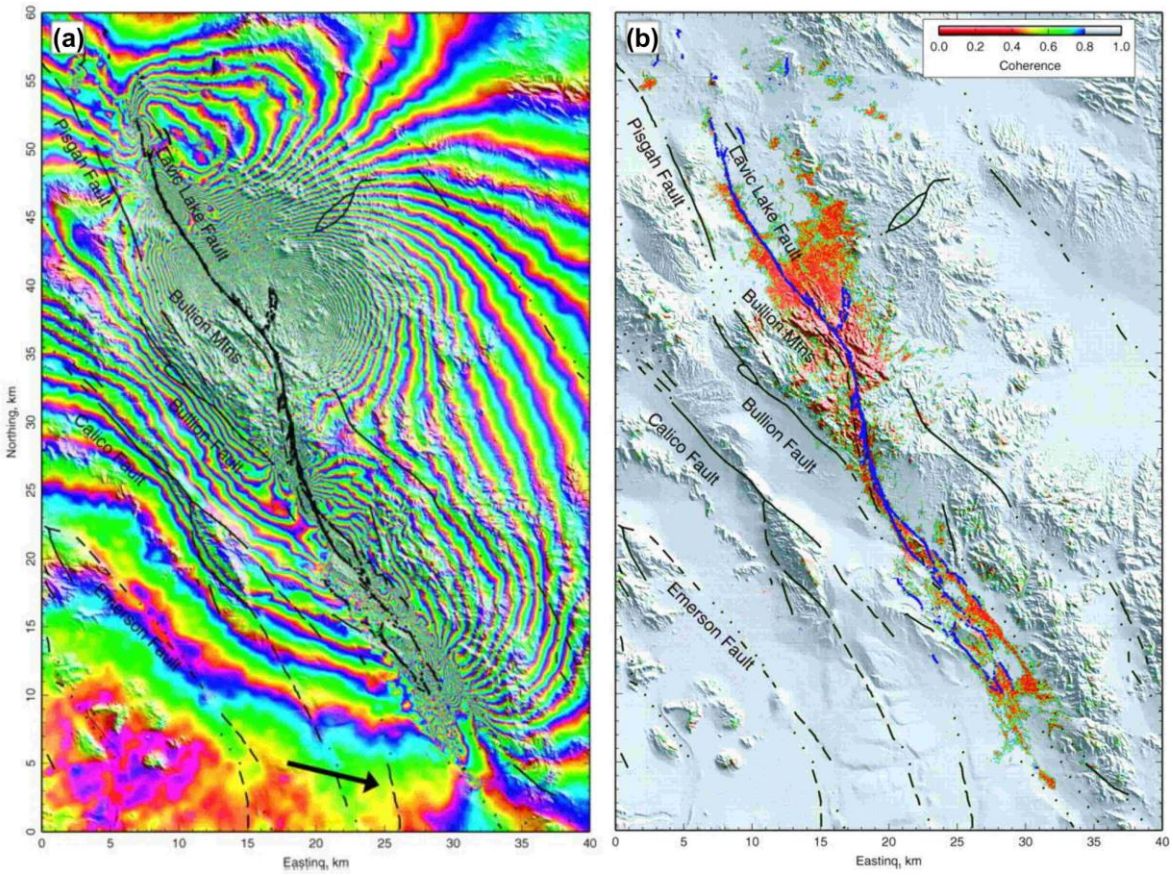

Figure 2-8(a): Wrapped phase for 1999 Hector Mine earthquake. Each colour cycle represents 0.028 m of motion in the LOS direction, indicated by the black arrow. The fringe frequency significantly increases with distance towards the fault (Simons *et al.*, 2002 p. 1392).

Figure 2-8(b): Corresponding coherence map showing decorrelation close to the fault in areas of the highest fringe frequency (Simons *et al.*, 2002 p. 1392).

Sharp boundaries between stable and unstable ground are characteristic of landslides, along with the possibility of episodic and spatially variable movements which may lead to the spatial displacement gradient being exceeded. Dependent upon the SAR wavelength,

image resolution and revisit frequency, L-band data have been preferred over shorter wavelengths due to the ability to reduce this intrinsic ambiguity of phase measurements to some extent (Strozzi *et al.*, 2005). However, the characteristics of X-band sensors are likely to be more influential given the higher revisit frequency and spatial resolution which increase the likelihood of non-linear landslide displacements (i.e. acceleration and deceleration) being resolved (Herrera *et al.*, 2011).

At the scale of a SAR image, landslides are relatively localised features and scale constraints imposed by the resolution of SAR data must finally be considered. Unstable areas should include at least a few hundred resolution cells. For a C-band imaging system, this could be 10 – 20 pixels in range and 50 – 100 pixels in azimuth which corresponds to 200 – 400 m and 200 – 400 m in range and azimuth, respectively (Colesanti and Wasowski, 2006). All these effects in terms of the spatial displacement gradient and scale constraints have been summarised in Figure 2-9, although it highlights the potential ability of higher resolution SAR data (e.g. from TerraSAR-X and COSMO SkyMed satellites) to monitor smaller and faster landslide movements than traditionally possible with older SAR sensors.

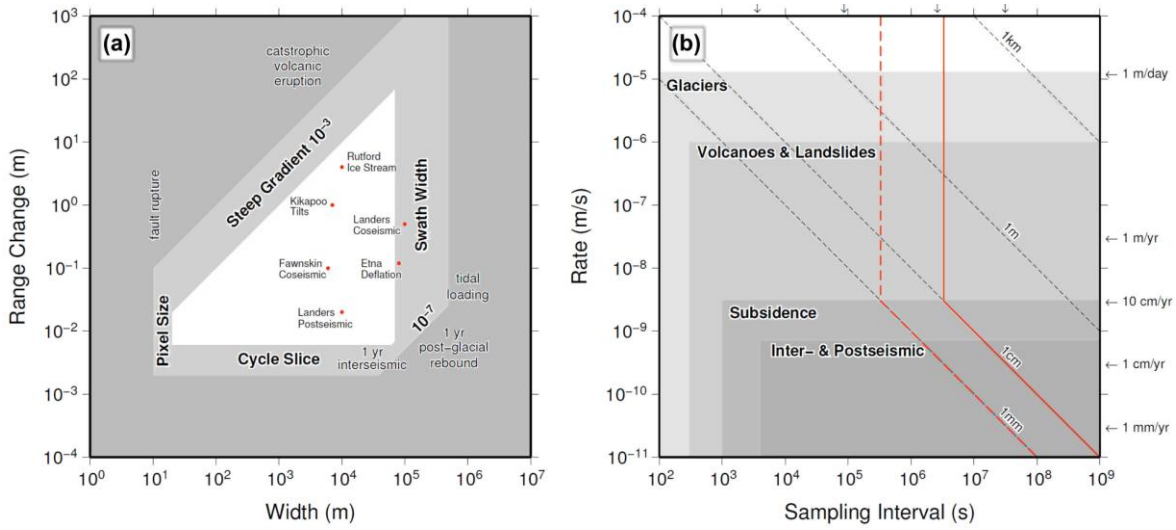

Figure 2-9(a): The range of applications for C-band deformation mapping in terms of the size and the magnitude of movement. Measurable phenomena are shown in the white polygon, whereas light grey bounding areas indicate the four limitations of (i) spatial displacement gradient, (ii) pixel size, (iii) wavelength precision, and (iv) swath width (Elliot, 2009 p. 101), adapted from Hanssen (2001) and Massonnet and Feigl (1998).

Figure 2-9(b): Classification of displacement signals by rate and duration. The product of these quantities gives the total amount of deformation in a given interval of time, shown by the black dashed lines. Detectable amounts are found to the right of the red lines for a C-band SAR sensor (Elliot, 2009 p. 101), adapted from Hanssen (2001) and Massonnet and Feigl (1998).

2.2.2.5 InSAR Time-Series Methods

A major and common limitation with traditional D-InSAR methods is the loss of coherence between image acquisitions, particularly in areas of dense vegetation. Using a stack of interferograms created by a large number of SAR images (e.g. >12), pixels with the highest signal-to-noise ratio can be selected in order for point-based measurements to be extracted from areas previously suffering from significant decorrelation. The scattering return from these pixels are normally dominated by non-vegetated objects such as bare rock, buildings or tree trunks and have led to the development of Permanent/Persistent Scatterer (PS) D-InSAR (e.g. Ferretti *et al.*, 2001; Hooper *et al.*, 2004; 2007). This characteristic has also led to the occasional installation of corner reflectors in known areas of deformation, which provide an artificially persistent response to incoming radar signals.

Using a network of 'small baseline' (SBAS) interferograms (minimising the perpendicular and temporal baselines to improve coherence) also enables time-series displacement curves and mean-velocity maps to be generated (e.g. Berardino *et al.*, 2002; Hooper, 2008). However, none of these techniques can overcome the theoretical limitations which commonly arise from geometrical decorrelation or exceeding the spatial displacement gradient and careful consideration is required to improve the validity of time-series results.

2.2.3 D-InSAR Landslide Applications

The ability to map surface displacements with centimetre-scale precision over wide areas (i.e. >tens of kilometres-wide) was first demonstrated for the coseismic and postseismic phases of the 1992 Landers earthquake, California (Massonnet *et al.*, 1993a; 1994). This technological breakthrough revolutionised the measurement of many geophysical processes, including very slow-moving landslides. The widely cited first instance of a landslide monitored using SAR interferometry is the Saint-Étienne-de-Tinée translational slope failure (Carnec *et al.*, 1996; Fruneau *et al.*, 1996), from which cm/day displacements were measured over a two week period using five ERS-1 tandem images. Subsequently, research at this time began to assess the capabilities of D-InSAR for measuring other landslides with widely varying spatial scales, velocities and controlling mechanisms (Squarzoni *et al.*, 2003; Singhroy and Molch, 2004; Catani *et al.*, 2005).

Rott *et al.* (1999) applied a similar D-InSAR technique to a far slower moving landslide (cm/year) in the Austrian Alps, concluding D-InSAR can generate complementary information to conventional ground-based techniques by providing spatially continuous

maps of surface deformation capable of highlighting inter-annual variations on landslide movements. However, some currently well-known benefits and limitations were also proposed for the first time.

D-InSAR has been employed to monitor the slow motion of many landslides and compared with (typically sparse) GPS point measurements (e.g. Wen-Yen *et al.*, 2012; Akbarimehr *et al.*, 2013), D-InSAR techniques are especially useful for providing spatially continuous coverage of surface displacement which can help define the boundaries of active landslides (Yin *et al.*, 2010b). Additional advantages over other conventional techniques are the possibility of very precise displacement measurements over large areas at a reasonable cost, along with the possibility of assessing historical movements if archive SAR data exist (Metternicht *et al.*, 2005).

Following the development of multi-temporal interferometry (e.g. Ferretti *et al.*, 2001; Berardino *et al.*, 2002; Hooper *et al.*, 2007), there has been an exponential growth of landslide-related investigations making a reference list of such papers beyond the initial studies (i.e. Colesanti *et al.*, 2003; Hilley *et al.*, 2004; Bovenga *et al.*, 2006; Colesanti and Wasowski, 2006) an almost arbitrary task. The development of new SAR sensors reducing the revisit time and improving the resolution provides many enhancements in terms of reduced temporal decorrelation and the ability to provide a denser network of measurement points which have generated successful results for landslide applications (e.g. Notti *et al.*, 2010; Prati *et al.*, 2010; Bovenga *et al.*, 2012; Herrera *et al.*, 2013).

Regardless of the sensor, these applications are considerably opportunistic in nature as they can offer valuable information only in areas mostly beyond the control of the user (Hanssen, 2005). The use of D-InSAR and multi-temporal techniques as operational tools are also limited by the large variability of slope movements (relating to the mechanism, geometry, material, vegetation cover, size and velocity) as well as the acquisition parameters of the SAR platforms and decorrelation sources (Rott *et al.*, 1999; Hilley *et al.*, 2004; Strozzi *et al.*, 2005). Whilst D-InSAR methods offer the possibility to detect and monitor landslides over large regions, landslide displacement should be considered slope-specific given their limited spatial extent relative to potential error sources. The insufficient appreciation of the inbuilt SAR configuration and processing techniques, coupled with the natural complexities of landslide movements can result in significant misinterpretations of D-InSAR results (Colesanti and Wasowski, 2006; Peduto *et al.*, 2010) and constitutes a serious threat to successful D-InSAR time-series applications (Bovenga *et al.*, 2006). This failure to recognise the technical difficulties is perhaps behind

the continued scepticism among practitioners and end-users on the use of D-InSAR for landslide investigations (Wasowski and Bovenga, 2014).

More detailed information is found in comprehensive overviews of interferometric SAR techniques for landslide studies by Colesanti and Wasowski (2006) and Rott and Nagler (2006) for sensors such as ENVISAT and RadarSat. However it should be noted these reviews pre-date the launch of the most recent commercial SAR sensors. Rott (2009) and Wasowski and Bovenga (2014) provide a slightly updated summary with reference to the TerraSAR-X (TSX) and COSMO SkyMed satellites.

2.3 SAR Sub-Pixel Offset Techniques

Although less precise than D-InSAR techniques, sub-pixel offset measurements using the SAR image amplitude information can partially overcome the limit on the spatial displacement gradient for mapping large surface movements and are far more robust (not requiring phase unwrapping, not limited to regions of high coherence and less affected by atmospheric water vapour (Raucoules *et al.*, 2013)). Sub-pixel offset techniques can also provide complimentary information since conventional interferograms are only sensitive to displacements in the sensor's line-of-sight direction (Michel *et al.*, 1999). Using just two images acquired at different times, displacement vectors can be decomposed into the sensor look direction (i.e. range) as well as the satellite flight (i.e. along-track or azimuth) direction. This is achieved by measuring the row and column offsets between the two acquisitions at defined intervals in range/azimuth in order to generate a sufficient coverage of offset measurements (Pathier *et al.*, 2006).

2.3.1 Overview

Correlation methods are often the most appropriate to estimate offsets as they can achieve sub-pixel level precision providing the displacement field can be estimated locally by a translation that varies smoothly over multiple pixels (Michel *et al.*, 1999; Hu *et al.*, 2014a). Normalised cross-correlation (NCC) algorithms were developed in order to calculate the line/column offset with the normalisation element accounting for differences in the brightness and contrast between two images (Lewis, 1995). An image (I_1) taken at time T_1 is compared with a second image (I_2) acquired at time T_2 (Figure 2-10). The term $f(x,y)$ stands for the intensity values of a subset area of I_1 and $t(x-u,y-v)$ stands for the identically-sized area in I_2, offset by u and v in the x and y directions respectively.

The area $f(x,y)$ is also referred to as the reference template and $t(x-u,y-v)$ is the search template (Debella-Gilo and Kääb, 2011).

To find the reference template within I_2, the maximum normalised cross-correlation coefficient (ρ) is found between $f(x,y)$ and all possible values of $t(x-u,y-v)$ within the search window (Equation 2-12):

$$\rho(x,y) = \frac{\sum_{x,y}\left(f(x,y)-\bar{f}\right)\left(t(x-u,y-v)-\bar{t}\right)}{\sqrt{\sum_{x,y}\left(f(x,y)-\bar{f}\right)^2 \sum_{x,y}(t(x-u,y-v)-\bar{t})^2}}$$

Equation 2-12: The normalised cross-correlation function (see also Figure 2-10). $\bar{f}$ and $\bar{t}$ = the mean of the intensities within the reference template and search window, respectively.

The Euclidean distance between the centre pixel in the reference image and the highest correlated matching point in the search image is therefore considered as the horizontal displacement with the magnitude $d(x,y)$.

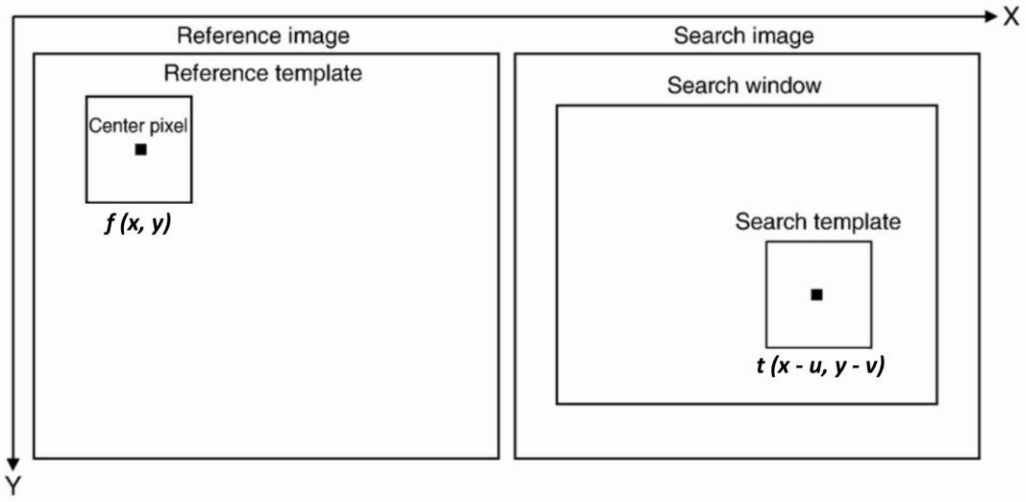

Figure 2-10: SAR pixel offset schematic showing the investigated pixel within the reference template and searching window (Debella-Gilo and Kääb, 2011 p. 132).

The parameters controlling the cross-correlation window size and sampling frequency should be carefully tuned with regard to the scale of the deformation features and the pixel size of the SAR images. The size of the search template should be large enough to maximise the signal-to-noise ratio whilst minimising the spatial velocity gradient, and the search window should be large enough to include the furthest moving distance whilst minimising the required processing time.

The accuracy of pixel-offsets can be expressed as the standard deviation (σ) of the pixel offset estimation error in pixel units, where N is the number of samples in the estimation window and ρ is the cross-correlation coefficient (Equation 2-13).

$$\sigma = \frac{1}{\sqrt{2}} \sqrt{\frac{3}{2N}} \frac{\sqrt{1-\rho^2}}{\pi\rho}$$

Equation 2-13: The achievable accuracy with incoherent cross-correlation methods (i.e. excluding phase values from the calculations) (Bamler and Eineder, 2005; Hu *et al.*, 2014b).

The accuracy can be improved when the cross-correlation is high and the number of samples in the reference template is increased. With a high cross-correlation close to 1, the precision in the offset fields can reach between 1/10 – 1/30 of a single-look pixel (Hanssen, 2001; Casu *et al.*, 2011; Hu *et al.*, 2014a). The advent of very high resolution SAR data with ground pixel spacings around 1 m therefore increases the sensitivity and precision achievable using NCC techniques.

General limitations with the NCC approach controlling its accuracy have been well documented (Delacourt *et al.*, 2004; Debella-Gilo and Kääb, 2011; 2012). The surface properties of the reference template must not be significantly changed, rotated or sheared between image acquisitions; merely shifted in position. NCC techniques can also be sensitive to noise in the images and requires the displacement to be greater than the mean error of the image registration. Finally other limiting factors also applicable to SAR interferometry such as high Doppler centroids, large perpendicular baselines, DEM errors and long temporal intervals can contribute to the loss of cross-correlation which subsequently affects the pixel-offset accuracy and increases the likelihood of spurious offset measurements.

2.3.2 Early Applications

Past studies using SAR pixel offset methods have been dominated by coseismic and glacial applications, due to the widespread decorrelation in conventional interferograms from high displacement gradients across ruptured faults or rapidly changing ice surfaces. As such, accurate fault traces have been revealed using pixel offset techniques applied to just two SAR images spanning coseismic events (e.g. Michel *et al.*, 1999; Fialko *et al.*, 2001; Jónsson *et al.*, 2002; Funning *et al.*, 2005; Pathier *et al.*, 2006; de Michele *et al.*, 2010; Li *et al.*, 2011b; Feng *et al.*, 2013). Similarly, studies have been successful in remotely measuring glacier/rock glacier flow (e.g. Scambos *et al.*, 1992; Strozzi *et al.*, 2002; Quincey *et al.*, 2005; Luckman *et al.*, 2007; Haug *et al.*, 2010).

More recently, developments have seen pixel offset methods used for increasingly diverse purposes. One example includes the use of range offset fields to correct interferograms where the spatial displacement gradient is exceeded due to large and episodic volcanic movements (Yun *et al.*, 2007). Range offsets contain the same information as a differential interferogram and can be used to reduce the interferometric phase gradient which increases the likelihood of successful phase unwrapping.

In a similar development to D-InSAR time-series methods, a SBAS inversion scheme applied to a stack of SAR images has been suggested to reduce errors arising from large perpendicular baselines in order to generate a time-series of offset displacement (Casu *et al.*, 2011). Similarly to PS point selection, point-like pixel offset measurements have most recently been developed to reduce processing time by only calculating offsets from the highest correlation points which display the greatest accuracy (Hu *et al.*, 2014b).

2.3.3 Application to Landslides

To date, only a relatively small number of studies have used pixel offset techniques for monitoring slope movements, the majority of which use optical imagery from airborne and spaceborne platforms (Kääb, 2002; Yamaguchi *et al.*, 2003; Delacourt *et al.*, 2004; Wangensteen *et al.*, 2006; Leprince *et al.*, 2008; Delacourt *et al.*, 2009; Debella-Gilo and Kääb, 2011; Travelletti *et al.*, 2012; Gance *et al.*, 2014; Lucieer *et al.*, 2014).

The sensitivities of normalised cross-correlation have been considered by Delacourt *et al.* (2004) and Debella-Gilo and Kääb (2011) which include: (i) noise in the images; (ii) rotation/shearing between the images to be correlated; and, (iii) the relationship between the pixel size and the precision of measurements. Additionally, the correlation of optical data require orthorectification of both images (ideally using different DEMs relating to the time period of image acquisition) as the accuracy is inversely related to the difference in viewing angles between images (Delacourt *et al.*, 2007). Given the high resolution available from various optical image products, NCC techniques can detect large motions over much longer time periods that would be decorrelated in interferograms spanning the same duration.

However, optical images can only be used to assess purely horizontal movements (north-south and east-west directions) without consideration of the vertical component and they

also suffer from variable solar conditions generating different shadow sizes/orientations (Berthier *et al.*, 2005).

Sub-pixel offset techniques applied to SAR images are of significant interest given their geometrical acquisition stability, independence from cloud cover and SAR image resolutions of ~1 m being equivalent to that of optical sensors. A sub-pixel offset technique was first applied to TerraSAR-X Spotlight SAR data by Li *et al.* (2011a) with promising results for monitoring the Shuping landslide in the Three Gorges region, although only four sets of measurements were shown in the paper (corresponding to four offset pairs). Sub-pixel offset techniques using the similar high resolution SAR data have subsequently been applied to La Valette, Montescaglioso and Vallcebre landslides with high correlation values and accuracies down to 0.01 pixels (Monserrat *et al.*, 2013; Raucoules *et al.*, 2013; Manconi *et al.*, 2014).

This motivates the investigation of high resolution TerraSAR-X Spotlight data for monitoring densely vegetated landslides with a temporal resolution up to every 11 days over a time period of several years. The ability to compare sub-pixel offset and D-InSAR techniques applied to lower resolution SAR data is also of interest for landslide studies.

2.4 Summary

Chapter 2 provides a fundamental introduction to the acquisition and properties of Synthetic Aperture Radar (SAR) images. Radar images are significantly different to optical satellite data due to the presence of speckle and side-looking image distortions which result in layover, shadow and foreshortening effects. A variety of spaceborne SAR sensors exist with different radar wavelengths, each capable of acquiring SAR data in different image modes with varying image resolutions.

A general processing chain of Differential Interferometry (D-InSAR) is outlined along with major sources of decorrelation between SAR image acquisitions. Causes of coherence loss are particularly focused on landslide applications as well as the implications of using different image mode data. The concept of a spatial displacement gradient threshold is explained and subsequently illustrated for a coseismic fault rupture.

Finally, a theoretical background to SAR sub-pixel offset techniques is provided. For both D-InSAR and offset methods, a review a major technological developments is provided along with a summary of literature specifically focused on landslide applications.

Chapter 3 : Landslides in the Three Gorges Region

At a length of ~6,300 km, the Yangtze River is the third longest in the world and has a catchment area of ~1.8 x 10^6 km^2 (Dai and Lu, 2010). Originating from the Tibetan Plateau, the river flows eastwards across south-western, central and eastern China before reaching the East China Sea at Shanghai. The Three Gorges region is located in the middle reaches of the Yangtze River which separate the Sichuan and Jinghan Basins (Fourniadis *et al.*, 2007a).

From west to east, the Three Gorges are comprised of the Qutang, Wu and Xiling Gorge, with the Three Gorges region defined as a 193 km stretch of the Yangtze River from Fengjie (the most westerly point of Qutang Gorge) to Yichang (the most easterly point of Xiling Gorge) (Figure 3-1). Most of the Three Gorges is underlain by carbonate rocks although the Three Gorges Project (TGP) was purposely constructed within the granitic outcrop of the Huangling anticline. The region has a subtropical monsoonal climate with rainfall heaviest in the summer and mean temperatures in January between 2 – 4 °C.

Between Badong and the TGP, hillslopes are steep-sided and densely vegetated with orange trees (Figure 3-2), the relief exceeding 2500 m within a 30 km buffer of the Yangtze River channel. The slopes exhibit shallow soils < 0.75 m (Fu *et al.*, 2012) overlying a variety of parent material, with land-use dominated by mixed-deciduous forest and cultivated land (Wang *et al.*, 2008c).

This chapter introduces the geological and hydrological situation of landslides within the Three Gorges region. A review of previous remote sensing applications for landslides in this area is also provided, particularly those using SAR images and D-InSAR techniques. Major discrepancies in SAR studies monitoring the Shuping landslide are outlined, which motivates a significant part of this research. Finally, geotechnical information about the Shuping landslide is reviewed, along with a consideration of previous modelling studies which aim to understand landslide mechanisms and triggering factors.

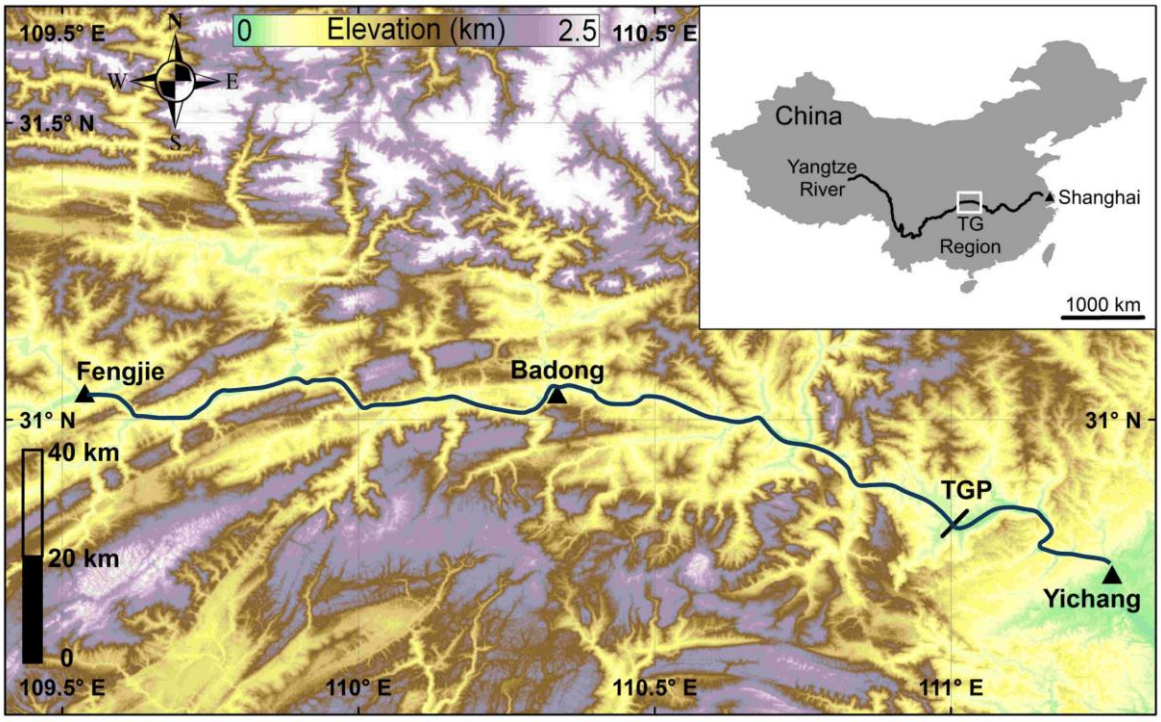

Figure 3-1: The Three Gorges region from Fengjie in the west to Yichang in the east. TGP represents the location of the Three Gorges Project dam.

Figure 3-2: Typical land cover of orange trees in the Three Gorges region. The picture shows dense vegetation on and around the Shuping landslide (30.99N 110.62E), 200 m in diameter.

3.1 Geological Background of the Three Gorges

The Central Asian Foldbelt is a combination of Precambrian microcontinents (Qiu *et al.*, 2000) and the geology of China is highly diverse, recording a history of crustal evolution from the Archean core of the Sino-Korean Platform to the active continental collision in

Tibet. South East China is composed of the Yangtze Platform in the west and the Cathaysian foldbelts (which include the Cenozoic mountain ranges of Taiwan) in the east (Chen and Jahn, 1998). The Three Gorges region is located at the western edge of the Yangtze Platform and several first-order geophysical contrasts are observed, such as variations in topography, crustal thickness and lithospheric thickness (Figure 3-3). From west to east, the topography decreases from an average surface elevation of 1000 – 2000 m a.s.l (herein referred to as 'm') to less than 500 m; the thick western crust (40 – 46 km) is separated from the thinner (30 – 36 km) crust by the north-south seismic belt; and the lithospheric thickness decreases from >200 km to 80 km (Zhang *et al.*, 2009a). These divisions within the Three Gorges region separate central China into a western region dominated by crustal shortening and mountain building related to the India-Asia collision, and an eastern region predominantly affected by the east-west compression of Pacific and Eurasian plates (Zhang *et al.*, 2009a).

River cutting of massive limestone mountains of Palaeozoic and Mesozoic age created the Three Gorges, but the timing is poorly constrained and disputed. The majority of discussion relates to the Yangtze's origins and when the drainage basin of the relatively smaller Paleo-Yangtze (Figure 3-4) was reorganised to include water originating from the eastern Tibetan Plateau, capable of incising the Three Gorges (Clark *et al.*, 2004).

Initial studies suggested the Three Gorges formed through incision along narrow fault zones in response to Quaternary uplift of the Sichuan basin, dating the gorges between 3.6 and 1 Ma B.P. (Late Pliocene to Early Pleistocene) (Li *et al.*, 2001; Yang *et al.*, 2006). However there is no direct onshore evidence for the timing of the Yangtze's expansion and offshore records are obscured by sediment storage in the lower Yangtze basin (Clift, 2006).

More recent studies suggest the long-term diversion of the upper/middle Yangtze away from the Red River occurred during the Cenozoic, induced by complex tectonic movements (Fan and Li, 2008). Such movements induced intense uplift of the Tibetan Plateau in the west and sustained subsidence of onshore and offshore plains in the east, triggering a topographic reversal and reorganisation of the Yangtze. Incision of the Three Gorges has therefore been proposed to occur over a much greater timescale, initiating in the Eocene, 56 – 34 Ma (Zheng and Li, 2009; Richardson *et al.*, 2010).

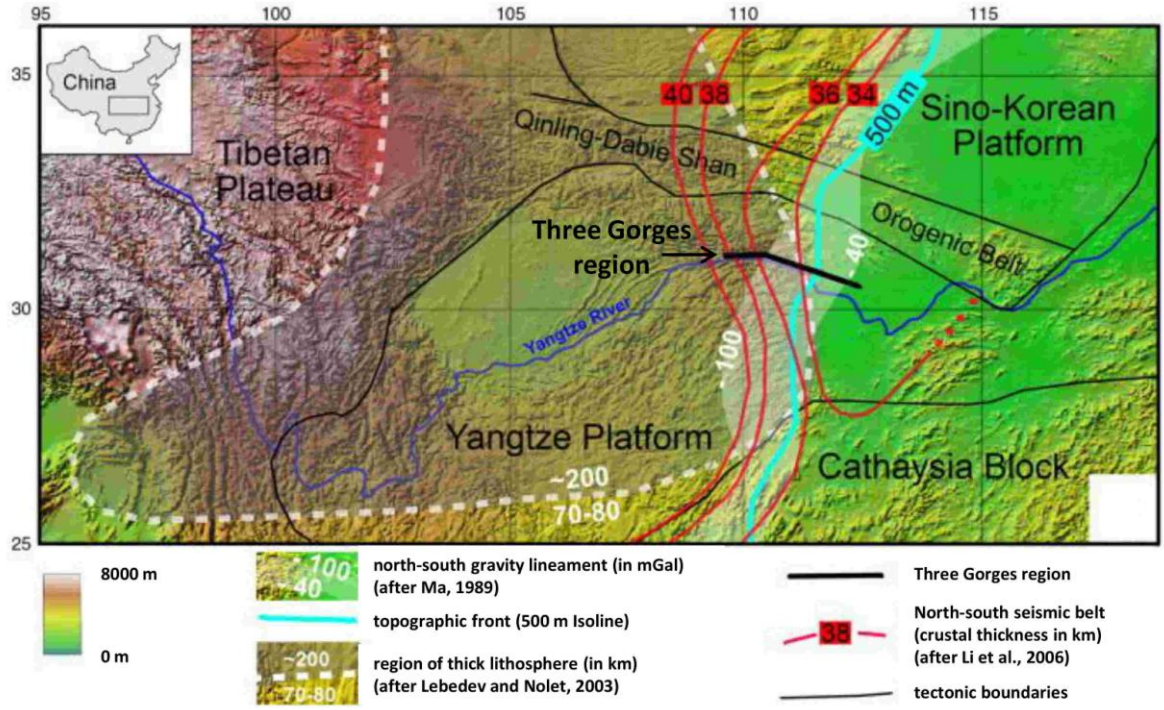

Figure 3-3: First order geophysical contrasts in topography, crustal thickness and lithospheric thickness around the Three Gorges region (Zhang *et al.*, 2009a p. 424).

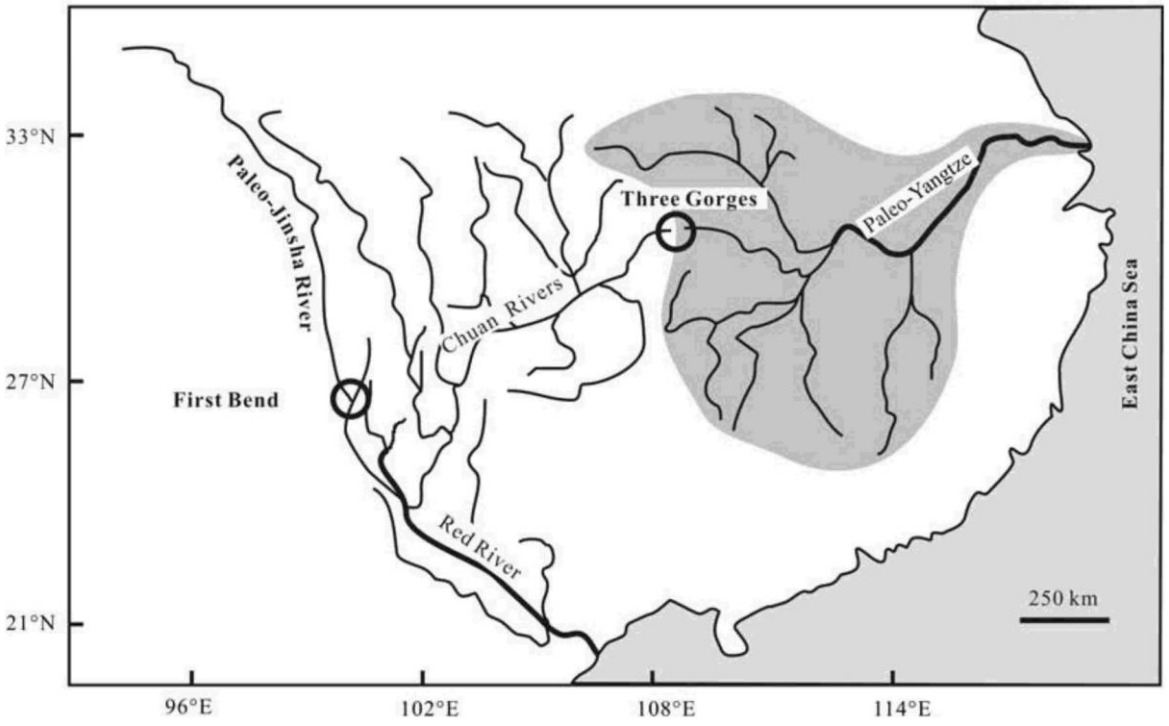

Figure 3-4: Hypothetical Paleo-Yangtze drainage basin with the original watershed close to the Three Gorges region (Fan and Li, 2008 p. 303).

3.1.1 Local Geology

The Yantgze Platform and the Three Gorges region have a doubled-layered rock construction, consisting of a crystalline baseline and a sedimentary cover (Wu *et al.*,

2001). The most widespread sedimentary cover (0 – 8.2 km thick), comprises interbedded carbonate, sandstone and shale formations of Paleozoic and Mesozoic age (Richardson *et al.*, 2010) whereas the Proterozoic crystalline basement (7 – 14 km thick) is composed of magmatic and metamorphic rocks (Zhang *et al.*, 2009a). This igneous-metamorphic basement complex consists of Precambrian granite, dioritic schist and black mica gneiss (Fourniadis and Liu, 2007) and only outcrops in the core of the Huangling anticline (Figure 3-5) where the TGP is located.

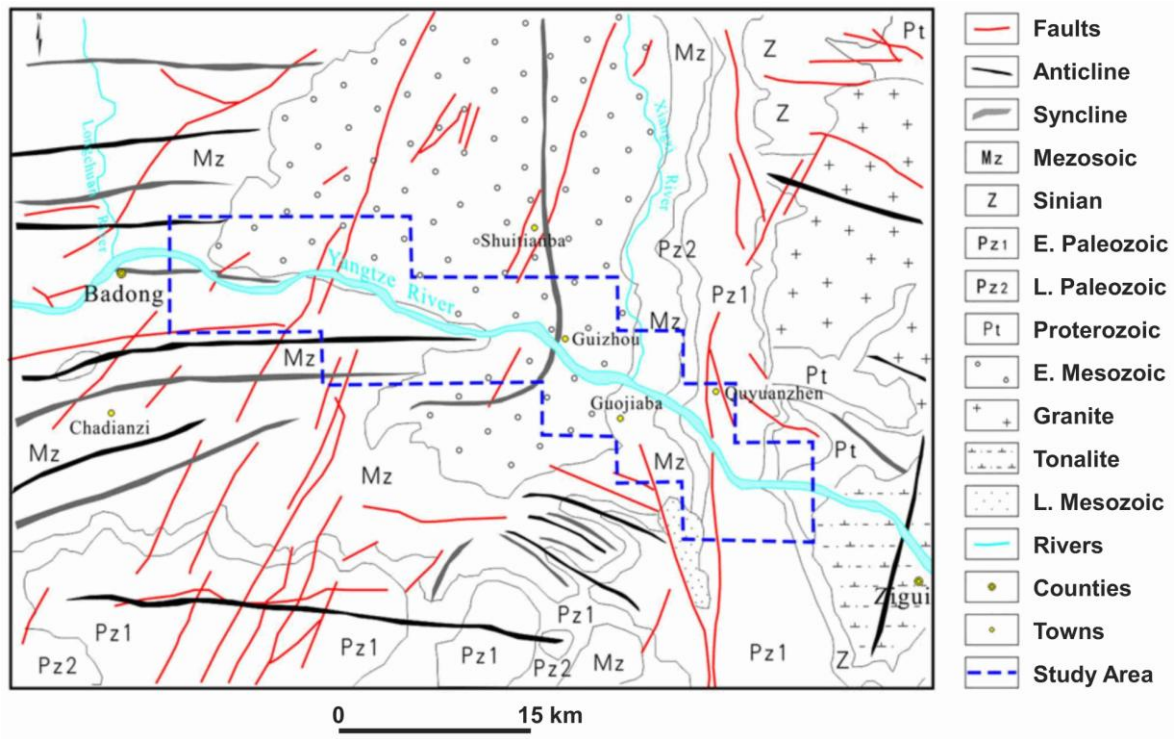

Figure 3-5: Geological setting of the Three Gorges region along the Yangtze River. The Huangling anticline forms a major NNE-SSW orientated structure ~50 km in length (to the far east of the map, near Zigui County) where the TGP is located (Wu *et al.*, 2013 p. 1310).

The Three Gorges are formed in massive limestone mountains, interbedded with reddish siltstone, shale and mudstone. As such, the limestones are characterised by steep slopes and ridges which can be heavily jointed and sheared where traversed by tectonic faults and lineaments. These lithological formations have been classified according to their competence into: (i) massive limestones and dolomites; (ii) sandstone-shale-marl interbeddings, and (iii) mudstone, slope deposits and Quaternary sand and gravel (Fourniadis and Liu, 2007).

Between the gorges, rocks are much less resistant and the valley is wider with shallower slope angles than in the gorges (Liu *et al.*, 2004). Sequences in these 'inter-gorge' areas comprise interbedded mudstone and sandstone, shale and interbedded marl and limestone,

while the major soil type is colluvium derived from these bedrocks (Wen *et al.*, 2007). Sandstones, shales and marls form complex interbeddings where lithologies of contrasting physical properties (such as shear strength and permeability) are frequently juxtaposed (Fourniadis and Liu, 2007). Additionally, mudstones are often weathered and comprise loose bedrock fragments within a matrix of finer material while Quaternary deposits tend to be locally distributed on gentler slopes or along the river valley where they form easily erodible terraces. Subsequently riverbank erosion, terrain dissection and slope failures tend to be concentrated in these inter-gorge areas (Wu *et al.*, 2001; Liu *et al.*, 2004).

Finally, the underlying lithology has been considered to determine the characteristics of slope failure. Rock falls are expected on steep limestone slopes whereas block slides along near-planar slip surfaces are expected to dominate steep slopes of sandstone and shale interbeddings (Fourniadis *et al.*, 2007a). Three categories of landslide types within the Three Gorges have been suggested (Wen *et al.*, 2007): (i) landslides located at the contact between colluvium and bedrock; (ii) major parts of the slip zone occurring along bedding planes of weak rocks; and, (iii) slip zones following joints or faults cutting across bedrock bedding planes. Type-I landslides (colluvial landslides) are by far the most common (accounting for more than 50% of all large-scale landslides in the region) and often formed in areas of interbedded mudstone and sandstone (Wen *et al.*, 2007). Combining knowledge of the lithology and slope failure type can improve susceptibility mapping (e.g. Fourniadis *et al.*, 2007b) compared to previous studies which assume a uniform influence of geological parameters on all modes of slope failure.

3.1.2 Tectonic Setting

Currently the Yangtze Platform and the South China block represent stable continental regions that behave as rigid blocks, with only minor internal deformation which lacks seismicity (Chen, 1999; Wang *et al.*, 2001; Calais *et al.*, 2006; Richardson *et al.*, 2010; Jia *et al.*, 2013). Previous studies have concluded the Three Gorges are in an area of low seismicity (e.g. Mason, 1999) with no earthquakes exceeding magnitude M_S 4.0 between the monitoring period of 2001 – 2006 (Mei *et al.*, 2013).

Historical records show 2910 events with a magnitude > 1 occurred in the past 2000 years within 300 km of the TGP, of which only a few exceeded a magnitude of 4 (Wang *et al.*, 2005b). Construction design ensures the dam has a high capability to resist earthquakes with a magnitude of M_W 7 (Li *et al.*, 2005) and seismic risk analysis indicates the recurrence period for the dam site encountering a magnitude 6 earthquake is 10,000 years.

This is equivalent to a 1% chance of a magnitude 6 event occurring in the next 100 years – the same anti-seismic standard for a nuclear power station (Chen, 1999).

The location of the TGP was selected from 15 candidate positions due to its good conditions for construction and its width which offers greater structural flexibility, along with "plenty of geologic and seismologic conditions being well suited for building such a large dam" (Chen, 1999 p. 183). Located on the ancient crustal landmass in the core of the Huangling anticline, the site of the TGP has good integrity, no strongly active fractures nearby, integral middle-upper crust, distanced from the epicentres of moderately strong historical earthquakes and has not experienced a seismic event greater than magnitude 5.1 which suggests the site is highly suitable (Tan *et al.*, 1997).

In the planning and construction of the TGP, the possibility of increased seismicity after the additional water loading on the landscape was considered (Yi *et al.*, 2012). The location of the TGP and associated 600 km reservoir means the reservoir area will lie on the granitic core of the Huangling anticline but also the limestone beds which have been associated with reservoir-induced seismicity (Chen and Talwani, 1998). Predictive models of surface deformation suggested a reservoir water level of 175 m would lead to 1- 48 mm of vertical displacement, useful for correcting engineering surveys using height data collected before and after reservoir filling (Wang, 2000; Wang *et al.*, 2002).

The frequency of seismic activity following reservoir filling has increased from 2003 onwards, demonstrating a significant positive correlation with the reservoir water level. The annual average frequency of seismic events over the 2003 – 2009 period was 1,288 events compared to the annual average frequency of just 29 for the period 1959 – 2003 (Xu *et al.*, 2013) and no event exceeded magnitude M_L 4.9. Patterns of reservoir-induced seismicity demonstrate an increased frequency of low magnitude events, with no increasing trend for earthquakes above magnitude M_L 4 (Xu *et al.*, 2013). There are no historical reports of significant earthquake-induced landsliding in the region, although this risk is heightened with increased seismic activity (Keefer, 1984). More direct causes of landsliding may include the hydrological influences of the fluctuating reservoir water level or heavy summer monsoonal rainfall.

3.2 Hydrological Influences on Landslides

Landslides located at the banks of reservoirs are well known to be influenced by periodic water level fluctuations as well as seasonal rainfall (Iverson, 2000; Paronuzzi *et al.*, 2013).

The groundwater table, pore-water pressures within the landslide body and the landslide failure surface are directly affected by reservoir levels and precipitation, resulting in the decrease of effective normal stress and the shear strength of soils (Luo *et al.*, 2009; Miao *et al.*, 2014). Catastrophic landslides in the Three Gorges region have been attributed to the initial reservoir inundation (Wang *et al.*, 2004; 2008b) and the reactivation of dormant landslides due to fluctuating water tables (Wang *et al.*, 2008a; Yin *et al.*, 2010b). With 5,386 potentially dangerous sites within the Three Gorges region and 70% more landslides/bank collapses than predicted after reservoir inundation (Li, 2012), hydrological factors affecting landslides need careful consideration.

3.2.1 Rainfall Patterns in the Three Gorges Region

The Three Gorges region experiences a subtropical wet monsoonal climate with significant differences in rainfall between the winter and summer months. Rainfall is mostly concentrated from late spring to mid-autumn with peak monthly rainfall in July (250 – 300 mm) compared with rainfall < 50 mm/month for the period September – March (He *et al.*, 2010). Rainfall is also spatially variable with the lowest annual values of ~990 mm around the TGP and Zigui County, compared with the highest values of ~1,200 mm around Fengjie (He *et al.*, 2008).

Rainfall-induced landsliding is the most common triggering mechanism in the Three Gorges region and the monthly distribution of landslides closely follows the months of heaviest rainfall between April and August (Figure 3-6). Given the lagged process of infiltration and saturation, landslides have been found to occur up to 10 days after a heavy rainfall event (He *et al.*, 2009), although this is heavily dependent upon the rainfall duration and prior cumulative rainfall. A critical cumulative rainfall value of 70 mm over 10 days has been proposed for when landslide alerts should be issued (He *et al.*, 2008).

Importantly, the above analysis is only applicable to shallow slope failures rather than blocks with deep failure planes (>10 m). Infiltration of rainfall is unable to affect sliding zones at depth and it has also been found that cracks in shallow blocks help facilitate infiltration, decreasing the stability of the upper most sliding mass (Xia *et al.*, 2013).

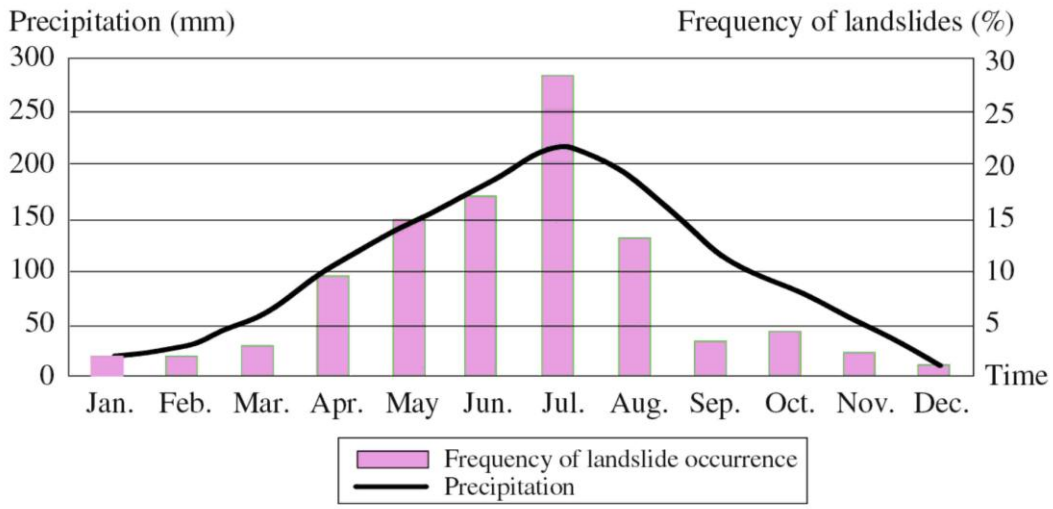

Figure 3-6: Relationship between landslide occurrence and precipitation in the Three Gorges reservoir region, 1971 – 2003 (He *et al.*, 2010 p. 1268).

3.2.2 The Three Gorges Project (TGP)

The Three Gorges Project (TGP) is currently the world's most powerful hydroelectric power station which brings valuable advantages of downstream flood protection, hydropower generation and improved navigation from the dam to Chongqing (Tullos, 2009). While these benefits are substantial, it has been a controversial project due to its environmental and social impacts (Gleick *et al.*, 2013).

The dam increased the water depth of the Yangtze River by more than 100 m, creating a 600 km long reservoir which reaches the city of Chongqing. The visible impact of water level rise is clear (Figure 3-7), increasing the likelihood of old (and previously elevated) landslide deposits being reactivated as well as triggering new landslides (Liu *et al.*, 2004). In addition, the displacement and relocation of whole towns results in land clearing and farming on newly occupied ground that may further destabilise slopes (Tullos, 2009).

Figure 3-7: Impact of the Three Gorges reservoir impoundment on the Dragon Gate Bridge (31.1N, 109.9E). The bridge was overtopped by the reservoir, destroyed, and replaced by a higher bridge.

The reservoir water level annually fluctuates between 145 and 175 m.a.s.l (m herein), being lowered in the winter during power generation and increasing in the summer to accommodate monsoonal rainfall (Figure 3-8). It was predicted that the period of slower reservoir drawdown (January – June) should only have relatively small impacts upon slope instability as opposed to the shorter rapid drawdown in July – August (He *et al.*, 2008).

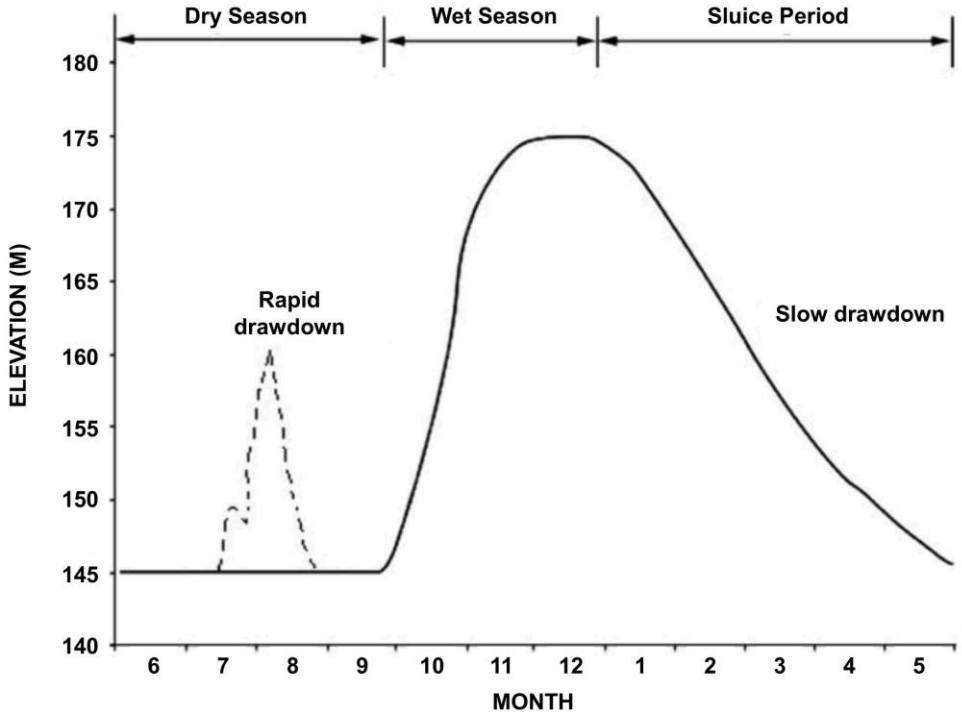

Figure 3-8: Annual operations of the Three Gorges reservoir and the associated water level changes (Yuan *et al.*, 2013 p. 7095). The short–lived reservoir increase and rapid drawdown in July – August following monsoonal rain has occurred annually since 2009.

Around 2,490 landslides were identified in the Three Gorges region before construction of the dam, although a more detailed survey after reservoir impoundment revealed more than 5,700 landslides, many of which have been reactivated (He *et al.*, 2009; Liu *et al.*, 2009; Miao *et al.*, 2014). It is well known that reservoir water level fluctuation plays a key role in the initiation of slope instability due to the change in water content and seepage conditions in the slope (Miao *et al.*, 2014).

The fluctuating reservoir water level has been shown to be the dominant triggering factor for numerous landslides, e.g. the Baishuihe, Shiliushubao and Shuping landslides (Li *et al.*, 2010; Wang *et al.*, 2013b; Xia *et al.*, 2013). For these deep-seated landslides, all displacement was most highly correlated with the slower, yet sustained, drawdown in the

January – June window which contradicts the prediction of (He *et al.*, 2008). The significant degree of reservoir fluctuation, combined with widespread landslide hazards in the region, warrants further investigation and provides a good opportunity to observe the response of landslides to such large water level changes.

3.3 Remote Sensing of Landslides

The past two decades have seen an increasing amount of studies focused on the applicability of Earth Observation (EO) satellite data for investigating slope instability (Tralli *et al.*, 2005). This rise is due to launches of both optical and radar platforms (e.g. Landsat TM, IKONOS, QuickBird, ERS-1/2, RADARSAT, ENVISAT, TerraSAR-X), improved capabilities of space sensors and the development of more advanced data processing techniques (Colesanti and Wasowski, 2006).

Observations from satellite platforms are complementary to both in-situ and airborne surveys, being capable of detecting and monitoring landslides over wide areas with a regular repeat interval. Particularly for preliminary investigations, these data are cost-effective and reduce the risk/time spent in the field. Additionally, archived satellite imagery can also provide useful information on past movement episodes (Hervás *et al.*, 2003), either assessing the terrain prior to failure or interpreting the landslide morphology post-failure from the source/deposition area.

The distinction between optical and radar imagery is also significant. Optical imagery (e.g. stereo aerial photography or high resolution satellite imagery) is mostly used to qualitatively determine landslide characteristics over large areas, describing the distribution and classification of landslide types in relation to factors such as slope, aspect, lithology, land cover (Hervás *et al.*, 2003; Metternicht *et al.*, 2005). This spatial analysis often results in the generation of regional maps of known landslides and/or landslide susceptibility. Active monitoring of landslide activity (e.g. determining mean annual velocities) has mostly used radar imagery and D-InSAR techniques, although this is restricted by the limitations outlined in Chapter 2. Given the absence of a remote sensing technique applicable to all situations (Scaioni, 2013), further data/sensor integration is encouraged to extract the maximum amount of information from remotely-sourced data products.

A comprehensive and very well documented evaluation of all remote sensing techniques applied to a wide variety of landslide types is available from the EU-funded SafeLand

Project (Michoud *et al.*, 2010; Stumpf *et al.*, 2010). Subsequently, this section only reviews previous work within the Three Gorges region which uses either spaceborne optical or radar imagery for landslide investigations.

3.3.1 Spaceborne Optical Imagery

An initial group of studies employed imagery and elevation data from the Advanced Spaceborne Thermal Emission and Reflection Radiometer (ASTER) satellite sensor to produce susceptibility/hazard maps of different landslide types for slopes bordering the Yangtze River from Wushan to Zigui (Liu *et al.*, 2004; Fourniadis *et al.*, 2007a, b). The high spatial and spectral resolution of the ASTER sensor (14 spectral bands, up to 15 m resolution) in the visible and infrared bands is well suited to geological and geomorphological interpretation. Following the extraction of regional parameters affecting slope stability (namely slope, bedding dip angle, bedding aspect, slope-drainage distance, lithology), these are combined to create an index of stability and a regional landslide hazard map (e.g. Figure 3-9). Slopes bordering the Yangtze River between Badong and the TGP are mostly classified as having intermediate – high susceptibility to landsliding which reinforces the focus of this study to detect, map, monitor and characterise landslides in this region.

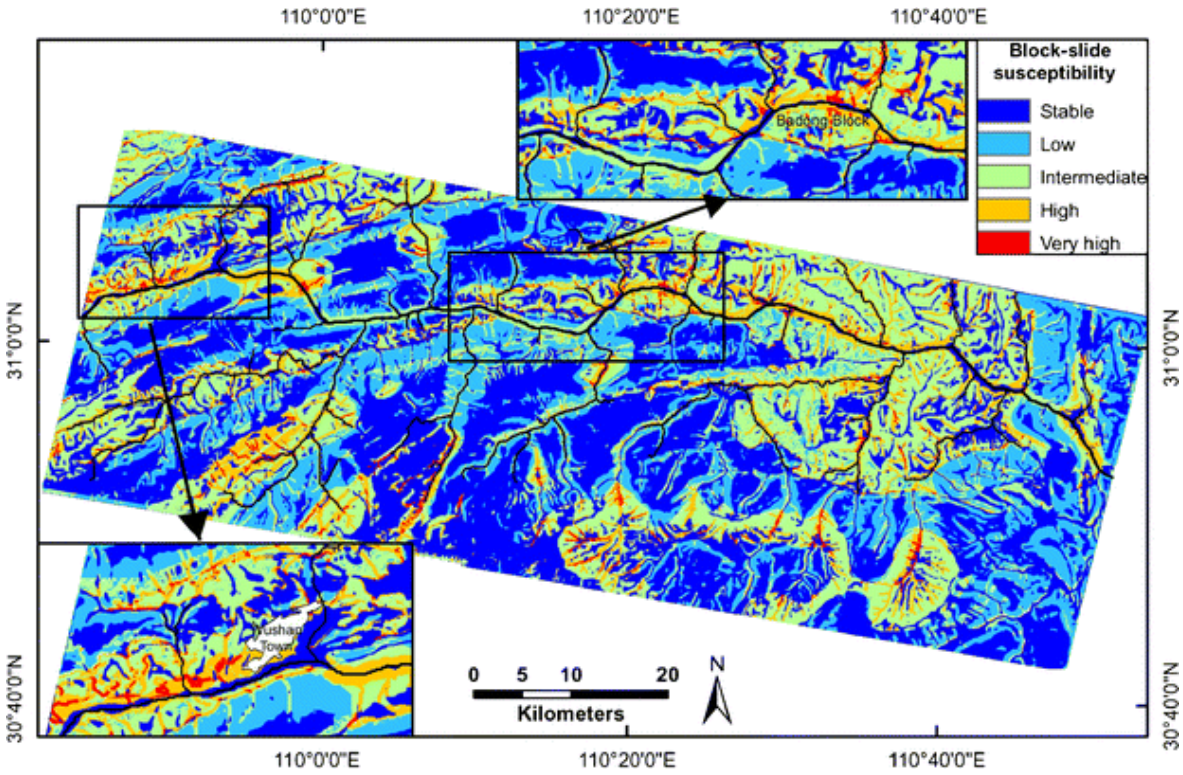

Figure 3-9: Susceptibility to block-type landslides between Wushan in the west and Zigui in the east. The enlarged left inset focuses on Wushan, the right inset focuses on Badong (Fourniadis *et al.*, 2007b p. 272).

These landslide hazard models have developed to include variable susceptibility maps adapted for different landslide failure mechanisms. Combined with socio-economic information on the affected populations, industry and transport networks, areas of greatest potential landslide impact can then be mapped.

Similar susceptibility approaches have been applied to the Three Gorges region over smaller scales to generate a spatial forecast of landsliding at varying degrees of resolution (Wang and Niu, 2009; Bai *et al.*, 2010; Austin *et al.*, 2013).

The most recent study employed 20 categorical variables believed to influence landslide susceptibility, obtained from a DEM, satellite and aerial imagery (Peng et al., 2014). The final result (Figure 3-10) is relatively consistent with that in Figure 3-9, although with a different number of classification categories, direct comparisons are difficult. The steepest areas closest to the Yangtze River are generally deemed most at risk of landslides.

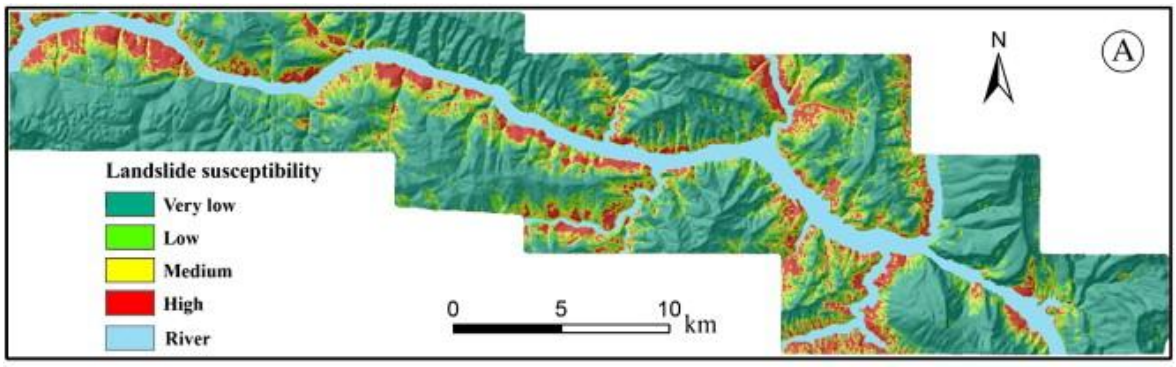

Figure 3-10: Landslide susceptibility mapping of the Three Gorges from Badong in the west to Zigui in the east (Peng *et al.*, 2014 p. 296).

Despite the use of susceptibility maps for land-use planning, the maps are strongly influenced by the choice of parameter inclusion which often lack information on triggering factors (Petschko *et al.*, 2014). Additionally, the frequency/time dependence of landslide events is rarely considered and the designation of susceptibility classes remains a qualitative process relative to the geographical region under study. Finally, verification of these results is always difficult since known landslide sites are typically used to determine the highest risk parameter classes. The division of landslide observations in both space and time is necessary for modelling and verification (Fourniadis *et al.*, 2007b), although this also becomes a qualitative process.

3.3.2 Spaceborne Radar Imagery

Rather than assessing the probability of slope failure across the Three Gorges region, D-InSAR techniques are capable of detecting and measuring the displacement of active instabilities. However, the terrain in the Three Gorges region is very challenging for D-InSAR primarily due to the dense vegetation affecting the interferometric coherence.

From the handful of studies that exist, the installation of corner reflectors over known landslide sites has been used to generate consistent D-InSAR results using ENVISAT data (Xia *et al.*, 2004; Fu *et al.*, 2010; Xia, 2010). An old landslide deposit of the Xintan landslide is one such site with corner reflectors installed which was found to be stable over the period November 2000 – November 2001. The stable Kaziwan landslide has also been measured following the same method, along with the Shuping landslide which was found to be active between September 2005 and June 2007 at a rate of 10 – 30 mm/yr.

In the Three Gorges region, the most successful case of D-InSAR monitoring without the use of corner reflectors has been the Huangtupo landslide in Badong, using ENVISAT SAR data (Perissin and Wang, 2011; Liu *et al.*, 2013; Tomás *et al.*, 2014) and ALOS PALSAR data (Tantianuparp *et al.*, 2013). A variety of Persistent Scatterer (PS) techniques have been applied, with all results matching those presented by Liu *et al.* (2013). Two subsidence regions are evident, with the fastest moving (Huangtupo slope) to the east of Badong (Figure 3-11). Division of the landslide body into various slumping masses was possible by interpreting the various measurement points, and the most active mass can be decomposed into linear creep movement (governed by geological conditions) as well as seasonal fluctuation (related to factors such as reservoir changes) (Tomás *et al.*, 2014). The success of these studies is mostly related to the extremely slow rate of movement and the density of built infrastructure on the slope. The lack of dense vegetation therefore permits the generation of high-coherence interferograms of varying time intervals.

Finally, the launch of the TerraSAR-X sensor in 2007 offers the highest resolution of SAR data which are better suited for monitoring landslides in the Three Gorges region (Xia, 2010). The finer pixel spacing and its more frequent 11-day revisit frequency can increase the interferometric coherence, although its spatial coverage is limited. Both TerraSAR-X (TSX) Spotlight and Stripmap image mode SAR data exist over the Shuping landslide, overlapping in time with some ENVISAT data. Exploitation of this TSX data for monitoring the Shuping landslide has been the focus of the most recent studies.

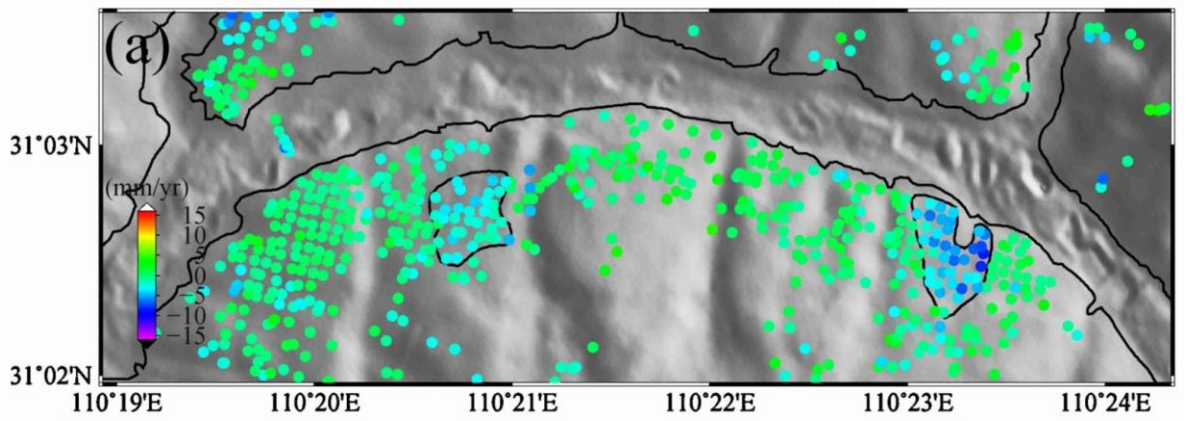

Figure 3-11: Mean Line-of-Sight (LOS) velocity of the Huangtupo landslide (right landslide block), between August 2003 and July 2010 (Liu *et al.*, 2013 p. 257).

3.3.2.1 Shuping Landslide Observations

Previous studies monitoring the Shuping landslide using D-InSAR techniques have yielded highly varied results. Fu *et al.* (2010) used 12 corner reflectors installed over the landslide to obtain a single measurement of displacement between September 2005 and March 2006 using ENVISAT data. Good agreement with GPS measurements was reported, but it should be noted this result did not cover the months of April – June where the fastest movements are normally observed (and when the assumptions for reliable D-InSAR analysis are most likely to be broken).

Extensometer measurements over the time period of September 2005 and June 2007 show minimal displacements until around May – June 2007 when there is a rapid increase of ~0.4 m in the accumulated movements (Wang *et al.*, 2013b). Whilst recognising the different vectors of measurement sensitivity, this contradicts the results of Xia (2010) who used the same 12 corner reflectors to calculate a time-series of displacement over the same time period, presenting very linear rates of downward movement for all points.

This landslide has been divided into eastern and western parts with the eastern block, also known as Block 1 (Figure 3-12), found to be most active (Wang *et al.*, 2008a). The motion of Block 1 has been recorded primarily using 21 extensometers from 2004 until 2010 (Wang *et al.*, 2008a; 2013b) and these results display high spatial variability along with a stepped behaviour in time. Particularly using the longest record from August 2004 until May 2010, the periods of greatest movement have been suggested to relate to the drawdown of the Three Gorges reservoir (Wang *et al.*, 2008a).

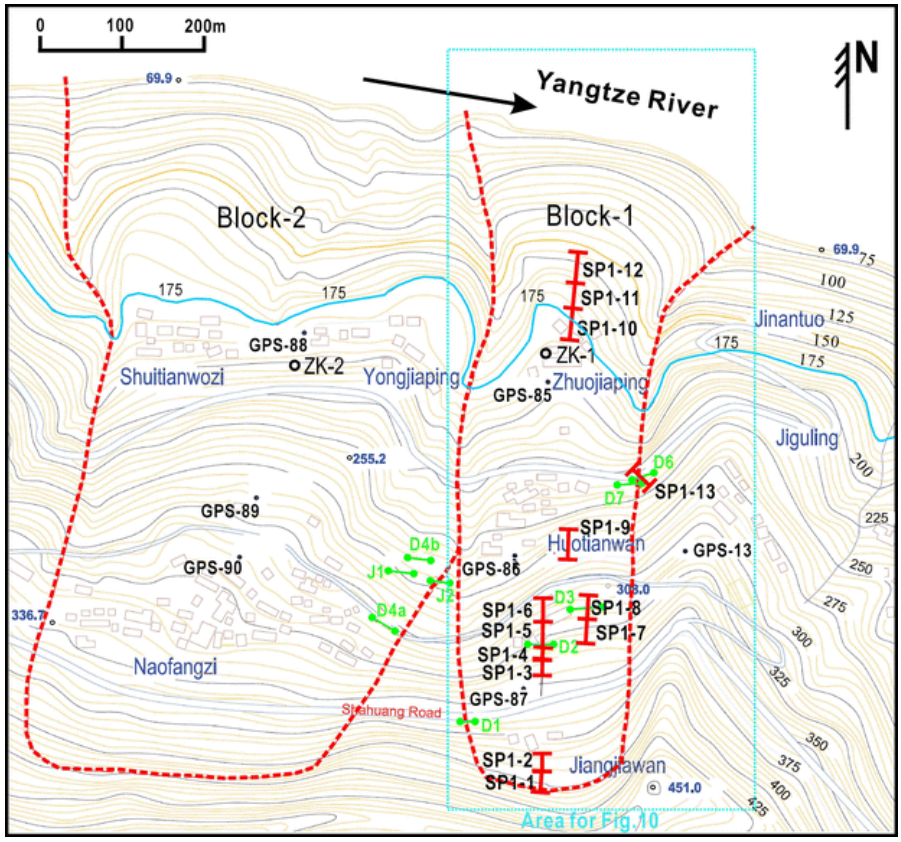

Figure 3-12: Published boundaries of Block-1 and Block-2 for the Shuping landslide (red dashed lines). Extensometers used between 2004 – 07 have been installed on Block-1 (red solid lines). Ten more extensometers were added to Block-1 for the period 2007 – 2010 (Wang *et al.*, 2008a p. 323).

Liao *et al.* (2012) used Persistent Scatterer (PS) interferometry with TerraSAR-X Stripmap data to show movement up and down in the LOS direction in the order of ± 5 mm between February 2008 and January 2010 (Figure 3-13). These measurements are unusual given they are an order of magnitude lower than the extensometer data (< 10 mm displacement in 2009 compared to ~500 mm from extensometer data). The highly non-linear velocity trend revealed by in-situ measurements and the disparities between D-InSAR studies promotes further analysis of the Shuping landslide using SAR data.

Most recently, four months of TSX Spotlight data have been processed using PS-InSAR techniques between January and April 2012 (Perski *et al.*, 2014). Velocities up to 250 mm/yr are reported which more accurately reflects the magnitude of extensometer measurements over the same time period. However, this D-InSAR study also fails to obtain measurements over the fastest period of displacement from May-June and therefore underestimates the total annual displacement by extrapolating just four months of data.

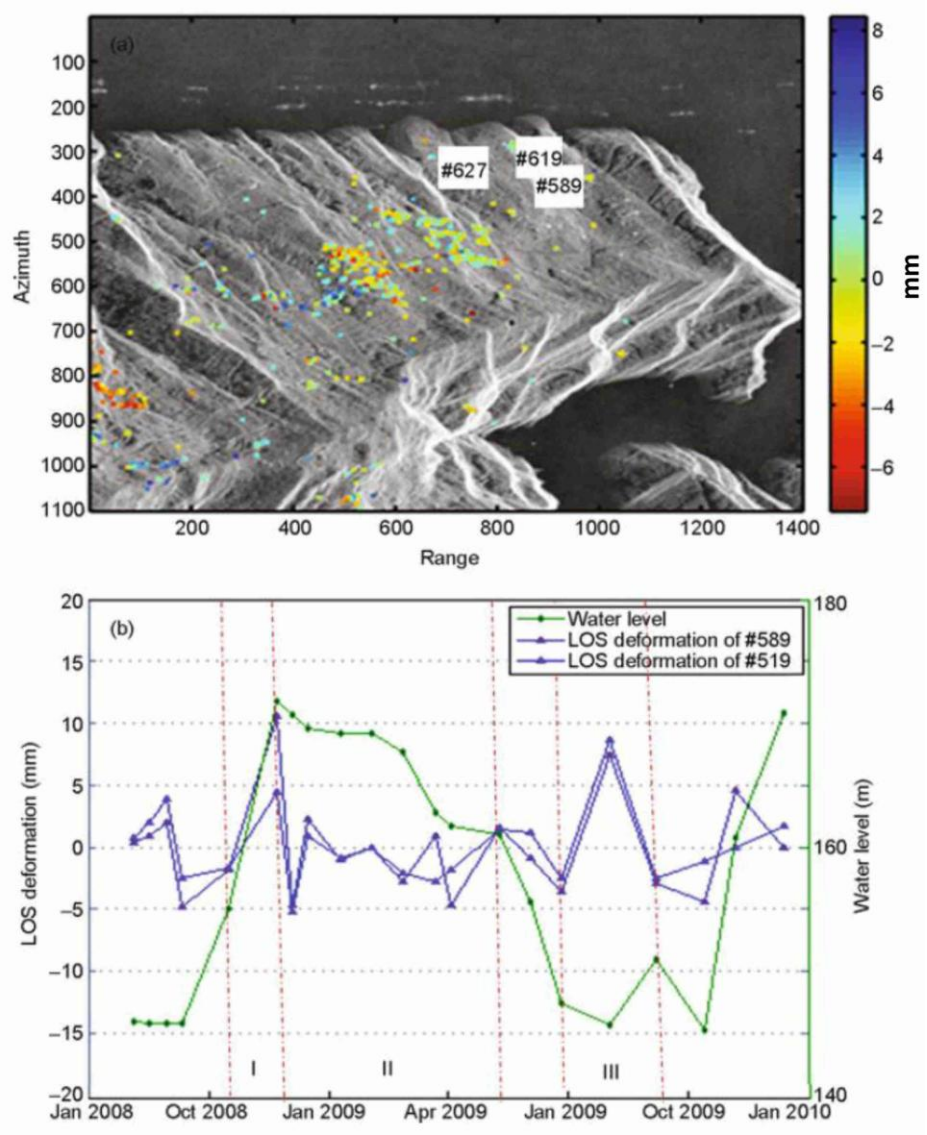

Figure 3-13(a): Noisy mean velocity map over the Shuping landslide for the period January 2008 – January 2010 (Liao *et al.*, 2012 p. 597).

Figure 3-13(b): Noisy time-series curves of displacement, in relation to variation of the Three Gorges reservoir (Liao *et al.*, 2012 p. 597). The magnitude of measurements is within the expected uncertainty associated with the technique.

A sub-pixel offset technique was first applied to TerraSAR-X SAR data by Li *et al.* (2011a) with promising results for monitoring the Shuping landslide, although only four sets of measurements were shown in the paper (corresponding to four offset pairs). This study attempts to recover landslide movements from TerraSAR-X data with a temporal resolution up to every 11 days over a time period of four years.

For this research, the Shuping landslide was selected as a case study and regular SAR data were commissioned in three different image modes over the landslide and over the same time period. The landslide is densely vegetated with orange trees, representative of

the majority of hillslopes in the surrounding areas of the Three Gorges region, making the application of D-InSAR techniques very difficult. The north facing landslide orientation also makes it insensitive to LOS measurements. Independent of this study, corner reflectors have been installed over the landslide which aids the analysis of SAR data (shown in Appendix A, Figure A-1).

Given the active state of the Shuping landslide, continued monitoring is required to determine periods of abnormal acceleration which may indicate an upcoming propensity to catastrophically fail. The case of the Xintan landslide closer to the TGP is an example of successful monitoring as increased activity was detected and followed by the installation of a comprehensive in-situ displacement monitoring system. This led to the successful evacuation of the affected population prior to its catastrophic failure on 12th June 1985 (Huang *et al.*, 2009; Xue, 2009).

Overall, there is scope for further investigation of SAR imagery applied to landslides in the Three Gorges region, particularly comparing significant archives of SAR data from three different spaceborne sensors. In addition to the possibility of identifying previously unknown landslides, there is a demand for increasing the application of D-InSAR techniques beyond the most urbanised areas in the region. Finally, the development of sub-pixel offset techniques using SAR images will be a new application for landslide monitoring and may be applicable for many other landslide prone regions. These techniques can make use of SAR images which may be unsuitable for D-InSAR.

3.4 Large Colluvial Landslides

Colluvium refers to loose, heterogeneous regolith deposits formed by biologic, pedogenic and gravitational slope processes (Schulz *et al.*, 2008), generally characterised by a loose composition, high porosity and high permeability (He and Wang, 2006). Because of complex boundaries and variable compositions of the sliding mass, colluvial landslides have deformation and slippage properties which are different from other types of landslides. The flanks of movement may often be indistinct as shear displacement is distributed over a wide area and for landslides in thick colluvium, movements are typically in the range of centimetres to one metre per episode often in response to above-average rainfall (Fleming and Johnson, 1994). The non-linear and episodic nature of failures in colluvial landslides also means they cannot be easily evaluated by simply considering a mean displacement velocity (He and Wang, 2006).

In the Three Gorges region, colluvial landslides refer to landslides in Quaternary sediments. With slip zones located at the contact between colluvium and bedrock, these landslide types are most common, accounting for more than 50% of all large-scale landslides in the region (Wen *et al.*, 2007). Around 30 large colluvial landslides exist within the Three Gorges (He *et al.*, 2008), examples including the Anlesi, Baishuihe, Bazimen, Xintan and Yuhuangge landslides (He and Wang, 2006; Jian *et al.*, 2009; Yin *et al.*, 2010a; Du *et al.*, 2013).

In the Three Gorges region, displacement curves of most colluvial landslides show a stepwise evolution (Figure 3-14) influenced by precipitation and reservoir fluctuations, often prior to catastrophic failure (Du *et al.*, 2013). For continuously creeping landslides, periods of (sometimes sharp) acceleration and deceleration are also evident.

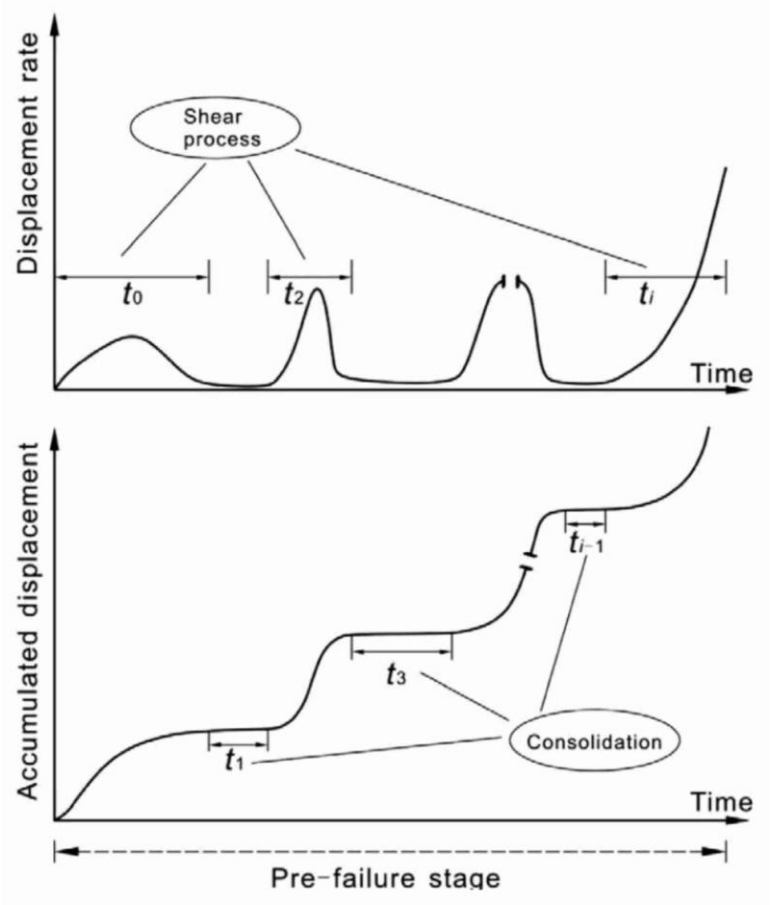

Figure 3-14: Conceptual model for the slow and episodic movement of landslides observed in the Three Gorges region (Miao *et al.*, 2014 p. 62).

Areas of thick colluvium may be formed in mountainous regions from large and ancient catastrophic landslides. Reactivation of these landslide deposits may then be triggered by

external factors such as groundwater changes or increased loading on the slope. The river level rise and fluctuation of the Three Gorges reservoir has been proposed for the reactivation of the colluvial Shuping landslide (Wang *et al.*, 2008a).

3.4.1 Geological Description of the Shuping Landslide

The Shuping landslide is located on the southern banks of the Yangtze River, approximately 45 km upstream from the TGP. The sliding body is approximately 500 m wide and 600 m long, extending from the Yangtze River level (the toe of the landslide is most likely submerged by the reservoir) up to an elevation of ~400 m. The overall slope of the landslide ranges from 10 to 35°.

A gully divides the whole landslide site into an eastern and western block (labelled Block 1 and 2 respectively), although both have similar geological characteristics. It is a multi-period landslide with complicated material composition. The colluvial nature of this ancient landslide deposit is characterised by a body of sliding material (a product of the Triassic Badong group, consisting of brown-red sandy mudstone, muddy siltstone and dust coloured marlite) which sits above a bedrock of fragmented Triassic sandstone, siltstone and shale (Ailan *et al.*, 2008; Qin *et al.*, 2010).

A borehole (Figure 3-15) has indicated the depth of the sliding surface is between 40 – 70 m (Wang *et al.*, 2008a), allowing its volume to be estimated around 26 million m^3 (Wang *et al.*, 2008d). Reactivated in 2003 following reservoir inundation, the landslide has been monitored using extensometers until 2010 (Wang *et al.*, 2013b). During this period the landslide has appeared most susceptible to periods of reservoir lowering.

This description summarises all the known geological information on the Shuping landslide making further interpretations difficult. The use of frequently acquired SAR images for particular monitoring of the Shuping landslide is also encouraged given how in-situ results cease in 2010 despite the active nature of the landslide.

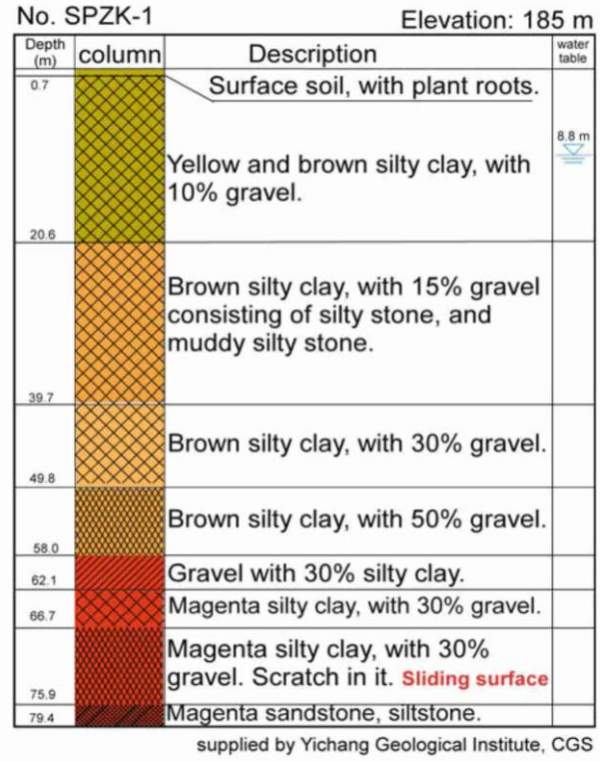

Figure 3-15: Lithological column diagram of the borehole located towards the middle/bottom of Block 1 in the Shuping landslide (Wang *et al.*, 2005a p. 318).

3.5 Slope Stability Modelling

Calculating the Factor of Safety (F_S) for a specific slope is a common engineering practice and an important step in assessing the stability of slopes. An index of stability for an appropriate geotechnical model can be classified by various approaches, such as limit equilibrium or finite element methods. Lacking detailed and spatially varied geotechnical measurements of soil properties, most slope stability analysis employs a 2D limit equilibrium method which requires values for the strength of soil/rock but does not need information about their shear-strain behaviour (Wang *et al.*, 2007).

Within the Three Gorges, very few modelling studies have been published related to the stability of known landslides within the region. In a similar respect to remote sensing applications, the most modelled landslide is the Huangtupo slope in Badong due to its well known geotechnical parameters for various subsurface layers. Using limit equilibrium and finite element methods, the slope has been assessed under both static conditions and dynamic situations of fluctuating reservoir levels (Cojean and Caï, 2011; Hu *et al.*, 2012b).

With the reservoir at its lowest level of 145 m the factor of safety value for the Huangtupo slope is ~1.24, compared with a value of ~1.22 when the reservoir is at 175 m (Cojean and Caï, 2011). In the case of a rapid reservoir drawdown, the factor of safety is shown to

decrease up to 3% compared with the static scenarios of stable water levels, although this may be small given the uncertainties of estimating F_S. Additionally, the toe of the landslide within the reservoir fluctuation zone exhibits the greatest simulated displacement due to its increased sensitivity to hydraulic effects (Hu *et al.*, 2012b).

The same effects of reservoir drawdown were found in another slope modelling study of the Qiaotou landslide (30.1N, 110.8E) in the Three Gorges region (Jiang *et al.*, 2011a). Numerical simulation using a finite difference method was applied to the slope after detailed fieldwork, in-situ testing and laboratory experiments. Assuming drawdown of 0.25 m/day, a maximum displacement of 0.24 m was found with vulnerable landslide areas migrating from the head to the toe of the landslide. This may reflect a mechanism change from initial seepage forces causing displacement, to later stages of soil consolidation.

Both these results, along with the famous Vajont landslide and other major events highlight the potential influence of reservoir fluctuations on slope stability (Petley, 2013) which will be explored as a potential triggering factor for landslides identified in this study.

3.6 Summary

Chapter 3 provides a background to landslides in the Three Gorges region. The geological setting and the local geology of the region is outlined as well as descriptions of the different landslide types. Hydrological influences on landslides in the region are considered, such as the annual rainfall regime and also the development of the Three Gorges Project. The 600 km long reservoir generated by the dam has significant implications on the landscape, along with its operational annual fluctuation of ~30 m in elevation.

A review of significant remote sensing studies on landslides in the Three Gorges is provided. The use of optical imagery combined with a DEM is most commonly used for hazard assessments whereas radar imagery has been used to measure displacements, albeit with a focus on urban areas. Conflicting D-InSAR results over the same time period for the Shuping landslide are presented, warranting further investigation.

The progression of temporally variable, stepwise movements for colluvial landslides are explored and previous modelling results in the Three Gorges show these are linked to reservoir fluctuations. A greater understanding of landslide behaviour in response to such influences is required and has generic implications for slopes bordering other reservoirs.

Chapter 4 : Evaluating D-InSAR Use in the Three Gorges Region

Despite the advantages of D-InSAR methods outlined in Chapter 2, limitations should always be considered, namely: geometric decorrelation; temporal decorrelation; atmospheric artefacts; scale constraints; limits on the spatial displacement gradient; geometric distortions; and, a 1-dimensional Line-of-Sight (LOS) measurement sensitivity (Colesanti and Wasowski, 2006). Whilst time-series D-InSAR methods developed over the last 15 years can partly overcome some of these limitations using a long series of SAR images (e.g. Ferretti *et al.*, 2001; Berardino *et al.*, 2002; Hooper *et al.*, 2007; Hooper, 2008; Perissin and Teng, 2012), fundamental theoretical constraints still exist given the SAR data characteristics and D-InSAR processing strategies. An insufficient appreciation of these inherent limitations, combined with the natural complexities of landslide movements can lead to the misrepresentation of satellite SAR data (Colesanti and Wasowski, 2006; Peduto *et al.*, 2010). Consequently, end-users may lack confidence in these remotely-sensed results unless verified with ground data, thereby negating some of the benefits of using remotely collected data. It is important to understand controlling factors upon the quality of D-InSAR results specifically in relation to the phenomena under investigation, the landcover / climatic conditions of the study area and the available SAR image data.

To address the first research question (page 10), this chapter investigates the capabilities and limitations of D-InSAR techniques for monitoring slopes in the Three Gorges region that border a ~30 km stretch of the Yangtze River. The availability of three spatially and temporally overlapping SAR data series in various image modes (TSX Spotlight, TSX Stripmap and ENVISAT Stripmap) allows useful comparisons to be made between the data sets since the differences (particularly in the radar wavelength, range/azimuth resolution and the satellite revisit time) often have significant implications for successful landslide monitoring (Metternicht *et al.*, 2005; Herrera *et al.*, 2011; 2013). For each image mode, the ability to detect unstable slopes, map landslide boundaries and acquire regular measurements is assessed whilst considering the limitations of geometric and temporal decorrelation, scale constraints, geometric distortions and the spatial displacement gradient.

4.1 Study Area and Data Sets

The Three Gorges were formed by incision along narrow fault zones of massive limestone mountains interbedded with siltstone, shale and mudstone (Wang *et al.*, 2008c), although between gorges the lithologies are much less resistant. Dominated by weathered mudstones, these inter-gorge areas favour river bank erosion, terrain dissection and the development of slow-moving slope failures (Liu *et al.*, 2004).

This study focuses on a ~30 km stretch of the Yangtze River in the eastern Three Gorges region, predominantly located between the Wu Gorge and Xiling Gorge (Figure 4-1). This area was selected because regular SAR data in three different image modes have been acquired, overlapping in both time and space. The mountainous area is densely vegetated with orange trees and, being representative of the majority of hillslopes in the Three Gorges region, makes the application of D-InSAR techniques a very difficult task. Small villages can be found on slopes bordering the Yangtze River, but these typically have low populations of 50-200 people, housed in small buildings amongst the dense vegetation. Therefore, any permanent/persistent scatterer (PS) analysis would only generate a sparse network of points throughout the region.

There are at least eight previously known landslides within the TSX Stripmap data coverage (Figure 4-1) and the most recent published monitoring data cease in early 2010. Continued monitoring of these landslides is required and the use of SAR satellite data can measure slope movements as well as potentially detect previously unknown landslides.

Figure 4-1 and Table 4-1 give the locations of many known landslides within the TSX Stripmap coverage. The predominant north-south sliding direction coupled with the orientation of the descending SAR data makes six of the landslides quite insensitive to LOS measurements from conventional D-InSAR techniques (explored further in Section 4.6). This provides an additional opportunity to test the suitability of D-InSAR for monitoring these landslides.

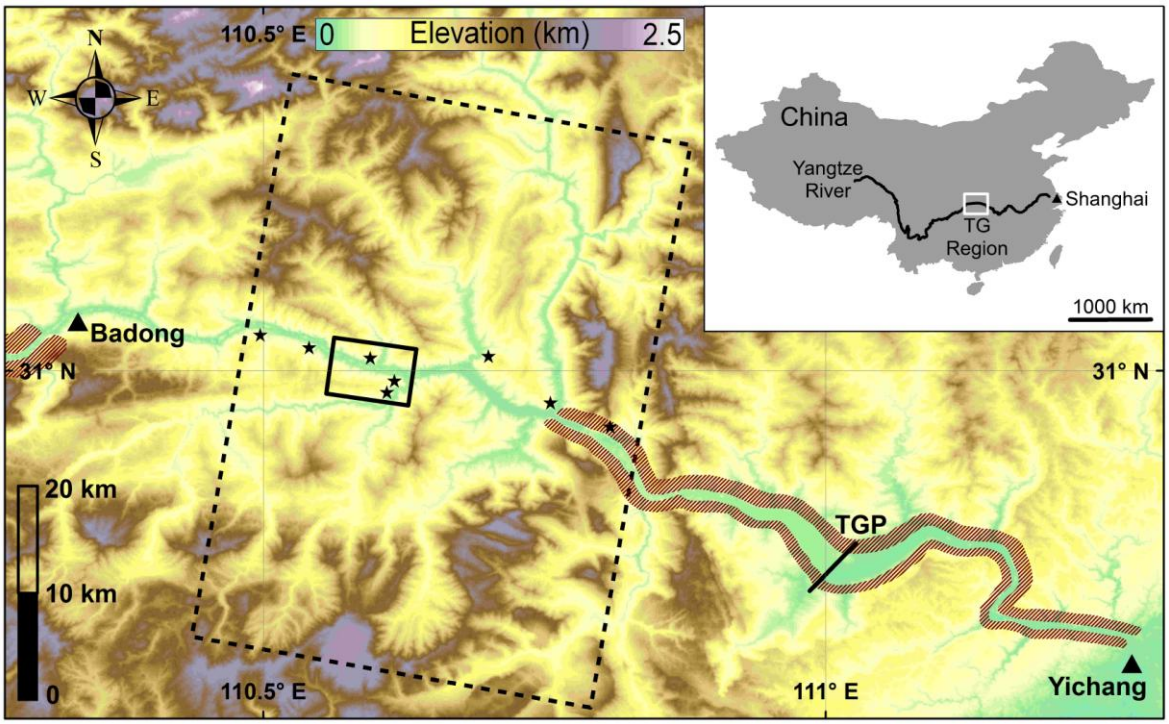

Figure 4-1: Location map and elevation of the eastern TG region. TSX Spotlight data coverage is shown by the solid box and TSX Stripmap data coverage is shown by the dashed box. Descending ENVISAT data covers the whole map. Red hatching indicates the two gorges in this area, Wu gorge to the west of Badong and Xiling gorge further east. Black stars indicate known landslides, listed in Table 4-1 in the order they appear from east-west.

Table 4-1: Basic information about previously known (i.e. published) landslides in the study area. These are shown in Figure 4-1 and are listed by location, from east-west.

Landslides	Location (N/E)	Distance from TGP (km)	Volume (10^6 m^3)	Reference
Xintan	30.944° 110.805°	26	30	(He *et al.*, 2008)
Bazimen	30.967° 110.761°	30	2	(Du *et al.*, 2013)
Kaziwan	31.013° 110.698°	40	34	(Xue *et al.*, 2009)
Shuping	30.993° 110.619°	46	20	(Wang *et al.*, 2008e; Wang *et al.*, 2013b)
Qianjiaping	30.970° 110.607°	47	20	(Wang *et al.*, 2004; Wang *et al.*, 2008b)
Xietan	31.009° 110.595°	48	9	(Zhang *et al.*, 2009b)
Baishuihe	31.024° 110.540°	54	12.6	(Li *et al.*, 2010; Du *et al.*, 2013)
Fanjiaping	31.034° 110.497°	58	125	(He *et al.*, 2008)

Finally, various studies monitoring the Shuping landslide using D-InSAR techniques were shown in Chapter 3 to yield highly varied results over the same time period of the available SAR data (Fu *et al.*, 2010; Xia, 2010; Liao *et al.*, 2012). Given the highly non-linear velocity trends revealed by in-situ extensometer measurements (Wang *et al.*, 2013b) and the disparities with previous D-InSAR studies, this prompts particular analysis of the Shuping landslide using SAR data.

4.1.1 TerraSAR-X Spotlight Data

The longest series of data over this study area was obtained in High Resolution Spotlight (HS) image mode from the TSX sensor. A total of 57 HH-polarised images were available between 21st February 2009 and 23rd February 2013 acquired from a right-looking sensor orientation on a descending orbit with a scene-centre incidence angle of 44° (from 43.5° to 44.4°, east-west). The majority of images were acquired at 11-day intervals, although there is a gap in the data series between 15th April 2010 and 2nd January 2012. It should also be noted that around half of the second data series was acquired at monthly (~33-day) intervals (Figure 4-2b).

With a chirp bandwidth of 300 MHz, the data have a slant range resolution of 0.6 m and an azimuth resolution of 1.1 m, although this imaging mode subsequently has the smallest areal extent of ~38.5 km^2 (7 x 5.5 km, range x azimuth). Figure 4-2 shows the temporal, spatial and Doppler Centroid (D_C) separation between subsequent image acquisitions. The constant and precise orbit control has always kept the satellite platform within its predefined orbital tube of 250 m (Yoon *et al.*, 2009) which ensures any interferometric image pair has a perpendicular baseline far below the critical baseline value of ~17,700 m.

Finally, the D_C difference between image pairs was considered since this is of particular importance in forming a coherent TSX Spotlight interferogram. The ground projected range-spectra of both SAR images must overlap (Gatelli *et al.*, 1994) as well as the received Doppler frequency spectra (Bamler and Hartl, 1998). Fulfilling the second condition is more difficult in a spotlight imaging mode since both images may have different acquisition start times and different squint angles even if the beam sweep rates are equal (Eineder *et al.*, 2009). Incorporating real-time GPS measurements and star trackers to control the antenna's position and look direction (which determines the D_C frequency), the pointing error is less than 20 m on the ground which generates D_C differences typically less than 120 Hz (Eineder *et al.*, 2009). The D_C differences within the

TSX Spotlight data set are consistently below this threshold and the maximum value of 100 Hz corresponds to < 2% of the azimuth bandwidth in high-resolution spotlight mode (focused azimuth bandwidth ≈7300 Hz). As complete decorrelation occurs when the D_C difference equals the azimuth bandwidth, all image pairs fall well within this threshold.

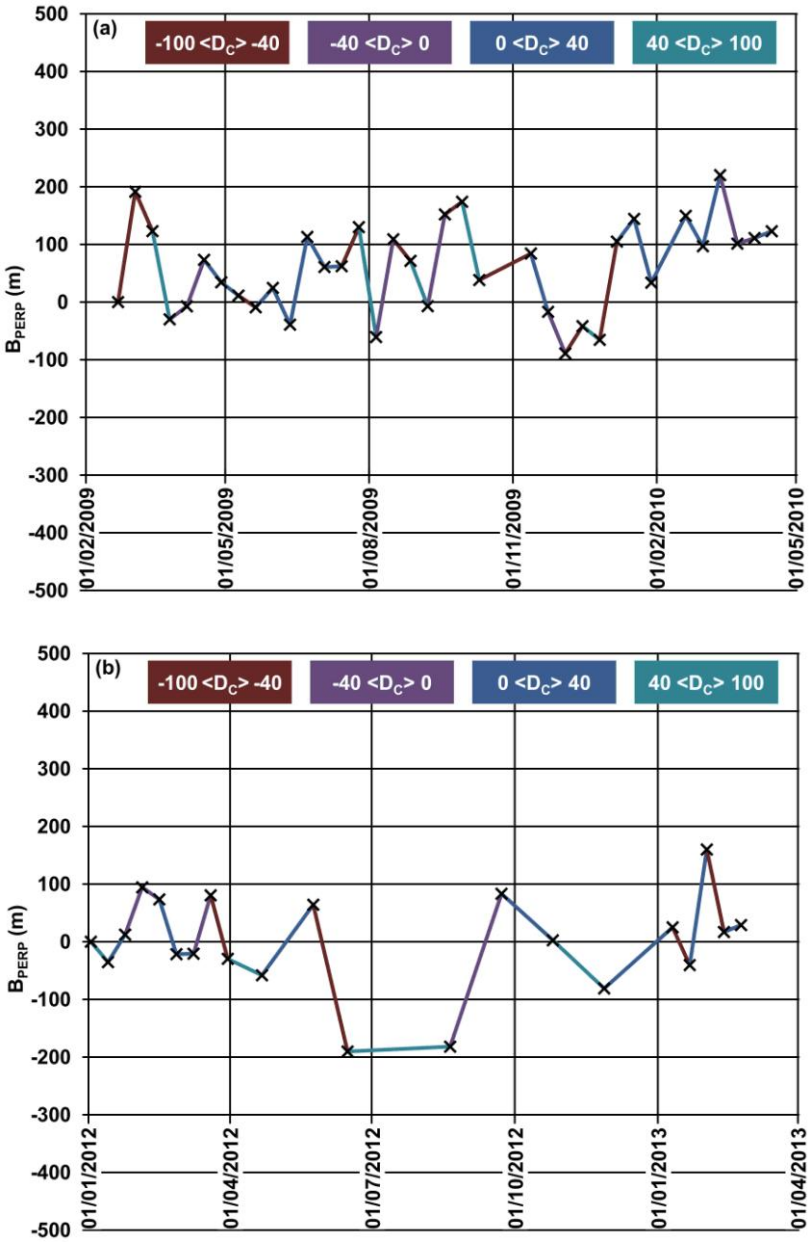

Figure 4-2(a): Baseline plot of TSX Spotlight data from 2009 – 2010. The Doppler Centroid (D_C) difference (Hz) is shown by the different colours linking consecutive image pairs.

Figure 4-2(b): Baseline plot of TSX Spotlight data from 2012 – 2013.

4.1.2 TerraSAR-X Stripmap Data

The shortest series of SAR images over this study area was Stripmap (SM) image mode data from the TSX sensor. A total of 23 VV-polarised images were available between 22nd

April 2009 and 31st December 2009, acquired from a right-looking sensor orientation on a descending orbit with a scene-centre incidence angle of 23° (from 24.5° to 28.2°, east-west). Except for the very last image acquisition, every image was acquired at 11-day intervals (Figure 4-3) and falls completely within the temporal coverage of the TSX Spotlight data.

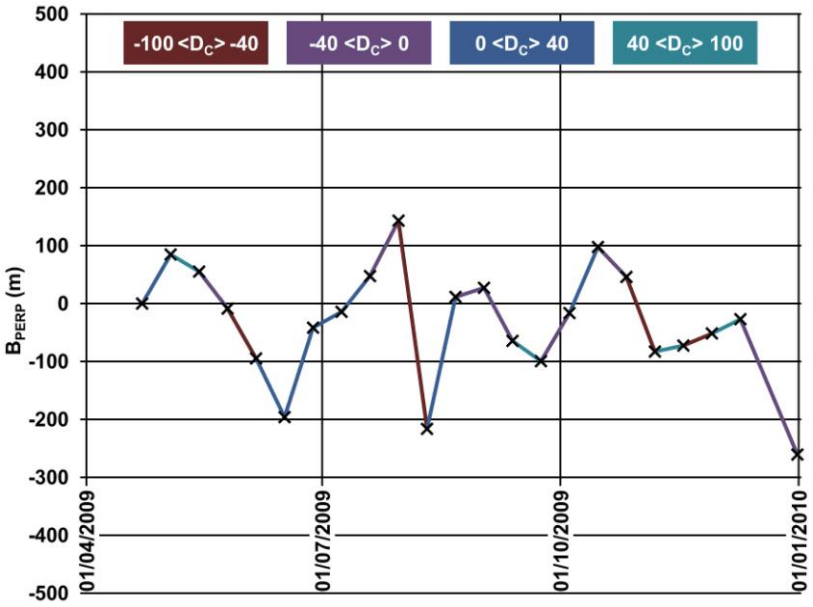

Figure 4-3: Baseline plot of TSX Stripmap data. The Doppler Centroid (D_C) difference (Hz) is shown by the different colours linking consecutive pairs.

With a chirp bandwidth of 150 MHz, the data have a slant range resolution of 1.2 m and an azimuth resolution of 3.3 m, covering an area of ~1500 km^2 (30 x 50 km, range x azimuth). The baseline plot for the TSX SM data (Figure 4-3) again shows the TSX satellite remained within its 250 m orbital tube ensuring any interferogram image pair has a perpendicular baseline far below the critical baseline value of ~4,000 m. The D_C differences are also consistently below ± 100 Hz, which is far below the total focused azimuth bandwidth of ~2765 Hz.

4.1.3 ENVISAT ASAR Stripmap Data

Finally, a series of data covering a very large area of the Three Gorges region was obtained in Stripmap (SM) mode from the ENVISAT sensor. A total of 14 VV-polarised images were available between 28th December 2008 and 2nd May 2010 acquired from a right-looking sensor orientation on a descending orbit with a scene-centre incidence angle of 22.8°. Again, except for the very last image acquisition, every image was acquired at the shortest possible repeat interval of 35-days (Figure 4-4) and completely covers the first half of the TSX Spotlight data series.

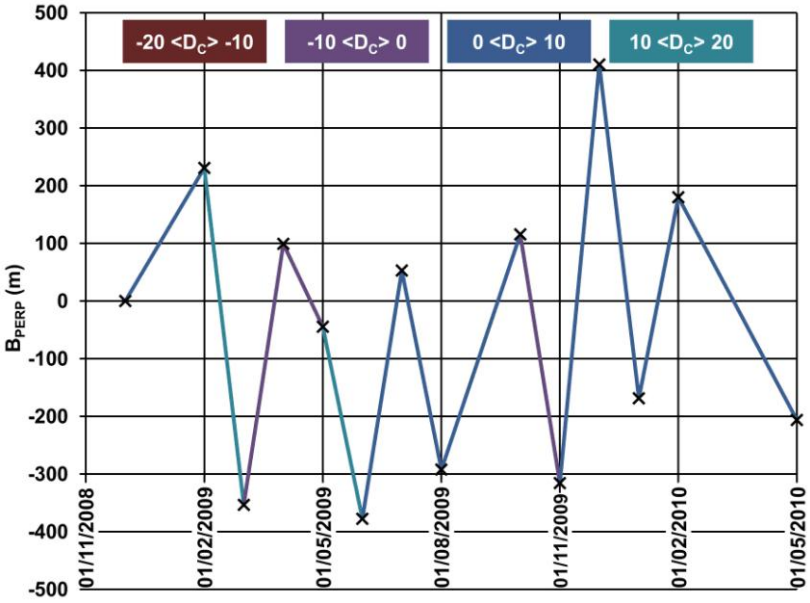

Figure 4-4: Baseline plot of ENVISAT Stripmap data. The Doppler Centroid (D_C) difference (Hz) is shown by the different colours linking consecutive pairs.

With a chirp bandwidth of 16 MHz, the data have a slant range resolution of 7.8 m and an azimuth resolution of 4.22 m, covering both the TSX HS and SM image areas. The baseline plot for the ENVISAT SM data (Figure 4-4) shows the ENVISAT satellite stays within an orbital tube of 400 m which results in far higher perpendicular baselines between interferometric pairs, although they all stay below the critical baseline value of ~930 m. Finally the D_C differences are far smaller than TSX interferometric pairs, with differences always less than ± 20 Hz and well below the critical D_C value of ~1500 Hz.

4.2 Coherence Analysis

The principles of interferometric coherence (γ) and decorrelation have been outlined in Chapter 2. The success of D-InSAR analysis is highly related to coherence since interference phenomena such as deformation fringes can only be observed when there is at least partial coherence between two SAR images (Wegmuller and Werner, 1995). Decorrelation sources have been well documented (Zebker and Villasenor, 1992; Bamler and Hartl, 1998; Hanssen, 2001) and this section specifically analyses coherence factors influencing the quality of D-InSAR results for the available data over the Three Gorges study area. Defining decorrelation as the noise caused by error sources with a correlation length smaller than the coherence estimation window (Hanssen, 2001), factors such as orbit errors and atmospheric heterogeneities are excluded from this section.

Using D-InSAR techniques to investigate landslides, geometrical and temporal decorrelation are considered the dominant factors reducing coherence (Rott and Nagler, 2006). Particularly in densely vegetated areas such as forests and agricultural areas, signals can decorrelate within a few days due to plant growth and disturbance by wind (Colesanti and Wasowski, 2006; Rott and Nagler, 2006; Ahmed *et al.*, 2011) causing the distribution of wavelength-scale scatterers within a resolution cell to change between SAR acquisitions, uncorrelated with other resolution cells (Hanssen, 2001). In addition to vegetation properties, variable quantities such as rainfall between image acquisitions can alter the dielectric properties of the ground, reducing coherence (Askne and Santoro, 2005; Ahmed *et al.*, 2011). L-band SAR data can penetrate vegetation to a greater extent than shorter wavelengths and can achieve higher coherence interferograms (Raucoules *et al.*, 2003; Strozzi *et al.*, 2005), although these data were unavailable for this study. Subsequently, the coherence of three data modes from the TSX and ENVISAT ASAR sensors was analysed to understand the most suitable data for D-InSAR landslide monitoring in the Three Gorges region.

4.2.1 Coherence Processing

Differential interferograms were generated with a multi-look factor of two applied in both range and azimuth directions for the TSX data, and factors of 2 and 10 in range/azimuth, respectively were applied to the ENVISAT data. The topographic phase component was removed using the Advanced Spaceborne Thermal Emission and Reflection Radiometer (ASTER) Global Digital Elevation Model (GDEM) v2, a product of METI and NASA (http://earthexplorer.usgs.gov/). No spectral shift filter, Doppler filter or post-processing filter was applied during the processing. Finally, a sample estimate of the coherence was measured using a 9 x 9 window which provides an adequate statistical sample for coherence analysis since the number of resolution elements is >50 (Rott and Nagler, 2006) and the large number reduces the inherent bias in coherence estimation which often tends to overestimate low coherence values (Bamler and Hartl, 1998; Touzi *et al.*, 1999).

The mean coherence value was obtained from a 5 km^2 area of land adjacent to, but excluding, the Shuping landslide. The slope and land cover in this area are very typical of many landslides within the study area. Seasonal patterns were assessed by plotting the mean coherence for every 11-day (TSX) or 35-day (ENVISAT) image pair over time and effects of the perpendicular baseline (B_{PERP}) were considered by plotting the mean coherence for the same 11-day / 35-day image pairs with respect to the B_{PERP}. Temporal

decorrelation was assessed by plotting the mean coherence for all pairs with a B_{PERP} less than 25 m (TSX data) or 50 m (ENVISAT data) with respect to the time interval between image acquisitions.

All the results presented below were produced using the SARscape® software package (SARMAP, 2012) which includes interferometry modules capable of processing all the necessary data formats included in this study.

4.2.2 Coherence Results

The coherence for all 11-day or 35-day image pairs between December 2008 and May 2010 for all image modes (Figure 4-5a: left-hand column) is very low throughout the 1.5 years, never exceeding 0.37, although a consistent seasonal pattern is shown for the TSX imagery with the highest coherence found between November and February each year.

Plotting the coherence against 10-day accumulated rainfall values (Figure 4-5a: left-hand column, black bars), the months of November – February had a far lower mean monthly rainfall (~19 mm/month) compared to the other months (~100 mm/month). Given the sensitivity of radar backscatter to the dielectric effects of changing surface moisture content (Smith, 2002), it is very likely this reduction in coherence between March and October is attributable to the heavy rainfall.

The seasonality in coherence and rainfall may also be interrelated with the dense orange tree vegetation throughout the region. A Normalised Difference Vegetation Index (NDVI) map from Landsat 8 shows the dominance of vegetation throughout the Three Gorges region (Figure 4-6a). After the ENVI® calibration procedure converting digital numbers to reflectance values, seasonal vegetation change between December 2008 and May 2010 can be visualised (Figure 4-6b). For all Landsat 5/7 cloud-free images acquired over the SAR data time period, cumulative NDVI values follow a clear gradient with lowest values in December/January, and highest values in May.

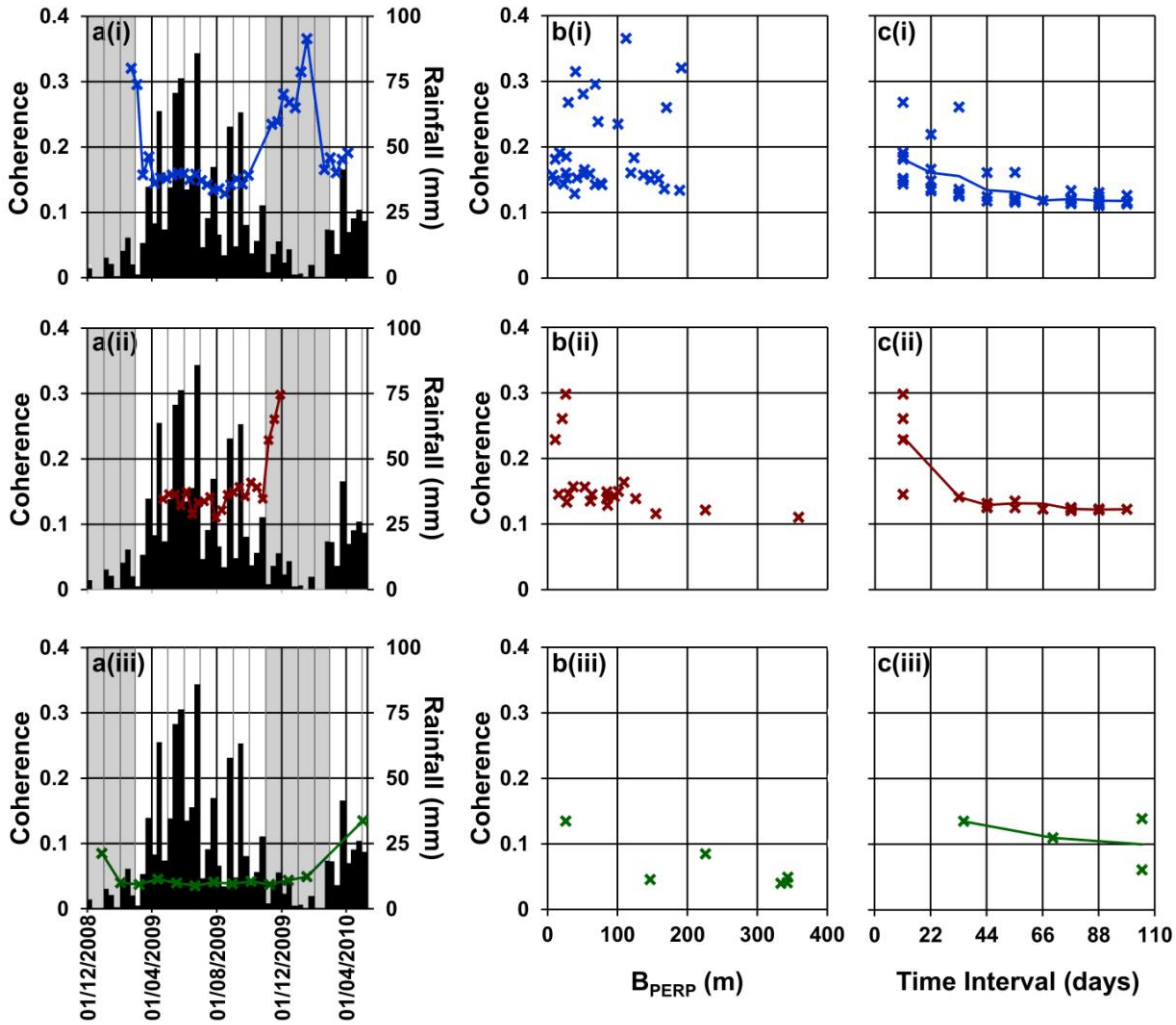

Figure 4-5: Coherence analysis for the three SAR imaging modes from December 2008 – May 2010. (i) TSX Spotlight data; (ii) TSX Stripmap data; (iii) ENVISAT Stripmap data. (a) Mean coherence of all 11-day (TSX) or 35-day (ENVISAT) interferograms showing the highest values between November and February when rainfall (values plotted every 10 days) and vegetation cover are at a minimum. The coherence standard deviation varies between 0.08 – 0.15 for TSX Spotlight data; 0.07 – 0.1 for TSX Stripmap data; and, 0.02 – 0.06 for ENVISAT data; (b) Mean coherence of all 11-day/35-day interferograms plotted against B_{PERP}; (c) Mean coherence of interferograms (all $B_{\perp} < 30/50$ m for TSX/ENVISAT data) with respect to the time interval of image acquisitions showing a decline after ~33 days.

The NDVI is commonly used to provide information about the spatial and temporal distribution of vegetation and its biomass. Whilst the NDVI is not able to differentiate between plant species (Pettorelli *et al.*, 2005), the fluctuation of median NDVI values between ~0.2 and ~0.5 is consistent with chaparral/forest vegetation values as opposed to tall grasses and crops (Reed *et al.*, 1994). The seasonal variation also matches the conclusion of Dzikiti et al (2011) who found canopy reflectance of citrus trees changes significantly over a year even if orange trees are evergreen. It is difficult to separate the combined effects of rainfall and vegetation change on interferometric coherence, but the

variation in coherence shows the importance of choosing the optimal image mode, time interval, perpendicular baseline or season to generate the best quality interferograms.

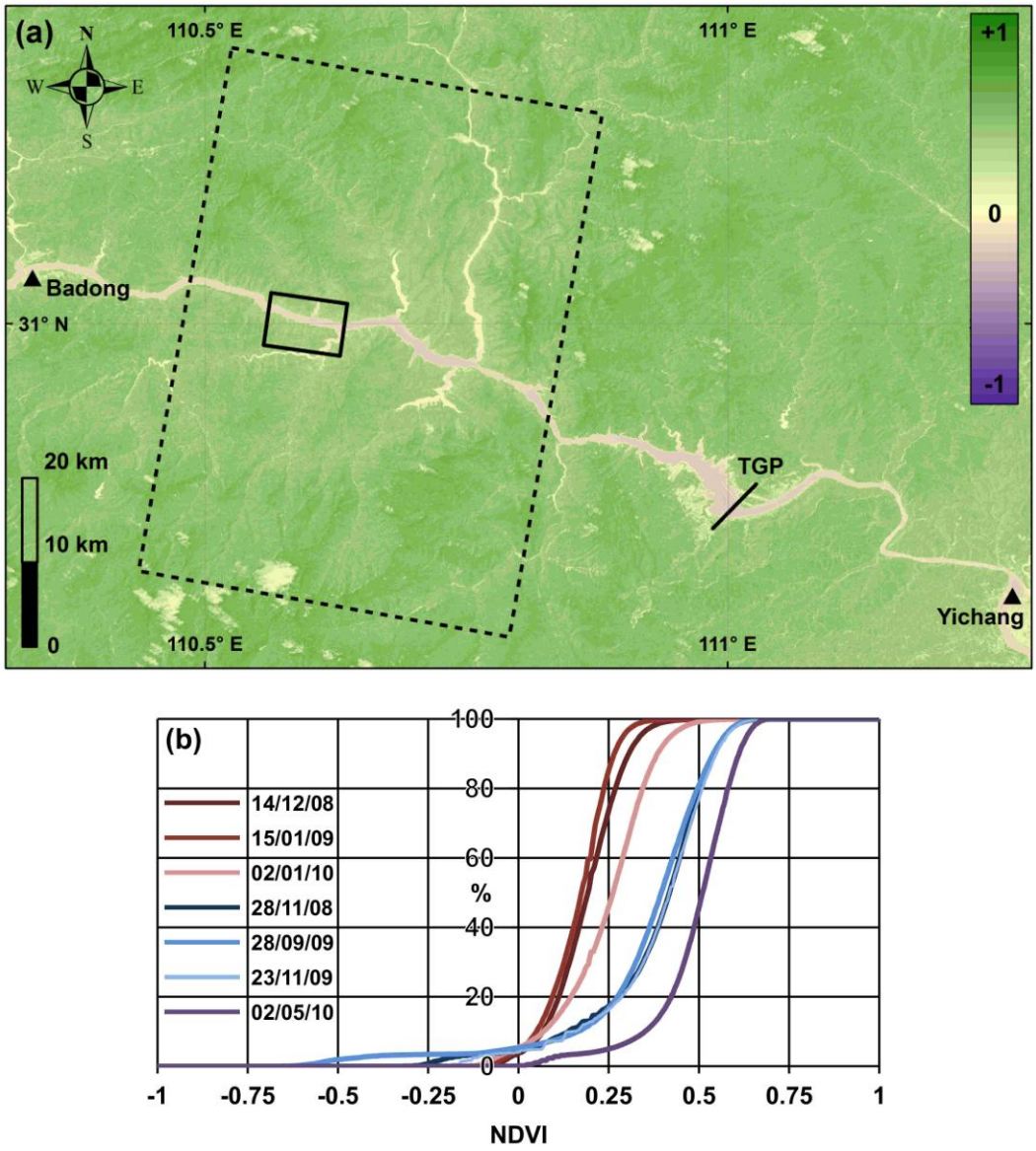

Figure 4-6(a): NDVI map of the eastern TG region from the Landsat 8 OLI sensor. Image taken on 22nd June 2013. Values closer to +1 result from healthy vegetation reflecting a higher proportion of near-infrared light than visible (red) light, highlighting the density of vegetation throughout the region. There are very few urban areas or exposures of bare rock.

Figure 4-6(b): Cumulative distribution of NDVI values in the TG region. These values were extracted from all pixels within the TSX Stripmap image coverage, shown by the dashed box in Figure 4-6(a). Acquisitions on 23/11/2009 and 02/05/2010 were Landsat 5 TM images, the remainder being Landsat 7 ETM+ images.

Despite its shorter wavelength, TSX data display consistently higher coherence values than the ENVISAT data, most likely due to the significantly higher resolution and much shorter repeat interval of the TSX satellite compared with ENVISAT. The coherence for each 11-day (TSX) or 35-day (ENVISAT) interferogram with respect to the perpendicular

baseline (Figure 4-5b: middle column) shows no definitive trend over the range of relatively short baselines (up to 400 m), and coherence values > 0.2 are always from the TSX interferograms created in the dry winter period.

The right-hand column of Figure 4-5 shows the coherence for all interferograms with a baseline less than 25 m (TSX) or 50 m (ENVISAT) in relation to the time interval between acquisitions. A relatively fast fall in coherence is seen with the TSX data until the interval exceeds ~33 days where it remains at a constant non-zero level. This constant value is considered to represent the natural bias in estimating the coherence correlation magnitude (Touzi *et al.*, 1999). The almost complete loss of coherence beyond 33 days could also explain why no significant seasonal coherence pattern is observed from the ENVSIAT data as ground vegetation and moisture are likely to be more varied over a 35-day interval compared with the 11-day interval of TSX data.

Lastly, the same analysis was carried out for the extra TSX data acquired between January 2012 and February 2013 (Figure 4-7). Very similar patterns are generally observed although some important distinctions should be noted. Given the 11-day acquisitions do not continue between April and December 2012 (reduced to one image per month), it is not possible to obtain measurements during this period. However, higher coherence values are mostly observed during the same winter months of November to February each year (Figure 4-7a: left-hand column). Unfortunately no suitable rainfall data are available for this period, but the exceptionally high value between the 4 – 15th February 2012 could be caused by a complete absence of rainfall. Similarly, the two exceptionally low points in January/February 2013 could be caused by heavy rainfall on or around the shared middle date of February 1st 2013, in addition to these pairs having the highest perpendicular baseline values.

For the 2012/13 data, care should be taken when assessing the effects of the perpendicular baseline on coherence (Figure 4-7b: middle column) and the effects of different time intervals (Figure 4-7c: right-hand column) since >80% of 11-day image pairs were acquired in the winter months. However, since image pairs with an equal time interval and perpendicular baseline have varied coherence values, this supports the argument that seasonality and the variable vegetation/ground moisture are dominating factors. Also, coherence is shown to quickly decline for time intervals beyond the shortest 11-day interval, although the time taken to reach a 'stable' non-zero level is longer perhaps due to the skewed distribution of images being acquired in the winter period.

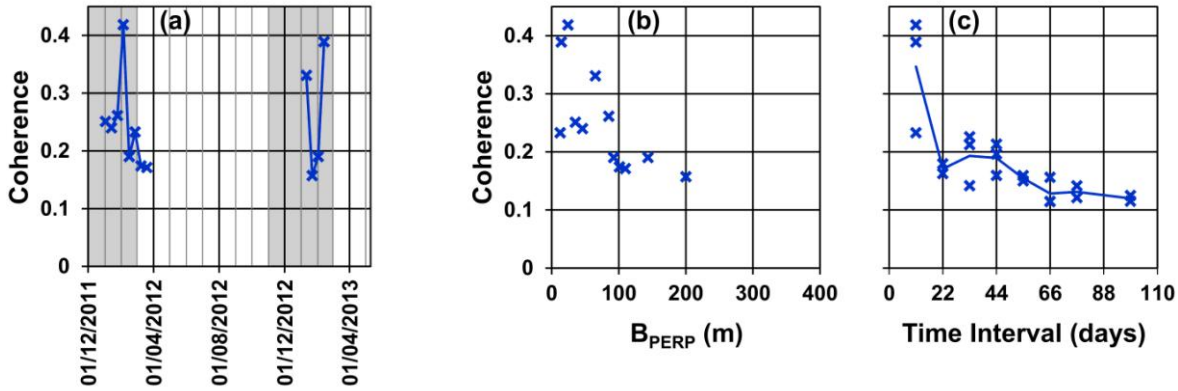

Figure 4-7: Coherence analysis for TSX Spotlight data from January 2012 – February 2013. (a) Mean coherence of all 11-day interferograms; (b) Mean coherence of all 11-day interferograms plotted against B_{PERP}; (c) Mean coherence of interferograms (all $B_{\perp} < 30$ m) with respect to the time interval of image acquisitions.

4.3 Identifying Landslides from D-InSAR Analysis

To remotely monitor landslides with high precision, the optimal approach would employ high coherence interferograms with minimal geometric distortions which cover the whole time period. Given the low values of coherence presented above, this section presents interferograms from all three image modes to demonstrate the capabilities and limitations of D-InSAR data for detecting and monitoring landslides in the Three Gorges region.

The processing of all interferograms followed the same steps as the coherence analysis, with the addition of a spectral shift filter to account for the difference in incidence angles between master and slave images (Gatelli *et al.*, 1994), a Doppler filter to remove the non-overlapping azimuth spectra and a Goldstein filter (Goldstein and Werner, 1998) applied to the interferograms prior to geocoding.

4.3.1 DEM Selection

The ASTER GDEM v2, a product of METI and NASA, was selected as the best available DEM in the region in terms of accuracy and spatial resolution. The DEM has an RMSE of 12.1 m and a correlation of 0.97 compared with 121 GPS benchmarks around the Badong area of the Three Gorges region, which is a good improvement in relation to SRTM data (RMSE = 24.5 m and $r = 0.92$) (Li *et al.*, 2012). This agrees with the conclusion from a national study in Japan that found ASTER GDEM is superior to SRTM for most landforms, including steep mountainous areas, due to its higher resolution and less missing data which leads to more realistic representations of topography (Hayakawa *et al.*, 2008).

Extending the analysis for the whole study area, the ASTER DEM was also compared with the Shuttle Radar Topography Mission (SRTM) DEM v4 and a 16-bit GeoTIFF Raw DEM with a pixel spacing of 40 m initially generated by the German Aerospace Centre (DLR) from a TanDEM-X (TDX) image pair. The results are presented in Figure 4-8. The single TDX image pair was not processed to a full resolution DEM as it is commonly accepted that dense vegetation and mountainous areas increase the interferometric phase uncertainty and susceptibility to unwrapping errors (Martone *et al.*, 2013) reducing the quality of the final DEM. Additional acquisitions from a variety of different viewing positions are required to improve the accuracy of the final TDX DEM and will be acquired in a dedicated mission phase (Borla-Tridon *et al.*, 2013).

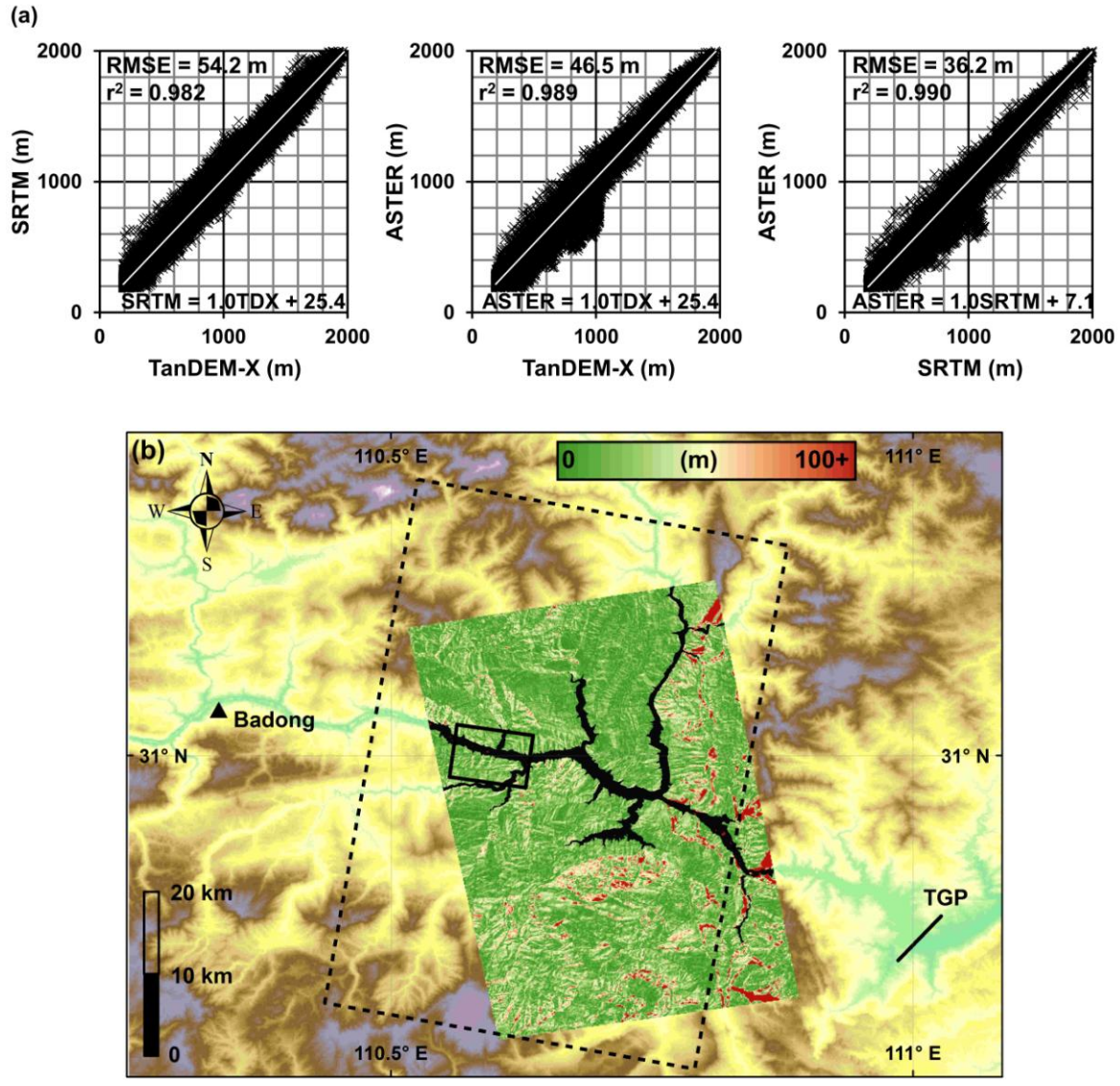

Figure 4-8: DEM comparisons between STRM, ASTER and TanDEM-X (TDX) data.
(a) Linear regression analysis between the three data sets over the full coverage area of TDX data; (b) Absolute difference between SRTM and ASTER elevation values, over the full coverage area of TDX data. Solid box represents TSX Spotlight data; dashed box represents TSX Stripmap data.

The RMSE, correlation values and the bias (shown by the trend line intercept) for TanDEM-X data comparisons are worse than the relationship between ASTER and SRTM data (Figure 4-8a). Although some data from the ASTER elevation model appear to diverge from the y = x trend line (approximately when SRTM = 1000 m and ASTER = 700 m), these absolute differences in elevation values are not apparent over the study area, only being found to the eastern areas of the TDX coverage (Figure 4-8b). This is where the Xiling gorge starts and where almost vertical slopes are likely to generate the largest differences between elevation values. For these reasons, the ASTER DEM is deemed the most accurate and suitable available DEM for use in D-InSAR processing.

4.3.2 TSX Spotlight Interferograms

Results from the coherence analysis (Section 4.2.2) help inform decisions on how to generate the best quality interferograms; namely using the highest resolution SAR data pairs with short time intervals (< 33 days) acquired during the winter period between November and February. However, given that useful landslide monitoring strategies must be capable of detecting, mapping, characterising and obtaining regular long-term measurements throughout the year, the remainder of Chapter 4 demonstrates the capabilities and limitations of TSX Spotlight, Stripmap and ENVISAT interferograms.

Continuing to explore the significance of seasonality, temporal separation and perpendicular baseline between SAR data pairs, Figure 4-9 to Figure 4-14 present a sensitivity analysis for TSX Spotlight data varying one parameter at a time, as shown in Table 4-2. The strategic variation of parameters should help visualise and compare the best possible interferograms (in winter, separated by 11-days, with a short perpendicular baseline) with less optimal interferograms. If the interferogram quality is not satisfactory for all parts of the year, D-InSAR time-series analysis becomes a less favoured and potentially unviable technique.

Table 4-2: Parameter selection to assess the impact of seasonality, perpendicular baseline and time interval on interferogram quality.

	Season	**Time Interval**	B_{PERP}
Figure 4-9	Winter	11-days	< 30 m
Figure 4-10	Winter	11-days	> 30 m
Figure 4-11	Summer	11-days	< 30 m
Figure 4-12	Summer	11-days	> 30 m
Figure 4-13	Winter	Various	< 30 m
Figure 4-14	Summer	Various	> 30 m

15th – 26th Dec 2009:

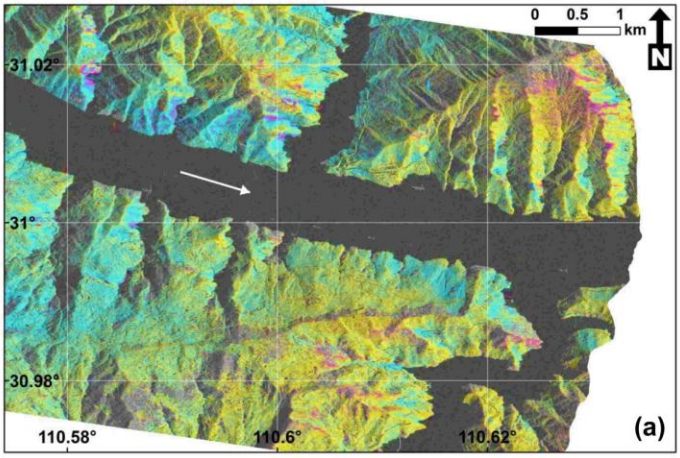

4th – 15th Feb 2012:

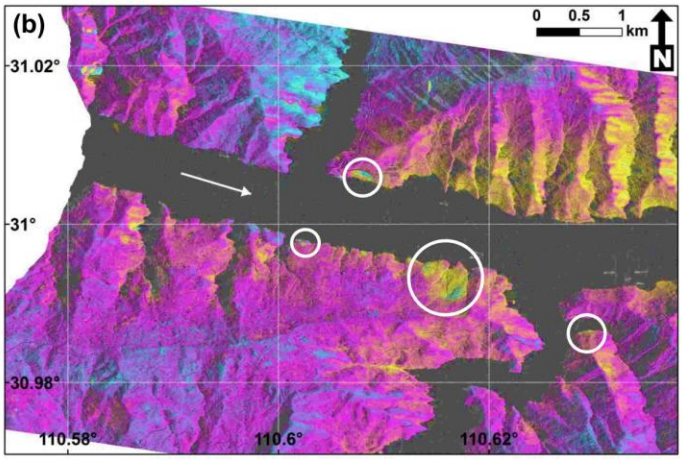

26th Feb – 8th Mar 2012:

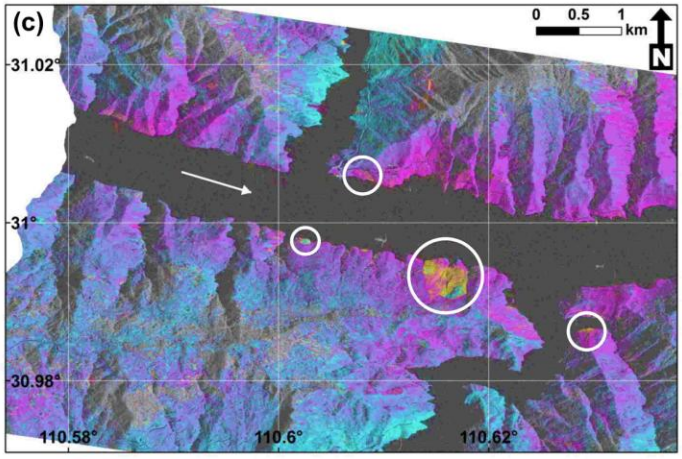

12th – 23rd Feb 2013:

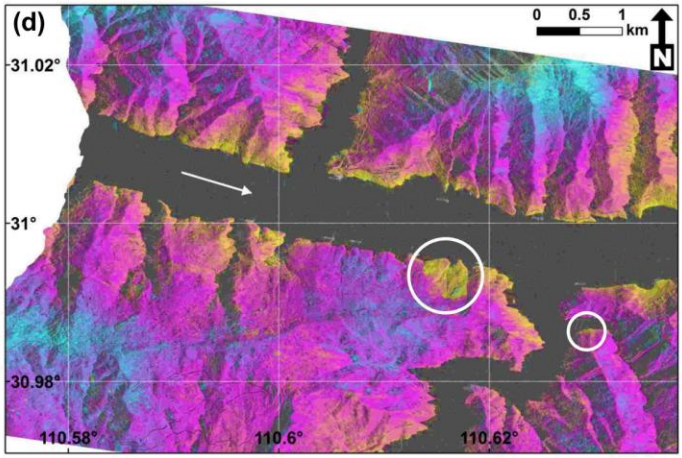

Figure 4-9: TSX Spotlight, wrapped winter 11-day interferograms with $B_\perp < 30$ m. White circles show displacement in independent interferograms. (a) 15th – 26th Dec 2009 [$B_\perp$=29.8 m]; (b) 4th – 15th Feb 2012 [24.3 m]; (c) 26th Feb – 8th Mar 2012 [12.5 m]; (d) 12th – 23rd Feb 2013 [14.2 m].

4th – 15th Dec 2009:

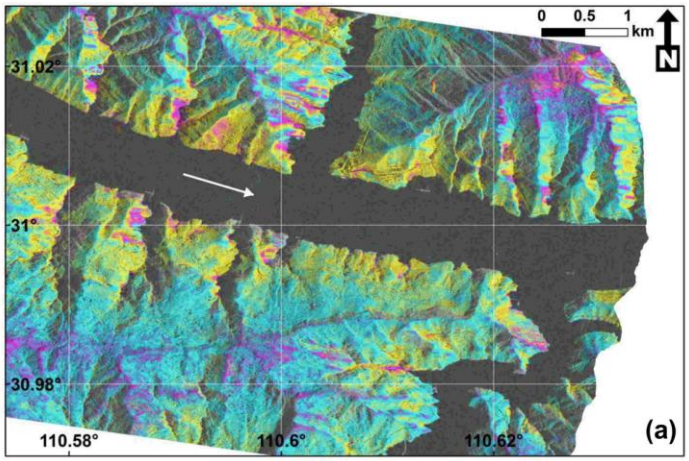

26th Dec 2009 – 6th Jan 2010:

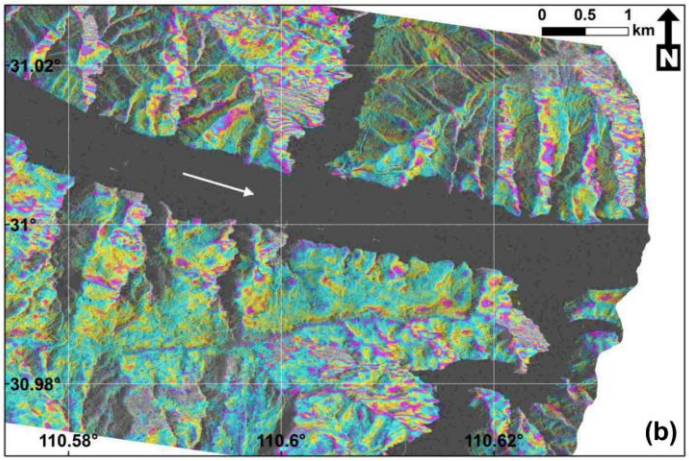

15th – 26th Feb 2012:

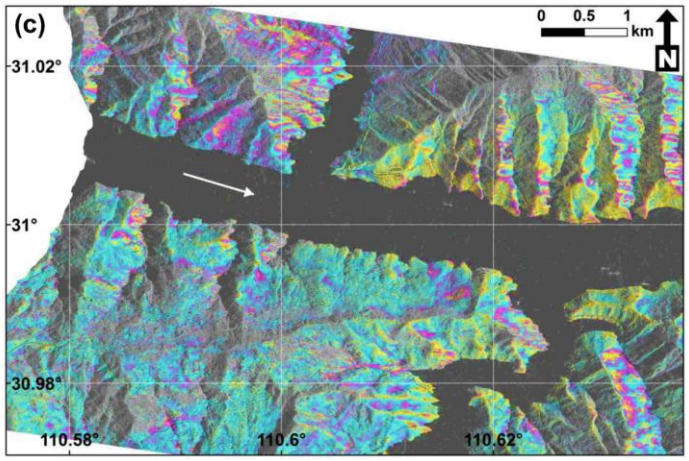

1st – 12th Feb 2013:

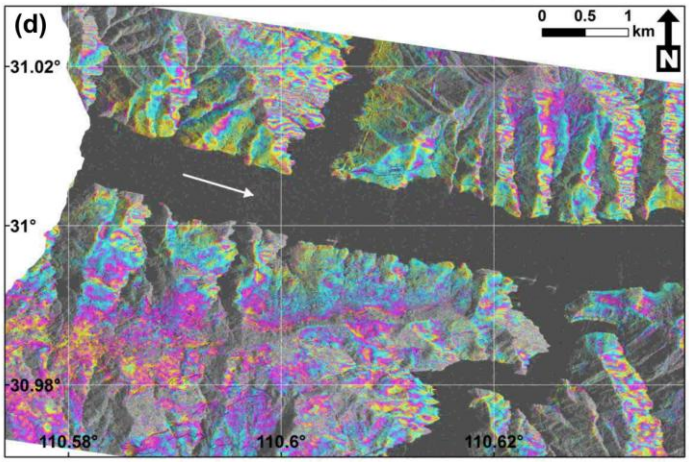

Figure 4-10: TSX Spotlight, wrapped winter 11-day interferograms with $B_\perp > 30$ m. (a) 4th – 15th Dec 2009 [$B_\perp = 51.0$ m]; (b) 26th Dec 2009 – 6th Jan 2010 [170.1 m]; (c) 15th – 26th Feb 2012 [92.5 m]; (d) 1st – 12th Feb 2013 [143.5 m].

26th Mar – 6th Apr 2009:

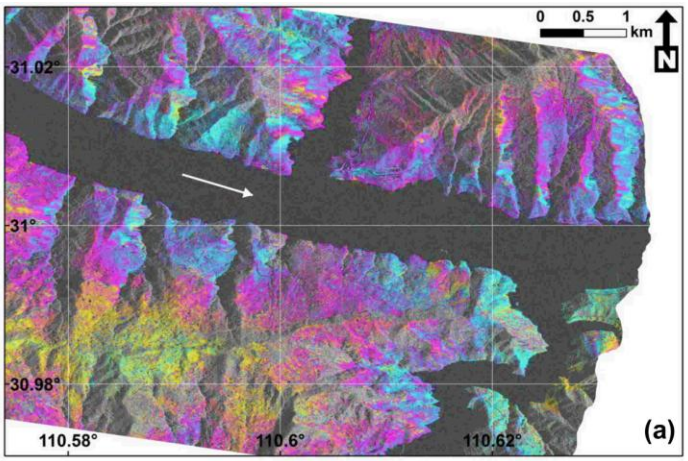

28th Apr – 9th May 2009:

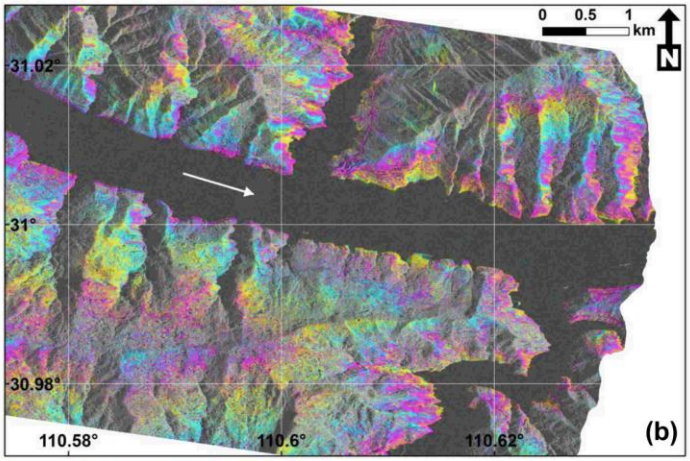

18th – 29th Sep 2009:

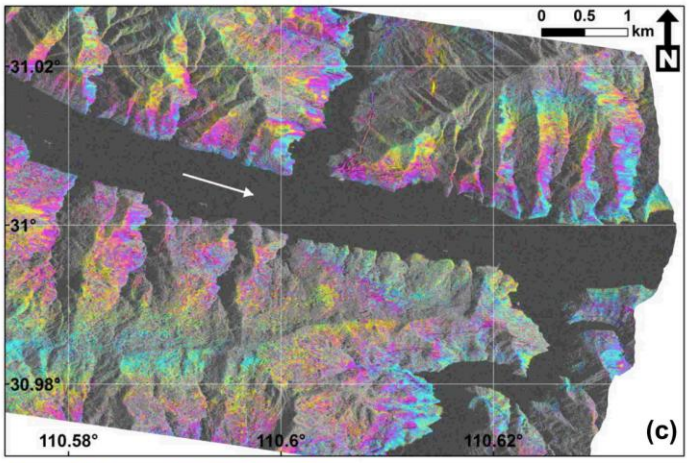

24th Mar – 4th Apr 2010:

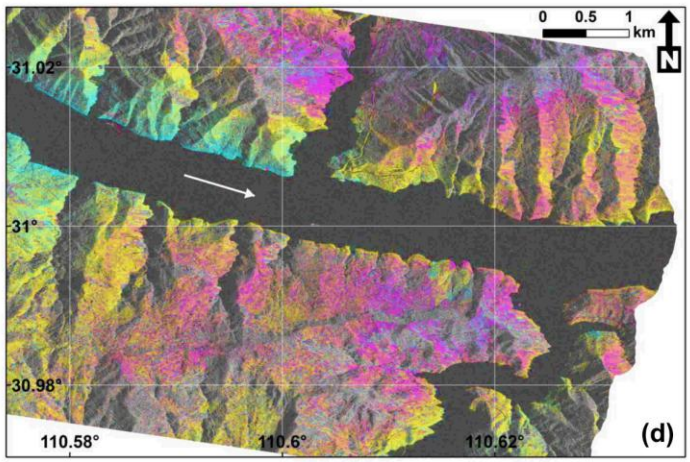

Figure 4-11: TSX Spotlight, wrapped 11-day interferograms outside the winter months with $B_\perp <$ 30 m. (a) 26th Mar – 6th Apr 2009 [$B_\perp$ = 26.8 m]; (b) 28th Apr – 9th May 2009 [27.3 m]; (c) 18th – 29th Sep 2009 [23.0 m]; (d) 24th Mar – 4th Apr 2010 [10.5 m].

15th – 26th Mar 2009:

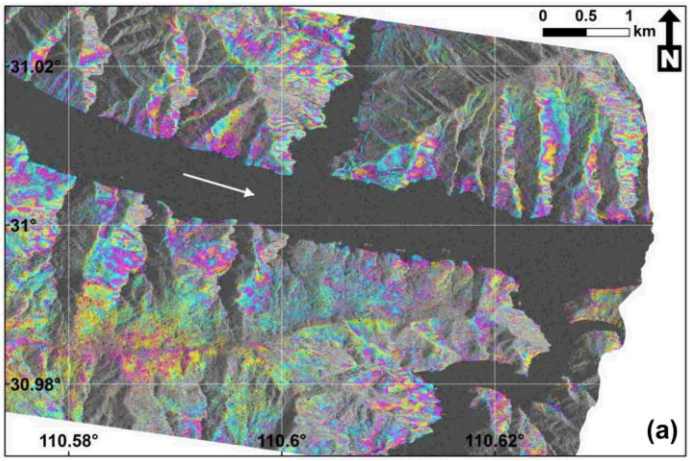

17th – 28th Apr 2009:

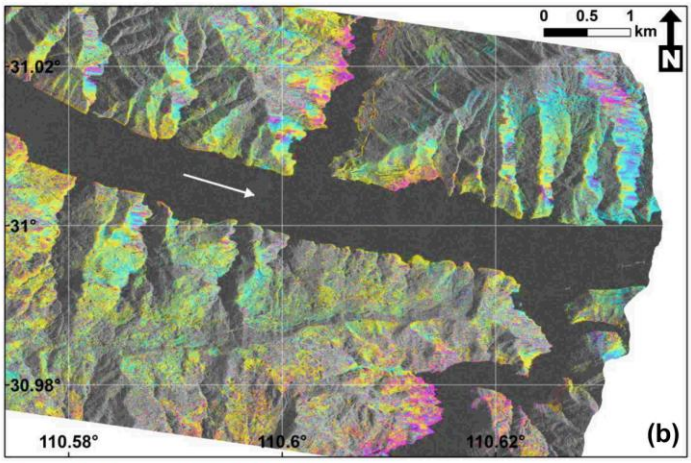

27th Aug – 7th Sep 2009:

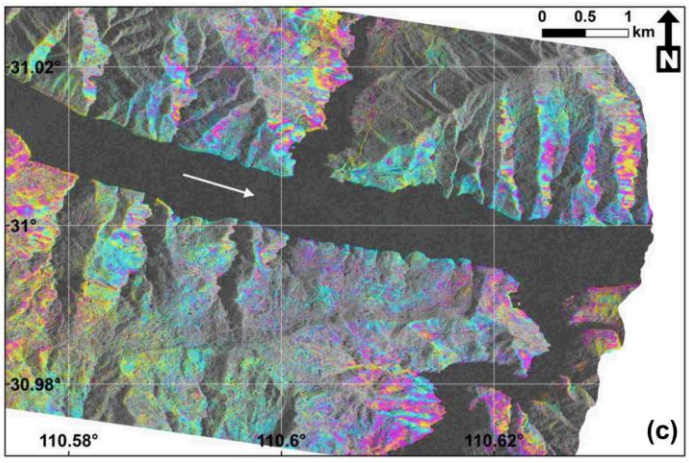

13th – 24th Mar 2010:

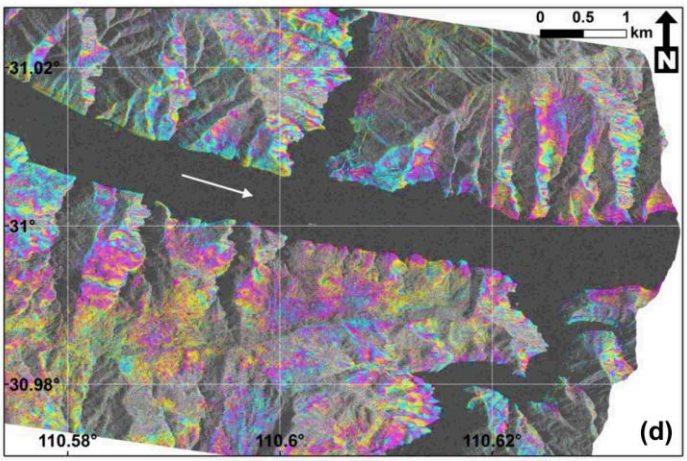

Figure 4-12: TSX Spotlight, wrapped 11-day interferograms outside the winter months with $B_{\perp} >$ 30 m. (a) 15th – 26th Mar 2009 [$B_{\perp}$= 152.9 m]; (b) 17th – 28th Apr 2009 [42.1 m]; (c) 27th Aug – 7th Sep 2009 [77.9 m]; (d) 13th – 24th Mar 2010 [119.2 m].

4th – 26th Dec 2009:

17th Jan – 19th Feb 2010:

13th Jan – 26th Feb 2012:

2nd Jan – 26th Feb 2012:

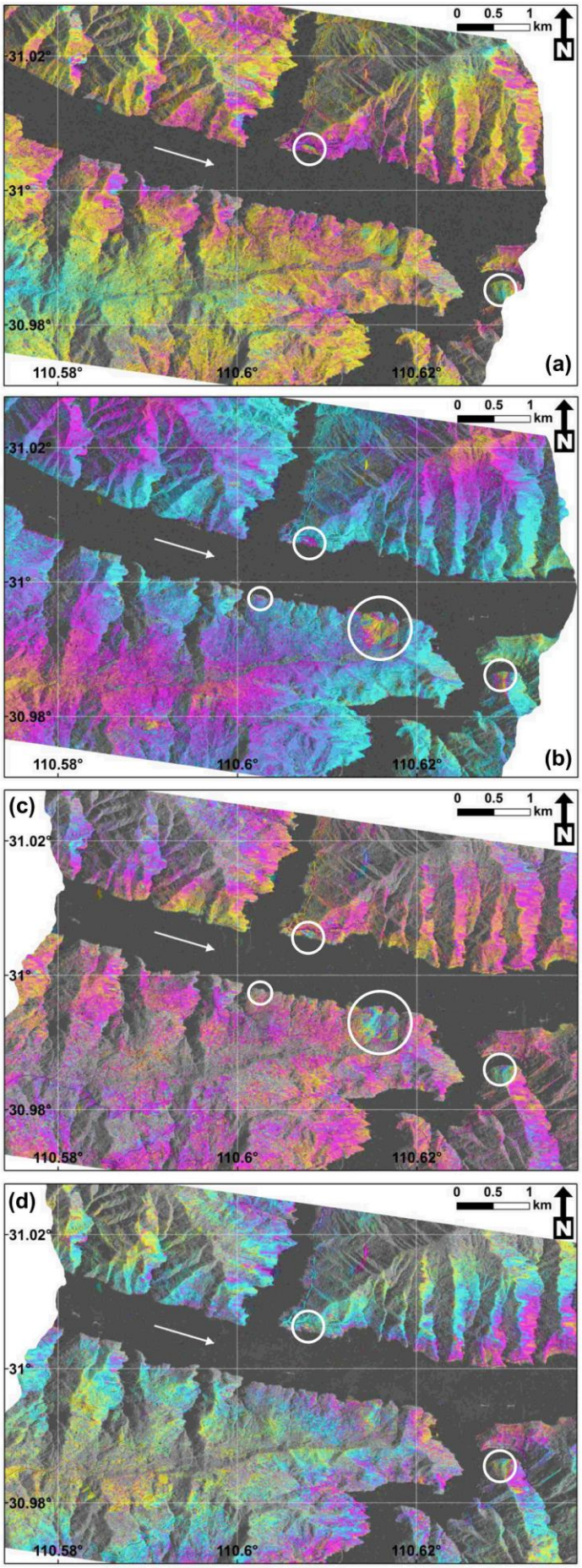

Figure 4-13: TSX Spotlight, wrapped winter interferograms of different time intervals with $B_{\perp}$ < 30 m. (a) 4th – 26th Dec 2009 [$B_{\perp}$=23.9 m, 22 days]; (b) 17th Jan – 19th Feb 2010 [22.7 m, 33 days]; (c) 13th Jan – 26th Feb 2012 [17.1 m, 44 days]; (d) 2nd Jan – 26th Feb 2012 [21.6 m, 55 days].

25th Jul – 16th Aug 2009:

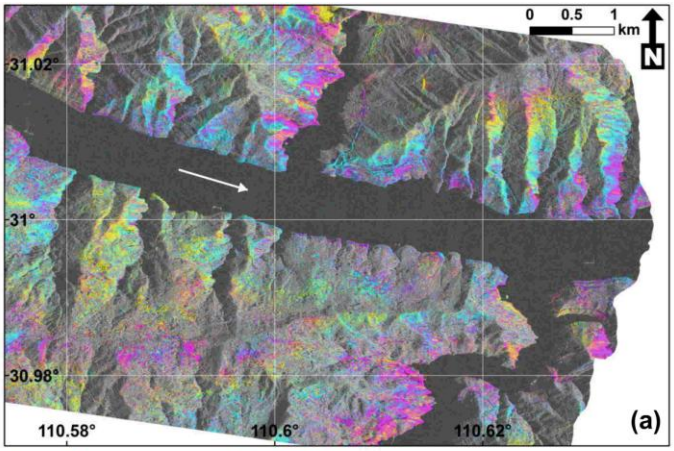

22nd Jun – 25th Jul 2009:

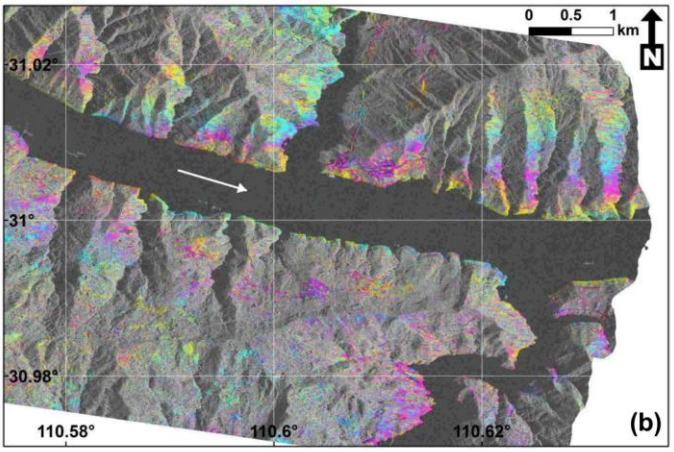

14th Jul – 27th Aug 2009:

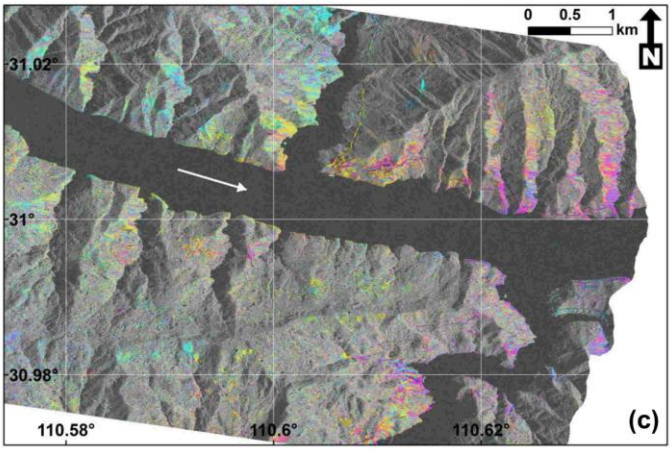

Figure 4-14: TSX Spotlight, wrapped interferograms of different time intervals outside the winter months with $B_{\perp} < 30$ m. (a) 25th Jul – 16th Aug 2009 [$B_{\perp} = 22.7$ m, 22 days]; (b) 22nd Jun – 25th Jul 2009 [29.2 m, 33 days]; (c) 14th Jul – 27th Aug 2009 [10.6 m, 44 days].

It is very clear that 11-day, winter interferograms with perpendicular baselines < 30 m generate very high quality measurements (Figure 4-9) due to the high interferometric coherence. Given the small baselines, sharp localised colour changes allow areas of surface displacement to be easily identified and mapped. The largest circled feature corresponds to the Shuping landslide. Furthest east, movement of the Dujiawu landslide can be observed which was confirmed in the field (Figure A-2). There are other smaller features of surface displacement mapped in the area (i.e. the two furthest west circles) which illustrates a significant advantage of this highest resolution SAR data, and since these interferograms

are independent (i.e. they do not share any SAR images), repeated identification of movement in different interferograms boosts confidence in these observations.

To assess the effects of increasing perpendicular baselines, four more interferograms were generated using 11-day SAR image pairs also acquired in the winter months (Figure 4-10). The level of coherence has slightly decreased, albeit not drastically and some displacement features can still be observed in the same locations as Figure 4-9. However, the biggest issue is the phase noise concentrated on east-facing slopes. In these areas of both active and passive layover (and to a far lesser extent radar shadow), it becomes clear that both SAR amplitude and phase data are of very limited use (Colesanti and Wasowski, 2006) making the application of D-InSAR very unreliable for these slopes. This terrain distortion at such small scales results from DEM errors, known to increase linearly with the perpendicular baseline (Ducret *et al.*, 2014).

Figure 4-11 displays 11-day interferograms with perpendicular baselines < 30 m outside the winter months of November – February. These interferograms are acceptable, although there is a definite increase in noise compared to the winter interferograms in Figure 4-9. Consistent displacement signals are also observed in Figure 4-11a,d. For 11-day image pairs outside the winter months with baselines > 30 m (Figure 4-12), a further increase in noise is observed with similar layover and shadow problems as seen in Figure 4-10. Large parts of these interferograms are dominated by incoherence, particularly in August/September when heavy monsoonal rains are common and when the vegetation coverage is most dense. These interferograms could be used as input to some form of D-InSAR time-series analysis, however it is suggested that any final mean velocity map would have a very sparse network of Persistent Scatterer (PS) points or coherent pixels.

Finally, the impact of the time interval between image acquisitions is assessed. Figure 4-13 shows interferograms with increasing time intervals, all acquired in the winter months with a perpendicular baseline < 30 m. Even with a 55-day separation, significant coherence remains within these longer interferograms with clear displacement signals at the previously identified locations. It is also interesting to note how displacement signals related to the Shuping landslide are lost between Figure 4-13c and d. Given the 55-day interferogram covers the full time period of the 44-day interferogram, it is assumed the displacement magnitude of the Shuping landslide over 55-days exceeds the spatial displacement gradient and therefore causes this loss of coherence. Even when coherence is generally maintained over the whole image, shorter time intervals are therefore optimal to avoid loss of coherence due to large movements.

Carrying out the same analysis for varying time intervals outside the winter months (Figure 4-14), a significant loss of coherence becomes increasingly apparent beyond 22-day image pairs. Therefore, if one or two SAR images are skipped in the acquisition schedule outside the winter months (such as with this TSX Spotlight data set), it becomes very difficult to obtain reliable measurements over this gap. Any D-InSAR time-series network would have to rely upon long time interval interferograms (of 33 days or more) which are likely to be dominated by incoherence. It might be advisable to process data separately for the two epochs either side of any data gap, however to increase the accuracy of the estimated look angle error (and in turn the estimated deformation signal), it is desirable to use as many images as possible during the time-series analysis (Hooper *et al.*, 2007). Also, splitting any time-series into two different epochs does not enable measurements to be obtained over the data gap.

4.3.3 TSX Stripmap Interferograms

A brief assessment was also undertaken for the TSX Stripmap data. A full sensitivity analysis of seasonality, time interval and perpendicular baseline could not be undertaken due to the far shorter acquisition length of the SAR images (and with only five images collected in the winter months). However, the full capability of these data can be demonstrated using only 11-day acquisitions with baselines < 30 m (Figure 4-15).

Despite the larger pixel spacing of TSX Stripmap data compared to the Spotlight data, very similar patterns in coherence can be observed which matches the initial coherence analysis (Figure 4-5). An 11-day image pair with a perpendicular baseline of only 26 m acquired at the end of the summer period shows almost complete decorrelation (Figure 4-15a) and the same level of coherence (or worse) is observed for other 11-day pairs around this time. In contrast, 11-day pairs with similarly small baselines acquired in winter show markedly greater coherence. In these cases no displacement signals are obvious, but this is consistent with the TSX Spotlight data covering the same time period of late Nov – early Dec 2009 (Figure 4-10a). Again the most significant problem caused by the lower resolution and incidence angle of the TSX Stripmap data is the dominant layover effects found on all east-facing slopes.

Given the 9-month period of TSX Stripmap data collection, low coherence outside the winter months and large layover effects, time-series analysis of these data is not deemed feasible and would likely result in a sparse network of PS points or coherent pixels.

21st Aug - 1st Sep 2009:

17th – 28th Nov 2009:

28th Nov – 9th Dec 2009:

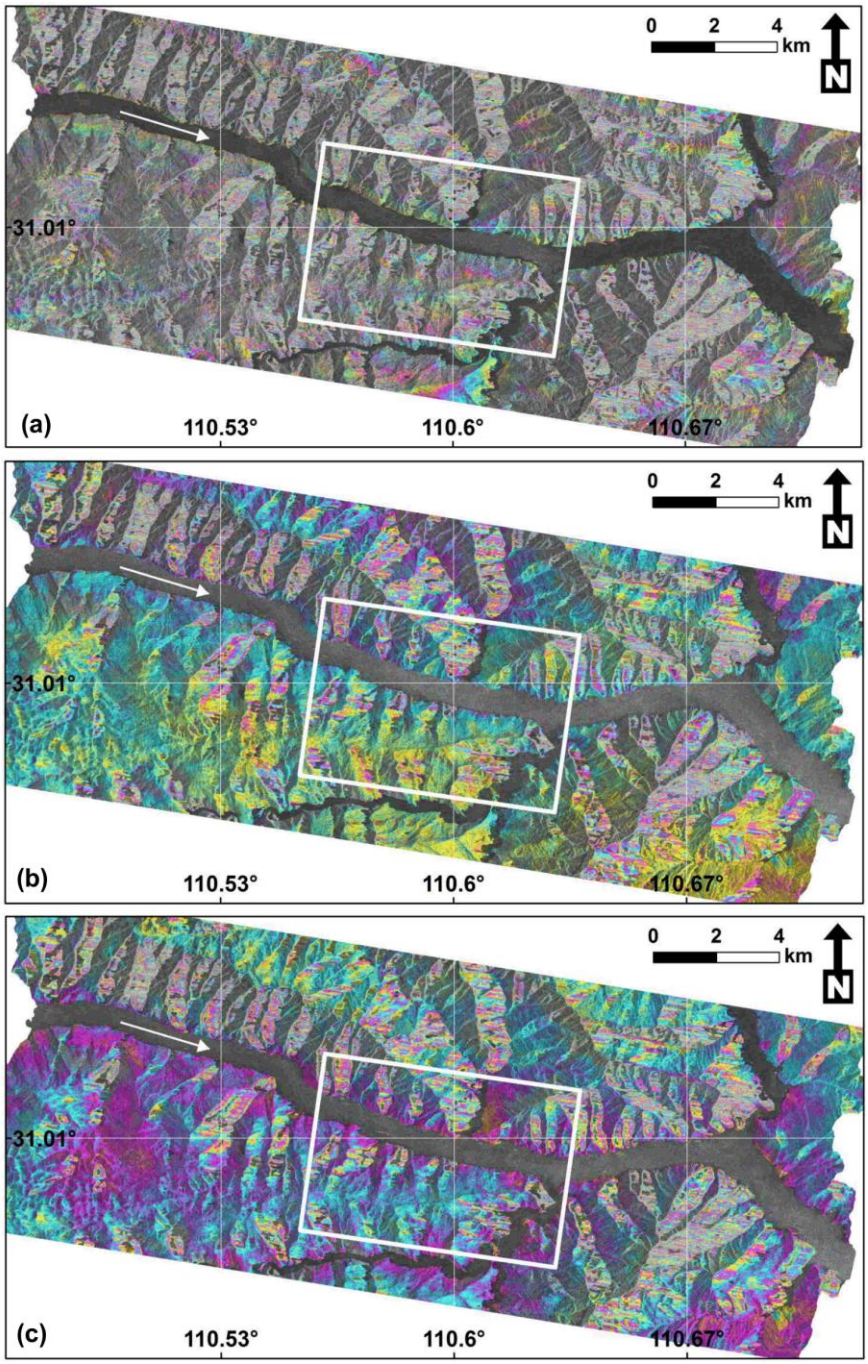

Figure 4-15: TSX Stripmap, wrapped 11-day interferograms with $B_\perp$ < 30 m showing the difference between summer/winter coherence. The white box shows the TSX Spotlight coverage. (a) 21st Aug – 1st Sep 2009 [$B_\perp$= 15.6 m]; (b) 17th – 28th Nov 2009 [21.0 m]; (c) 28th Nov – 9th Dec 2009 [26.0 m].

4.3.4 ENVISAT Stripmap Interferograms

The third available data set which covers the same region and time period as the TSX data is ENVISAT Stripmap-mode SAR data. Given its less frequent repeat cycle of 35-days, the ENVISAT data series contains the fewest SAR images again preventing a full

sensitivity analysis from being undertaken. However, the same issues of summer decorrelation and significant image distortions are evident (Figure 4-16).

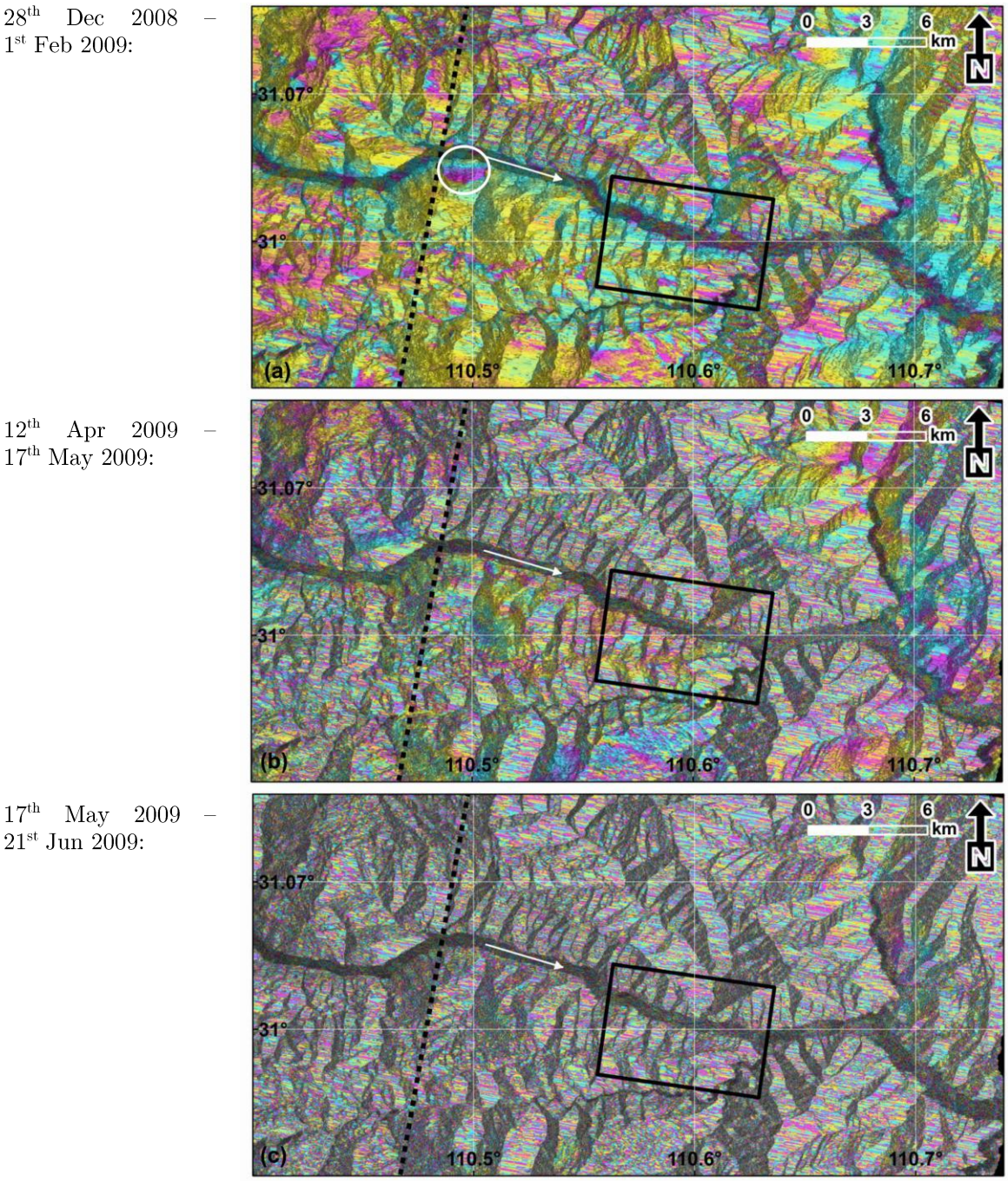

Figure 4-16: ENVISAT Stripmap wrapped 35-day interferograms showing the difference between summer/winter coherence. The solid black box outline shows the TSX Spotlight coverage, and the dashed black line shows the western edge of TSX Stripmap coverage. (a) 28th Dec 2008 - 1st Feb 2009 [$B_\perp$ = 224.7 m]; (b) 12th Apr - 17th May 2009 [149.6 m]; (c) 17th May - 21st June 2009 [333.8 m]

Despite a baseline of 225 m, the 35-day image pair in the winter months (Figure 4-16a) shows the best coherence along with a significant displacement signal (~2 cm) on the western border of the TSX Stripmap image corresponding to the Fanjiaping landslide

(circled in white). This cannot be assessed with higher resolution imagery as no TSX data were collected before February 2009. The other ENIVSAT interferograms were generated from SAR images outside the winter period and coherence is completely lost by May – June (Figure 4-16c). Given the lower resolution of this descending ENVISAT SAR imagery, layover continues to dominate east facing slopes and even if signals were observed, accurate landslide boundary delineation would be far more difficult compared to higher resolution data.

Overall, it is concluded that resolution and the SAR orbit repeat cycle are more influential factors on interferogram quality than the SAR sensor wavelength, with the highest resolution TSX Spotlight data providing the best results. Compared to the ENVISAT data, the shorter revisit frequency of 11-days is definitely beneficial in reducing temporal decorrelation. But the improvement shown by the TSX Spotlight data relative to the Stripmap data also demonstrates the known advantage of high resolution Spotlight data (Iglesias *et al.*, 2012), most likely caused by small point-like targets being focused to individual pixels with a far smaller percentage of incoherent surrounding clutter (Eineder *et al.*, 2009). Subsequently the stable phase of these targets will dominate the phase of clutter in the resolution cell and lead to higher overall coherence.

4.3.5 Geometrical Distortions

Steep-sided hillslopes and imaging geometry of the various SAR sensors have been interpreted as a significant issue in the interferograms displayed in Sections 4.3.2 - 4.3.4. To confirm this explanation, the 'R-index' (proposed by Notti *et al.*, 2010) was calculated for each SAR image mode coverage and used to assess the best slopes for applying D-InSAR techniques.

The R-index equation (Equation 4-1):

$$R = -\sin(\tan^{-1}(\tan Sl \cdot \sin A) - \theta)$$

Equation 4-1: The 'R-index' equation (from Notti *et al.*, 2010). Sl = Slope derived from a DEM. A = DEM-derived aspect corrected with the difference between north and the satellite heading, e.g. A = aspect – 10° for TSX descending mode images. θ = Local incidence angle.

is the ratio between the slant range and the ground range considering the acquisition geometry of the radar sensor and the geometry of the ground surface (employing the slope and aspect modelled from a DEM). The maximum value of R occurs when the slope is parallel to the sensor LOS and therefore the best geometry to detect PS in mountainous

areas (Notti *et al.*, 2010). Negative values are the worst, highlighting areas of layover and shadow effects, whilst those just above 0 are also far from optimal, indicating cases of foreshortening. It has been suggested that values above 0.33 should be used to select slopes with a favourable geometry for D-InSAR analyses in relation to the satellite acquisition geometry (Bianchini *et al.*, 2013).

The results in Figure 4-17 are very consistent between all (descending) imaging modes and illustrate the problem of layover throughout this mountainous region. Matching the interferograms in earlier sections and the conclusions of Notti *et al.* (2010), descending geometry is best for west-facing slopes and problematic for east-facing slopes.

4.4 Spatial Displacement Gradient Limitations

Introduced in Chapter 2, one major limitation of D-InSAR techniques is their inability to measure high spatial gradients of rapid deformation. To observe interferometric fringes without ambiguity, the theoretical maximum displacement between two neighbouring pixels in a wrapped interferogram (Ω) must not exceed one fringe per pixel (Massonnet and Feigl, 1998; Metternicht *et al.*, 2005), or the dimensionless ratio of the pixel size to the sensor wavelength (Equation 4-2):

$$\Omega = \frac{\lambda}{2\eta}$$

Equation 4-2: Ratio of the pixel size to half the sensor wavelength. Ω is the maximum spatial displacement gradient (m/m); λ is the SAR sensor wavelength; η is the width of the smallest pixel dimension.

Hanssen (2001) explains the maximum proportion of fringes per pixel is reduced to 0.822 for the ERS sensor given the increased noise due to non-overlapping parts of the spectrum and from the viewpoint of successful unwrapping, the maximum displacement gradient should be less than 0.5 fringes per pixel (Spagnolini, 1995; Michel *et al.*, 1999; Jiang *et al.*, 2011b) (Equation 4-3):

$$\Omega = \frac{\lambda}{4\eta}$$

Equation 4-3: Dimensionless ratio of the pixel size to a quarter of the sensor wavelength. Ω is the maximum spatial displacement gradient (m/m); λ is the SAR sensor wavelength; η is the width of the smallest pixel dimension.

These theoretical limits do not consider noise in the radar observations caused by temporal decorrelation effects (Zebker *et al.*, 1997) and hence the maximum realistic measureable displacement gradient should be reduced even further (Baran *et al.*, 2005; Jiang *et al.*, 2011b).

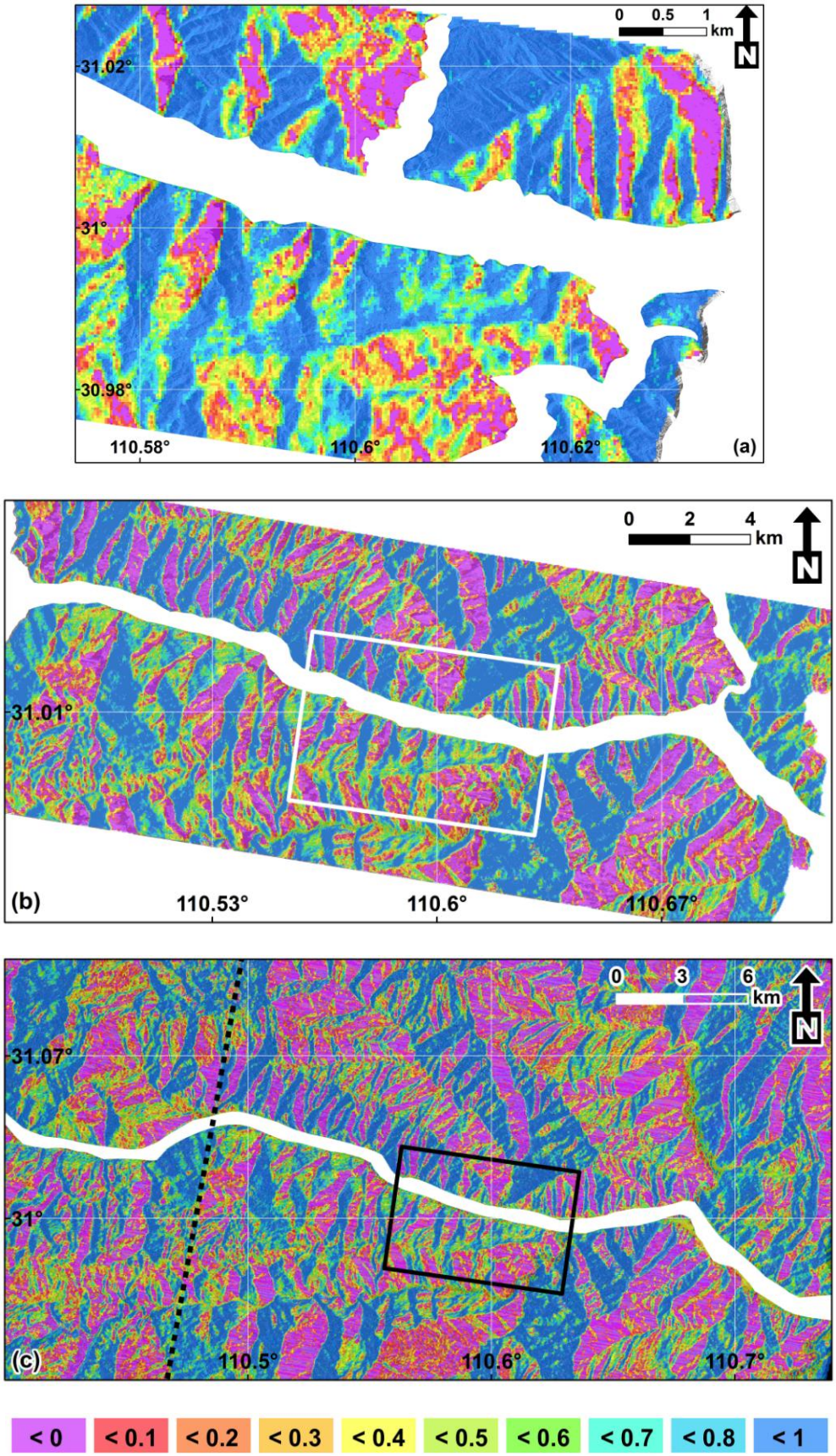

Figure 4-17: R-index calculated for the three different satellite imaging modes, showing the degree of image distortion. (a) TSX Spotlight; (b) TSX Stripmap; (c) ENVISAT Stripmap. Smallest box in (b) & (c) shows the TSX Spotlight coverage, whilst the black dotted line in (c) shows the TSX Stripmap coverage.

For the three different available image modes, the maximum spatial displacement gradients were calculated from the metadata shown in Table 4-3.

Table 4-3: Metadata for the available stacks of SAR images used in this study. The second half shows the data used to find the smallest pixel dimension (the highlighted figures) which was subsequently used to calculate the displacement gradients in Table 4-4. The parameters come from the first image for each image mode, although the values remain very similar for all subsequent image acquisitions.

	TSX Spotlight	TSX Stripmap	ENVISAT Stripmap
Pixel ratio (range : azimuth):	1 : 1	1 : 1	1 : 5
Wavelength (m):	0.031	0.031	0.056
Range pixel spacing (m):	0.46	0.91	7.80
Incidence angle (°):	43.7	26.26	22.81
Ground range pixel size (m):	0.66	2.06	20.13
Azimuth pixel size (m):	0.86	1.97	21.10 (after 1:5 ratio)

The ground range pixel size (r_g) was calculated according to Equation 4-4:

$$r_g = \frac{r_s}{\sin\theta}$$

Equation 4-4: Calculating the ground range resolution (r_g); r_s is the pixel spacing in slant range; θ is the incidence angle.

and compared with the azimuth size to select the smallest pixel dimension for the displacement gradient calculations.

Table 4-4 shows the displacement gradients for an interferogram produced at the original SLC resolution and after considering a small multi-look factor of two (as applied to the interferograms in Section 4.3). From these results, even for the highest resolution TSX Spotlight imagery, it would not be possible to measure a difference in displacement of more than 0.12 m (or 0.06 m after multi-looking) over a distance of 10 m between image acquisitions. Considering the SAR sensor wavelength with respect to the variation in pixel sizes between image modes, the pixel spacing controls the maximum measurable displacement and despite the slightly longer wavelength of ENVISAT data, the larger pixel size is a significant disadvantage for measuring spatially variable movements over short distances.

Recognising the limits on the spatial displacement gradient are theoretical maxima assuming the radar observations are unaffected by noise from temporal decorrelation, the low coherence throughout the time period under investigation suggests the maximum displacement gradient is below the theoretical values presented in Table 4-4.

Table 4-4: Displacement gradients for the three image modes used in this study. Displacement gradients are shown for the original resolution interferograms and for interferograms with a small multi-look factor of 2. These values should be multiplied by the distance between two points on the ground to calculate the maximum detectable difference in the rates of displacement.

Sensor / Image Mode	Maximum Displacement Gradient (Ω)	Ω after multi-looking (using a small factor of 2)
TSX Spotlight	0.01177 m/m	0.00589 m/m
TSX Stripmap	0.00394 m/m	0.00197 m/m
ENVISAT Stripmap	0.00070 m/m	0.00035 m/m

4.5 Decorrelation from Landslide Movements

Having processed every 11-day image pair for all TSX data, important observations were made regarding the Shuping landslide. Figure 4-18 shows three (wrapped) interferograms for adjacent 11-day intervals between the 9th May and 11th June 2009. The landslide boundary is mapped by the black line following the sharp colour changes, and this remains consistent over the 33-day period (i.e. 3 x 11-day interferograms). The boundary of active slope movement for Block 2 of the landslide, obtained from D-InSAR results, is also less extensive than the original assessment made by Wang *et al.* (2008a) – shown by the black dashed line. This could indicate a change in landslide behaviour over time, or the advantage of using high resolution SAR data capable of generating a high density of ground measurements compared to geomorphological interpretations.

An increase in the fringe rate can also be observed from Figure 4-18 a(ii) – c(ii), left to right, which relates to an increase in landslide movement over each time interval. The landslide moves approximately 1.6 cm, >5 cm and >6 cm for the three consecutive time intervals, respectively, However, Figure 4-18 b(ii) and c(ii) show a loss of coherence particularly towards the head of the landslide that is most likely due to displacements exceeding the maximum measurable limit of 0.00589 m/m (see Table 4-4) across the sharp boundary between stable ground and the active landslide. The sole use of these TSX Spotlight images for any D-InSAR time-series analysis would erroneously underestimate the true magnitude of the landslide displacement and further investigation is required to verify if this coherence is lost due to the fast landslide movement or other factors.

Verification from the TSX Stripmap data is not possible due to increasing coherence loss across the whole scene for each subsequent 11-day period (Figure 4-19). However, given the reduced maximum spatial displacement limits for the TSX and ENVISAT Stripmap

data (Table 4-4), these would be unable to recover the larger landslide movements given that coherence is lost even for the highest resolution TSX Spotlight data.

If the theoretical maximum spatial displacement gradient is broken by the magnitude of landslide movement, this invalidates long-term regional D-InSAR analysis. It would be impossible to accurately unwrap any interferogram which spanned this movement episode without the use of in-situ data or independent data such as range offsets (Yun *et al.*, 2007). This issue can perhaps explain the variety of D-InSAR measurements for the Shuping landslide outlined in Chapter 3. Certainly this time-period should not be analysed using D-InSAR time-series methods since an even sparser network of measurements (relative to the original interferograms) generated from any form of persistent scatterer interferometry would be less able to resolve such spatially variable measurements.

Compared to C-band, the use of L-band SAR data have been preferred for mapping rapid displacements particularly in vegetated regions (Strozzi *et al.*, 2005) since the decorrelation is lower and in some cases can avoid problems related to the intrinsic ambiguity of phase measurements (Strozzi *et al.*, 2004). Despite no L-band data being available for investigation, assuming a wavelength of 0.235 m and a 10 m ground pixel size for ALOS data in fine resolution mode (single polarisation), the spatial displacement gradient would be 0.0059 without any multi-looking. Combined with a far longer revisit frequency of 46-days, it is unlikely these data would be capable of resolving the ambiguity of fast Shuping landslide movements towards the end of May 2009, providing no improvement upon the TSX Spotlight results over the same time period.

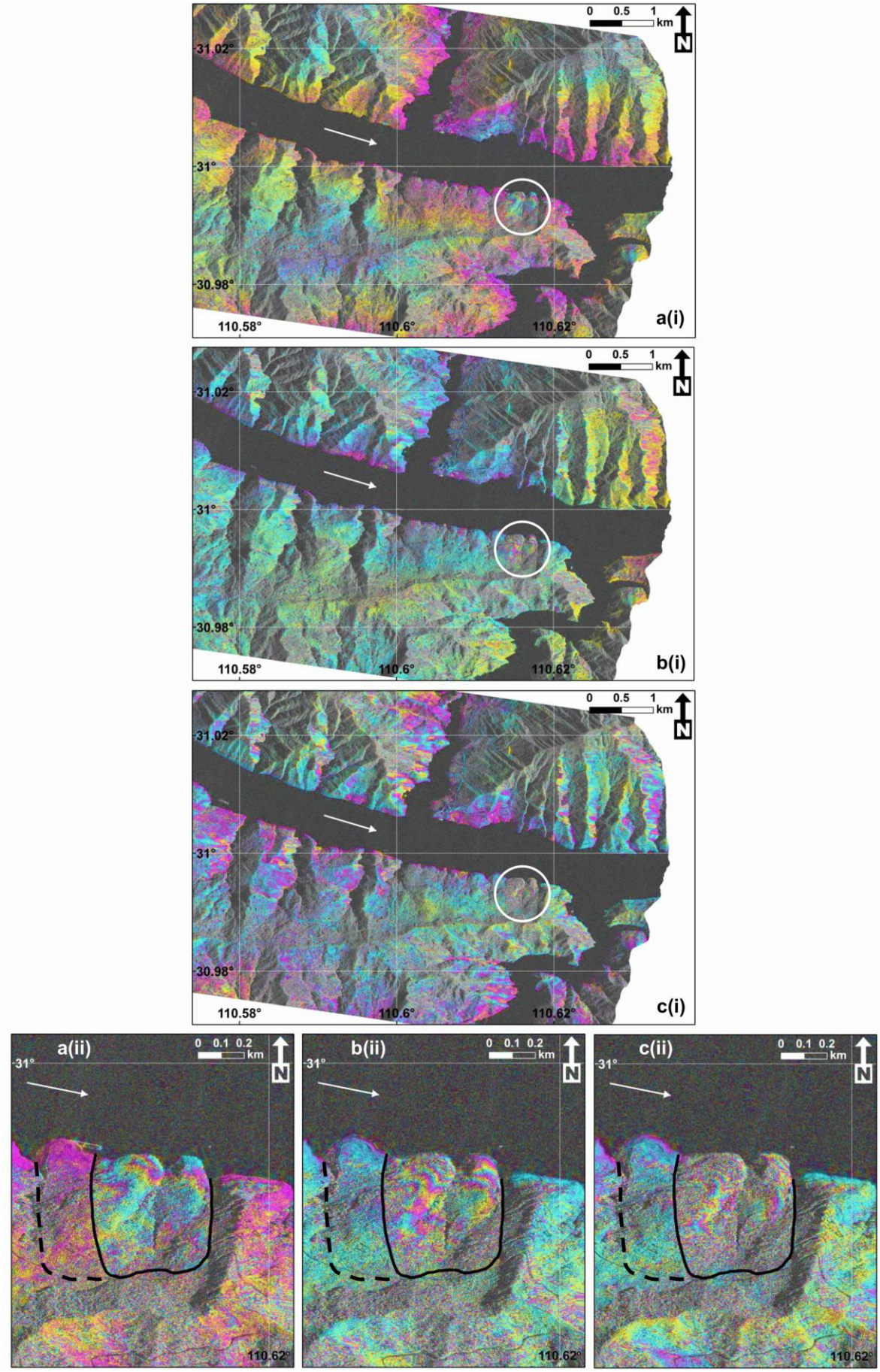

Figure 4-18: TSX Spotlight wrapped 11-day consecutive interferograms showing the Shuping landslide exceeding the spatial displacement gradient. (i) Whole scene; (ii) Shuping landslide crop. (a) 9th – 20th May 2009 [$B_\perp$ = 7.3 m]; (b) 20th – 31st May 2009 [$B_\perp$ = 26.2 m]; (c) 31st May – 11th June 2009 [$B_\perp$ = 60.4 m]. Dashed line shows the previously mapped boundary (Wang *et al.*, 2008a).

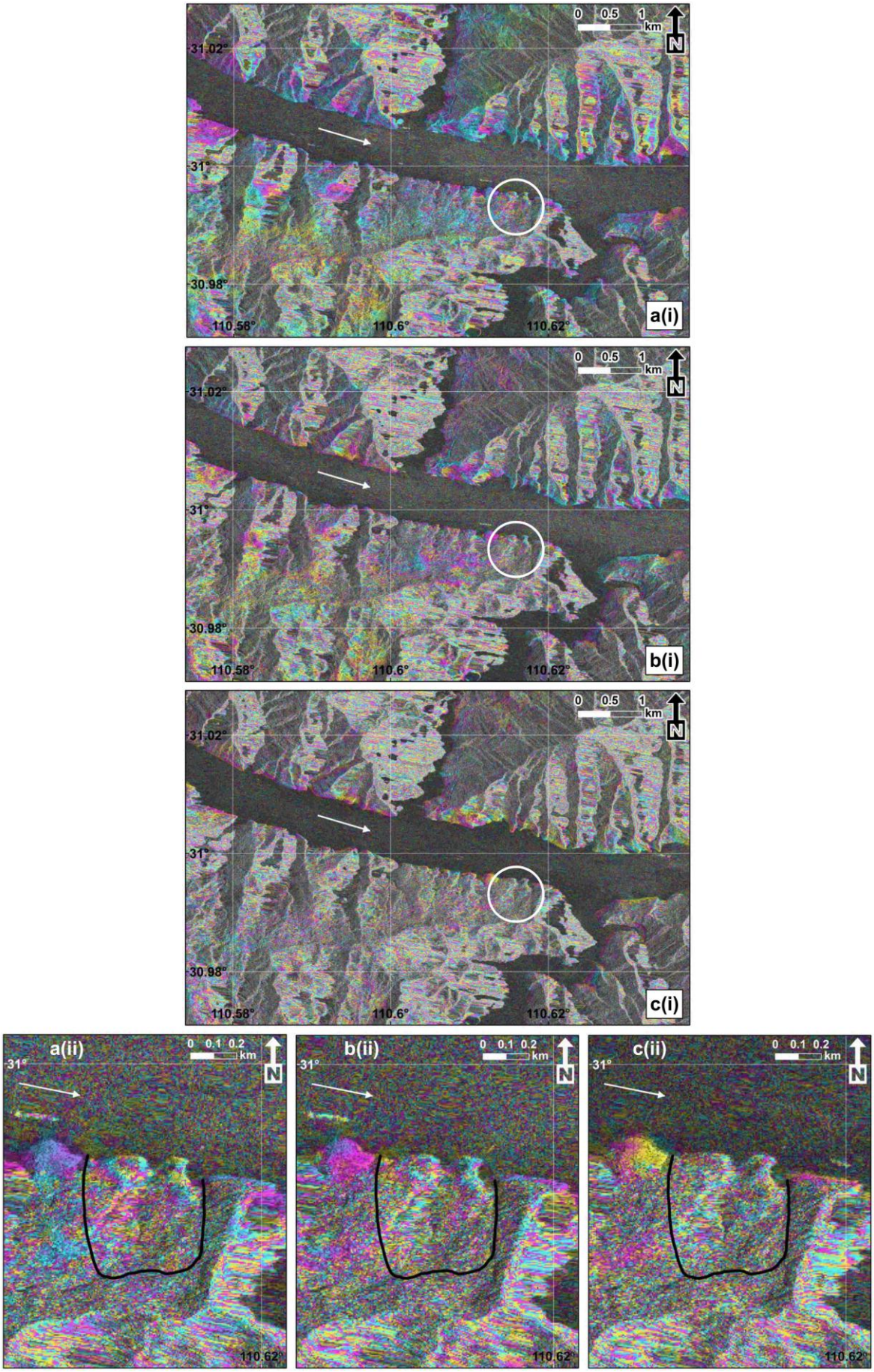

Figure 4-19: TSX Stripmap wrapped 11-day consecutive interferograms showing incoherence over the Shuping landslide over the same period as Figure 4-18. (i) Whole scene; (ii) Shuping landslide crop. (a) 3rd – 14th May 2009 [$B_\perp$ = 29.9 m]; (b) 14th – 25th May 2009 [$B_\perp$ = 63.3 m]; (c) 25th May – 5th June 2009 [$B_\perp$ = 85.3 m].

4.6 Downslope Sliding Velocities

A final consideration assesses the use of scaling factors for re-projecting line-of-sight measurements into other directions. Assuming a purely translational failure mechanism parallel to the slope surface, sliding velocities can be projected into the downslope sliding direction (e.g. Hilley *et al.*, 2004). However, given these SAR sensors have quasi-polar orbits, radar systems are limited in their ability to measure translational displacement in a north-south direction from individual ascending or descending tracks (Cascini *et al.*, 2010; Plank *et al.*, 2012).

A three dimensional displacement vector (d_R) with components $[d_E\ d_N\ d_U]$ representing east, north and up directions, respectively is projected into one Line-of Sight dimension. For a satellite orbit with an azimuth heading (α) and incidence angle (θ), this is calculated by Equation 4-5 with the results for each image mode presented in Table 4-5.

$$d_R = d_U \cos(\theta) - \sin(\theta)\left[d_N \cos(\alpha - {}^{3\pi}/_{2}) + d_E \sin(\alpha - {}^{3\pi}/_{2})\right]$$

Equation 4-5: Decomposition of the 3-dimensional displacement vector d_R (Massonnet and Feigl, 1998; Hanssen, 2001). $\alpha - {}^{3\pi}/_{2}$ corresponds with the angle to the azimuth look direction, which is perpendicular to the satellite for a right-looking geometry.

Table 4-5: Parameters and unit vectors of the satellite look direction and the downslope sliding direction. The unit vectors are specified in relation to a positive up, left-handed coordinate system.

	TSX Spotlight	TSX Stripmap	ENVISAT Stripmap
Satellite heading:	190°	190°	195°
Incidence angle:	44°	26°	23°
Satellite look unit vector $[d_E\ d_N\ d_U]$	d_R = $[-0.68\ \ 0.12\ \ -0.72]$	d_R = $[-0.43\ \ 0.08\ \ -0.90]$	d_R = $[-0.38\ \ 0.10\ \ -0.92]$

Landslide body heading:	25°
Average slope angle:	22°
Unit vector of downslope sliding direction $[u_E\ u_N\ u_U]$:	$u_D = [0.39\ \ 0.84\ \ -0.37]$

The larger incidence angle for TSX Spotlight data shows similar sensitivity to both east and vertical movements, whereas smaller incidence angles for the TSX Stripmap and ENVISAT data are mostly sensitive to vertical changes. However, very little north-south displacement is projected in the satellite Line-of-Sight for all image modes which is a disadvantage for the majority of slopes bordering the Yangtze River in this study area.

The amplification scaling factor (S) is calculated using Equation 4-6

$$S = \frac{1}{(d_R^T u_D)}$$

Equation 4-6: Computing the amplification of the range change rate when projected into the downslope landslide direction (Hilley *et al.*, 2004).

where d_R^T is the transposed three dimensional displacement vector (d_R) and u_D is the downslope sliding direction unit vector. For the TSX Spotlight, TSX Stripmap and ENVISAT Stripmap mode, the scaling factors are 9.8, 4.3 and 3.6, respectively. Given this assumes a completely translational slide mechanism along the unit vector direction specified in Table 4-5, these amplification factors would yield the maximum rate of downslope displacement.

However, using a scaling factor impacts on the precision of measurements (Colesanti and Wasowski, 2006; Cascini *et al.*, 2010). For ENVISAT and ALOS data, an upper scaling factor threshold of ~3.3 was applied to select suitable 'projectable' PS points (Cascini *et al.*, 2013; Herrera *et al.*, 2013), beyond which downslope displacement velocities are deemed unreliable. For the Shuping landslide orientation, all data modes exceed this scaling factor threshold, further demonstrating the difficulty in extracting useful displacement information – beyond the Line-of-Sight dimension – from D-InSAR results.

4.7 Summary

Chapter 4 outlines the available SAR data sets and known landslide sites for the study area within the Three Gorges region, before presenting the results and limitations of D-InSAR analyses. Assessing the interferometric coherence for all SAR image modes shows the highest values for TSX Spotlight data due to its higher spatial resolution and revisit frequency, particularly compared to the ENVISAT sensor. Seasonal variations show the highest coherence values between November – Feburary each year, linked to the lowest amounts of rainfall (i.e. soil and atmospheric moisture) and density of vegetation.

The best interferograms were produced from 11-day TSX Spotlight data with baselines < 30 m which allow the detection, mapping and measurement of various active landslides. Lower coherence or greater image distortions are predominantly observed for other TSX Spotlight image pairs or other image modes. Most significantly, large movements of the Shuping landslide are shown to exceed the spatial displacement gradient, highlighting a general danger of using D-InSAR time-series techniques for landslide applications.

Chapter 5 : SAR Sub-Pixel Offset Time-Series Results

A range offset map from SAR pixel offset methods contains the same information as a differential interferogram (Jónsson *et al.*, 2005; Furuya, 2011), except that it has a different noise character and magnitude (Yun *et al.*, 2007). Range offsets therefore provide complementary results to D-InSAR techniques especially since they are capable of measuring larger, more complex displacement patterns (Fielding *et al.*, 2013; Raucoules *et al.*, 2013) and are less restricted by the assumption of a low spatial displacement gradient. SAR images are also well suited to cross-correlation methods given the ubiquitous presence of speckle which results in sharp correlation peaks, providing speckle patterns are similar in both images (Michel *et al.*, 1999). As such, cross-correlation offsets have been successfully applied to estimate single displacement episodes (e.g. Scambos *et al.*, 1992; Peltzer *et al.*, 1999; Fialko *et al.*, 2001; Strozzi *et al.*, 2002; Luckman *et al.*, 2007; Yun *et al.*, 2007; Giles *et al.*, 2009; Grandin *et al.*, 2009; Li *et al.*, 2011b).

Although less sensitive and accurate than conventional D-InSAR methods (Pathier *et al.*, 2006), sub-pixel offset techniques using SAR amplitude images can overcome the D-InSAR limitation on the spatial displacement gradient and are far more robust (not requiring phase unwrapping; not limited to regions of high interferometric coherence; significantly less affected by atmospheric water vapour due to an independence on the use of phase values; and capable of extracting measurements from longer time interval image pairs). Additionally, pixel offset data provide complimentary information since conventional interferograms are only sensitive to displacements in the sensor's LOS direction (Michel *et al.*, 1999). Using just two images acquired at different times, displacement vectors can be measured in the sensor look direction (range) as well as the satellite flight (along-track, or azimuth) direction (Furuya, 2011). The two-dimensional movements are obtained by measuring the row and column offsets between the two image acquisitions at defined intervals in range/azimuth in order to generate sufficient coverage of offset measurements (Pathier *et al.*, 2006). Using multiple SAR images, Sub-Pixel Offset Time-series (SPOT) approaches are possible, helping identify acceleration and deceleration episodes of displacement at a high spatial resolution (e.g. Raucoules *et al.*, 2013).

To address the second research question (page 10), this chapter investigates the capabilities and limitations of SPOT techniques for long-term monitoring of slopes in the Three Gorges region. The availability of three data modes (TSX Spotlight, TSX Stripmap and ENVISAT Stripmap) allow useful comparisons to be made especially since the variable pixel spacing in range and azimuth strongly influences the precision of measurements (Michel *et al.*, 1999; Bechor and Zebker, 2006). For each data set, the robust selection of SPOT processing parameters is considered, and very high cross-correlation values attributed to installed corner reflectors demonstrate movement of the Shuping landslide exceeds the spatial displacement gradient for valid D-InSAR analysis. Other landslides in the region with corner reflectors are measured, before exploring suitable time-series approaches for stacks of SAR data. Finally the precision of sub-pixel offset measurements from natural terrain (i.e. beyond corner reflector points) is investigated for the densely vegetated terrain of the Three Gorges.

5.1 SAR Sub-Pixel Offset Parameter Selection

SPOT techniques are capable of measuring more spatially variable movements than D-InSAR although the results from sub-pixel offset methods are highly dependent upon the various processing parameters; notably the cross-correlation window size and oversampling factor (Casu *et al.*, 2011). These should be carefully tuned to the pixel spacing of the SAR image mode and the scale of deformation feature(s) under study (Bechor and Zebker, 2006; Yun *et al.*, 2007). Consequently, the size of the moving window should be large enough to maximise the signal-to-noise ratio whilst minimising the spatial velocity gradient. The search area must also be large enough to include the fastest moving distance whilst minimising the computational cost of the process (Debella-Gilo and Kääb, 2011).

Following an approach outlined by Yun *et al.* (2007), the cumulative distribution for a land area of 2 km^2 (adjacent to the Shuping landslide site and believed to be stable from the TSX Spotlight interferograms in Section 4.3.2) was analysed with a combination of different processing parameters, at intervals of two pixels in both range and azimuth (Figure 5-1 - Figure 5-4). Visual inspection from these tests provided a heuristic way of tuning the moving window size and oversampling parameters to suitable values, considering the data characteristics and the phenomenon under study. Contrary to Yun *et al.* (2007), a piecewise linear fit was not used to exclude extreme values in the final offset maps since large landslide movements would be concentrated in one tail of the distribution and therefore at risk of being filtered out.

All the offset results presented in this chapter were produced using the SARscape® software package (SARMAP, 2012) which includes an Amplitude Tracking module capable of processing all the necessary data formats included in this study. Prior to generating the sub-pixel offset measurements, SAR images were aligned using a simple translational shift based on the orbital data and the digital elevation model. A standard normalised cross-correlation procedure based on the optimal window size and oversampling factor (shown below) was then applied without any filtering in any part of the processing. Estimated offsets were also corrected for image distortions given that the images were not acquired from exactly the same position (Pathier *et al.*, 2006). For range offsets, distortions were modelled using the ASTER GDEM and precise orbital data.

Over a completely stable area, offset values should be normally distributed with a mean and high concentration of values around zero. However, with no oversampling and small moving window sizes (4 – 16 pixels), the distribution of values is determined by the size of the moving window (Figure 5-1a-c – Figure 5-4a-c) due to spurious correlation. As the oversampling factor increases, the range of possible offset values increases to eradicate the step-like behaviour of the cumulative distribution, although the linear trend shows no concentration around zero for the small window sizes. Using a window size of 32 x 32 pixels, ~75% of the offset values are between ± 0.5 pixel units and the oversampling factor was increased until no observable improvement is seen (i.e. an oversampling factor of 16 is identical to an oversampling factor of 24). The tests for TSX Spotlight and TSX Stripmap data are very consistent and the same optimal parameters are used for both data sets. This parameterisation is matched by previous studies using other data (e.g. Michel *et al.*, 1999; Jónsson *et al.*, 2002; Delacourt *et al.*, 2004; Jónsson *et al.*, 2005; Yun *et al.*, 2007; Giles *et al.*, 2009; Casu *et al.*, 2011; Travelletti *et al.*, 2012; Raucoules *et al.*, 2013) who found 32 x 32 pixel window sizes and oversampling factors of 16 generated a dense coverage of independent measurements and best meets the assumption of displacements modelled locally by a translation that varies smoothly over a number of pixels.

Increasing the window size and oversampling factor does improve the results, but the processing time should also be considered. For example, doubling the window size from 32 x 32 pixels to 64 x 64 pixels increases the processing time for each offset pair from 01:41 hours to nearly 05:37 hours (Table 5-1). Given these processing times for one range and azimuth offset map, the final selection of a 32 x 32 pixel window size and an oversampling factor of 16 was deemed preferable. Larger window sizes also reduce the resolution and can increase the size of artefacts from cross-correlation procedures (Yun *et al.*, 2007). Keeping the parameters as multiples of two was important to maintain computational efficiency when using the Fast Fourier Transform (FFT) for the normalised cross-correlation.

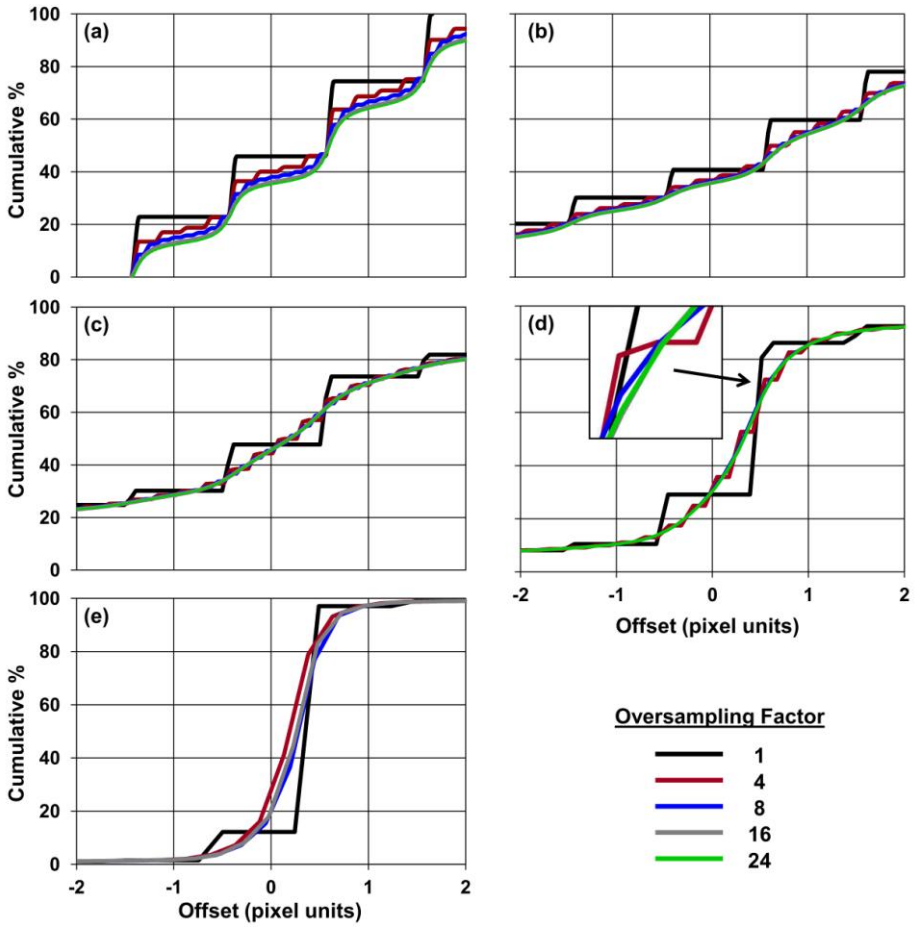

Figure 5-1: Cumulative percentage of TSX Spotlight sub-pixel offset values in azimuth direction for different window sizes: (a) 4 x 4 pixels (b) 8 x 8 (c) 16 x 16 (d) 32 x 32 (e) 64 x 64.

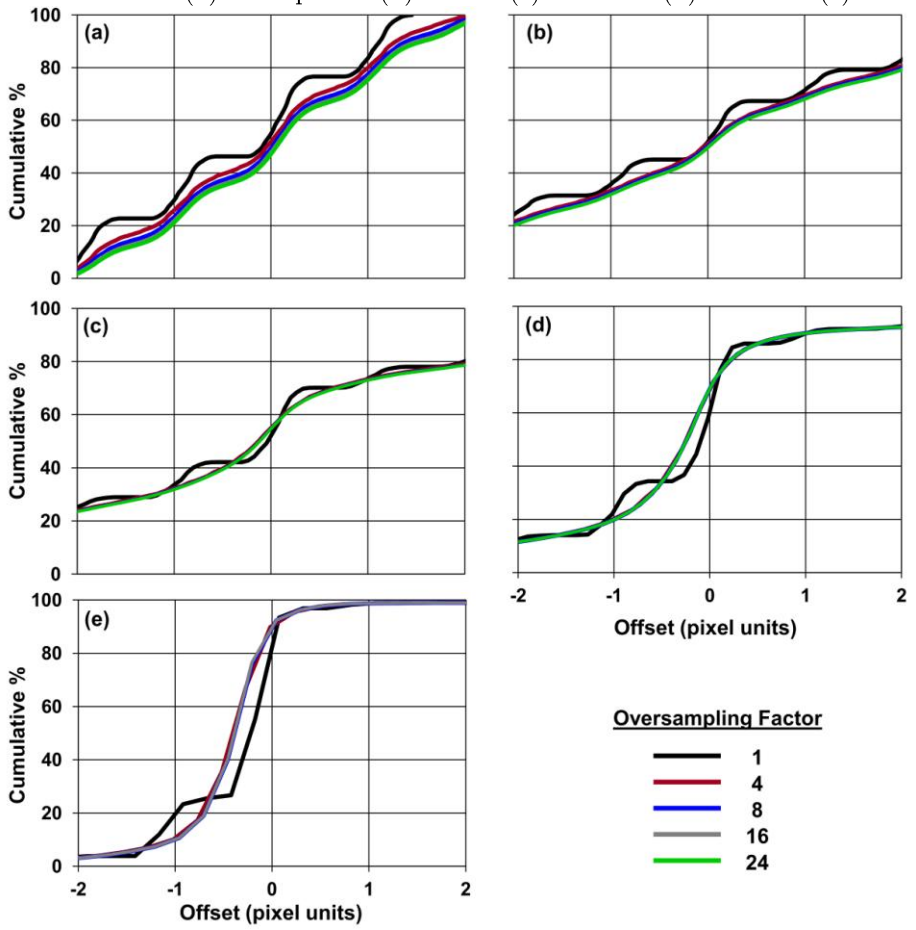

Figure 5-2: Cumulative percentage of TSX Spotlight sub-pixel offset values in range direction for different window sizes: (a) 4 x 4 pixels (b) 8 x 8 (c) 16 x 16 (d) 32 x 32 (e) 64 x 64.

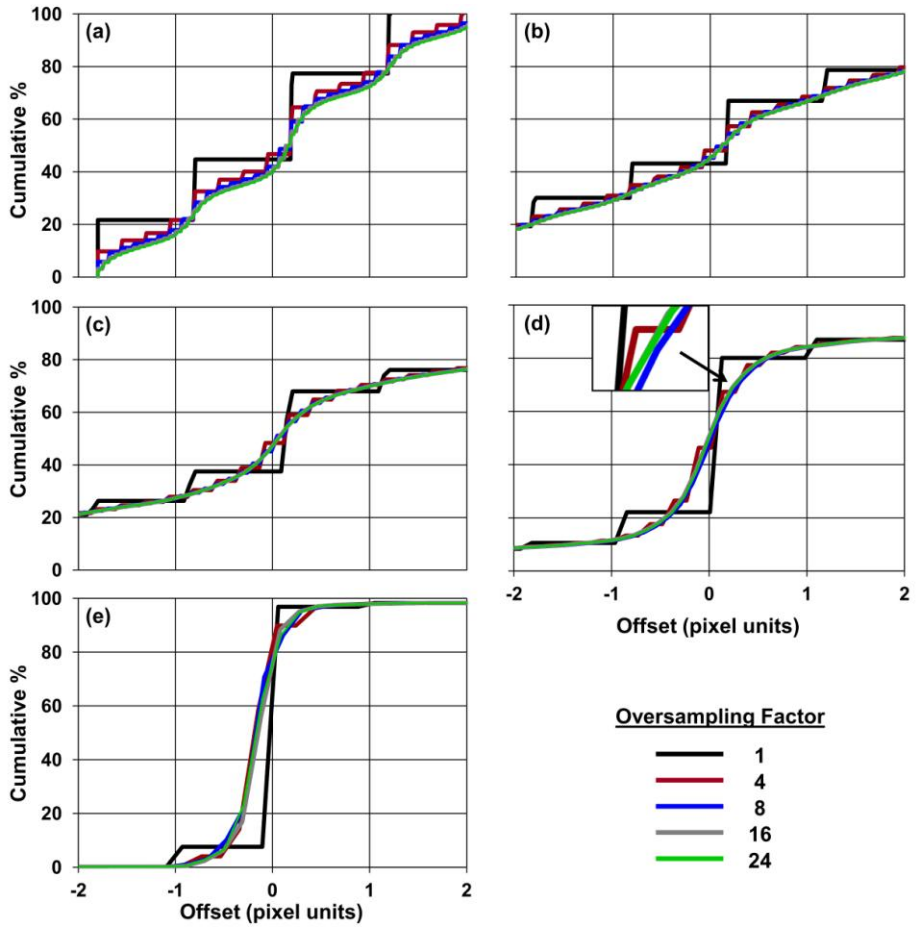

Figure 5-3: Cumulative percentage of TSX Stripmap sub-pixel offset values in azimuth direction for different window sizes: (a) 4 x 4 pixels (b) 8 x 8 (c) 16 x 16 (d) 32 x 32 (e) 64 x 64.

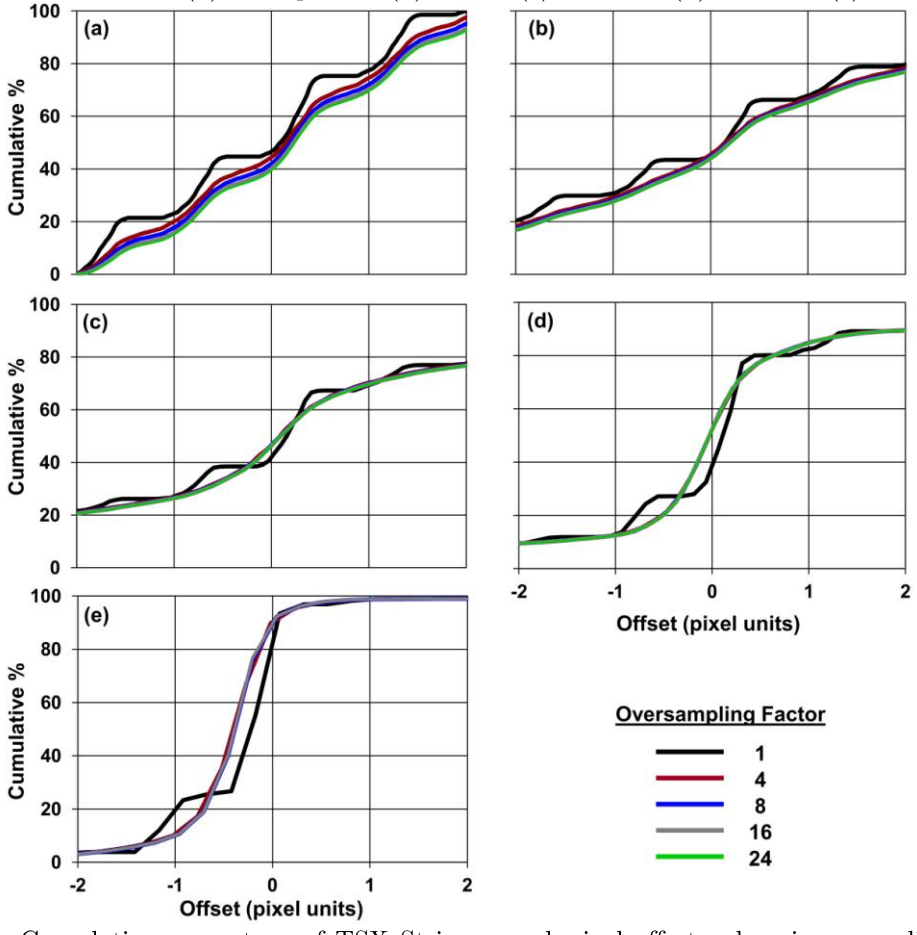

Figure 5-4: Cumulative percentage of TSX Stripmap sub-pixel offset values in range direction for different window sizes: (a) 4 x 4 pixels (b) 8 x 8 (c) 16 x 16 (d) 32 x 32 (e) 64 x 64

Table 5-1: Time taken to process TSX Spotlight offsets (HH:MM) using different parameter settings for a reference area assumed to be stable, adjacent to Shuping landslide. The grey highlighted number shows the time of the chosen parameter set. For the same areal coverage, times for the TSX Stripmap data are greatly reduced due to its larger pixel spacing.

Processor Speed:	2.93 GHz
RAM:	16 GB
Operating System:	Windows 7 – 64 bit
Area of stable ground:	2 km^2
Image dimensions (Spotlight):	2238 (range) x 1294 (azimuth)
Pixels processed:	Offsets calculated for every 2^{nd} pixel in range & azimuth

Oversampling Factor	**4 x 4 pixels**	**8 x 8**	**16 x 16**	**32 x 32**	**64 x 64**
1	00:34	00:35	00:41	01:03	02:07
4	00:36	00:37	00:41	01:06	02:15
8	00:36	00:38	00:43	01:23	02:53
16	00:40	00:43	01:00	**01:41**	05:37
24	00:42	00:48	01:07	02:41	

The SARscape® Amplitude Tracking module also permits coherence tracking, but this was not pursued given the substantially low coherence results in Section 4.2.2. Results were processed using only the amplitude (intensity) data and therefore required large cross-correlation window sizes (Strozzi *et al.*, 2002).

5.2 TerraSAR-X SPOT-CR Results for the Shuping Landslide

Having observed decorrelation within the boundary of the Shuping landslide potentially caused by movements exceeding the spatial displacement gradient, SPOT processing was initially focused on this site. Following the results of the first offset pair, the cross-correlation values associated with each offset measurement (Figure 5-5a) show that points with very high correlations (> 0.92) are distributed across the landslide in positions which correspond to corner reflector locations (cf. Fan *et al.*, 2010). Given the significant contrast in radar backscatter between the corner reflectors and natural terrain (shown in Appendix Figure A-1), these points result in a very high cross-correlation value when they are within the total area covered by the moving window used in the offset calculation. For this reason, use of larger window sizes (e.g. 64 x 64 pixels) would also reduce the spatial coverage of measurements from natural features surrounding the corner reflectors.

Following the numbering scheme displayed in Figure 5-5b, the final offset values were taken as the mean from a small window of 10 x 10 pixels within these high correlation areas to generate a Sub-Pixel Offset Time-series applied to Corner Reflectors (SPOT-CR).

The same window position in rows/columns was used to extract measurements from every subsequent slave image for the time-series. It is clear that most corner reflectors are within the landslide boundary, although a number of points are situated outside the landslide on ground that is assumed to be stable which may help identify the potential noise level of the offset measurements.

A final step in the processing strategy considered how best to generate a time-series of measurements. The two simplest approaches are to: (i) use the same master image with subsequent slave images; or, (ii) process every 11-day offset pair to generate a cumulative time-series of displacement. The first of these possibilities was preferred since the temporal decorrelation from the corner reflector points is believed to be negligible, and this strategy ensures that errors in each offset measurement are independent from the results of previous image pairs. For example, using consecutive image pairs, the first measurement would be the result of just one offset pair, whereas the last measurement would be calculated as the sum of all previous offset measurements. A large error in one offset map would therefore have consequences on the remaining time-series. The simplest approach (i.e. (i) above) of using one constant master image for all the offset pairs therefore met the requirements of this SPOT-CR analysis.

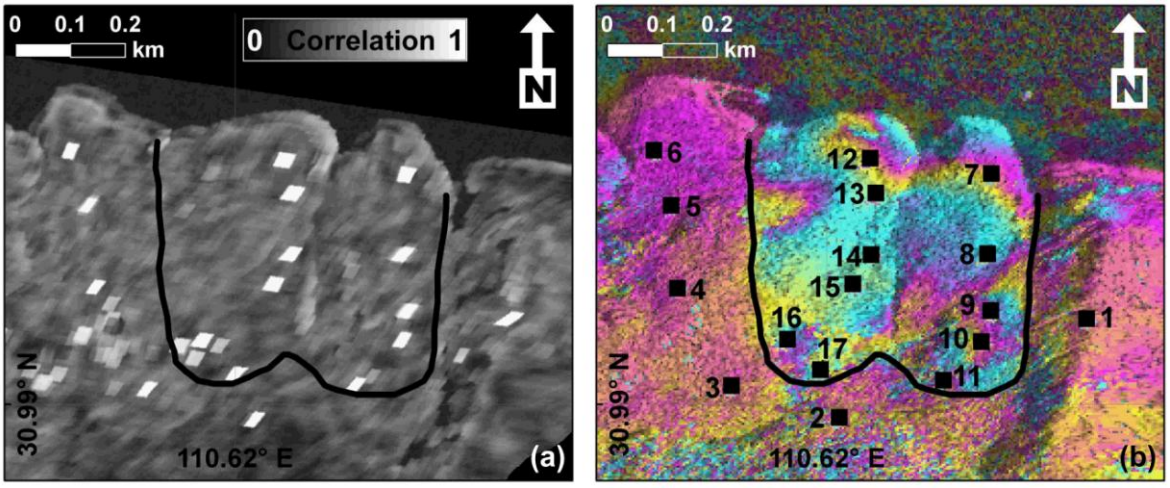

Figure 5-5(a): The value of peak correlation used for the TSX Spotlight offset measurements. 11-day pair, 21st Feb – 4th Mar 2009, showing the minimum temporal decorrelation. The high correlations (the white areas) are caused by a high-contrast feature (corresponding to corner reflector locations) within the cross-correlation window. The same features are observed for the TSX Stripmap offset measurements.

Figure 5-5(b): The numbering of corner reflectors used to extract time-series of displacement, overlain on an interferogram showing the landslide boundary. 11-day interferogram, 9th May – 20th May 2009. Point 1 is outside the landslide and used as the reference for all other points. Points 2 – 6 are also outside the landslide boundary. Points 7 – 11 ascend up the east part of the landslide. Points 12 – 17 ascend up the west part of the landslide. Point 3 was excluded from analysis after results suggested it had shifted unnaturally (see Appendix Figure A-3).

5.2.1 TerraSAR-X SPOT-CR Results: 2009 - 2010

The corner reflector offset time-series graphs from TSX Spotlight and Stripmap data (Figure 5-6) show a significant step in landslide movement in both range and azimuth directions towards the end of May 2009 and the start of June 2009. Movements of more than 0.1 m recorded towards the head of the landslide over an 11-day period confirm the loss of coherence from the interferograms presented in Figure 4-18 was caused by the spatial displacement gradient threshold being exceeded. It would be impossible to unwrap any interferograms over this time period and means the previous D-InSAR results over the same period (outlined in Chapter 3) are likely to be erroneous.

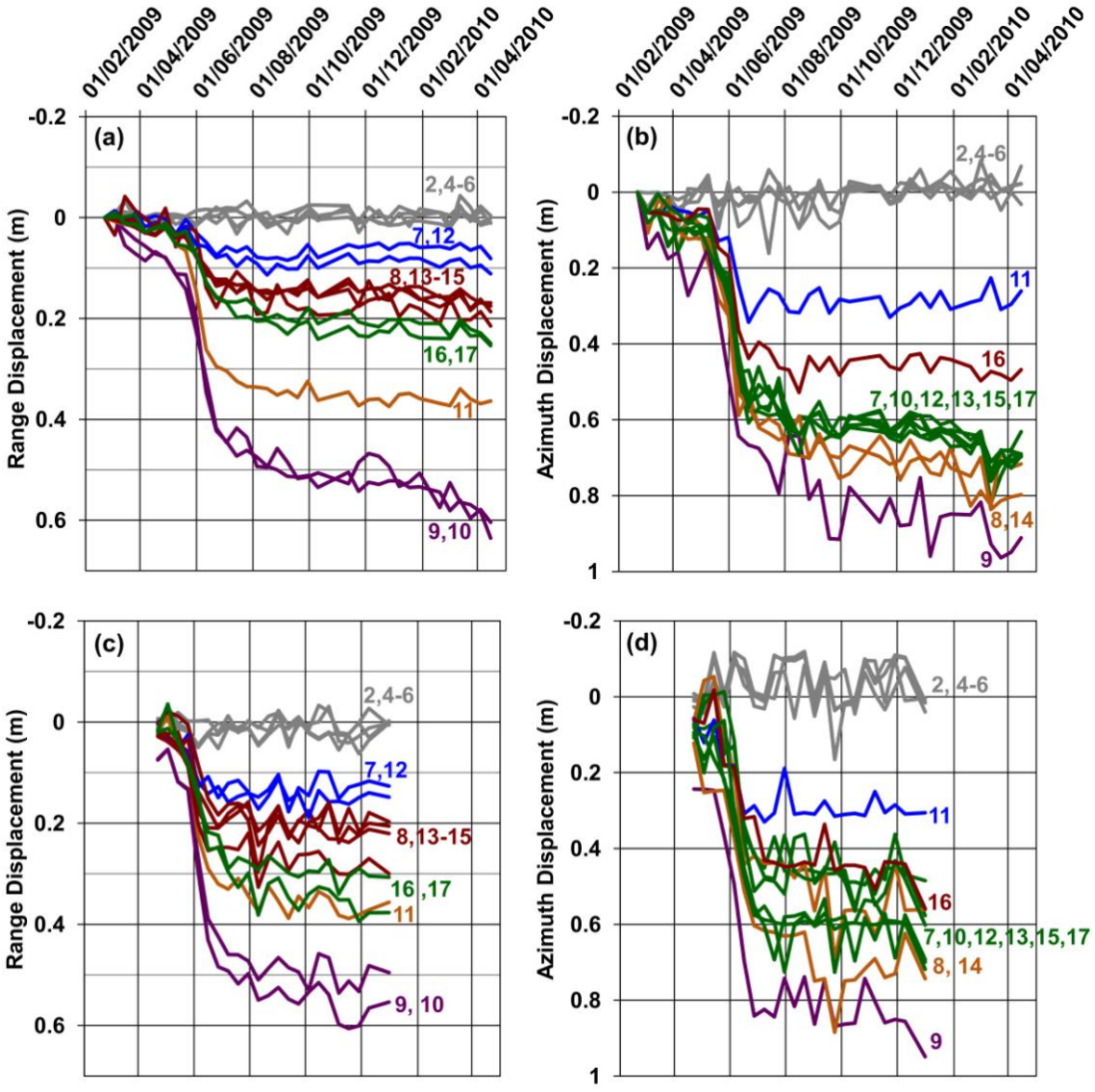

Figure 5-6: Offset displacements for the corner reflectors labelled in Figure 5-5 from Feb 2009 – April 2010. (a – b) Range and azimuth offsets measured from TSX Spotlight data. (c – d) Range and azimuth offsets measured from TSX Stripmap data. The positive scale is away from the sensor in range dimension and the reverse along-track direction (i.e. predominantly northwards) in azimuth dimension.

Considering the topographical location of the corner reflectors, a strong association is found between elevation and the range displacement. Displacement in the LOS (which includes a vertical component of movement) is up to ten times greater towards the head of the landslide and no such topographic dependence is shown by the azimuth offset results. These patterns in both range and azimuth are very consistent between the TSX Spotlight and Stripmap data and given the independence of the data sets, the duplicate measurements over the same time period help verify the results without the requirement for ground data.

From the time-series curves for CRs outside the landslide boundary (lines 2 – 6 in Figure 5-6), the variability of these assumedly stable points in the azimuth direction exceeds the variability in the range direction, a result caused by the larger azimuth pixel spacing. Additionally the variability in the corresponding offset values from the TSX Stripmap data is greater than the Spotlight data, which is another likely consequence of the larger pixel spacing.

Confidence in the SPOT-CR results is boosted by a qualitative comparison to extensometer data over the same time period (Figure 5-7) presented by Wang *et al.* (2013b). The maximum step-like displacement of ~0.5 m occurred in May 2009 before stabilising for the remainder of the year. Despite these extensometer measurements being located at different points within the landslide boundary, the magnitude and timing of movements recorded by the extensometers closely follow the SPOT-CR results presented in Figure 5-6. Additionally, the magnitude and linearity of repeated GPS measurements closely follow the range offset results for the survey period August 2009 – April 2010 (Liao *et al.*, 2013).

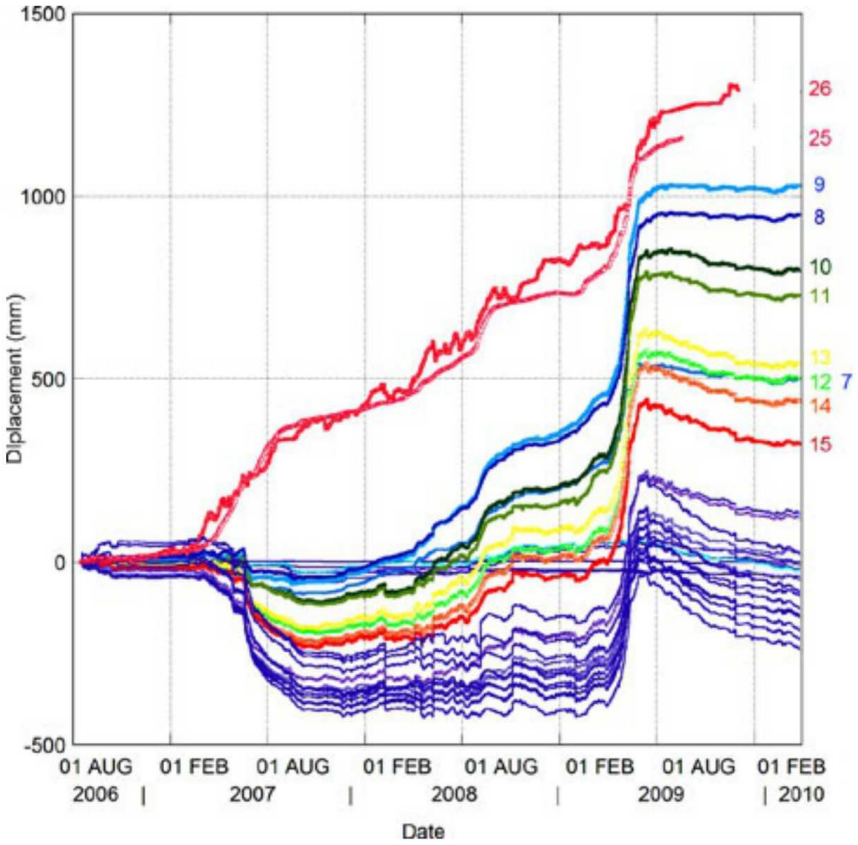

Figure 5-7: Accumulated displacement of all extensometer monitoring points on the Shuping landslide, August 2006 to May 2010 (from Wang *et al.*, 2013b p.238).

5.2.2 TerraSAR-X SPOT-CR Results: 2009 - 2013

Clearly the Shuping landslide has experienced significant episodic movements from February 2009 – April 2010 and should continue to be monitored. A second series of TSX Spotlight images was acquired between January 2012 and February 2013 for this purpose and the use of SPOT-CR techniques with a single master image allows landslide movement over the data gap to be recovered, albeit without the high sampling interval achieved using regularly acquired SAR images. Again it should be noted SAR images for the majority of the second period of TSX Spotlight data were only acquired at monthly intervals, reducing the temporal resolution at which landslide movements can be observed.

Figure 5-8 shows the continued monitoring of TSX Spotlight range and azimuth offsets beyond April 2010. Another large, episodic landslide movement episode is observed in both range and azimuth directions at the end of May and the start of June 2012. The large movement in 2012 (of similar magnitude to that in 2009), coupled with the reduced frequency of SAR image acquisitions (33-days), again suggest this movement would be irretrievable using standard D-InSAR or D-InSAR time-series techniques due the spatial

displacement gradient being exceeded. The variability of the stable points (lines 2 – 6) also remains consistent over the whole 4-year time period.

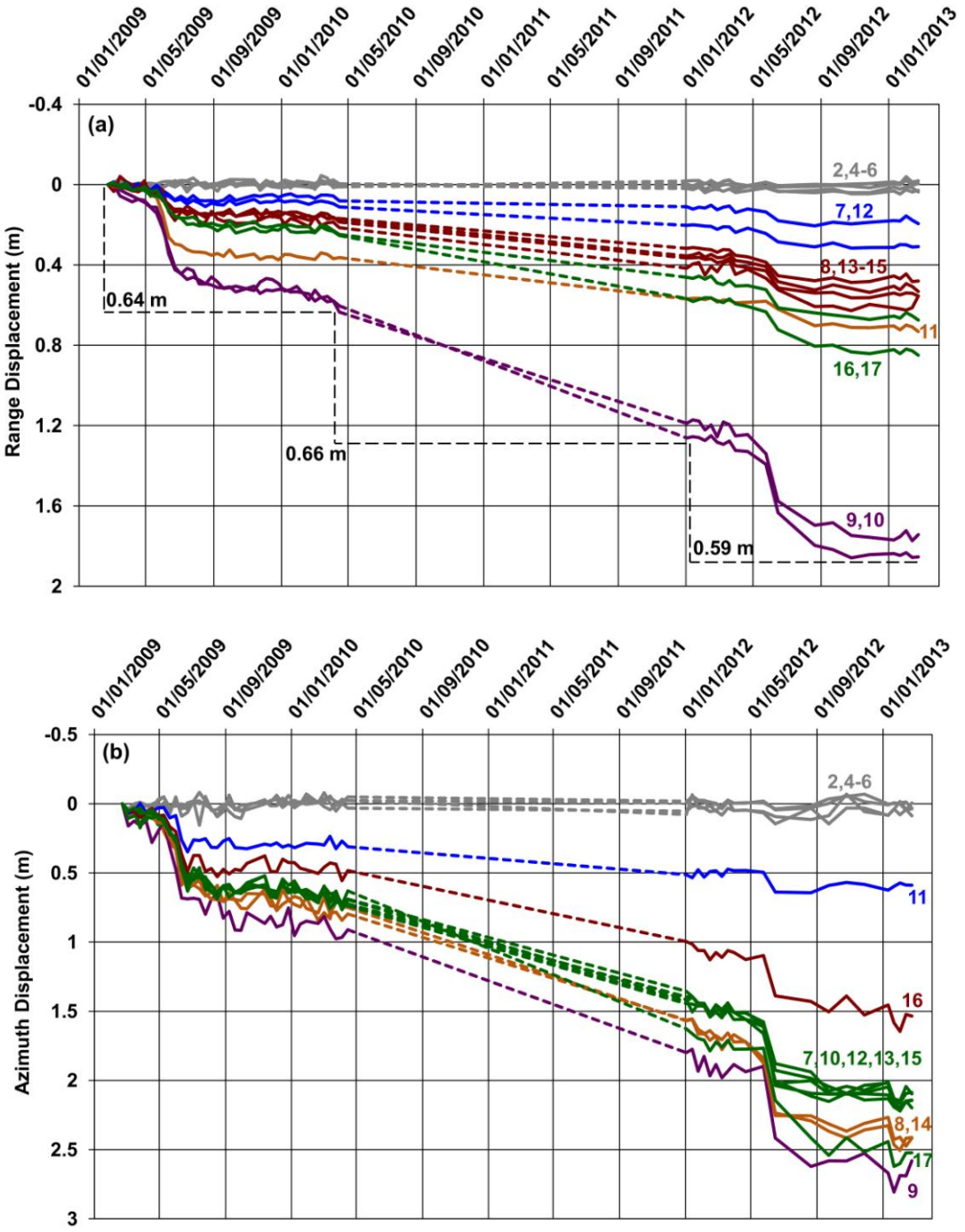

Figure 5-8: TSX Spotlight offset displacements for the corner reflectors labelled in Figure 5-5 from Feb 2009 – Feb 2013. (a) range and (b) azimuth displacements. The positive scale is away from the sensor in range dimension and the reverse along-track direction (i.e. predominantly northwards) in azimuth dimension. The dotted line shows the gap of TSX Spotlight data.

As the vast majority of lines in Figure 5-8 do not cross each other for the whole time period, the patterns of displacement from the landslide head to toe are shown to be consistent in time. The only time-series curve to change order from 2009 to 2013 (in both

range and azimuth graphs) is corner reflector 17, with a greater relative movement after April 2010. Given its location at the head of the landslide, the increased movement of corner reflector 17 could be explained by a small degree of undercutting and/or headward erosion at the upper boundary.

The concurrence of movements at the same time of year could suggest a seasonal triggering factor such as hydrological events, seasonal rainfall or seismic activity. However, if the largest movements of ~0.6 m are assumed to occur every year in May-June, the inferred offsets between April 2010 and January 2012 (shown by the dashed lines in Figure 5-8) are much lower than expected. The data gap spans 20 months containing two periods of May-June, and therefore displacement up to 1.2 m could have been anticipated. Potential triggering factors and further investigation into the period of no data are further investigated in Chapter 6.

5.2.3 TerraSAR-X SPOT-CR Precision

An assessment of the SPOT-CR errors was undertaken using two independent offset pairs which significantly overlap in time. The offsets were measured between the first and penultimate available images, and compared with the offsets between the second and last images (covering ~9 months for the first TSX Spotlight period, ~4 years for the whole TSX Spotlight period and ~5 months for the TSX Stripmap data). Since using two independent offset pairs to assess the error assumes the displacement between first/second image and penultimate/last image is equal, all images were chosen at times when the landslide velocity had significantly reduced.

The differences between the independent offset measurements from these overlapping image pairs are shown in Table 5-2. Using the differences between 17 corner reflector points to generate the statistics, the RMS errors are all less than 0.038 m and 0.071 m in range and azimuth directions respectively. This matches the relative measurement errors found with ERS, ALOS and COSMO SkyMed Stripmap data (Jónsson *et al.*, 2002; Strozzi *et al.*, 2002; Feng *et al.*, 2013; Fielding *et al.*, 2013).

The errors are always lower for the TSX Spotlight imagery than for the Stripmap imagery and the errors are also consistently lower for the range offsets than for the azimuth offsets. Again these are likely consequences of the reduced pixel spacing between TSX Spotlight/Stripmap data and the range/azimuth dimensions. In all cases, the range and azimuth error values are order of magnitudes lower than the total accumulated landslide

displacement. Finally, comparing the difference between the ~9 month and ~4 year TSX Spotlight statistics, it is apparent there is no significant difference which highlights the benefits of corner reflectors for generating precise, 2-dimensional SPOT measurements as well as reinforcing the choice using a single master image to generate the SPOT-CR time-series curves.

Table 5-2: Comparison of all CR offset measurements between two independent offset calculations from two image pairs significantly overlapping in time. The first two images in August were used as the two master images, with the last two available images used as the respective slave images. This can help assess the errors between different SAR image modes and time periods.

	Range Offsets		Azimuth Offsets	
Sensor / Image Mode	Mean Difference (m)	RMS Error (m)	Mean Difference (m)	RMS Error (m)
TSX Spotlight: (2009 – 2010)	0.008	0.011	0.055	0.060
TSX Stripmap:	0.040	0.038	0.059	0.071
TSX Spotlight: (2009 – 2013)	0.018	0.024	0.050	0.070

5.3 TerraSAR-X SPOT-CR results for other landslides

SPOT-CR techniques were applied to the Shuping landslide to demonstrate the significant advantages of SPOT methods over D-InSAR analysis. The precision statistics for TSX Spotlight and Stripmap data (Table 5-2) show that SPOT-CR techniques provide precise offset measurements for points with a very high cross-correlation value, such as those associated with installed corner reflectors. Mean differences and RMS error values for both sensors in each dimension are in the order of $1/20^{th}$ – $1/30^{th}$ of a pixel. This also justifies wider analysis of other similar landslides using TSX Spotlight or Stripmap data, although the reliance upon installed corner reflectors is an obvious disadvantage for wider investigations.

Within the study area of this investigation, two other landslides have corner reflectors installed; the Kaziwan landslide (Xia, 2008; 2010) and the Xintan landslide (Xia *et al.*, 2004; Xia, 2010; Liao *et al.*, 2012). Unfortunately both these landslides are located outside the TSX Spotlight coverage (see Figure 4-1) and therefore only TSX Stripmap SPOT-CR measurements with a lower precision than TSX Spotlight data are possible.

5.3.1 Kaziwan and Chalukou Landslide Complex

Bordering a tributary of the Yangtze River, the Kaziwan and Chalukou landslide complex is shown covering most of Figure 5-9a. Data prior to 2008 showed most corner reflectors are stable, although points 3 and 4 moved up to 0.38 m and 0.08 m respectively in range direction over a time-period of nearly two years (Xia, 2010).

The SPOT-CR analysis for the Kaziwan landslide throughout 2009 (Figure 5-9b) shows no significant displacement for any corner reflector. Whilst corner reflector 2 deviates from the main group towards the end of the time period, this is not significantly different from other corner reflectors when considering the RMS error is ~0.04 m in range direction.

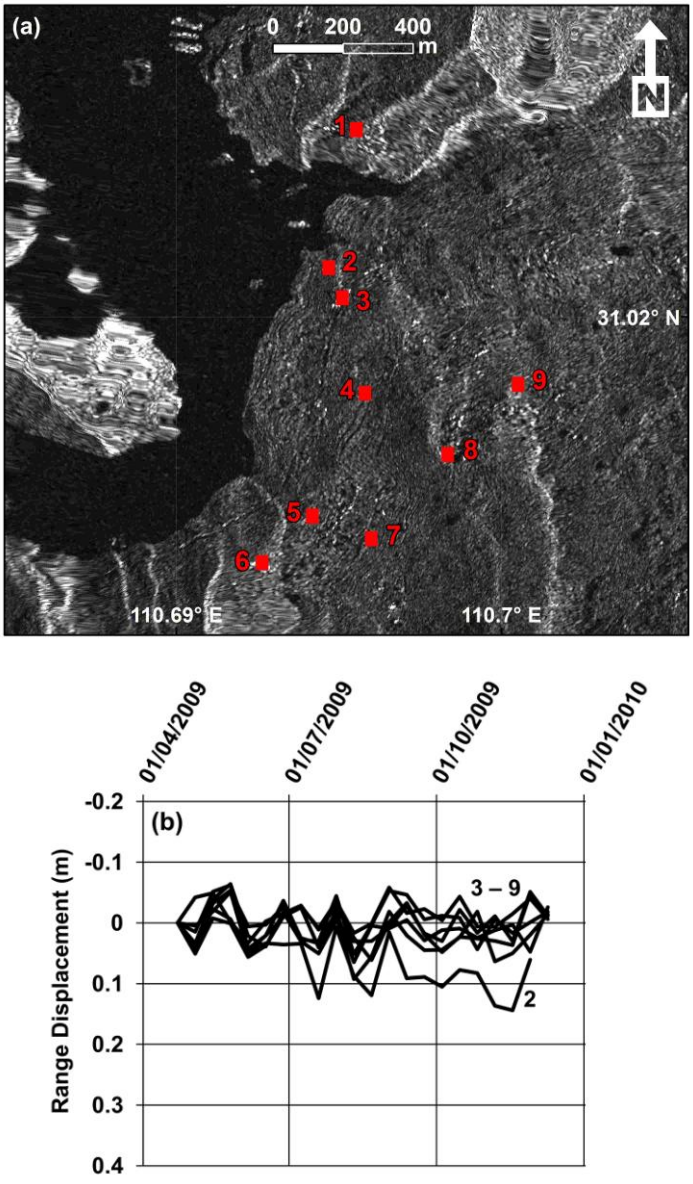

Figure 5-9: TSX Stripmap range offsets across the Kaziwan and Chalukou landslide complex showing no significant displacement. Point 1 is outside the landslide and used as a reference for other points.

5.3.2 Xintan Landslide

The most easterly known landslide in this study area is the Xintan landslide (location shown in Figure 4-1). Following its catastrophic failure in 1985, continued monitoring has been attempted to detect periods of reactivation. Corner reflectors were installed on the landslide in 2000 (Figure 5-10a) and short-term analysis over four dates in 2000/2001 showed the landslide was stable (Xia *et al.*, 2004). The same conclusion stating the landslide was "very stable" was also found by ground monitoring data spanning almost two years (Xia, 2008 p.1242).

The SPOT-CR analysis for the Xintan landslide throughout 2009 (Figure 5-10b) shows no significant displacement for any corner reflector, suggesting the landslide remains stable and has not reactivated over the various monitoring periods.

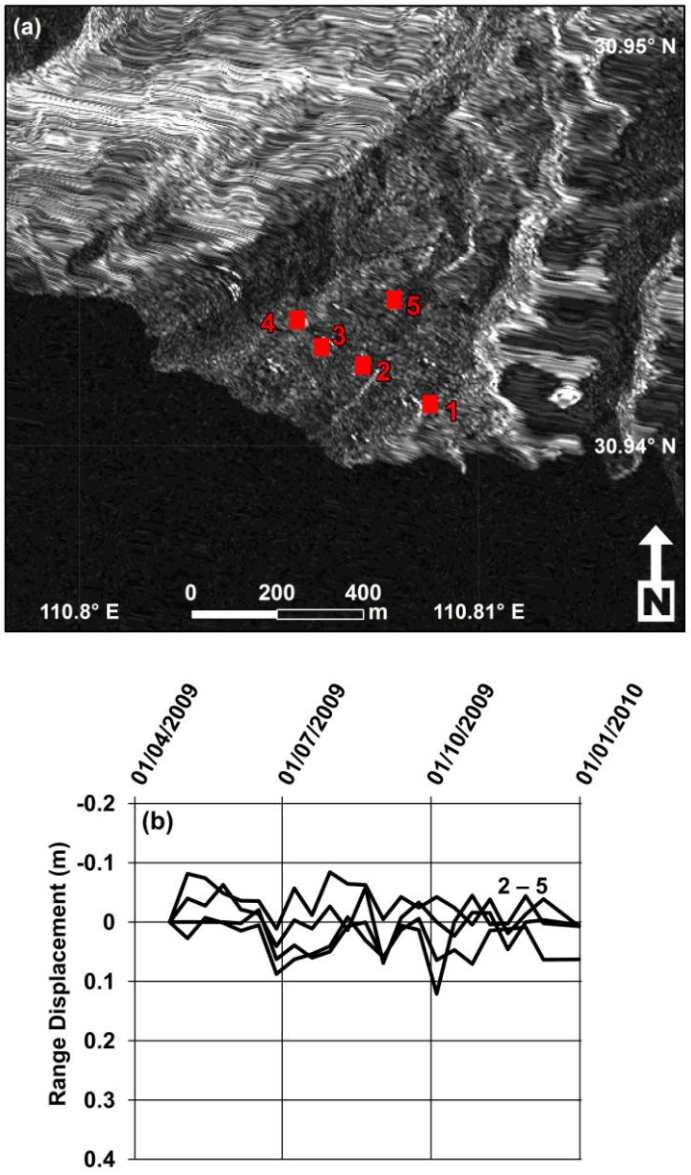

Figure 5-10: TSX Stripmap range offsets across the Xintan landslide showing no significant displacement. Point 1 is outside the landslide and used as a reference for other points.

5.4 Measuring Landslides with Point-Like Pixel Offsets

Using SPOT-CR techniques from SAR data are beneficial to generate precise offset measurements. However this assumes knowledge of currently or potentially active landslide locations and the subsequent installation of corner reflectors. The application of SPOT techniques to natural terrain beyond corner reflectors could generate a wider coverage of measurements with the potential to detect previously unknown areas of slope instability. Using a cross-correlation threshold of 0.92 (matching the minimum correlation found for the corner reflector offsets) does not increase the coverage of measurements across the whole SAR scenes for either TSX data modes. The cross-correlation threshold should be relaxed to increase the density of measurements by including natural point-like pixel offset features, although given how lower cross-correlation values increase the pixel offset estimation error (Hu *et al.*, 2014b), a lower limit on the acceptable measurement precision should be found.

To assess the relationship between cross-correlation values and the precision of measurements, a similar approach to the validation statistics in Section 5.2.3 was applied to the whole TSX Spotlight scene. Using independent image pairs with master images acquired in August (away from the main deformation period), pixels were classified into cross-correlation bins with a width of 0.04. Where pixels in the same cross-correlation bin were found in both independent offset maps, the offsets were compared in both range and azimuth dimensions. This was done for all possible time intervals (see Figure 5-11) to assess any effects of temporal decorrelation on the SPOT measurements. The overlapping time period obviously increases for longer time intervals and assumes that displacement between first/second image and penultimate/last image is equal. However, the difference between independent offset maps should still be very small for the shortest image pairs outside the periods of greatest deformation.

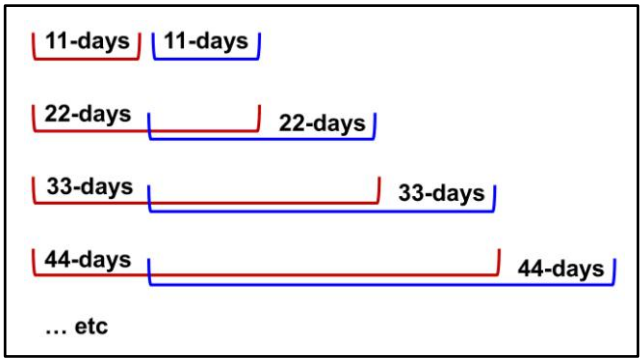

Figure 5-11: Schematic diagram of significantly overlapping, independent SAR offset pairs. The difference and standard deviation between the two independent offset maps for each time interval helps assess the effects of temporal decorrelation and perpendicular baseline.

The results of four different time intervals (Figure 5-12) helped select the lowest acceptable cross-correlation threshold in order to obtain precise offset values beyond the corner reflectors. For all time intervals, the mean differences and associated standard deviations remain low for pixels with high cross-correlation values, suggesting the precision of these points does not significantly decrease over time. As the cross-correlation values decrease, the mean difference and standard deviation between offsets of independent pairs increase, indicating a reduction in the precision of measurements. Noting the different vertical axis scales used for range and azimuth plots, the lower precision of azimuth offsets with respect to the range dimension is also apparent.

To quantitatively determine an acceptable cross-correlation threshold, a 3-part piecewise linear regression function is fitted to the standard deviation values (shown by the background colour changes in Figure 5-12). The upper boundary is used to determine the 'breaking point' beyond which the standard deviations are low enough to provide an acceptable precision for offset values. For all time intervals these values are relatively consistent, ranging from 0.70 – 0.86 in both range and azimuth dimensions. The mean and median cross-correlation is ~0.78 and used as the lowest cross-correlation threshold for producing a regional coverage of offset measurements across the TSX Spotlight scene.

The standard deviation for range offsets estimated from the cross-correlation of amplitude images has been derived for homogenous (i.e. featureless) patches (Bamler, 2000; Bamler and Eineder, 2005) (Equation 5-1):

$$\sigma_{offset} = \left(\sqrt{\frac{3}{2N}}\right)\left(\frac{\sqrt{1-r^2}}{\pi\, r}\right)\left(\chi^{3/2}\right)$$

Equation 5-1: Standard deviation from cross-correlation operations for homogenous regions (Bamler, 2000). N is the number of samples in the cross-correlation block; r is the cross-correlation; and, χ is the oversampling factor.

Using the selected processing parameters, a cross-correlation value of 0.78 and range pixel spacing of 0.455 m, this produces a range offset uncertainty of 0.28 m. This theoretical value is far higher than the standard deviations of the TSX Spotlight data (Figure 5-12), indicating many features exhibiting a cross-correlation above 0.78 are likely to be point-like targets rather than areas of homogenous ground cover.

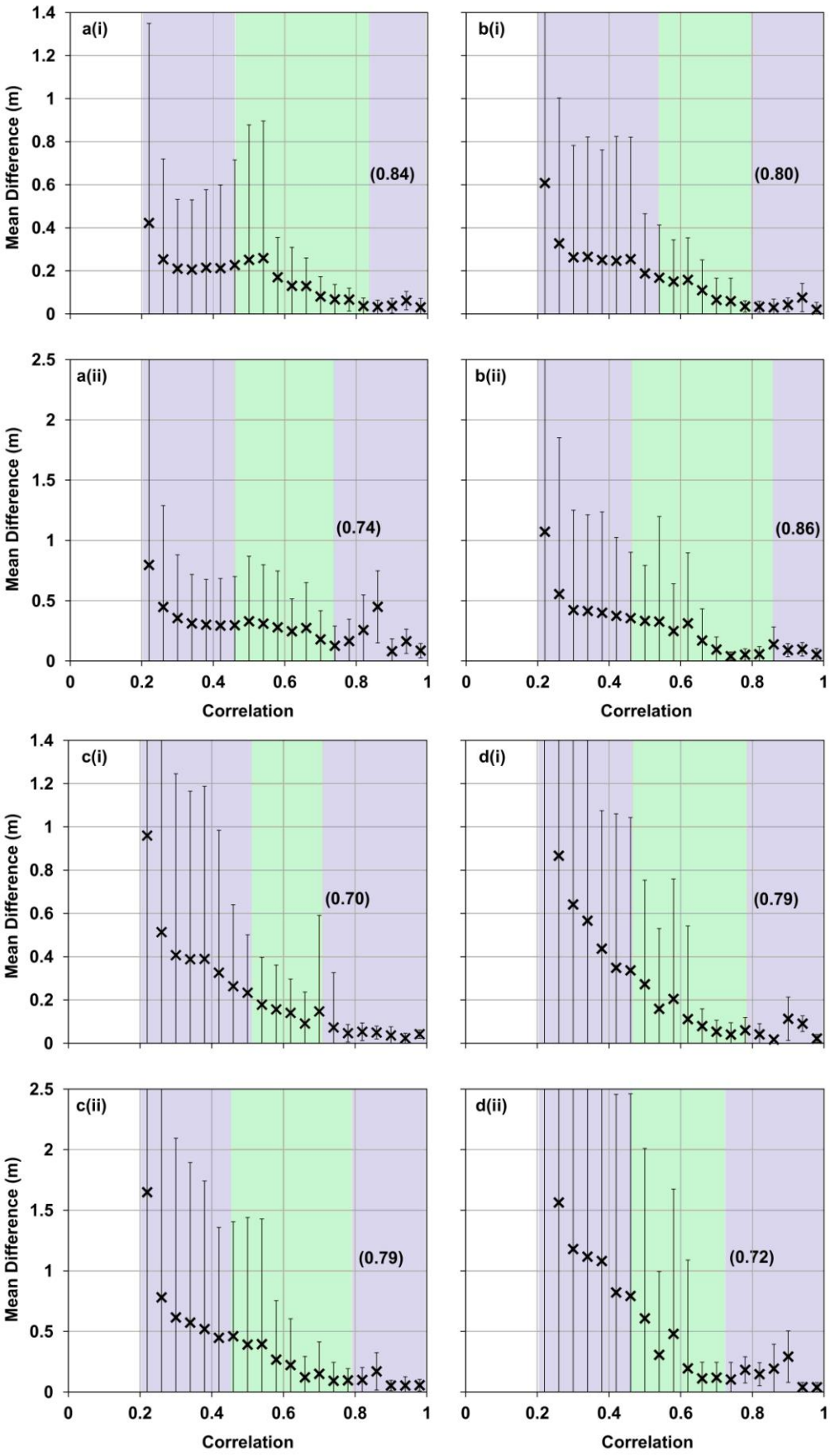

Figure 5-12: Mean difference between two independent TSX Spotlight offset maps overlapping in time, classified by offset cross-correlation values. (i) range and (ii) azimuth directions. (a) 11-day (b) 33-day (c) 242-day (d) 1287-day image pairs. Points are plotted for correlation bins, with a width of 0.04. Error bars represent one standard deviation. Colour changes represent cut-off values for a 3-part linear regression on the standard deviation values.

An increasing negative gradient of points with lower cross-correlation values is observed as the time interval increases (Figure 5-12), signifying lower cross-correlation values are subject to temporal decorrelation and decreasing precision over time. However the precision remains consistently high for pixels with a cross-correlation above the threshold of 0.78, even over the longest time interval of 1287 days.

Having reduced the cross-correlation threshold to include natural point-like targets in a regional offset map, the strategy of generating a time-series of measurements should also be reconsidered. In addition to a single-master approach or using consecutive image pairs (as discussed in Section 5.2), another alternative method considers inverting a small-baseline (SBAS) network of offset pairs, as proposed by Casu *et al.* (2011). Using ENVISAT data, Casu *et al.* (2011) attempted to reduce the perpendicular baselines of offset pairs which influenced the quantity of reliable measurements generated. The following results assess the effects of temporal decorrelation and perpendicular baseline upon the precision and density of offset measurements for different cross-correlation values.

The error bars in Figure 5-12, showing the standard deviation of the difference between independent offsets overlapping in time, were used as a measure of precision. Having processed these results for all image pairs, the variation of standard deviation with respect to the time interval was plotted to assess the effects of temporal decorrelation (Figure 5-13). The high cross-correlation pixels are again shown to maintain a consistent precision level over the whole time period, whereas for cross-correlation values < 0.78, the standard deviations increased over time. This pattern would be amplified if cross-correlation values below 0.5 were included in the graphs. The conclusion remains that pixel offsets with a cross-correlation > 0.78 do not significantly suffer from temporal decorrelation (Hu *et al.*, 2014a), also agreeing with the results of Casu *et al.* (2011).

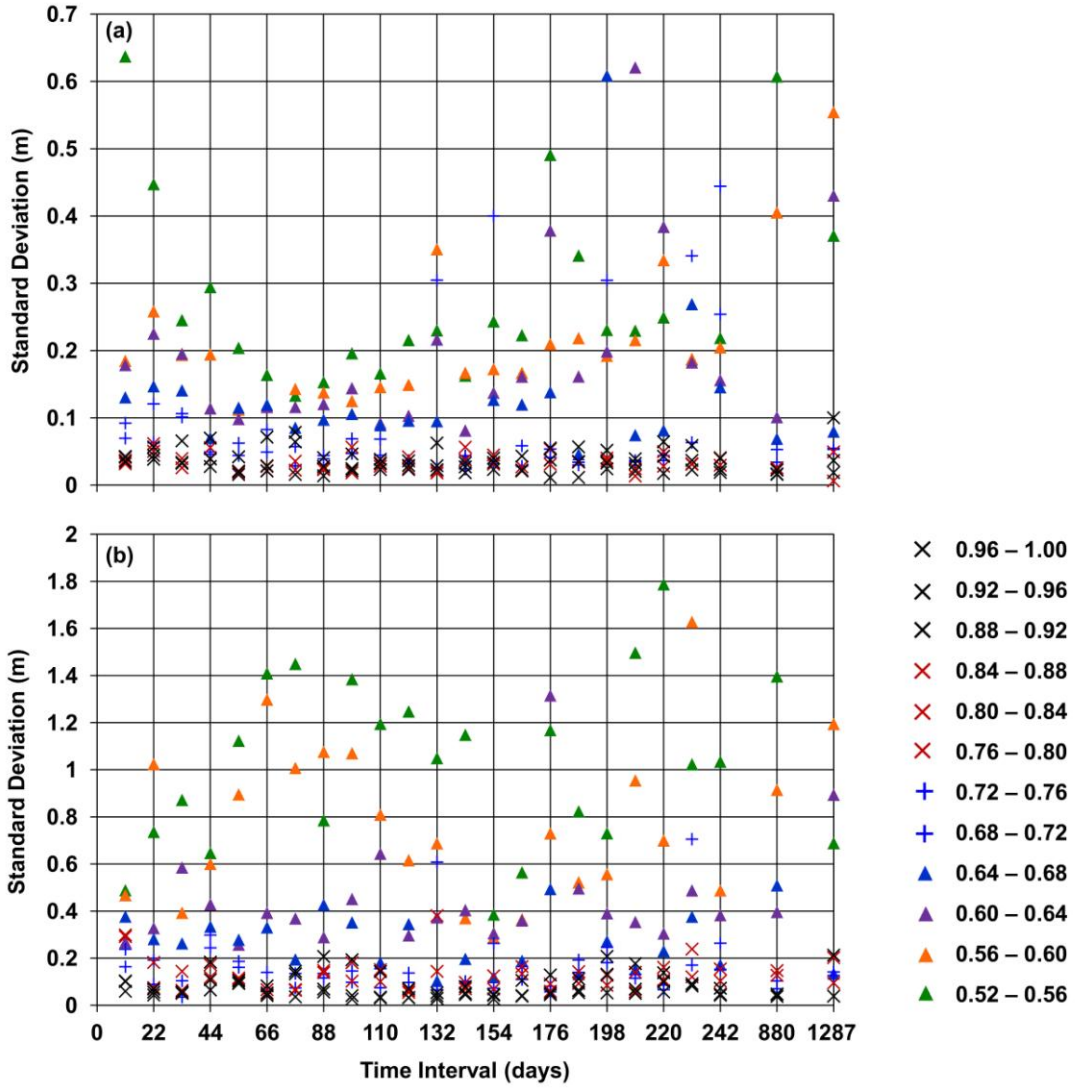

Figure 5-13: Standard deviation of the difference in offset values from independent TSX Spotlight offset maps overlapping in time, in relation to offset correlation values and SAR image time interval. (a) range and (b) azimuth directions. For pixels with high correlation offset values (approx. $r > 0.78$), the standard deviation of the difference between two independent offset maps does not increase over time. This illustrates the robustness of these offset measurements which do not experience significant temporal decorrelation effects.

For the TSX Spotlight data in this study, no significant dependence upon the perpendicular baseline is observed. For all the time intervals shown in Figure 5-13, the same standard deviation data were plotted against the larger of the two perpendicular baselines values associated with the independent offset pairs (Figure 5-14). No significant dependence upon the perpendicular baseline is shown, most likely due to the consistently short perpendicular baseline values of the TSX satellite which never exceeded 300 m. This is not contradictory to the results of Casu *et al.* (2011) who only found a degradation in pixel reliability for ENVISAT data when the perpendicular baseline exceeded 400 m. For this principal reason, the benefit of inverting a SBAS network of offset maps to generate a time-series of displacement is limited for TSX data with a small orbital tube.

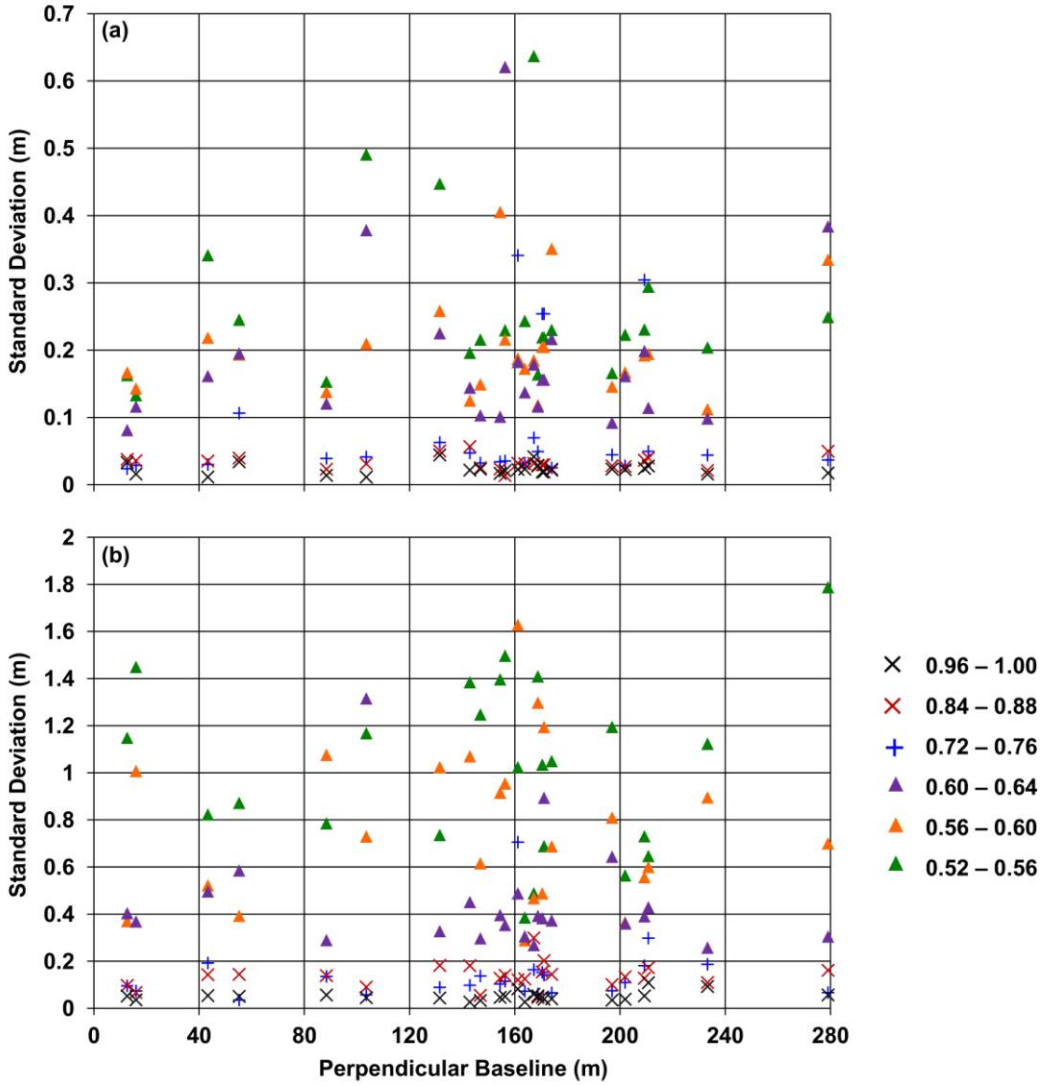

Figure 5-14: Standard deviation of the difference in offset values from independent TSX Spotlight offset maps overlapping in time, in relation to offset correlation values and perpendicular baseline. (a) range and (b) azimuth directions. There is no apparent relationship between the standard deviation and perpendicular baseline, particularly for pixels with a high correlation value (approx. $r > 0.78$) showing consistently low standard deviations.

Whilst the precision of pixels with a cross-correlation > 0.78 is not dependent upon the time interval or perpendicular baseline of the image pair, Figure 5-13 and Figure 5-14 fail to consider the number of pixels (and therefore the coverage of measurements) within each cross-correlation bin. Offset measurements selected using the cross-correlation threshold may not deteriorate in quality over time, but could decrease in number.

Figure 5-15 shows the number of pixels within each cross-correlation bin related to the image pair time interval. The first noticeable feature is the large number of pixels associated with the highest cross-correlation bin (0.96 – 1.00). This reflects the dominance of a corner reflector within the search area and a disadvantage of using a large window size parameter. Every pixel within the search window around the corner reflectors (or

other point-like targets) will be characterised by the same offset and high cross-correlation values, resulting in this large number of pixels for the highest cross-correlation bin. The number of pixels for this category does not decrease significantly over time supporting the above strategy for SPOT-CR analysis.

For lower cross-correlation values (e.g. 0.52 – 0.56) there are significant temporal decorrelation effects caused by increasing time intervals, with pixel numbers dropping from ~2,300 pixels after 11-days to just ~800 pixels after 66-days. This would support the use of consecutive image pairs to generate a greater coverage of points for time-series analysis, however the precision of offsets with this level of cross-correlation is unacceptable (even over 11-days) for monitoring the magnitude of Shuping landslide movements (Figure 5-12a).

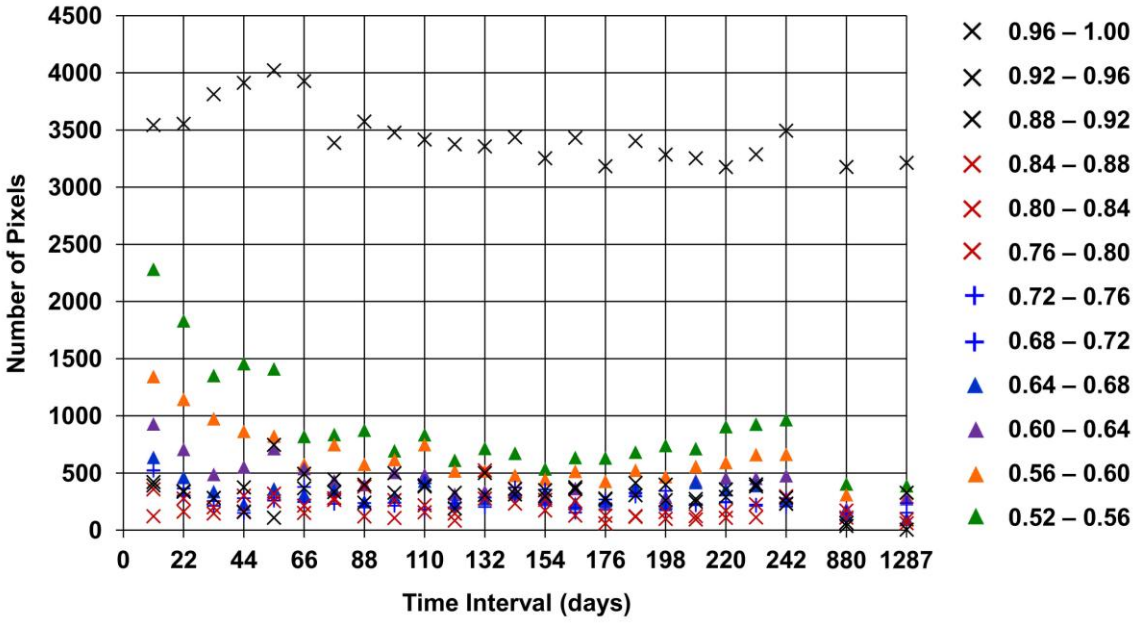

Figure 5-15: The number of mutual pixels with similar correlation values from independent TSX Spotlight offset maps overlapping in time, in relation to SAR image time interval. For high correlation values (approx. $r > 0.78$), there is no significant decrease in pixels until the time interval exceeds 1-year. For corner reflector correlations (i.e. $r > 0.96$), there is very little decrease in the number of pixels even after 1287 days (i.e. using the first and last available SAR image).

For higher cross-correlation values (> 0.78), the number of pixels over the TSX Spotlight scene does not decrease up to the 242-day interval (the whole duration of the first series of TSX Spotlight data). However, the number of pixels appears to drop beyond the 242-day limit when the master and slave images span the TSX Spotlight data gap. There are two possible causes for this, either changing terrain properties or an artefact caused by changes in the SAR acquisition plan for the second period of TSX Spotlight data. The imaging

mode, relative orbit and SAR beam are identical for both data collection periods, although the exact areal coverage and incidence angle are altered very slightly. Regardless of the cause, using one single master to generate regional offset maps for all SAR acquisition dates is not optimal and would lead to a reduction in measurement density by the end of the time-series. Subsequently different master images were used to generate the time-series for each data period (i.e. 21st February 2009 for the first period of TSX Spotlight data and 2nd January 2012 for the second period) to maintain a consistent density of measurements. The gap of TSX Spotlight data was spanned using the minimum time-interval image pair; 15th April 2010 as the master and 2nd January 2012 as the slave. It was assumed the vast majority of selected point-like targets in one data series will remain observable in other time-periods unless there is a physical change in its backscattering properties.

In all cases, no seasonal signals related to the offset precision or number of pixels across the scene were identified, suggesting these point-like targets are mostly artificial and therefore unrelated to vegetation changes.

5.5 TerraSAR-X Spotlight Regional Point-Like Pixel Offsets

Using a cross-correlation threshold of 0.78 and the above time-series strategy, various regional offset maps were produced for the following periods; 21st February 2009 – 15th April 2010; 15th April 2010 – 2nd January 2012, and, 2nd January 2012 – 23rd February 2013 (Figure 5-16 – Figure 5-18). A final offset map was produced using the first and last available Spotlight images, from 21st February 2009 – 23rd February 2013 (Figure 5-19).

The coverage now extends beyond the 17 corner reflector points installed over the Shuping landslide (shown in the lower inset of Figure 5-16 – Figure 5-19) although the density of measurements is sparse for the whole scene, illustrating the difficulty obtaining precise offsets in densely vegetated terrain (Jónsson *et al.*, 2005; Grandin *et al.*, 2009). To generate time-series measurements using three different master images as opposed to one single master is also beneficial, shown by the greater density of measurements in Figure 5-16 – Figure 5-18 compared with Figure 5-19 (see the upper insets for a detailed view). To ensure the three-master approach was not influencing the final measurements, the time-series of corner reflector displacement was compared to the results from the single-master approach (Figure 5-8). For the 312 potentially different measurements, the mean difference and RMSE was 0.010 m and 0.014 m respectively for range offsets, 0.035 m and 0.043 m for azimuth offsets. These are within the noise levels presented in Table 5-2.

Very similar patterns for the range and azimuth displacements are observed across the Shuping landslide for each shorter time interval (lower inset of Figure 5-16 – Figure 5-18) as well as the accumulated displacement over the whole period of TSX Spotlight SAR data (lower inset of Figure 5-19). Range offsets are always greatest for corner reflectors 9 & 10, whilst the azimuth offsets are more consistent across the whole landslide body matching the results from Section 5.2.2.

Displacement signals are additionally found to the west of the Shuping landslide between January 2012 and February 2013 (lower inset of Figure 5-18 – Figure 5-19). These are unrelated to the Shuping landslide given the stable corner reflectors separating these areas of displacement, although evidence of new slope movements was found during a fieldtrip to the region in April 2012 (see Appendix Figure A-4). GPS-tagged photos were used to match the building damage to the offset displacement signals to the west of the Shuping landslide.

Finally, an area of instability that has not previously been reported is identified on the opposite riverbank to the Shuping landslide (upper inset of Figure 5-17). Note the azimuth displacement displays a negative value due to southerly movements towards the river. The slope appears stable between 21st February 2009 – 15th April 2010; becomes unstable between 15th April 2010 – 2nd January 2012, and stabilises between 2nd January 2012 – 23rd February 2013. However, the sum of accumulated displacement over these three time intervals is ~70% lower than the magnitude of displacement calculated from the first and last available TSX Spotlight image (Figure 5-19).

Using a single-master approach for the whole time-series, the range and azimuth displacement was plotted for the whole 4-year period of data (Figure 5-20). The slope is stable for the first time interval (matching Figure 5-16), shows displacement of 0.4 m in range and 0.5 m in azimuth for the second time interval (matching Figure 5-17), but shows a large displacement for the third time interval which contradicts the results of Figure 5-18.

Three geo-tagged photos of this slope (in the years 2007, 2009 and 2011), appear to show a tall building on this slope has been evacuated and partially demolished whilst concrete slope reinforcements have been engineered to stabilise this slope (Figure 5-21). It is hypothesised the building was demolished prior to 2009 (otherwise it would appear as a large range displacement of several metres in the time-series measurements). The slope must have moved and been reinforced with concrete sometime between 15th April 2010 – 2nd January 2012.

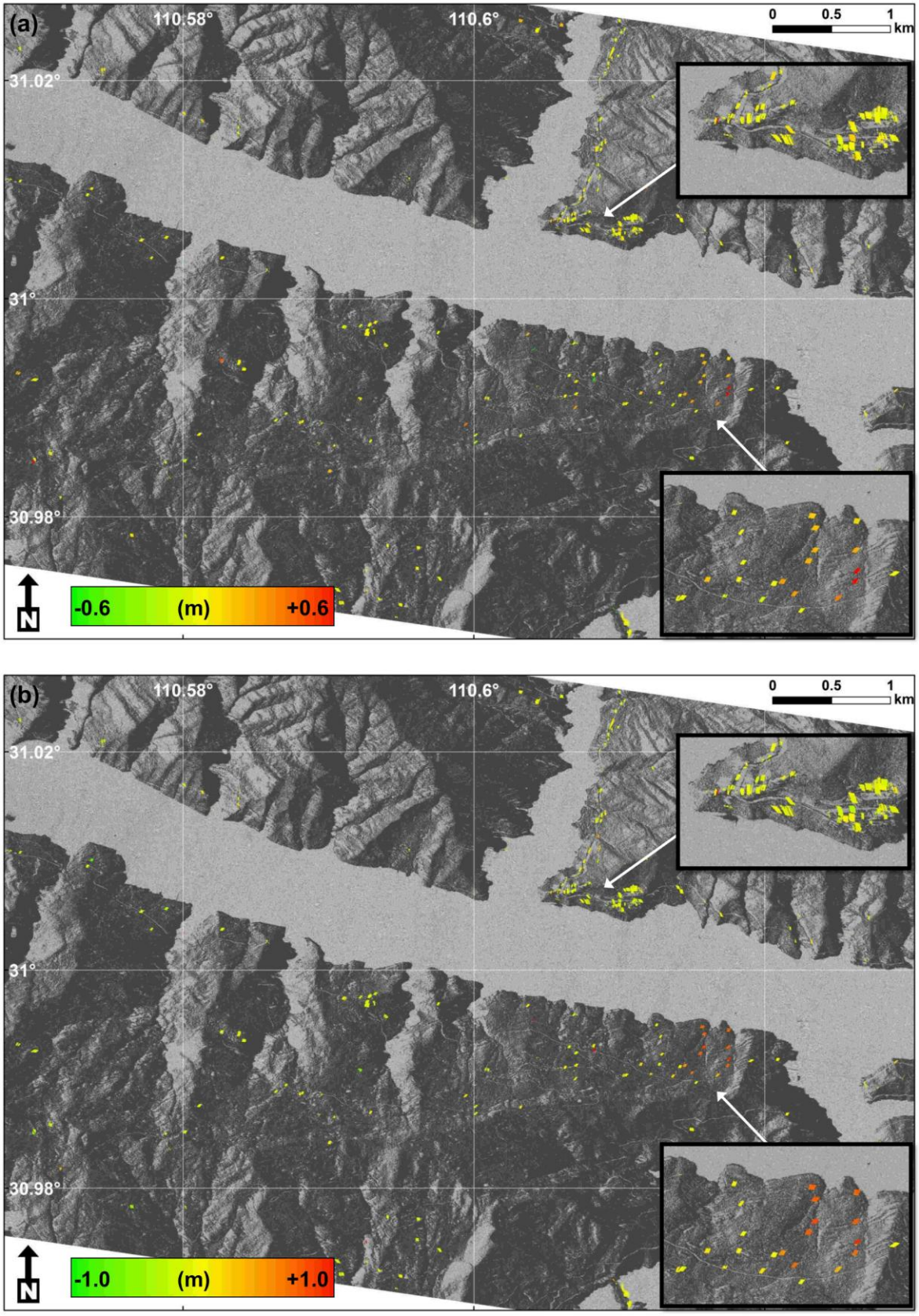

Figure 5-16: Regional offset maps for the TSX Spotlight scene from 21st Feb 2009 until 15th April 2010. (a) range and (b) azimuth directions. Positive range values correspond with movement away from the sensor and positive azimuth values correspond with predominantly northwards movement. Upper inset focuses on a new riverbank instability, lower inset focuses on the Shuping landslide.

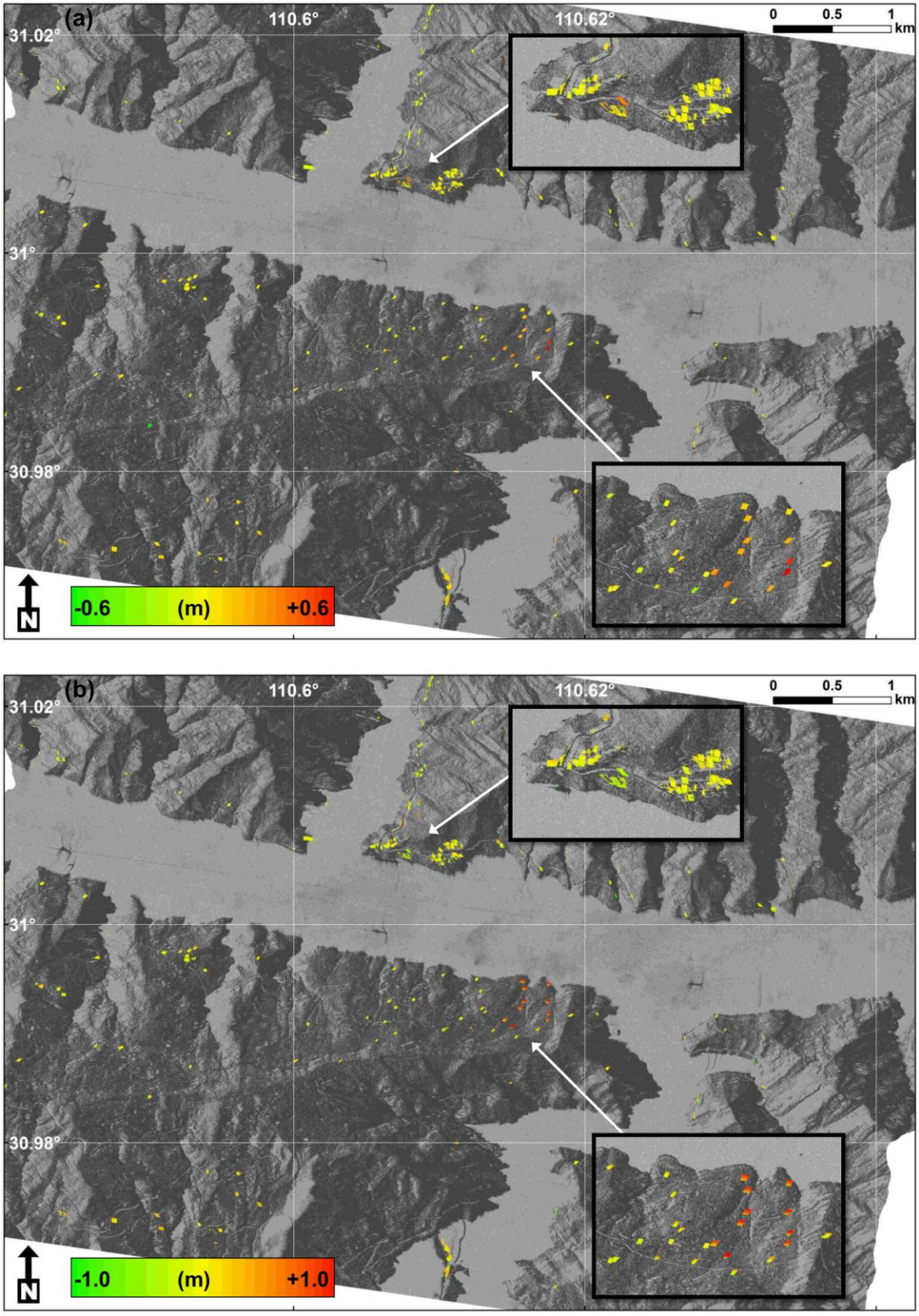

Figure 5-17: Regional offset maps for the TSX Spotlight scene from 15th April 2010 until 2nd Jan 2012. (a) range and (b) azimuth directions. Positive range values correspond with movement away from the sensor and positive azimuth values correspond with predominantly northwards movement. Upper inset focuses on a new riverbank instability, lower inset focuses on the Shuping landslide.

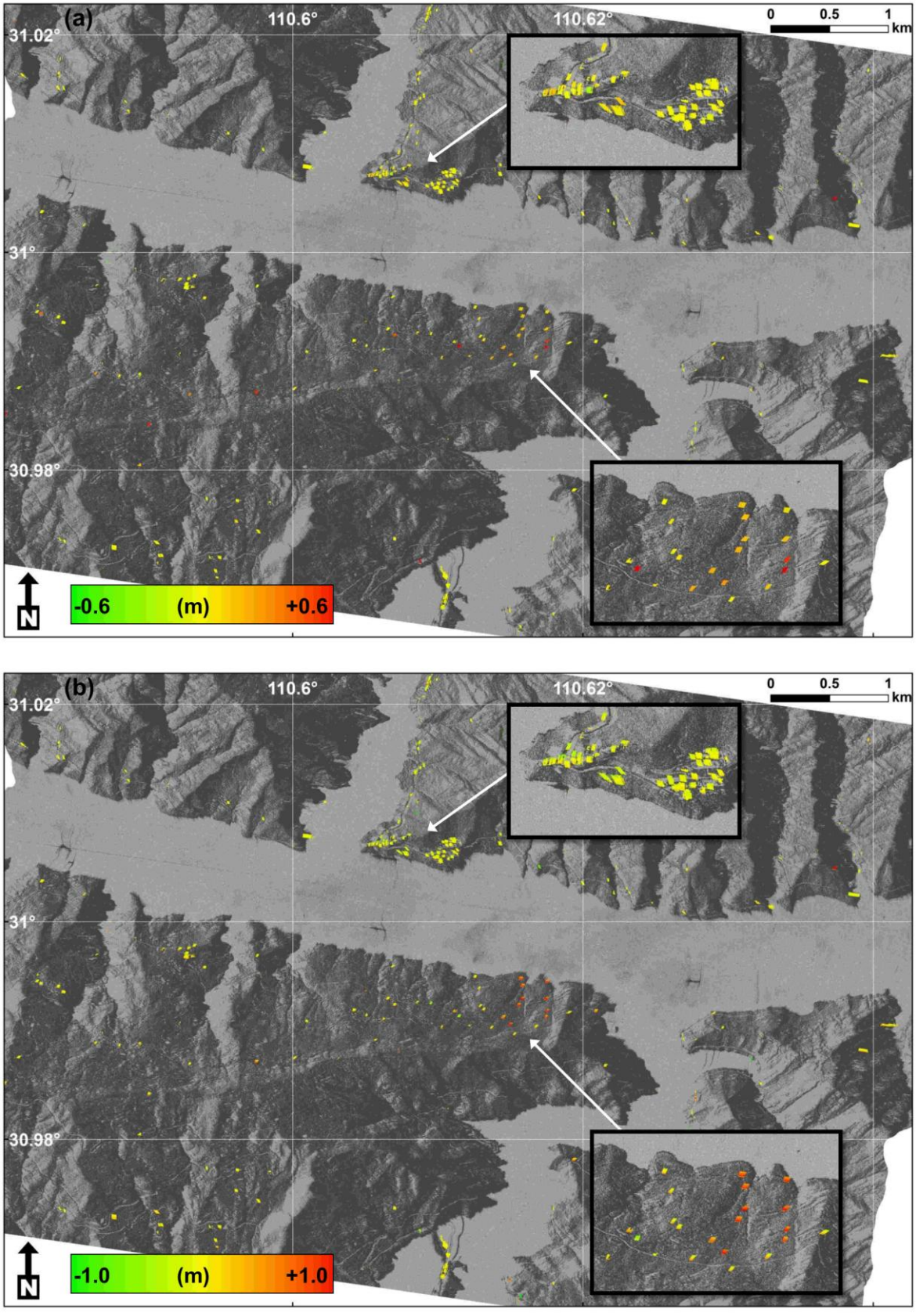

Figure 5-18: Regional offset maps for the TSX Spotlight scene from 2nd Jan 2012 until 23rd Feb 2013. (a) range and (b) azimuth directions. Positive range values correspond with movement away from the sensor and positive azimuth values correspond with predominantly northwards movement. Upper inset focuses on a new riverbank instability, lower inset focuses on the Shuping landslide.

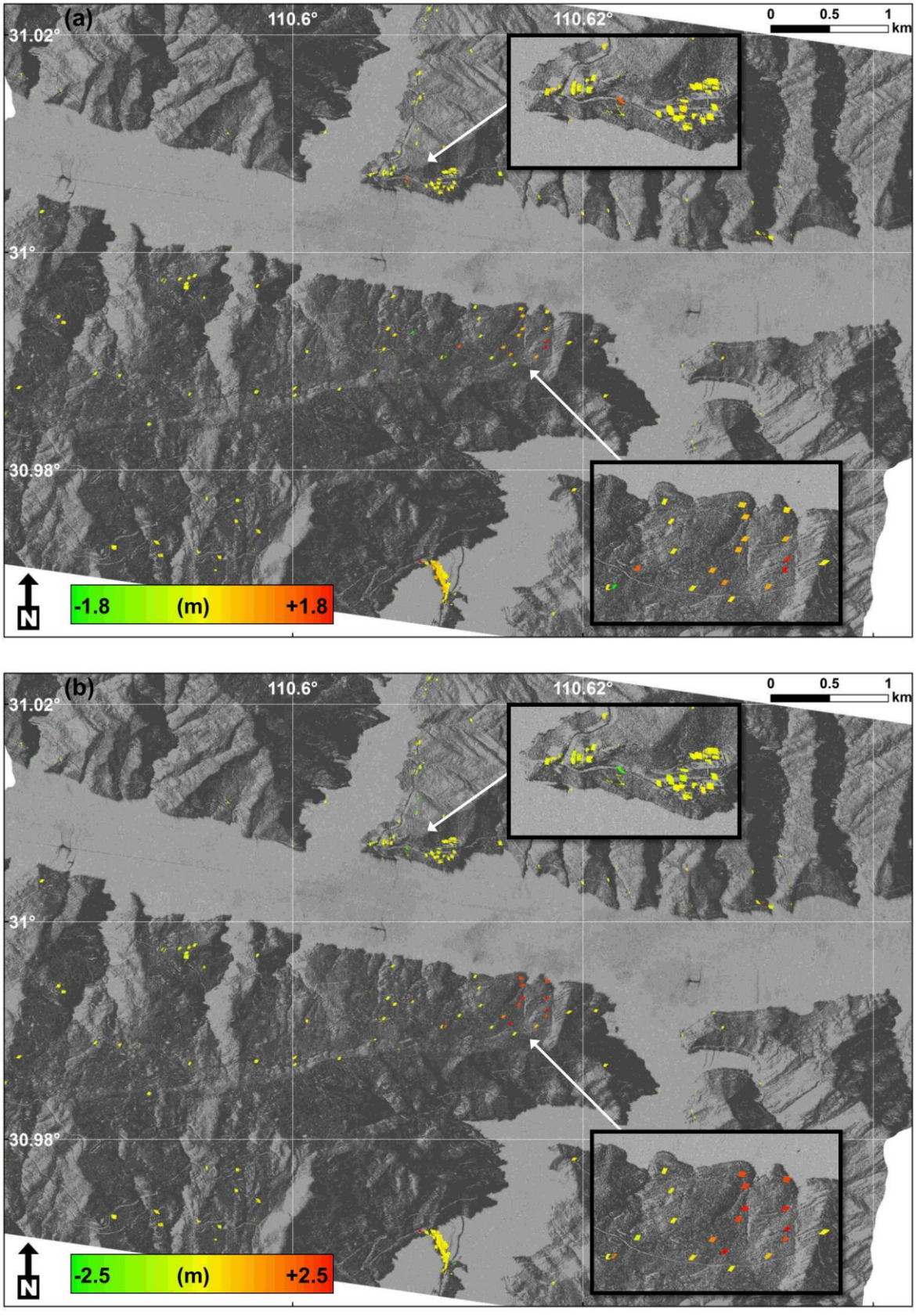

Figure 5-19: Regional offset maps for the TSX Spotlight scene from 21st Feb 2009 until 23rd Feb 2013. (a) range and (b) azimuth directions. Positive range values correspond with movement away from the sensor and positive azimuth values correspond with predominantly northwards movement. Upper inset focuses on a new riverbank instability, lower inset focuses on the Shuping landslide. Note the larger colour bar scale compared with Figure 5-16 – Figure 5-18.

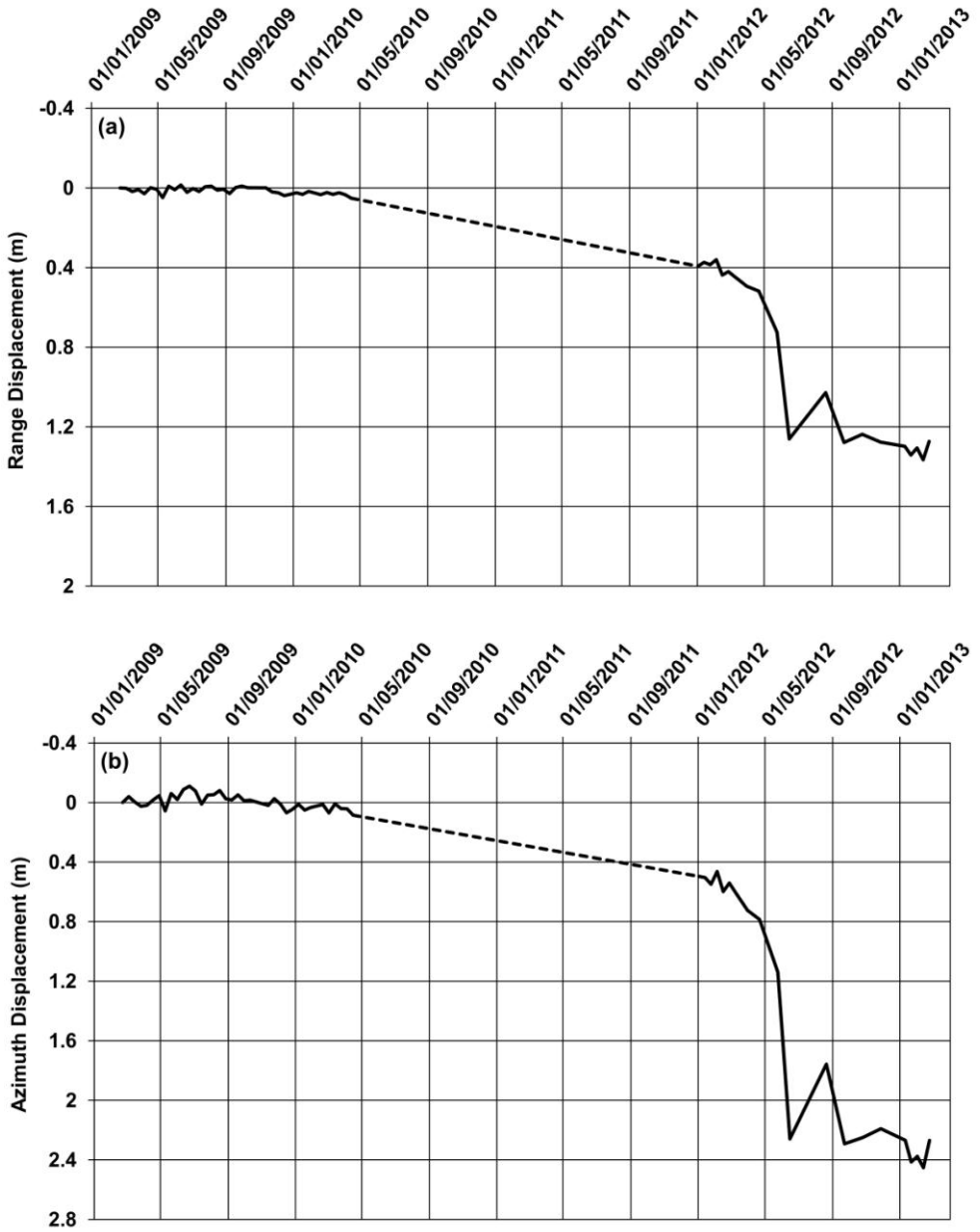

Figure 5-20: Offset displacements for the new riverbank instability identified in Figure 5-17 & Figure 5-19, from Feb 2009 – Feb 2013. (a) range and (b) azimuth offsets measured from TSX Spotlight data. The positive scale is away from the sensor in range dimension and in the along-track direction (i.e. predominantly southwards) in azimuth dimension.

This newly indentified slope instability has experienced significant man-made changes as management strategies were implemented. The large displacement shown in June 2012 (black line in Figure 5-20) is most likely to be a spurious offset between partially demolished buildings and newly constructed slope reinforcements over the 4-year period of TSX Spotlight data. This demonstrates another advantage of dividing this time-period into three since the probability of correlating the same ground features increases.

Figure 5-21: Online photos of the new riverbank instability area in three different years, from Panoramio & Google Maps. The red box highlights the same building to aid comparisons between images. The slope cutting above the road appears to have been reinforced by concrete and a tall building towards the base of the slope has been reduced in height, but not totally demolished.

5.6 TerraSAR-X Stripmap Limitations

The same process of determining an acceptable cross-correlation threshold (see Section 5.4) was attempted for TSX Stripmap data (Figure 5-22). The patterns are quite different to the TSX Spotlight data, with mean differences and standard deviations between offset maps rising sharply below cross-correlation values of 0.92. This is caused by the greater pixel spacing and the relatively homogenous vegetation cover in the region. For this reason, generating regional offset maps from points beyond the corner reflectors is not viable. A far greater contrast in the ground terrain backscatter at similar scales to the window size parameter, much faster ground movements or consistent movements over a larger area would all increase the likelihood of obtaining reliable SPOT results from TSX Stripmap offsets of natural terrain. Such circumstances could include monitoring m/day glacier movements (e.g. Fallourd *et al.*, 2010), earthquake movements covering large areas (e.g. Fielding *et al.*, 2013) or more rapid landslide movements (Manconi *et al.*, 2014).

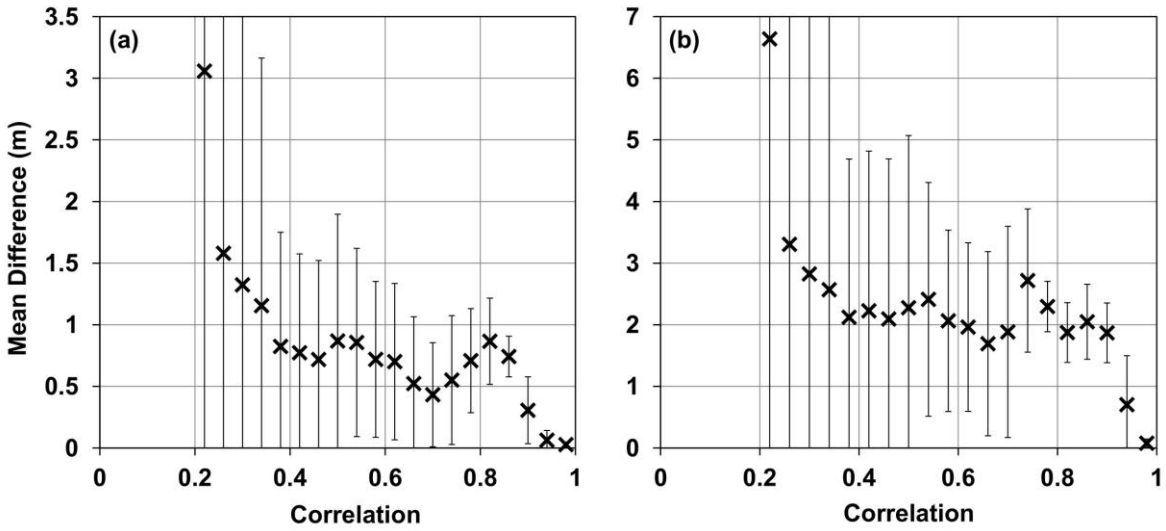

Figure 5-22: Mean difference between two independent TSX Stripmap offset maps overlapping in time, in relation to offset correlation values. (a) range and (b) azimuth directions. Error bars represent one standard deviation. The time interval was 110-days between the first and last suitable images. Below a correlation value of 0.92 (i.e. beyond the correlation values associated with corner reflectors), the mean difference and standard deviations exceed the magnitude of seasonal landslide movements.

5.7 ENVISAT Limitations

ENVISAT data failed to produce successful offset results due to its significantly larger pixel spacing covering the relatively small landslide area. Faster-moving phenomena or more contrasting terrains (as stated in Section 5.6) would make the use of ENVISAT data

more feasible. All previous studies mentioned in this chapter employing ENVISAT offsets have measured either larger magnitude displacements or displacements over much wider areas, relative to the Shuping landslide.

5.8 Summary

Chapter 5 evaluates the use of Sub-Pixel Offset Time-series (SPOT) techniques applied to three different SAR image modes for monitoring landslides in the Three Gorges region. A heuristic technique for selecting the optimal parameters, aimed at reducing spurious correlations and the duration of processing, resulted in a square moving window size of 32 pixels and an oversampling factor of 16 being applied to the data.

Compared to D-InSAR, SPOT techniques are capable of measuring two dimensions of displacement (in range and azimuth directions) and are more robust given their independence from phase values. Corner reflectors (CRs) installed on landslides are shown to be beneficial for SPOT techniques, due to the significant contrast of high amplitude values compared to the vegetation. The Shuping landslide is covered by both TSX data sets and verifiable displacement time-series measurements were generated from the TSX Spotlight and Stripmap image modes. Episodic and non-linear displacement trends match the magnitude and timing of extensometer measurements presented by Wang *et al.* (2013b). The concurrence of movements suggests the same triggering factor affects the whole landslide, although the displacements are spatially variable in elevation.

The use of corner reflectors in SPOT analysis generates precise results with RMSE values of 0.038 m and 0.071 m in range and azimuth directions, respectively for TSX Stripmap data. The difference between the displacement dimensions is attributed to the varying pixel spacing, also evident for the higher precision generated from TSX Spotlight data. Expanding the SPOT-CR analysis to other landslides in the study area shows the Xintan and Kaziwan landslides to be stable over the nine months of the TSX Stripmap data.

Finally, a minimum cross-correlation threshold with an acceptable level of precision is investigated in order to generate a regional coverage of measurements beyond the corner reflectors. The cross-correlation is set at 0.78 for the TSX Spotlight data and shows no significant dependence on perpendicular baselines or the time interval of the offset pair over periods of 1-2 years. Only a sparse network of measurements is generated, although a potentially unknown slope instability is discovered. The precision of TSX Stripmap and ENVISAT data is not high enough to measure landslides without CRs.

Chapter 6 : Investigating the Shuping Landslide

A well-developed early warning system for landslides should include various elements such as understanding the local knowledge of risks, communicating timely and reliable warnings, and building local capacity to respond to warnings (UN-ISDR, 2004). However, one other important technical component involves monitoring the hazard(s) which requires the (i) detection; (ii) rapid mapping; (iii) characterisation; and, (iv) long-term monitoring of landslides (Tofani *et al.*, 2010).

Frequently acquired SAR imagery has been identified as a useful tool for investigating landslides and also as part of a warning system. Chapters 3, 4 and 5 comprehensively evaluated D-InSAR and SPOT techniques, illustrating SPOT techniques applied to point-like targets can extract numerous measurements of displacement across a landslide body. These measurements can not only identify and map the actively deforming slopes (significantly reducing uncertainty in landslide inventory maps (e.g. Cascini *et al.*, 2010)), but can also help to characterise the landslide mechanism (Berardino *et al.*, 2003; Tofani *et al.*, 2013). Deduction of the failure surface geometry and triggering mechanisms is possible by combining information on the landslide topography, boundaries and displacement (Carter and Bentley, 1985; Tofani *et al.*, 2010).

Further interpretations of landslide processes can then be inferred by comparing a time-series of displacement with potential triggering factors such as rainfall, seismicity and site-specific factors such as fluctuating reservoir water levels (e.g. Tolomei *et al.*, 2013). Whilst these methods will not replace the value of in-situ investigations, landslide characterisation from remote sensing imagery can help target field analyses using geophysical profiles or boreholes within the landslide body (Casson *et al.*, 2005).

Further investigation of slow-moving, reactivated landslides is also necessary. For these cases, the hydrology is often very complex and display erratic and complex displacements due to the presence of small-scale anisotropy and large-scale heterogeneity in their permeability (van Asch *et al.*, 2007; 2009). Repetitive patterns of faster and slower displacement, separated by periods of rest are very common to slow, reactivated landslides

and can help to determine dominant mechanisms such as basal sliding, plastic deformation or (recoverable) seasonal shrinkage/swelling of sediments (Massey *et al.*, 2013).

To answer the third and fourth research questions (page 10), this chapter investigates the triggering factors and geotechnical controls of the Shuping landslide. The Shuping landslide is by far the most active within the study area and further investigation is required to determine why this landslide continues to be active, particularly since a resident population still lives inside the landslide boundary.

The long time-series of displacement obtained from SPOT-CR techniques allows useful comparisons with potential triggering mechanisms including reservoir water level change, rainfall or regional seismicity. Since SPOT-CR techniques can measure 2-dimensions of movement (in range and azimuth directions), it is possible to estimate the purely vertical and horizontal movements of the Shuping landslide and subsequently characterise the most likely failure surface. Finally, with the use of published geotechnical parameters from nearby landslides, a 2D limit equilibrium method is applied to establish the most likely failure depth and the model's sensitivity to principal controlling factors (e.g. water table position and cohesion, internal friction angle or unit weight of the subsurface materials). An understanding of these factors would help determine suitable remedial measures and help target future in-situ geotechnical analysis.

6.1 Landslide Triggering Factors

Processes leading to landslides can be separated into causes and triggers, with landslides being caused by morphological, geological and historical factors that set the stage for a landslide to occur (Lu and Godt, 2013). Landslide triggers are the events that initiate landslide motion and shift the slope from being marginally stable to actively unstable. The trigger and cause can be classified by the timescale of the associated processes, although often it is difficult to identify the precise trigger for a given landslide (Evans *et al.*, 2007). In other cases, the trigger can be easily identified by a correlation between the displacement and potential triggering factors, particularly for slopes already in a marginally stable state (Glade and Crozier, 2005).

The Shuping landslide has been divided into two parts: eastern and western blocks with a combined width of about 600 m (Wang *et al.*, 2008a). Whilst the rates of displacement are different over the whole landslide body, the timing of faster and slower episodes (Figure 5-8) is very consistent for all measurement points, suggesting the same causal factors are

affecting the whole landslide body. The variation in displacement rates is more likely to be caused by the relationship between the geometry of the landslide's failure surface relative to the sensor Line-of Sight (LOS) direction, rather than a variation in causal factors.

A wide range of geological, meteorological and hydrological factors can trigger landslides such as volcanic eruptions, earthquakes and heavy precipitation. In addition human activities such as slope excavation, reservoir operations and irrigation may also initiate landsliding. The slope is predisposed to landsliding given the ancient origin of the Shuping landslide (Wang *et al.*, 2008a), matched with evidence in the field (Figure 6-1). This makes the landslide very susceptible to smaller perturbations from landslide triggers compared to first time failures (Lee and Jones, 2004). In this section, the potential triggering factors assessed include changes in the Three Gorges reservoir water level, rainfall and regional seismicity within a 50 km radius of the landslide – far above the expected area affected by earthquakes of magnitude five (Keefer, 2002).

Figure 6-1: Large boulders found amongst a finer matrix of softer sediments within the boundary of the Shuping landslide. Indicative of an ancient landslide deposit.

6.1.1 Reservoir Drawdown

Riverbanks connected to rivers and reservoirs often experience instability as a result of fluctuations in water levels adjacent to the slope (Fujita, 1977; Jia *et al.*, 2009). When landslide deformation is slow, understanding how changing groundwater level influences slope behaviour is important for its management (Kalenchuk *et al.*, 2013) and many

examples exist where groundwater is a common controlling factor in the deformation of large active landslides, e.g. Aknes (Nordvik and Nyrnes, 2009); Beauregard (Barla *et al.*, 2010); Huangtupo (Tomás *et al.*, 2014); La Clapière (Cappa *et al.*, 2004); Ruinon (Crosta and Agliardi, 2003); and, Vajont (Hendron and Patton, 1987; Semenza and Ghirotti, 2000).

The Three Gorges reservoir was created in three stages. The first stage raised the water level from 68 – 135 m between 1st – 15th June 2003. In September 2006 the water level reached 156 m and following completion of the Three Gorges dam, the reservoir reached its final height of 175 m in October 2010 (Luo *et al.*, 2009; Jiang *et al.*, 2011a). At the dam, the fully-functional Three Gorges reservoir annually fluctuates from 145 m in the summer (May – October) up to 175 m in the winter (November – April) for downstream flood control and power generation, respectively (Zhang and Lou, 2011). The catastrophic failure of the nearby Qianjiangping landslide is attributed to the first stage impoundment in 2003 (Wang *et al.*, 2004; 2008b) as is the slow reactivation of the Shuping landslide (Wang *et al.*, 2013b).

The period of most rapid landslide displacement around May-June each year corresponds with the annual lowering of the Three Gorges reservoir (Figure 6-2). The faster the rate of change in the reservoir level, the longer the groundwater levels take to adjust. When water levels are lowered, drainage of the landslide lags the reservoir drop which results in high downslope hydraulic gradients and favours slope instability (Wang *et al.*, 2008d). Displacement appears proportional to the rate of reservoir lowering, as the initial reservoir lowering from January to May each year results in small landslide displacements, whereas the fastest drop in the months of May and June corresponds with the fastest landslide movement. This matches the conclusions of Wang *et al.* (2013a). It should also be noted that increases in the reservoir water level are not shown to encourage slope instability.

These patterns match the results of Xia *et al.* (2013) who found a similar relationship of the nearby Shiliushubao landslide to fluctuations in the Three Gorges reservoir. Assuming a high cohesiveness and low permeability coefficient for both landslides, a decline in groundwater level will lag behind a sudden drop in the reservoir water level. This favours slope instability by maintaining high pore pressures and generating high seepage forces away from the landslide body. If the reservoir water level was stabilised for a significant period of time, pore water pressures and seepage forces would reach a stable state conducive to landslide stability.

Following the same logic, rising reservoir water levels have the effect of generating high seepage forces towards the landslide body and provide a force resisting slope movements which is beneficial for landslide stability. However, eventual saturation from the lagged rise of the water table would saturate the sliding mass, decreasing the effective strength and increasing the likelihood of slope movement relative to a lower static reservoir water level (Xia *et al.*, 2013).

As mentioned in Section 5.2.2, displacements in the years 2010 and 2011 (0.66 m in total) were not at the same magnitude as in 2009 and 2012 (i.e. 0.60 – 0.65 m each year). Qualitatively, this may be related to shorter periods of the most rapid reservoir lowering. By the month of May in 2010 and 2011, the water level had already been gradually lowered to ~157 and 155 m, respectively before a more rapid drop down to 145 m. This contrasts the years 2009 and 2012 where the range in reservoir water level change was more than 15 m over the months of May – June.

From studies of the Shuping landslide using extensometers up to February 2010, the displacement rate is shown to be highly related to the patterns of water level fall and this rate of reservoir lowering is postulated as a predictor of landslide movement (Wang *et al.*, 2008a; 2013a; 2013b). Given the temporal resolution at which the water level data are plotted, this thesis finds landslide movement most significant when the reservoir is persistently lowered at the rate of 0.5 – 0.8 m per day. A more gradual lowering of the reservoir water level would likely reduce the magnitude of Shuping landslide displacement, such as the case of the Canelles landslide (Pinyol *et al.*, 2012).

Finally, comparing the water level change with the landslide displacement (Figure 6-3), the fastest rate of reservoir lowering consistently occurs in August. However, this very large and rapid fall is always preceded by an equivalently large increase in water level as downstream areas are most likely protected from flooding during the rainy season. The time lag of landslide movements and groundwater variation in response to reservoir change must exceed 10 days given no increase in landslide displacement is observed over the same time period.

Both the managed and natural changes in reservoir water level are related to the seasonal variations in rainfall, so an analysis of landslide movement in relation to both factors is required to fully understand the mechanisms of movement for the Shuping landslide.

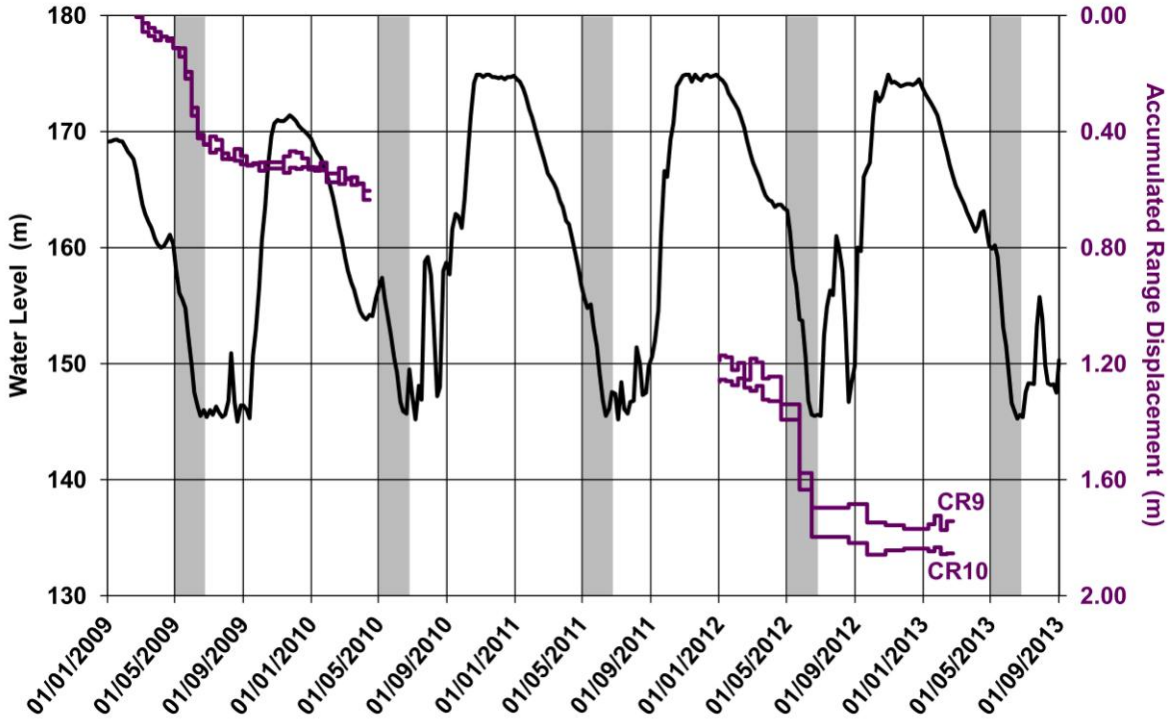

Figure 6-2: Range displacement of the fastest moving corner reflectors (CRs 9 & 10), in relation to water level changes of the Three Gorges reservoir. The largest, episodic landslide movements occur in May-June each year (grey columns), which correspond to the fastest lowering of the Three Gorges reservoir. Location of CRs found in Figure 5-5b and daily water level data are available from the China Three Gorges Project Corporation website (www.ctgpc.com.cn).

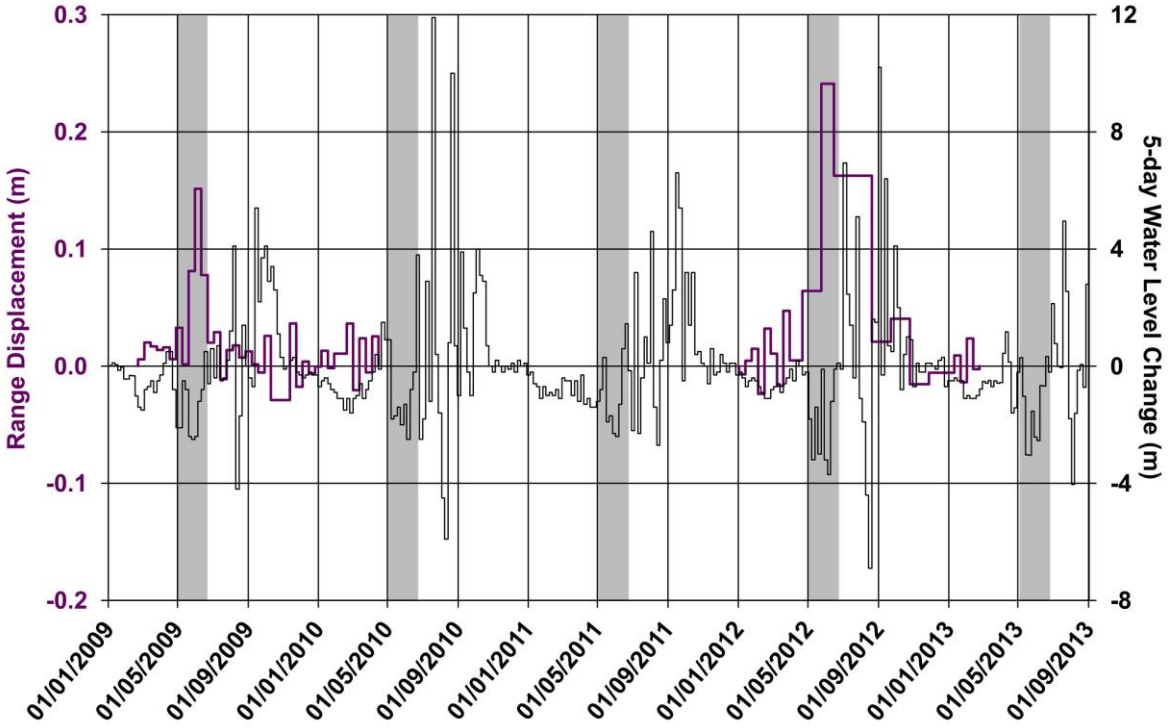

Figure 6-3: Range displacement of the fastest moving corner reflector (CR 10) in relation to the 5-day water level change. There are 5-day periods with very significant reservoir lowering, but these are always preceded by a significant reservoir rise. The largest, episodic landslide movements correspond to significant and persistent lowering of the reservoir (also see Figure 6-2).

6.1.2 Rainfall

Precipitation is known as one of the major landslide triggers and the temporal occurrence of landslides can be controlled by rainfall patterns and duration (van Asch *et al.*, 1999). The most direct relationship between rainfall and landsliding often refers to highly mobile debris flows and shallow landslides, where researchers look for a threshold in rainfall duration, intensity, or other property as a landslide predictor (e.g. van Asch *et al.*, 1999; Guzzetti *et al.*, 2007). In the Three Gorges region where annual rainfall can exceed 1000 mm, 80% of shallow landslides occur between April and August (He *et al.*, 2008; 2010). However other landslides respond slowly to rainfall and move at imperceptible speeds (e.g. Iverson, 2000; Herrera *et al.*, 2011; Tomás *et al.*, 2014). Figure 6-4 shows the same landslide displacement data as Figure 6-3, in relation to the accumulated rainfall over a 10-day period from January 2009 until June 2011, as measured from a meteorological station less than 25 km away.

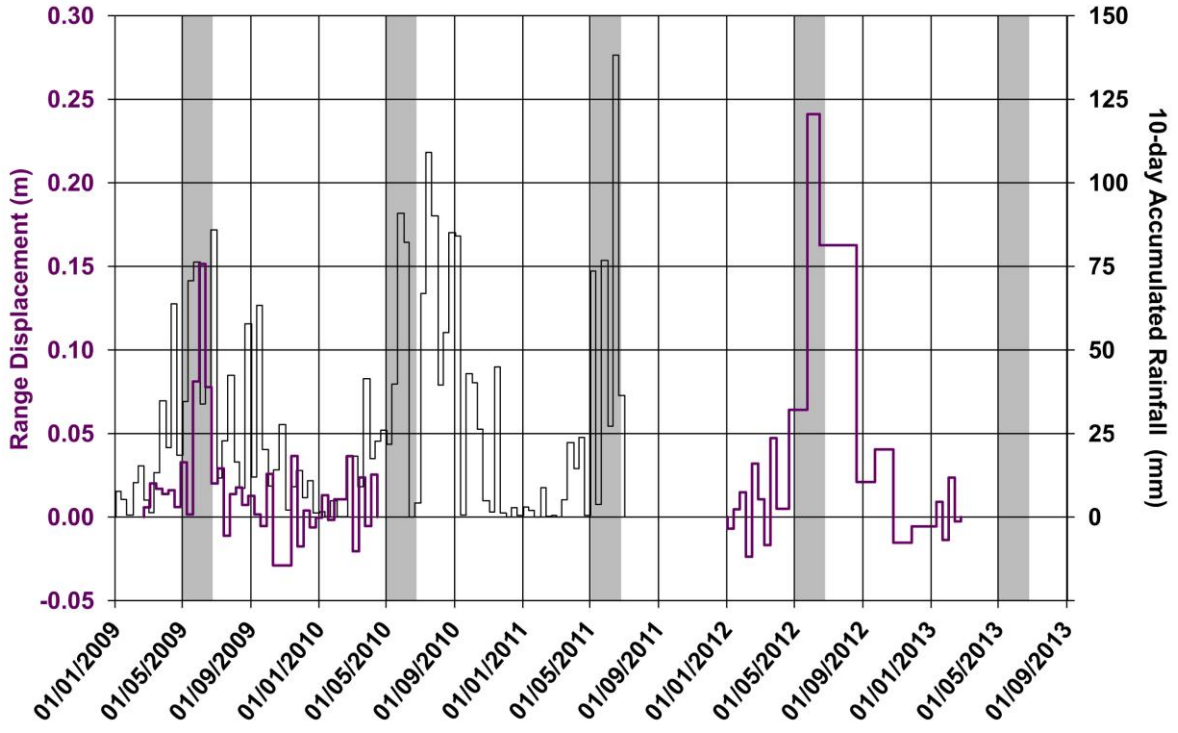

Figure 6-4: Range displacement of the fastest moving corner reflector (CR 10) in relation to 10-day accumulated rainfall. Significant rainfall is observed during the months of May-June when the landslide movement is greatest. However, equivalent rainfall quantities during other months do not have the same effect on landslide movement, indicating that rainfall is at most a secondary triggering factor behind reservoir drawdown. Rainfall data come from the Meteorological Station at Badong, less than 25 km away from the Shuping landslide.

During the months where landslide movement is greatest, significant rainfall is also observed (Figure 6-4), making it difficult to fully separate the effects of reservoir water level fluctuations from precipitation. However, other periods of equally heavy rainfall outside the months of May-June are also evident which do not appear to increase the rate of landslide displacement. Given the very direct link between landslide movement and reservoir drawdown shown in the previous section, it is believed rainfall plays a far lesser role in triggering the Shuping landslide. This could be due to the depth of the sliding surface – between 45–75 m (Wang *et al.*, 2008a) – being unaffected by the infiltration of precipitation as well as large surface gullies which help drain the landslide surface and prohibit the pooling of water. Note the rainfall record beyond June 2011 was not available to compare with the 2012 – 2013 monitoring data.

6.1.3 Seismicity

A final consideration investigates whether regional seismic events could trigger the episodic landslide movements. Earthquakes have caused widespread landsliding due to the addition of gravitational and seismic accelerations which cause short lived stresses in excess of the cohesive and frictional strength of landslides (Densmore and Hovius, 2000; Meunier *et al.*, 2007). The creation of the Three Gorges reservoir has also been hypothesised to induce seismicity (Xu *et al.*, 2013). Whilst seismic activity has increased since 2003, 96% of these events were less than magnitude M_L 2.0 and the seismic condition remains weak given no major faults exist in the reservoir area (Xu *et al.*, 2013).

Figure 6-5 shows the greatest landslide displacement curve plotted against all detectable earthquake events within a 50 km radius of the Shuping landslide (obtained from the China Seismic Network (CSN): www.csndmc.ac.cn/newweb/data/csn_catalog_p001.jsp). The frequency of earthquakes appears relatively constant over time, and they are all low magnitude events with only one exceeding M_L 3.5. The epicentres of all events within the highlighted months of May-June are also more than 25 km away from the landslide, indicating that any influence from ground accelerations are likely to be very small.

The distance and the low magnitude of earthquakes within the months of May-June suggest this is an unlikely landslide triggering factor. Earthquakes of the same magnitude and frequency also occur outside the period of greatest landslide displacement which again suggests the dominant control upon the landslide is reservoir drawdown.

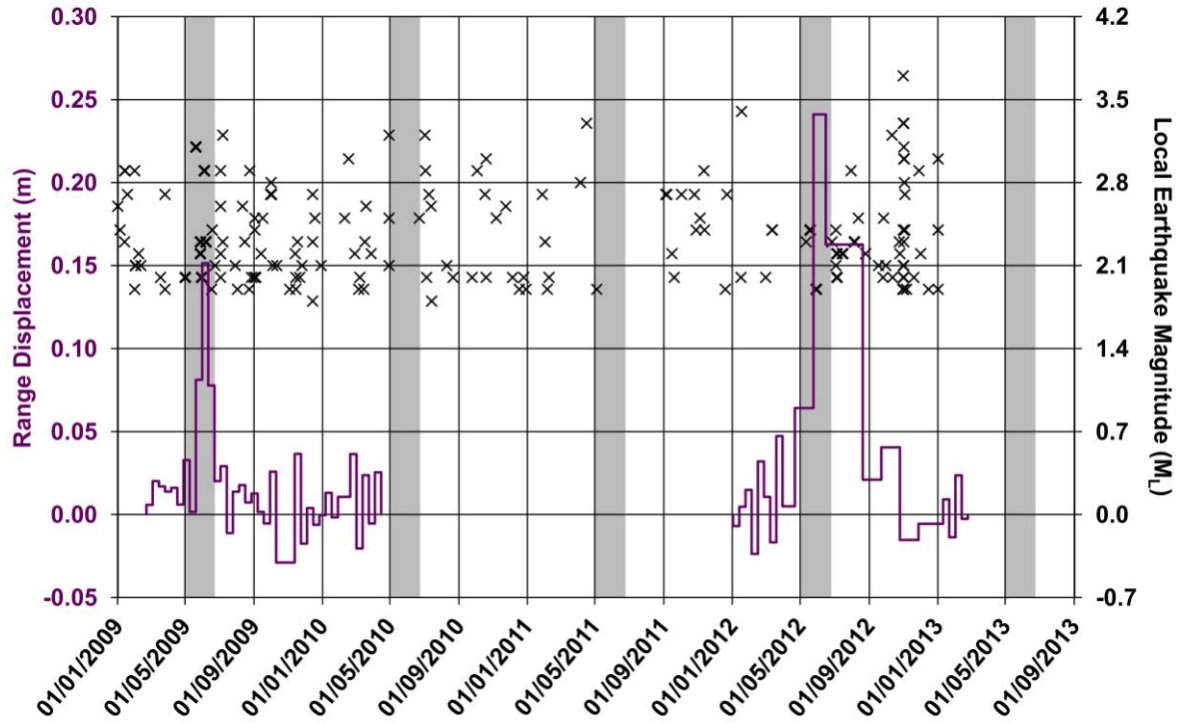

Figure 6-5: Range displacement of the fastest moving corner reflector (CR 10) in relation to seismicity within a 50 km radius of the Shuping landslide. No large event or cluster of events appears to trigger the landslide movement in May-June. All seismic events in the months of May-June are small (<3.5 M_L) and occurred more than 25 km away from the Shuping landslide. Seismic data are available from the China Seismic Network Centre website (www.csndmc.ac.cn).

6.2 Landslide Failure Mechanism

The subsurface geometry of a landslip is defined by the shape, orientation and depth of a slip surface and these are essential for stability analysis or the design of remedial works (Carter and Bentley, 1985). Without the use of costly site investigation employing pits and boreholes, it is intuitive to estimate the slip surface geometry at depth from movements obtained from the landslide surface. This requires the use of cumulative displacements to categorise the style of movement displayed by a landslide (Petley *et al.*, 2005) and enables the landslide typology to be classified (e.g. Tofani *et al.*, 2013).

Two major types of slow-moving landslides are categorised by the geometry of the slip surface (Varnes, 1978): rotational landslides with curved slip surfaces and translational landslides with planar (or near planar) slip surfaces. Assuming the landslide behaves as a rigid block along each cross-profile, internal deformation is negligible, and a single failure surface exists, the distribution of directional displacement vectors and any topographic variation is a function of the slip surface geometry (Casson *et al.*, 2005). This method also requires multiple surveying points to be available across the landslide body over a period

of time sufficiently long to accumulate movements larger than the errors inherent in the surveying procedures (Carter and Bentley, 1985). The Shuping landslide has a good distribution of corner reflectors from which the precise SPOT-CR analysis was used to measure relatively large movements (Figure 5-5).

Surface displacements are most easily interpreted in vertical and horizontal orientations, although D-InSAR results only provide sensitivity in the sensor's LOS direction. To obtain vertical and horizontal movements, D-InSAR measurements have been combined from different SAR viewing angles (e.g. Wright *et al.*, 2004) or employing the multi-aperture D-InSAR approach (e.g. Bechor and Zebker, 2006; Hu *et al.*, 2012a).

A useful capability of sub-pixel offset measurements allows the displacement vectors from the range and azimuth directions to help estimate the purely northward (d_N) and vertical (d_U) components of displacement. The measured LOS displacement represents a projection of the 3D displacements (d_E, d_N & d_U) onto the satellite look vector (see Equation 4-5). The azimuth offsets are a projection of a horizontal displacement component onto the satellite heading vector (Equation 6-1):

$$d_{AZIMUTH} = d_N \cos(\alpha) + d_E \sin(\alpha)$$

Equation 6-1: Decomposition of the azimuth offsets ($d_{AZIMUTH}$) into its horizontal components (d_N & d_E) (Fialko *et al.*, 2001). α represents the azimuth of the satellite heading vector.

Assuming landslide movement in the east-west direction (d_E) is zero (a relatively safe assumption given the orientation of the Shuping landslide with respect to the TSX Spotlight sensor), the following system of equations (Equation 6-2) can be solved to estimate the accumulated vertical and horizontal components of displacement for every corner reflector around the Shuping landslide:

$$d_{RANGE} = [-0.68\ 0.12\ -0.72]\ [d_E\ d_N\ d_U]^T$$

$$d_{AZIMUTH} = [-0.17\ 0.98\ 0]\ [d_E\ d_N\ d_U]^T$$

$$d_E = 0$$

Equation 6-2: System of equations used to estimate the vertical and horizontal landslide displacement from the accumulated range and azimuth offset results.

The results shown in Figure 6-6 have been divided into three different time periods to potentially observe any temporal change in the vertical and horizontal movements. These intervals correspond to the two sets of TSX Spotlight data and the data gap in between.

6.2.1 Vertical Movement (d_U)

The estimated vertical measurements (Figure 6-6a) show the total accumulated displacement increasing with elevation and distance from the Yangtze River. The topographic trend is very consistent for each of the three time periods with the head of the landslide moving downwards at least 25 times more than the toe of the landslide. This suggests the mechanism and principal triggering factor does not change over time.

6.2.2 Horizontal Movement (d_N)

In contrast to the vertical movements, the northward displacement results (Figure 6-6b) do not show the same topographic trend as the vertical dimension, instead displaying the greatest movements towards the middle of the landslide. The patterns are also quite consistent over time, although the velocity of corner reflector 17 (at the head of the western block) increases, compared with the first period, possibly due to gravitational failure on steep local slopes such as slope undercutting or headward erosion.

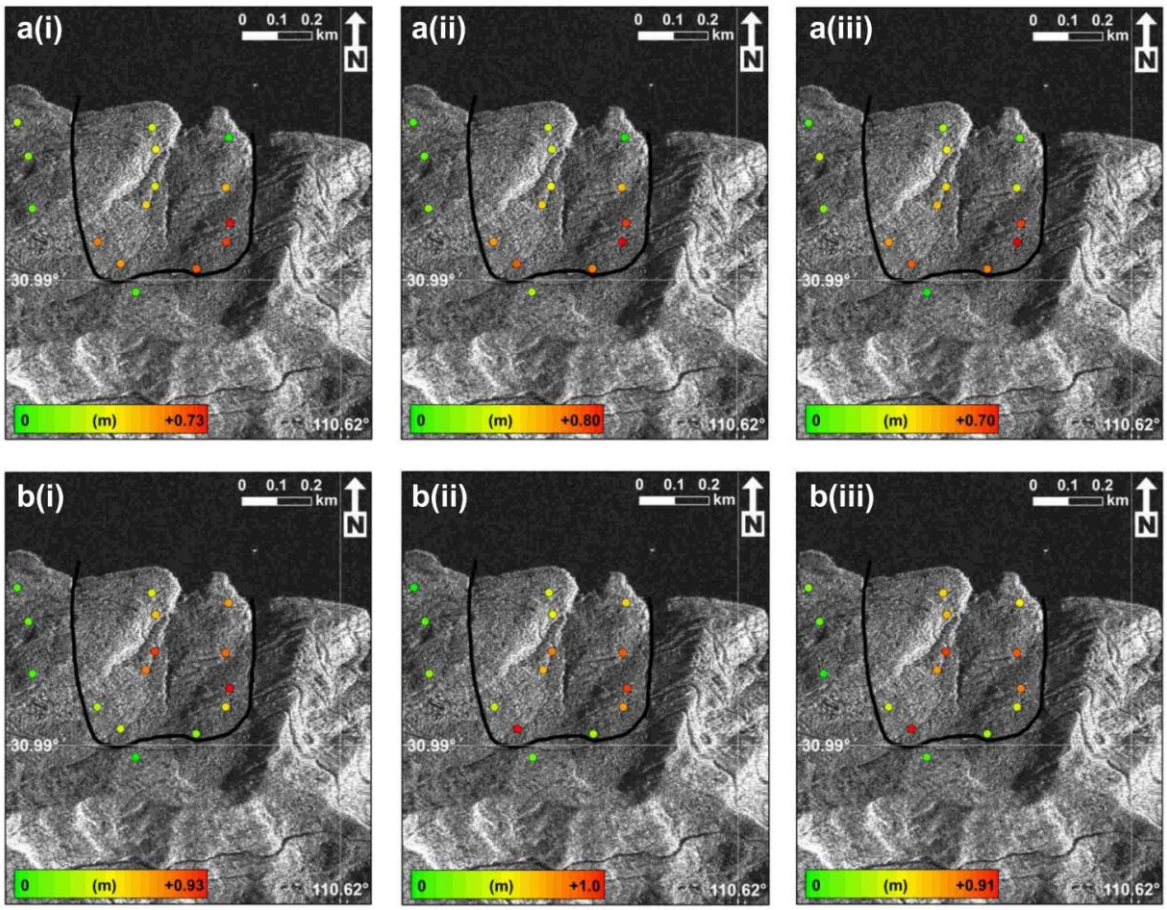

Figure 6-6: Accumulated displacement in (a) vertical direction and (b) horizontal direction, for three different time periods. (i) 21st Feb 2009 – 15th April 2010 (ii) 15th April 2010 – 2nd Jan 2012 (iii) 2nd Jan 2012 – 23rd Feb 2013. Positive values indicate downward and northward motion. Exact values can be found in Appendix A – Supplementary Tables & Figures.

6.2.3 Rotational Failure

The above surface data presented in Figure 6-6 can be used to qualitatively analyse the slip surface geometry of the Shuping landslide. Under the assumptions listed in Section 6.2, a uniform translational landslide would exhibit similar displacement vectors along a profile of the landslide from top to bottom whereas a rotational landslide would exhibit decreasing vertical displacements (Dikau *et al.*, 1996; Tofani *et al.*, 2013).

A rotational failure mechanism along a curved plane would be consistent with these 2-dimensional movements and is proposed as a first-order interpretation of the data. The head of the landslide shows the highest rates of vertically-downward movement for each time period whereas the middle section has the highest rates of horizontal movement, matching the displacements expected from a rotational slide (Figure 6-7). The designation of two adjacent blocks is also supported by these data as displacement rates at similar altitudes are not equal. However, the synchronicity of accelerated periods for all measurement points is evidence for a single, deep failure plane. Boreholes and inclinometers should be installed to more accurately determine the failure surface depth.

For significant degrees of rotation, landslides can be classified into zones of depletion, transfer and accumulation (Casson *et al.*, 2005). A zone of depletion and transfer could be delineated using these point data, however it is difficult to identify the toe of the landslide due its connectivity with the Yangtze River. It is suggested the toe of the landslide is close to the river bank given the very low vertical displacement rates at the lowest points, although geomorphological mapping from aerial images predating the reservoir impoundment would be required to accurately identify the lower landslide boundary.

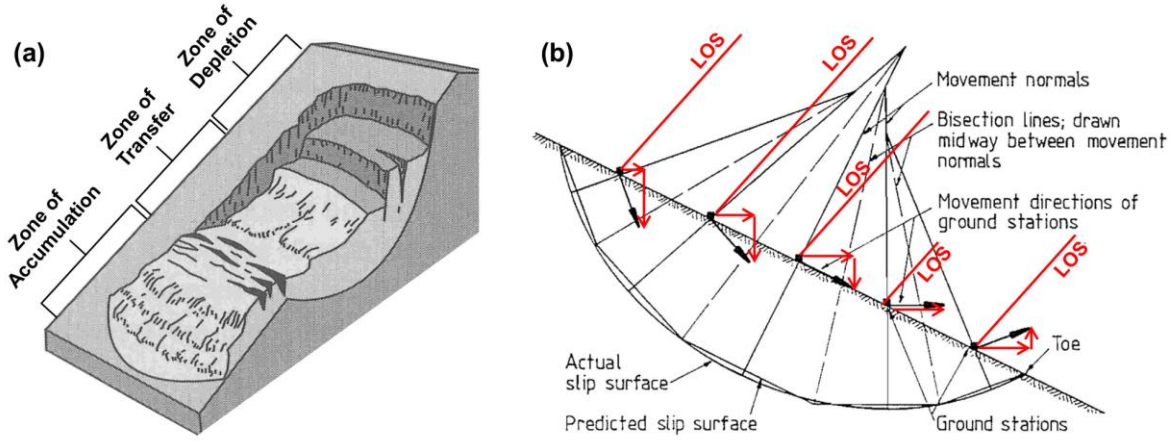

Figure 6-7(a): Schematic diagram of a rotational failure mechanism, as inferred from the results in Figure 6-6 (Lu and Godt, 2013 p. 8).
Figure 6-7(b): Construction of slip surface using ground station movements, relative to the SAR sensor Line-of-Sight (LOS) direction (adapted from Carter and Bentley, 1985 p. 235).

6.3 2D Limit Equilibrium Slope Stability Analysis

Quantitatively assessing the stability of the Shuping landslide can now proceed following the identification of the landslide failure plane geometry and the most likely triggering factor. Slope stability analysis commonly employs a limiting equilibrium approach for a two-dimensional model since extensive computing and concerns about laboratory soil tests have limited the use of finite element approaches to only a few cases (Abramson, 2002).

This section employs a classical non-linear method of slices to assess the stability of the Shuping landslide under different water level scenarios and the application of more complex methods such as Finite Element Methods (FEM) are not pursued given an almost complete lack of subsurface data at this location. An approach such as FEM would subsequently generate high levels of uncertainty and potentially not represent the real-world situation adequately. All slope stability calculations in this section used the Rocscience 2D limit equilibrium slope stability software 'Slide' (www.rocscience.com/products/8/Slide) which considers a plane strain situation.

Many soil mechanics and engineering geology textbooks introduce the concepts used in limit equilibrium methods of stability analysis (e.g. Anderson and Richards, 1987; Abramson, 2002; Aysen, 2002; Smith, 2006; Cheng and Lau, 2008; Lu and Godt, 2013), although a brief explanation adapted from these sources is provided here for completeness. A source of detailed information may also be found in the thesis of Aryal (2006).

The concept of limit equilibrium defines the limiting state when the shear stress in a slope is in a critical stable mechanical equilibrium with the shear strength of the slope material. Shear stress develops in a slope due to gravity and topographic relief and the ability of hillslope materials to resist this shear stress along the potential failure plane can be quantified using the shear strength of the materials (Lu and Godt, 2013). Therefore, stability of hillslopes can be assessed using the ratio of shear strength of the soil (τ_f) to shear stress developed for mechanical equilibrium (τ_d), termed the factor of safety, F_S (Equation 6-3). A F_S greater than one indicates the slope is stable, whereas the slope will fail if the value is less than one. Most modern building codes require both manufactured and natural slopes to have a long-term F_S greater than 1.5, which provides a margin of error in the measurements and overall calculations (Pipkin *et al.*, 2010).

$$F_S = \frac{\tau_f}{\tau_s}$$

Equation 6-3: Factor of safety (F_S) showing the ratio of available shear strength (τ_f) to shear stress (τ_s) required for stability.

The shear strength behaviour of hillslope materials (τ_f) under saturated conditions can be approximated using the Mohr-Coulomb failure criterion and the effective stress principal (Equation 6-4):

$$\tau_f = c' + \sigma' \tan \varphi'$$

Equation 6-4: Mohr-Coulomb failure criterion for effective stress analyses.

where the effective normal stress (σ', in N/m^2 = Pa) equals (Equation 6-5):

$$\sigma' = \sigma^T - u$$

Equation 6-5: Effective normal stress (σ') acting on any plane. σ^T represents total normal stress and u represents pore pressure.

Therefore the Mohr-Coulomb criterion (Equation 6-4) leads to a material's shear strength that is described by two components; effective cohesion (c') and the effective friction angle (φ'). However, effective strength may also include apparent cohesion due to plant roots which is not considered in this analysis. The effective stress between soil particles can be reduced by the pressure of water, particularly in fine-grained soils where a low permeability might cause the drainage/water movement to be lower than the rate at which total stress is changed. This can lead to the development of increased (i.e. excess, non-hydrostatic) pore water pressures. Effective stress analysis is more suitable for long-term natural scenarios as no additional loading is placed on the slope and undrained conditions need to be considered (Anderson and Richards, 1987).

Lu & Godt (2013) explain non-linear methods of slope stability assessment divide slopes into a number of (usually equal-width) slices separated by vertical boundaries. The geometry of slopes is predetermined, while the location of potential failure surfaces with the minimum F_S is found through an iterative process using a grid of different rotation centres (introduced in Figure 6-8) from which different radius surfaces are plotted.

Fellenius (1927) initially developed the Ordinary Method of Slices which only considered the forces acting on the potential failure surface and body forces in moment equilibrium. To improve the accuracy of stability analysis, Bishop (1955) considered the inter-slice forces (i.e. E_L, $E_{R,}$ X_L,X_R in Figure 6-8), with the full detailed formulation shown in Equation 6-6:

$$F_S = \frac{\sum \left[c'l + \tan\varphi' \left(\frac{W - (X_R - X_L) - \left(\frac{[c'l - \tan\varphi' ul] \sin\Phi}{F_S} \right)}{\cos\phi \left(1 + \frac{\tan\varphi' \tan\Phi}{F_s} \right)} - u\,l \right) \right]}{\sum W \sin\Phi}$$

Equation 6-6: Bishop's Simplified Method of Slices

Given how F_S appears on both sides of this equation, it is solved iteratively starting with a high factor of safety (e.g. $F_S = 5$) until the convergence between subsequent iterations falls below a threshold value (e.g. 0.005).

Force equilibrium implies the summation of all forces in both the horizontal direction and vertical direction should be zero. However, the above formulation Equation 6-6 is indeterminate and Bishop's Simplified Method of Slices only satisfies horizontal equilibrium by assuming that the resultant vertical shear forces between slices are zero (i.e. $X_R - X_L = 0$). Therefore Bishop's Simplified Method only fully satisfies overall moment equilibrium, and not overall force equilibrium.

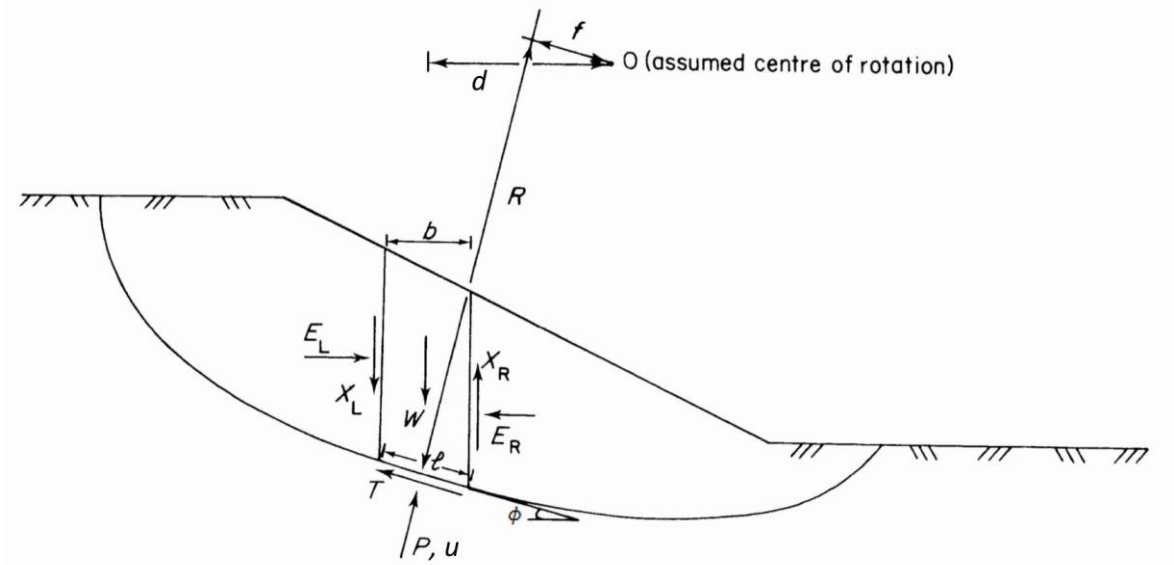

Figure 6-8: Illustration of the method of slices for limit equilibrium analysis. Forces acting on a typical slice are also shown (Anderson and Richards, 1987 p. 38).

O	= centre of rotation
R	= radius of failure surface
b	= width of slice
l	= length of slice base
Φ	= slice inclination
d	= distance of slice central axis to the centre of rotation
u	= pore pressure at the slice base centre
E_L and E_R	= horizontal lateral forces between slices
X_L and X_R	= vertical shear forces between slice
W	= weight of slice
P	= $\sigma^T \times l$ = total normal stress x slice length
T	= $\tau_s \times l$ = total shear stress x slice length

Limit equilibrium methods can be broadly classified into two main categories of 'simplified' and 'rigorous'. Simplified methods satisfy either force or moment equilibrium, but not both at the same time. For rigorous methods, both force and moment equilibrium

are satisfied but the analysis is longer and may sometime experience non-convergence problems (Cheng and Lau, 2008).

The chosen method for the following slope stability analysis is Spencer's rigorous method which satisfies both moment and force equilibrium by an additional iterative step to estimate $X_R - X_L$ by assuming the resultant angle of both horizontal and vertical interslice forces is constant throughout the slope (Anderson and Richards, 1987). This method is best suited to circular failure surfaces and whilst no method is considered better than others, rigorous methods (which more carefully consider internal forces) will often give better results than simplified methods (Cheng and Lau, 2008). The most commonly used rigorous methods generally give very similar results as the inter-slice forces only have a small effect on the overall factor of safety and to ensure this analysis is not biased by the use of Spencer's Method, many other approaches are also tested for comparison.

Despite its widespread use, fundamental assumptions are also recognised in the use of these techniques. These include assuming the failure mass acts as a single rigid body, the base normal force acts at the middle of each slice, the FOS along the entire slip surface is constant and that stress-deformation components are ignored (Abramson, 2002). Combined with the significant uncertainty and spatial variability in the material parameters (explored in the next section), this approach is not aimed at calculating absolute F_S values. Instead the relative differences between various model scenarios are used to assess the stability of the Shuping landslide under different real-world conditions.

6.3.1 Model Parameter Selection

Limit equilibrium is not an inverse technique, and therefore relies upon *a priori* specification of boundary conditions and input parameters such as the slope morphology, geological details, material parameters and pore water pressures (Abramson, 2002). The rotational failure mechanism of the Shuping landslide means a circular failure plane is employed in this model, although for most two-dimensional analyses, the failure surface is simplified allowing representative cross-sections to be drawn and divided into slices (Anderson and Richards, 1987).

The slope geometry shown by the cross profile in Figure 6-9 is taken from the centre of Block 1 (the eastward half of the landslide), shown in Chapter 5 to be the most active. The surface topography is extracted every 30 m (Figure 6-9) from the ASTER GDEM v2 DEM, a product of METI and NASA, and the initial reservoir water level is set at 145 m.

The uncertainty increases for the submerged portion of the slope where no DEM data were available. Classification of the subsurface into one slide body above bedrock is strongly supported by cross sections for the Shuping landslide found in other publications (Wang *et al.*, 2005a; Ailan *et al.*, 2008; Wang *et al.*, 2008d; Qin *et al.*, 2010) and the exact line is digitised from a scaled figure in Shimei *et al.* (2008d p. 986).

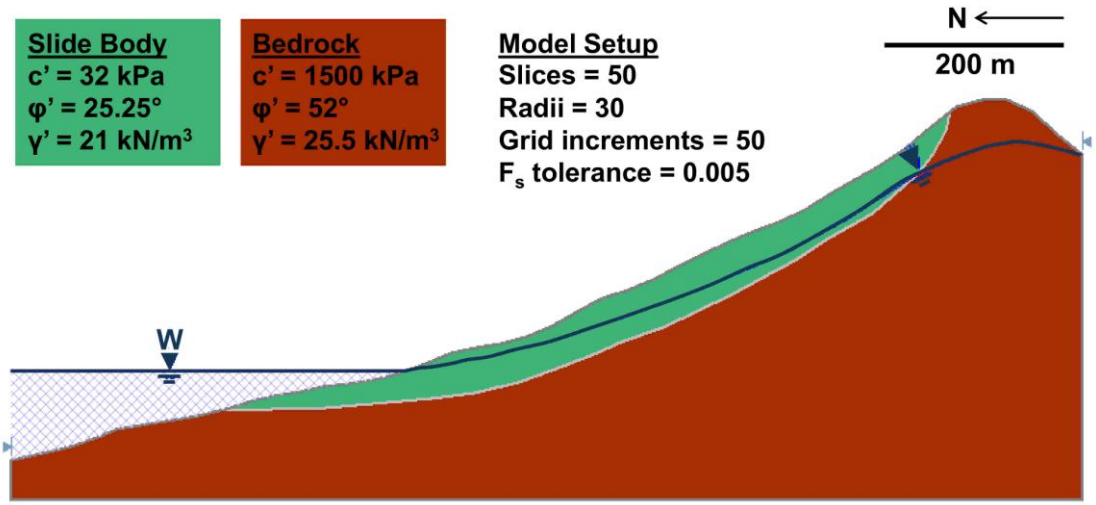

Figure 6-9: Geometry and parameterisation of a 2D profile through the centre of Block 1 of the Shuping landslide. Topographic profile was extracted from the ASTER GDEM v2, the landslide body was digitised from Wang *et al.* (2008d) and more detailed information on the parameters is shown in Table 6-1.

Data from one borehole at the toe of Block 1 has been published (Wang *et al.*, 2005a) and found the water table (at the time of survey) was 8.8 m beneath the surface. This helps constrain the water table at the lowest elevations, although uncertainty in the water table significantly increases towards the head of the landslide. Whilst this is not the optimal approach, uncertainty in the water table location is considered in later sections.

Finally, geotechnical parameters for the two distinct materials are required. Published information on the Shuping landslide was found (see Table 6-1 and Qin *et al.* (2010)) although these were not from laboratory or in-situ tests and are potentially quite unreliable. A literature search was conducted of other landslides within a 20 km radius of the Shuping landslide, from which effective mechanical parameters of cohesion (c'), friction angle (φ') and unit weight (γ_U or γ_S) had been obtained from laboratory or in-situ tests (Table 6-1).

Bedrock parameters appear to be varied and unrealistically high, although these artificial conditions are input to reduce the likelihood of failure surfaces within this highly resistant

layer. Values for the cohesion and friction angle within the slide body itself are also quite varied, although they are relatively consistent for the unit weight. For all parameters in both layers the median value is taken as the best estimate and uncertainty in these geotechnical values are dealt with in later sections.

The following analysis is divided into regular deterministic models, probabilistic analysis to allow for parameter uncertainty, sensitivity analysis and finally F_S calculations under rapid reservoir drawdown scenarios.

Table 6-1: Published geotechnical parameters for the Shuping landslide and from other landslides close to the Shuping landslide.

Landslide	Distance to Shuping (km)	Cohesion (c') (kPa)		Friction Angle (φ') (°)		Unit Weight (γ_U)* (kN/m^3)	
		Body	Bedrock	Body	Bedrock	Body	Bedrock
Huangtupo (Cojean and Caï, 2011)	20	100	3000	30	45	21.5	25.5
Zhujiadian (Hu *et al.*, 2013)	20	34	350	36	52	21	26
Xiangshanlu (Miao *et al.*, 2014)	3.5	18		13			
Qianjiangping (Zou *et al.*, 2013)	3	28.3		18		21	
Xietan (Loo, 2006)	3	30		22		17.5	
Shuping** (Qin *et al.*, 2010)	0	36	1500	28.5	80	19.82	24.5
	Median:	**32**	**1500**	**25**	**52**	**21**	**25.5**

* Assumed unsaturated unit weight

** Parameters for the Shuping landslide do not come from geotechnical or in-situ investigations. These parameters are "parameters proposed by the engineering geological model, compared to mechanical parameters of similar landslides, and agrees with regression of deformation observations" (Qin *et al.*, 2010 p. 541).

6.3.2 Deterministic Analysis

The model uses a large grid of 50 x 50 nodes and ensured the minimum F_S rotation centre is far from the grid boundaries. Each node also considers 30 radii between the minimum and maximum possible circular failure surfaces. The results are then calculated for static scenarios with the minimum and maximum reservoir water levels of 145 m and 175 m respectively, using a convergence value of 0.005 for the iterative F_S procedure.

6.3.2.1 145 m Water Level

The results of the first calculations are shown in Figure 6-10. With a F_S very close to 1.0, this suggests the Shuping landslide is in a critical condition even under the static scenario when the Three Gorges reservoir is at its lowest. The rotation axis is in the centre of the grid nodes (considering the grid in Figure 6-10 has been cropped from the top), indicating the solution is robust. This can also be seen by the predominance of minimum F_S planes from each grid node with values between 1 – 1.4 located in the slide body (Figure 6-10). The artificially high geotechnical parameters for the bedrock cause very few minimum failure planes to be located in this material.

The borehole towards the lower part of Block-1 (the eastern block) indicates the rupture zone surface is at a depth of 65 – 75 m, a zone where numerous slickensides were evident (Wang *et al.*, 2005a). This would also match the geometry and location of the weakest predicted failure plane, although the uncertainty in this measurement remains high.

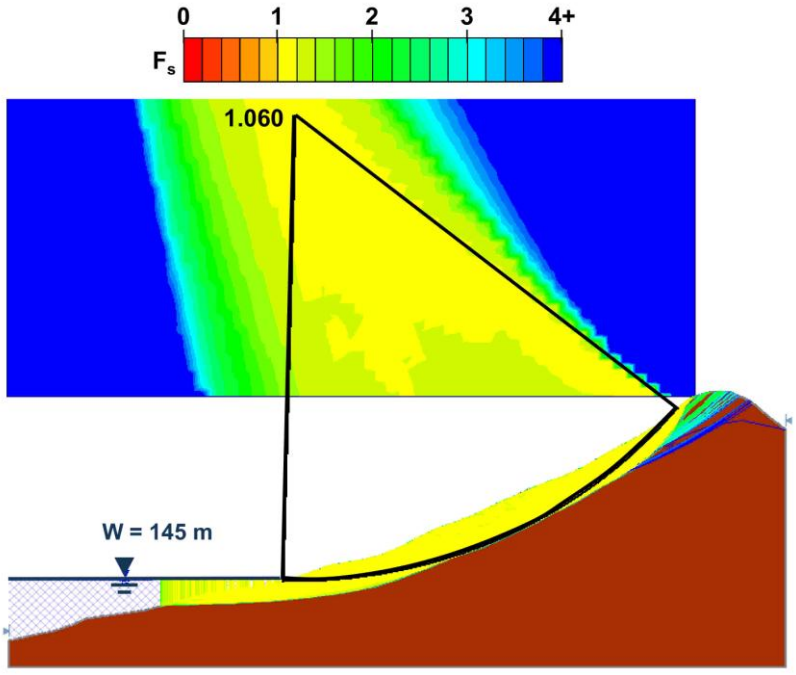

Figure 6-10: Factor of safety calculation using Spencer's method for a reservoir water level of 145 m. The factor of safety is very close to 1.0, indicating the slope is vulnerable to failure. Note the grid search window has been cropped from the top to save space.

6.3.2.2 175 m Water Level

With a stable, higher water level of 175 m, the F_S drops to 0.991 (Figure 6-11) indicating the likelihood of slope failure is higher when the reservoir level is at its maximum. The magnitude of decrease in F_S matches the findings of Cojean and Cai (2011) who analysed

the effects of rising water levels for the nearby Huangtupo landslide following reservoir impoundment.

The higher water level and increased weight of water will increase the resistance against slope movement. However, given the drop in F_S, this indicates that higher pore water pressures within the slide body lead to a greater reduction in effective normal stress in the toe of the slope and ultimately, slope failure. This reasoning has been used to explain many shallow landslides which followed the initial reservoir impoundment, as well as the large catastrophic failure of the Qianjiangping landslide (only 3 km away from the Shuping landslide) which occurred after the first stage of water level rise in 2003 (Wang *et al.*, 2004; 2008b).

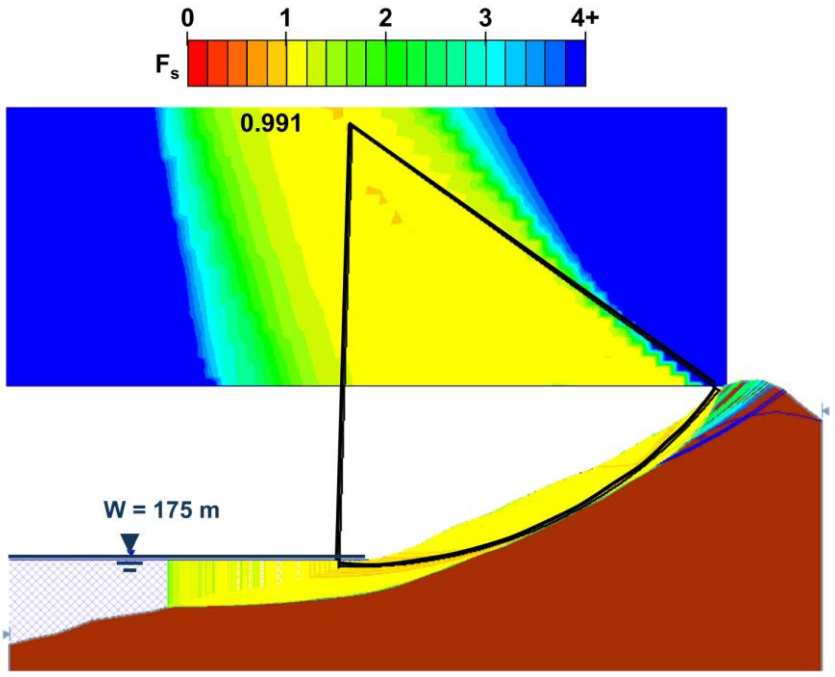

Figure 6-11: Factor of safety calculation using Spencer's method for a reservoir water level of 175 m. The factor of safety drops below 1, indicating the landslide is active under these conditions. Note the grid search window has been cropped from the top to save space.

The above analysis used Spencer's Method to calculate F_S, although many other formulations were tested (Figure 6-12). Notably, four methods (Bishop, Spencer, Corps of Engineers & Morgenstern-Price) result in almost identical factors of safety for both previous scenarios with different water levels. Only the Fellenius and Janbu Simplified method result in slightly lower values, although it has been found that simplified methods generally give conservative values for F_S when compared to more rigorous methods satisfying complete equilibrium (Carpenter, 1985). The choice of Spencer's Method is believed to be satisfactory for the purpose of this comparative analysis, the most

important feature being the method remains consistent for the different scenarios being investigated.

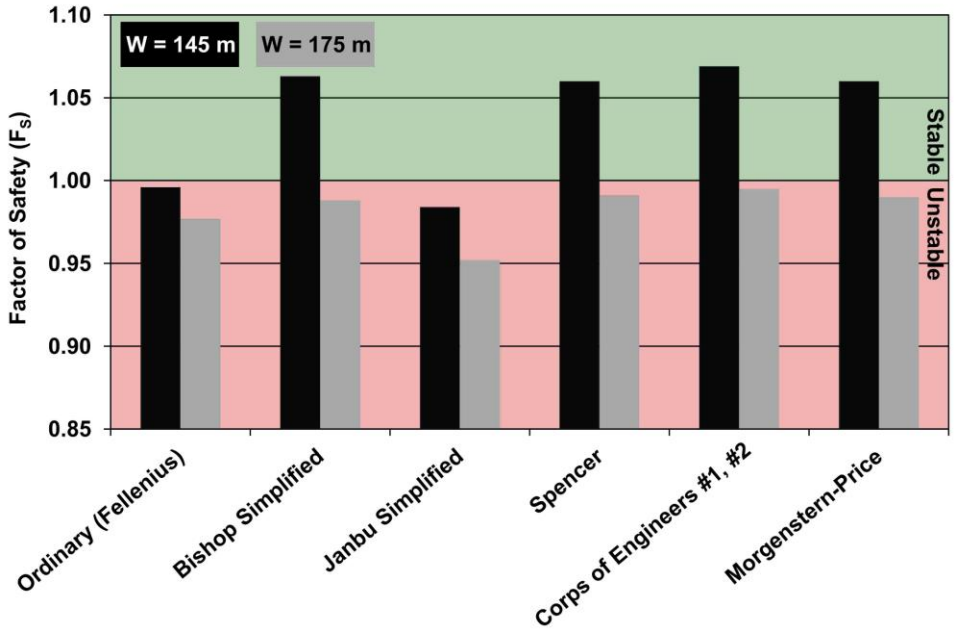

Figure 6-12: Comparison of factor of safety values from different methods. Bishop, Spencer, Corps of Engineers and Morgenstern-Price methods all produce very similar values under the two different reservoir water levels.

6.3.3 Probabilistic Analysis

Given the significant uncertainty in the geotechnical parameterisation, probabilistic analysis is undertaken in the form of a Monte Carlo simulation. For a range of possible values and a statistical distribution, random parameter combinations are selected for 2000 model runs to assess the impact upon the F_S results.

The Monte Carlo simulation uses the maximum and minimum values (symmetrical around the median) shown in Table 6-2 and Figure 6-13. A uniform distribution is employed to ensure all values are equally weighted and not concentrated around the initial median.

Table 6-2: The range of parameters, varied randomly and following a uniform distribution, for both the probabilistic and sensitivity slope stability analysis. Variation of the water table is displayed in Figure 6-13.

Section	Parameter	Distribution	Median	Minimum	Maximum
Slide Body	Cohesion (kPa)	Uniform	32	12	52
Slide Body	Friction Angle (°)	Uniform	25.25	20.25	30.25
Slide Body	Unit Weight (kN/m^3)	Uniform	21	19	23
Bedrock	Cohesion (kPa)	Uniform	1500	350	2650
Bedrock	Friction Angle (°)	Uniform	52	42	62
Bedrock	Unit Weight (kN/m^3)	Uniform	25.5	22.5	28.5
	Water Table (m)	Uniform	-	± 10	± 50

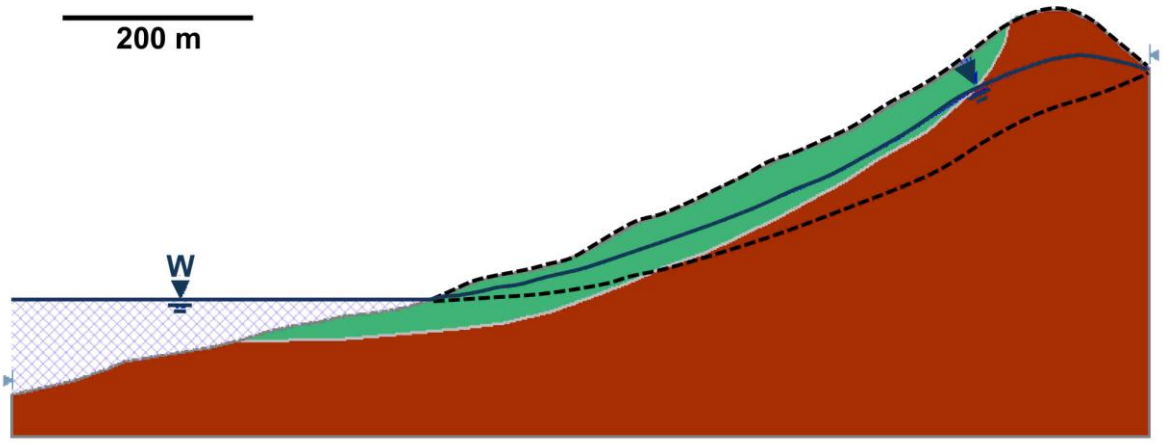

Figure 6-13: Upper and lower limits of the water-table for the probabilistic and sensitivity analysis. The position goes from the upper extreme (following the surface topography) and is reflected in the initial water table location to determine the lower extreme. The water table is varied randomly, following a uniform distribution.

Figure 6-14a displays the results of the probabilistic analysis, with the water level at 145 m. Recalculating the mean factor of safety after each run shows a convergence after 50 runs around the final mean F_S of 1.04. This is not significantly different to the deterministic analysis which gave a F_S of 1.06 (Figure 6-10).

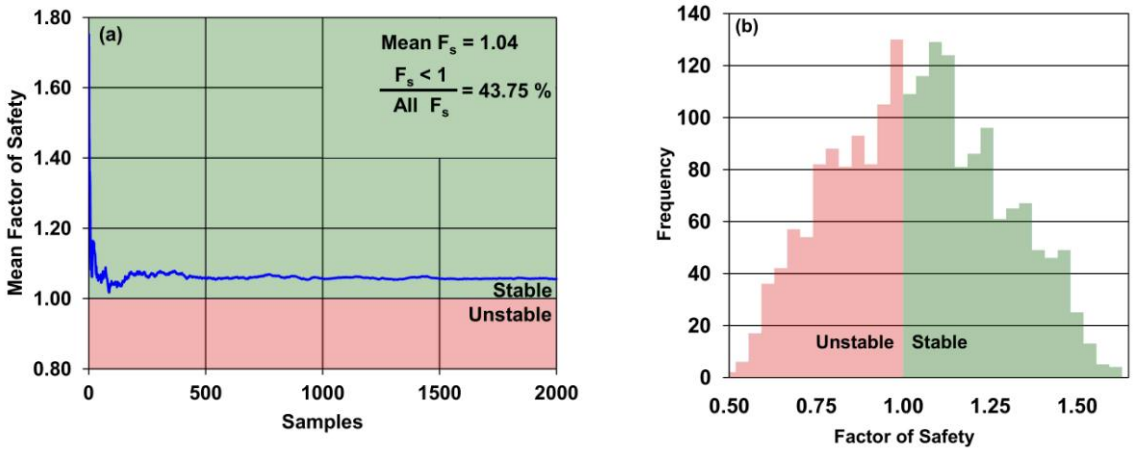

Figure 6-14(a): Convergence plot of 2000 samples following the random variation in model parameters. The mean factor of safety converges to 1.04 after approximately 500 samples, and the factor of safety falls below 1.0 in 43.75% of the samples.

Figure 6-14(b): Histogram of the minimum F_S calculated for each random variation in model parameters.

The probability of failure (defined by the ratio of $F_S < 1$ to all F_S values) is also high at 43.75% (see Figure 6-14a-b), although this is dependent upon the wide range of parameter values specified. Overall this test reinforces the conclusion that the Shuping landslide is very close to failure, allowing for significant variation in the geotechnical model inputs.

6.3.4 Sensitivity Analysis

Following a similar strategy to the probabilistic analysis, it is also important to understand the most influential parameters on the F_S calculation. Using the same parameter ranges specified in Table 6-2, each parameter is individually varied 2000 times between the maximum and minimum values whilst all other parameters stay constant.

The results are normalised to show the F_S calculations related to the percentage of the range in parameter values, allowing the factors to be plotted simultaneously (Figure 6-15). In terms of the material parameters, the steepest gradient relates to the friction angle and cohesion of the slide body indicating these are most influential on the final result, matching the conclusions of Baek *et al.* (2008). However, variations in the water table height are shown to have the greatest influence on the stability of the Shuping landslide.

One limitation of this technique is how the gradient of lines is fully dependent on the parameter range as specified by the minimum and maximum values under consideration.

However, it is believed reasonable parameter values and distributions have been defined and the three steepest lines represent the most influential parameters.

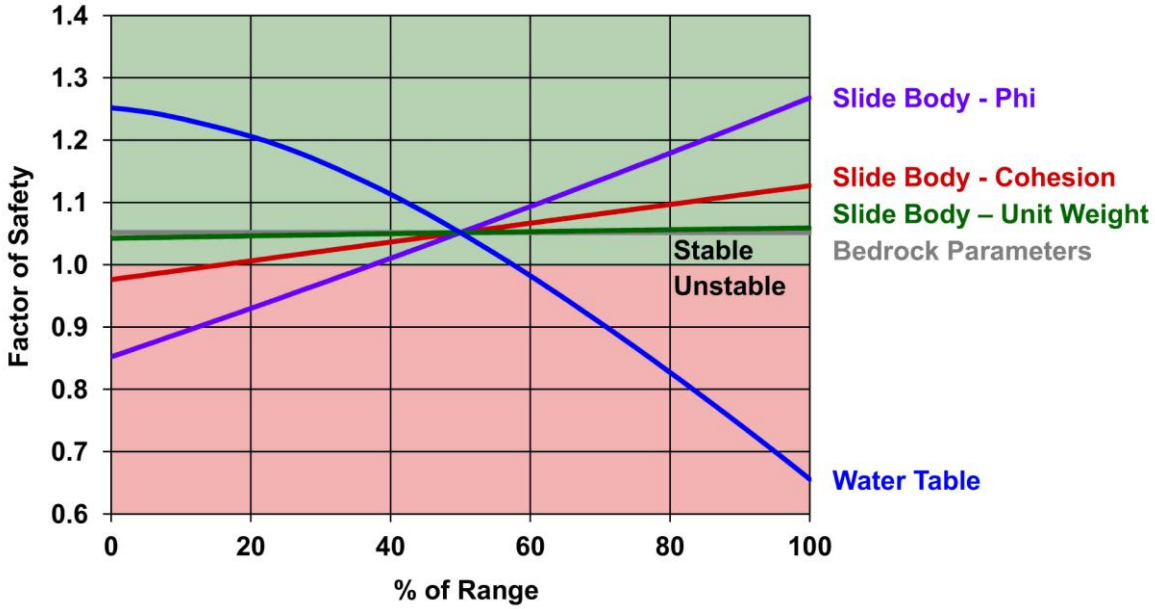

Figure 6-15: Sensitivity plot of the factor of safety, across the range of parameters specified in Table 6-2. As the water table exhibits the highest gradient, the factor of safety is most variable over the range of water table values, followed by the internal angle of friction and cohesion of the landslide body. At the mid-point (50% of range), the factor of safety will be identical to the deterministic calculation.

6.3.5 Rapid Drawdown Scenario

Slopes adjacent to reservoirs often experience instability as a result of fluctuations in water levels adjacent to the slope. There have been numerous reports of slope failure associated with reservoir drawdown (Jia *et al.*, 2009). With the Shuping landslide shown to be dominantly affected by rapid reservoir drawdown, this situation was also modelled to compare the F_S values with the static scenarios in Section 6.3.2. These previous cases only considered steady-state conditions, whereas the following analysis considers the most unfavourable transient situation.

The sudden reservoir drawdown modelling uses the initial high reservoir water table, whilst the lower reservoir level removes a buttressing load at the landslide toe. This assumes that pore pressures within the slope remain high and require some period of time to dissipate following rapid drawdown (Kalenchuk *et al.*, 2013). This is a reliable assumption given the time-delayed response to reservoir changes found in Section 6.1.1.

A drawdown of the full reservoir (from 175 – 145 m) is shown to produce the minimum F_S (Figure 6-16). More realistically, the fastest reservoir changes can be around 5 m and this

smaller drop is still shown to generate the lowest factor of safety (Figure 6-17), lower than both static scenarios in Section 6.3.2. A reduction in the F_S by a factor of ~3% was also found by Cojean and Caï (2011). Together this provides further evidence on how the Shuping landslide is dependent on the fluctuations in reservoir water level.

When the water in the Three Gorges reservoir has been kept at its highest level for some time, the groundwater level in the slope will have reached a high elevation. However before the summer monsoonal season, the reservoir is dropped rapidly. The groundwater level within the sliding zone will not fall at the same rate (dependent upon the coefficient of permeability) and this difference causes residual pore water pressure within the slope capable of perturbing its stability (Fujita, 1977).

Given the vulnerable situation of the Shuping landslide, preventative measures could include lowering the Three Gorges reservoir at a slower rate prior to the months of heavy rainfall. Whilst this may not completely stop displacements, the landslide movement is likely to be proportional to the drawdown magnitude and rate and therefore will not experience such significant episodic movements. If the reservoir operations are not flexible, then it may be possible to install a efficient drainage system (similar to that proposed for the Qiaotou landslide in the Three Gorges (Jiang *et al.*, 2011a)) in order to avoid the development of residual pore pressure in the landslide body during rapid drawdown.

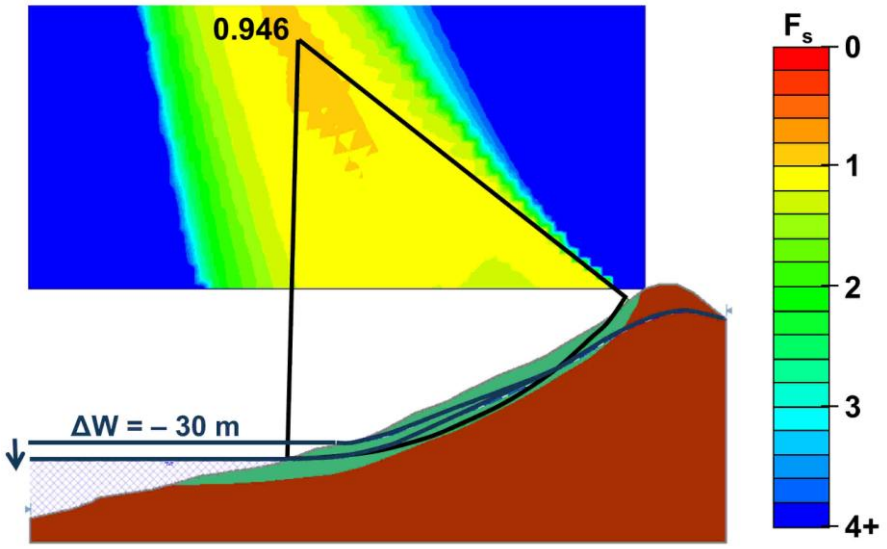

Figure 6-16: Factor of safety following the complete and rapid lowering of the Three Gorges reservoir from 175 m – 145 m. This is the lowest factor of safety compared with all previous examples.

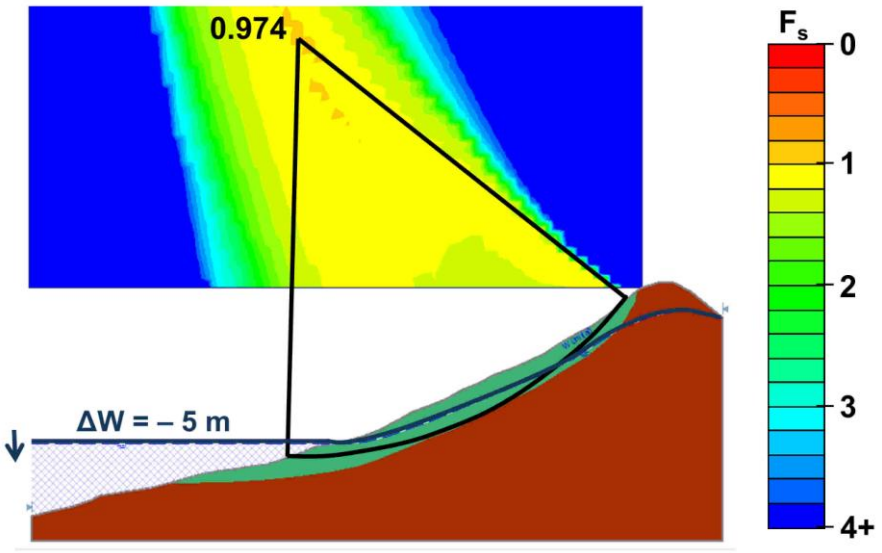

Figure 6-17: Factor of safety following a rapid, realistic 5 m drop in the Three Gorges reservoir. Compared to the static deterministic models (Figure 6-10 & Figure 6-11), the 5 m reservoir drop produces a lower factor of safety.

6.4 Summary

Chapter 6 investigates the slow-moving and reactivated sediment deposit associated with the Shuping landslide. Potential triggering factors of reservoir fluctuations, rainfall and seismicity are assessed given the increased susceptibility of ancient landslides to reactivation. Landslide movements are most highly correlated with long periods of reservoir drawdown and when a drop in water level is not preceded by an equivalent rise. There is no evidence to support seismically-triggered displacements and the effects of rainfall are considered at least secondary to the factor of reservoir drawdown.

Surface movements from the SPOT-CR analysis are estimated in the vertical and horizontal directions, helped by the Shuping landslide's north-south downslope sliding orientation. The spatial variation of movements can help infer a rotational landslide failure mechanism for the Shuping landslide and justifies the use of a circular failure surface for 2D limit equilibrium analyses.

The geometry and inferred geotechnical properties of the Shuping landslide show it is very vulnerable to failure given the F_S values are close to 1.0. Hydrological scenarios of reservoir drawdown produce the lowest F_S values and explain the periods of most rapid displacement. These movements are believed to represent block sliding along the plane separating colluvium and bedrock, although uncertainty and spatial variability in model parameters warrant further in-situ investigation to understand future landslide behaviour.

Chapter 7 : Discussion and Conclusions

The overall aim of this investigation was:

> *To evaluate the use of frequently acquired SAR imagery for detecting, mapping, monitoring and understanding the mechanisms of slow-moving landslide hazards in the Three Gorges region.*

Landslides are complex natural phenomena which often exhibit non-linear and spatially variable displacement patterns. The use of frequently acquired Synthetic Aperture Radar (SAR) imagery provided an opportunity to remotely monitor slow-moving landslides within the areal coverage of a radar image, reducing the cost and complexities of in-situ field-based monitoring. However significant limitations of the most potentially precise technique, Differential Interferometry (D-InSAR), required important considerations particularly in a low coherence environment. The more robust, although less precise, technique of SAR sub-pixel offset time-series analysis had not previously been applied to landslides for time periods of more than 1 year, meriting further research.

Many interesting landslides exist within the Three Gorges region, China (Section 3.3), which can benefit from regular monitoring and thorough investigation. However the characteristic densely vegetated slopes were challenging terrain for the exploitation of SAR data. The availability of three different SAR imaging modes which covered the same area and the same time period (Section 4.1), allowed for one of the most comprehensive comparisons of SAR data analyses to be undertaken in such a densely vegetated region.

Successful cases of monitoring active landslides require the detection, mapping, characterisation and long-term monitoring of slope movements (Tofani *et al.*, 2010) and this was achieved for the fastest-identified landslide within the study area – the Shuping landslide – which was covered by the highest resolution SAR data. Further analysis was then undertaken to characterise the landslide mechanism and triggering factors which

included a 2D limit equilibrium slope stability model to determine dominant controls on its factor of safety.

This chapter initially discusses each of the three results chapters, assessing the wider implications of the research findings and critically evaluating the strengths and weaknesses of the research strategy. This is followed by the main conclusions which directly answer the research questions outlined in Chapter 1. Finally, future research directions are suggested which aim to inform prospective research proposals on the remote investigation of landslides using SAR imagery. Recommendations for further, targeted work within the Three Gorges region are also outlined.

7.1 Discussion

7.1.1 D-InSAR use in the Three Gorges Region

A better consideration of the limiting factors to landslide analysis using D-InSAR techniques and selection of the most appropriate SAR imaging mode (albeit on a case-by-case basis) are required to achieve reliable and optimal results, avoiding the misrepresentation and over-interpretation of data (Colesanti and Wasowski, 2006). The rapid development and availability of D-InSAR time-series analysis methods allows fast and automated processing to derive a grid of points displaying their mean velocity and movement history over the time period of SAR data (e.g. Ferretti *et al.*, 2001; Hooper *et al.*, 2007). D-InSAR has been successfully applied in the Three Gorges region, particularly for E-W slope orientations which generally have the best geometry with respect to the satellite Line-of-Sight (LOS). However, many checks are recommended if this technique is selected given the apparent dangers highlighted in Chapter 4.

The mean coherence for consecutive image pairs gives an indication of the average annual coherence level for a region, along with any significant seasonal variations. Whilst the factors controlling coherence could be difficult to ascertain, periods of higher coherence may be evident which will generate the best results. Additionally the mean coherence of image pairs with varying time intervals may highlight the duration over which the coherence is lost for the majority of the image, helping to design the optimal baseline network for any small baseline (SBAS) time-series analysis.

Given the side-looking geometry of SAR sensors and the mountainous regions where landslides are most commonly located, an assessment of the likely image distortions should also be carried out. The R-index equation applied to a DEM (Notti *et al.*, 2010) can

calculate areas of foreshortening, layover and shadow which are unsuitable for D-InSAR analysis. Landslides in these areas cannot be measured using SAR imagery, although it is possible that one orbiting direction (i.e. ascending or descending) is more suitable than the other, depending on a specific landslide's orientation. This can be calculated and decided upon prior to ordering SAR data.

Visual inspection of interferograms is also important, particularly over known landslide sites. This approach identified a landslide with increasingly fast movements which eventually lost coherence due to the speed of its movement relative to the 11-day revisit time of the TerraSAR-X sensor (Section 4.5). Depending upon the resolution and wavelength of the desired image mode, the spatial displacement gradient (Baran *et al.*, 2005; Jiang *et al.*, 2011b) can be calculated to determine the maximum rate of measurable movement over a specified distance (Section 4.4). This rate should be compared with expectations or any previous observations (either terrestrial or spaceborne) to establish whether all historic movements are within the measureable threshold (recognising this assumes future movements will have similar magnitudes to historic movements). Such work can also be completed prior to ordering data. As the revisit time of SAR sensors is improving (e.g. four days for the COSMO SkyMed constellation or six days for Sentinel-1A and 1B SAR sensors), the measurable limits on displacement will improve.

The most important decision end users can make in terms of successful landslide monitoring relates to the choice of SAR imaging mode. Technical considerations are required regarding the sensor characteristics (e.g. wavelength, resolution, revisit frequency, data availability), the landslide properties (e.g. size, speed, geometry) and the desired monitoring strategy (e.g. regularity of measurements, areal coverage, resolution).

In the densely vegetated Three Gorges region, whilst ENVISAT data have a wavelength of ~0.056 m, TerraSAR-X data with a shorter wavelength of ~0.031 m have much higher coherence values. This is attributed to the higher resolution imaging modes and more frequent revisit frequency. In such a region, the frequency of image acquisitions is far more important than the baseline separation (given the precise orbital control of the TSX satellite) and gaps in the acquisition schedule of SAR images can be very problematic for D-InSAR time-series analysis (Section 4.2).

As the image resolution increases, the capability of mapping the boundaries of active landslides improves as well as increasing the spatial displacement gradient threshold. TSX data can also be acquired three times more frequently compared to ENVISAT data which allows more temporally-variable landslide movements to be resolved. However, a trade off

intrinsically exists between the resolution of the SAR image mode and the areal extent of the data frame. Whilst the resolution of TSX data is much higher, the length and width of the image scene is much smaller. Despite this fact, the highest resolution TSX Spotlight data are recommended given the complete loss of coherence for TSX Stripmap and ENVISAT Stripmap data over the summer months in the Three Gorges region (Sections 4.3 and 4.5).

Differences also exist in terms of developing a routine monitoring system using the TSX and ENVISAT platforms. Whilst the ENVISAT platform is no longer operational, it acquired images regularly (mostly every 35 days) in a background mode. In contrast, the TSX sensor only acquires images over an area once this has been tasked, i.e. there is no background acquisition mode. This means a long-term project proposal with frequent image acquisitions in the same mode over the same area is required for operational landslide monitoring. The ENVISAT background acquisition strategy generated a far larger archive of SAR images for assessing historic landslide movements. An obvious limitation of using SAR data for landslide monitoring is the opportunistic nature of image acquisitions, i.e. measurements can only be obtained at the time of imaging which is beyond control of the end users.

It is important to recognise this study has considered landslides in one type of terrain. Landslides with different surface features, in different topographic regimes, orientated differently with respect to the SAR sensor and with different movement behaviours may require different forms of analysis. Areas with less vegetation (either with more buildings or bare rock) which move at slower rates may be more successfully monitored using D-InSAR time-series techniques given the likelihood of higher coherence and staying within spatial displacement limits. Larger landslides with displacements spread over a bigger area, or moving less episodically, would also be more suited to D-InSAR time-series analysis. Finally, landslides more orientated in east-west directions would be suitable for estimating translational downslope sliding velocities, providing they are not in areas which suffer from geometrical image distortions.

7.1.2 SPOT use in the Three Gorges Region

Sub-Pixel Offset Time-series (SPOT) techniques using only the SAR amplitude information makes use of frequently acquired SAR images without some of the limitations associated with D-InSAR techniques. Unaffected by a threshold on the spatial displacement gradient, SPOT techniques are far more robust and should be undertaken

first to judge the suitability of using more precise D-InSAR methods. If fast, episodic and small-scale movements are identified, this could help assess the (un)reliability of other methods which exploit interferometric phase values. However just as changes in the surface reflectance between image acquisitions reduce interferometric coherence, cross-correlation of pixel offsets also decreases and subsequently reduces the precision of measurements. This makes velocity measurements impossible for catastrophic landslides and highly mobile failures such as debris flows.

The selection of parameters in the processing of SPOT techniques plays an important role in the quality of results (Casu *et al.*, 2011). Processing parameters were heuristically optimised to the study area in this study by testing many different combinations principally relating to the moving window size and oversampling factor (Section 5.1). However it is worth considering the application to other study areas.

Generally a larger window size and higher oversampling factor will generate more precise results, however the computation time should be considered. The size of the processing area and the density of measurements are therefore important decisions which will be determined by the desired landslide application. If a landslide is small (relative to the number of pixels within the sliding body) and slow-moving, then the processing area can be small and the density of measurements can be very high (e.g. every 1-2 pixels in range and azimuth). If a larger area is being covered or a landslide is moving fast then a larger processing area with less dense measurements (e.g. every 4-5 pixels) might be more suitable. Regardless of these factors, all parameters should be kept as multiples of two to maintain the computational efficiency of the Fast Fourier Transform (FFT) used in the cross-correlation calculations.

Verifiable and precise offset measurements were generated from TSX Spotlight and Stripmap data where corner reflectors are installed (Section 5.2). However, independent verification of the SAR-derived displacements should be conducted once such data become available. The approach employed in this study to estimate measurement precision provides good relative comparisons between data sets and image pairs with different properties (e.g. time interval and perpendicular baseline), but accuracy should be estimated by comparisons to independent data since some common errors may exist when an identical processing chain is used.

Contrasting features such as corner reflectors also pose problems relating to the window size parameter due to artefacts in data processing. The cross-correlation and offset value will be very similar when the searching window contains a dominant feature such as a

corner reflector (see the white squares in Figure 5-5a). The larger the moving window size, the larger the white squares which causes points surrounding the corner reflector to be effectively obscured from the offset calculations. Such processing artefacts will also have implications on the precise geolocation of the offset features being measured.

Extension of the SPOT-CR technique applied to natural point-like targets was only possible for the highest resolution TSX Spotlight data (Sections 5.4 and 5.5). Precision is dependent upon the pixel spacing of each image mode and in such a densely vegetated region as the Three Gorges, the pixel spacing of TSX Stripmap and ENVISAT Stripmap data exceeded that required to reliably measure the magnitude of landslide movements detected by the TSX Spotlight data. Even when setting a correlation threshold to obtain precise offset measurements across the whole TSX Spotlight scene, the density of points is still low which suggests the application of such techniques to densely vegetated areas is limited. At least one distinguishing feature (a building, large rock etc) is required within a landslide body to extract a measurement of its velocity. However where high correlation points exist, the offsets are not significantly affected by perpendicular baseline separation or temporal decorrelation (at least over periods of 1-2 years) and therefore provide a useful capability to cover SAR image gaps within a series of SAR data that would be irrecoverable using D-InSAR time-series techniques.

SPOT techniques should achieve better results for landslides with more contrasting surface features (either natural or constructed) or where the movement is greater with respect to the SAR image pixel size (up to the point when movement induces significant changes in the earth's surface and therefore changes in the radar backscatter). ENVISAT data acquired every 35 days would have an improved chance of success in less vegetated areas, measuring larger displacement fields and/or where the magnitude of movement is greater than a couple of metres. In all cases, the same image distortions which limit the spatial coverage of D-InSAR results affect the use of SPOT techniques.

7.1.3 Landslide Characterisation in the Three Gorges Region

The fastest moving landslide detected by frequently acquired SAR data, and with the longest series of observations, was the focus of further investigations aiming to understand its mechanism and response to triggering factors (Sections 6.1 and 6.2). A lack of published geotechnical studies and in-situ measurements of the Shuping landslide meant potential conditioning factors were not assessed, although its classification as an ancient landslide deposit (Wang *et al.*, 2008a) meant it was vulnerable to reactivation and

promoted the importance of assessing likely triggering factors. The most important local triggering factors included reservoir water level fluctuation, rainfall and seismic activity since other potential factors such as snowmelt, heavy construction works or volcanic activity were absent in this area.

Assessment of likely triggering factors was limited by the spatial and temporal resolution of secondary data. Reservoir water level was recorded at the Three Gorges dam site, 45 km away from the Shuping landslide. Data were also plotted at five-day intervals which could mask periods of faster reservoir lowering over periods of hours or individual days. Rainfall was recorded at the County Town of Badong and assumed to be representative of the rainfall regime at the Shuping landslide, 25 km away. Accumulative rainfall data were only recorded every 10 days and could again mask periods of more torrential rainfall.

Compared to the maximum 11-day frequency of SAR data, the frequency of available secondary data is acceptable as individual landslide movements are not identifiable at the exact time of occurrence and could not be matched with more precise timings of reservoir drawdown or rainfall episodes. The direct relationships apparent between landslide movement, reservoir drawdown and rainfall also indicate potential lag effects are included within the temporal averaging of measurements. Analysis is limited when the frequency of SAR image acquisitions is reduced (particularly in the 2012 – 2013 TSX Spotlight data set) and when the available rainfall data stop in 2011.

Patterns of surface movement were used to interpret the likely failure mode of the Shuping landslide. Significant uncertainty is associated with the limits and behaviour of the landslide toe given its submergence by the Three Gorges reservoir, which only field surveys could improve. The orientation of the Shuping landslide's downslope direction is also advantageous for this analysis. Its predominant south-north orientation permits the assumption that east-west movement is essentially zero, therefore allowing the vertical and northwards movement to be estimated from the range and azimuth offsets. Such an approach would be unsuitable for landslides with greater components of NE/NW/SE/SW movement. In these cases, three-dimensions of movement should be estimated which requires at least three independent observations of displacement from different viewing geometries. Both ascending and descending SAR data modes either from two incidence angles or in combination with azimuth offsets are required to generate a three-dimensional model of displacement (e.g. Fialko *et al.*, 2001; Wright *et al.*, 2004; Funning *et al.*, 2005). The ability to generate three-dimensional displacements places stricter demands on imaging modes and such available archive data sets are unlikely to exist in many cases.

Finally, assumptions on the factor of safety calculations for the Shuping landslide are acknowledged. A lack of detailed geological information for this site meant the subsurface landslide structure was solely based on previous studies which use one borehole to estimate the depth of soil/rock layers (Section 6.3.1). The model is only based on a single central profile through the most active landslide block, although the topography and subsurface properties are believed to be very similar for cross-profiles at other locations.

The general assumptions remain for factor of safety calculations (outlined in Section 6.3) and the parameterisation of the model was not based upon in-situ geotechnical analysis of Shuping landslide materials. However, rather than trying to achieve the most accurate and absolute measurements on slope stability, the relative differences between different scenarios were used to assess the conditions under which slope movement is most likely.

7.2 Conclusions

The above discussion assessed the limitations of this research as well as the wider implications of D-InSAR, SPOT and modelling techniques with respect to other SAR sensors and study areas. This section below presents the most important conclusions from the results of this investigation, directly related to the four research questions outlined in Section 1.5. The major contributions of this study to related research fields are outlined, followed by recommendations for future research directions.

Research Question (1): To what extent can Differential InSAR (D-InSAR) methods monitor landslides in the Three Gorges region?

D-InSAR measurements have been successfully used to detect slope movements in the Three Gorges region, although there were significant limitations that prohibit long-term D-InSAR monitoring using single-pair and time-series techniques. Interferometric coherence in the Three Gorges was always low for the image modes in this study due to the density of vegetation, the limited satellite revisit time and the steep slopes. However when the sampling frequency was high enough (e.g. from 11-day TSX image pairs), seasonal signals were evident. Coherence was highest for 11-day TSX Spotlight interferograms between November and February each year when rainfall and vegetation coverage was at a minimum. Annual reductions in coherence between the months of March and October were attributed to seasonal summer rainfall, the subsequent soil

moisture and increased vegetation density (Section 4.2). For all image modes, natural factors affecting temporal decorrelation appear more significant than coherence losses associated with large perpendicular baselines or Doppler centroid differences.

Despite problems of low coherence, at least four active landslides were reliably identified and mapped using the highest resolution D-InSAR measurements when the movement did not exceed the spatial displacement gradient (Section 4.3.2). This included the Shuping and Dujiawu landslides, as well as much smaller riverbank movements less than 200 m in diameter. Such high resolution SAR data also helped redefine the boundaries of the Shuping landslide (c.f. Wang *et al.*, 2005a; 2008a) to show that part of Block 2 is actually stable (Figure 4-18), a potentially useful conclusion for the authorities. The ENVISAT Stripmap data identified movement and the boundary of the Fanjiaping landslide, although this was prior to the start of TSX acquisitions from which no further movement was observed (Section 4.3.4). Both TSX Stripmap and ENVISAT interferograms exhibited complete coherence loss for the months between March and October, warranting the use of corner reflectors to extract measurements over this period.

At times, episodic and faster movements for the Shuping landslide in May – June exceeded the spatial displacement gradient (most notably around the landslide boundary) due to the high contrast in displacement rate between stable and moving land (Section 4.5). The pixel spacing of each image mode was the dominant factor on the displacement gradient threshold, but large movements of the Shuping landslide invalidated the use of D-InSAR and time-series methods for all three available SAR data sets. This is the most plausible explanation for conflicting results found in previous studies of the Shuping landslide (Xia, 2010; Liao *et al.*, 2012; Wang *et al.*, 2013b) or why the months of May – June are excluded from other D-InSAR analyses (Fu *et al.*, 2010; Perski *et al.*, 2014).

The R-index (Notti *et al.*, 2010) assessed slopes most suitable for D-InSAR analysis and highlighted the major problem of layover and shadow on east-facing slopes for the descending data used in this study (Section 4.3.5). Predominantly north-south facing slopes also prohibited the estimation of downslope sliding velocities from the one-dimensional line-of-sight measurements as the amplification scaling factor for all three image modes were above the recommended threshold value of 3.3 (Cascini *et al.*, 2013; Herrera *et al.*, 2013).

Research Question (2): To what extent can Sub-Pixel Offset Time-series (SPOT) techniques monitor landslides in the Three Gorges region?

To overcome the difficulties of using D-InSAR techniques, a Sub-Pixel Offset Time-series (SPOT) approach was investigated as a robust method to resolve time-varying landslide displacements. This was one of the first studies to generate time-series measurements from frequently acquired SAR imagery, particularly focused on landslide applications.

A quantitative, heuristic approach shows how the distribution of offset values for a stable reference area helped reduce the likelihood of spurious correlation effects (Section 5.1). Considering the pixel spacing of SAR data as well as the expected landslide movement enabled suitable sub-pixel offset parameters to be selected for the Three Gorges region. A moving window size of 32 x 32 pixels was used with an oversampling factor of 16.

Offset measurements from corner reflectors located amongst dense vegetation were shown to generate verifiable and precise cross-correlations for both TSX Spotlight and Stripmap data (Section 5.2). The RMS errors between two significantly overlapping and independent offset pairs were 0.038 m and 0.071 m in range and azimuth directions respectively for the Stripmap data (related to the different pixel spacing), and significantly lower for the Spotlight data due to its higher resolution. These errors were also at least one order of magnitude lower than the accumulated displacement for the Shuping landslide and the use of two independent series of SAR data helped verify the final results without ground data. This is the first demonstration of how corner reflectors are significantly beneficial for pixel offset techniques.

From the final SPOT-CR analysis, it is clear that large, episodic movements were responsible for a loss of interferometric coherence and the range offset displacement in May 2009 and 2012 towards the head of the Shuping landslide was shown to exceed the displacement gradient measurable by D-InSAR. Other landslides with installed corner reflectors and within the TSX Stripmap coverage (Kaziwan and Xintan landslides) were stable over the data coverage from April – December 2009.

To extend the spatial coverage of measurements beyond the installed corner reflector points, all TSX Spotlight pixels with a cross-correlation above 0.78 were used to represent point-like scatterers from which precise offset values could be extracted (Section 5.4). Over 1-2 years, these points did not display significant decorrelation due to perpendicular baseline or temporal effects, justifying the use of a single master image to calculate the

displacement time-series from subsequent slave images. This avoided the propagation of errors associated with an accumulative time-series curve generated from consecutive image pairs. Given the small range of TSX perpendicular baselines, the use of a small baseline approach for generating time-series displacement curves was not required.

The regional point-like offset measurements across the whole TSX Spotlight scene identified a potentially new slope instability although precise time-series measurements were not possible due to the (assumed) demolition and construction work within the landslide boundary (Section 5.5).

Without the use of corner reflectors, TSX Stripmap and ENVISAT data were not able to precisely measure the slow-moving landslides of the same magnitude shown by the TSX Spotlight results (Sections 5.6 and 5.7). The application of these techniques and data to less vegetated regions is expected to yield a greater coverage and precision of offset measurements.

Research Question (3): Can regularly-acquired SAR data characterise active landslide mechanisms and determine the associated triggering factors?

After obtaining precise two-dimensional offset vectors in range and azimuth directions over the four year period of TSX Spotlight data, characterisation of the Shuping landslide was possible.

Assuming the E-W component of displacement was zero, the range and azimuth offsets were decomposed into estimates of vertical and horizontal movement (Fialko *et al.*, 2001; Funning *et al.*, 2005) to help infer a rotational component of the Shuping landslide (Section 6.2). Vertical movements were greatest towards the head of the landslide, whereas the largest horizontal movements were in the middle of the landslide and this was consistent over the four year period from February 2009 – 2013. Differences between the eastern and western sides of the landslide imply the movements were spatially variable and related to different landslide blocks, however consistent timing of episodic movements suggested they were related to the same triggering factor. This is the first time a failure mechanism has been proposed for the Shuping landslide and the first time variations in block movement have been quantified.

Availability of secondary data sets for the potential triggering factors of reservoir drawdown, rainfall and seismicity were used for comparisons to the time-series of

displacement from SPOT-CR analysis. Landslide displacement was most obviously related to the faster rates of reservoir lowering (~0.5 – 0.8 m per day) in the first half of the year between May – June. More severe periods of reservoir drawdown occurred in August, although these were preceded by an equivalent rise in water level and did not increase the propensity of the landslide to move. It is also hypothesised that greater magnitudes of reservoir drawdown in 2009 and 2012 led to larger displacements than those estimated for 2010 and 2011 (Section 6.1.1).

Periods of heavy rainfall were also apparent during the months of fastest displacement in May – June 2009 (Section 6.1.2). However, equivalent (if not greater) periods of rainfall at other times did not lead to the same amount of landslide movement, supporting the argument that reservoir drawdown is the dominant triggering factor for the Shuping landslide. The low magnitude of earthquakes within a 50 km radius and their distance away from the landslide (obtained from the China Seismic Network, CSN [in Chinese]; www.csndmc.ac.cn/newweb/data/csn_catalog_p001.jsp) explains why no relationship was observed between regional seismicity and periods of greatest displacement (Section 6.1.3).

Research Question (4): What are the dominant geotechnical parameters controlling slope instability?

To assess the stability of the Shuping landslide under different reservoir water level scenarios, a 2D limit equilibrium model was employed (Section 6.3). The results are summarised in Table 7-1. The factor of safety (F_S) was 1.06 under static conditions when the reservoir was at its lowest level of 145 m. The F_S decreases to 0.99 when the water-level is maintained at 175 m, most likely due to the high pore water pressures within the slide body. In both cases the F_S indicates the critical state of the landslide and reflects the ease at which this ancient landslide can be reactivated.

Table 7-1: Summary table for factor of safety results for different hydrological scenarios affecting the Shuping landslide.

Water Level	Factor of Safety (Spencer's Method)
145 m (Static)	1.06
145 m (Probabilistic analysis)	Mean = 1.04
175 m (Static)	0.99
175 – 170 m (Partial drawdown)	0.97
175 – 145 m (Full drawdown)	0.95

There was significant uncertainty in the geotechnical properties of the model materials as well as the water table location. A probabilistic Monte Carlo analysis converges at a value very close to the deterministic analysis and a sensitivity analysis highlighted the most influential parameter on landslide stability was groundwater level, followed by the internal angle of friction of the slide body.

By far the lowest F_S values were calculated from reservoir drawdown scenarios. A full drawdown from 175 – 145 m generated the lowest F_S, but even a more realistic drawdown of 5 m led to a lower F_S than static water level scenarios. This was attributed to residual pore water pressures within the slope as the groundwater level lags behind the fall in the reservoir.

7.3 Research Contributions

The main contributions are summarised below:

(1) The largest evaluation of SAR image modes (TerraSAR-X Spotlight, Stripmap and ENVISAT Stripmap) applied to the challenging terrain of the Three Gorges region was undertaken.

(2) The boundary of active slope movement for the Shuping landslide was redrawn (Figure 4-18), relative to the study by Wang *et al.* (2008a).

(3) Episodic and occasionally fast moving movements of the Shuping landslide were discovered to break a theoretical assumption for reliable D-InSAR analysis, highlighting the dangers of using time-series D-InSAR techniques for landslide monitoring. This explains the conflicting results from previous studies employing D-InSAR time-series techniques (Xia, 2010; Liao *et al.*, 2012; Wang *et al.*, 2013b).

(4) A robust Sub-Pixel Offset Time-series (SPOT) technique was developed and applied to landslides for the first time. This provided a solution to some identified limitations of D-InSAR analyses and permitted landslide monitoring for a period of up to four years, although the density of measurements remained low.

(5) The benefits of using corner reflectors for offset measurements were presented for the first time.

(6) SPOT-CR results showed the Kaziwan and Xintan landslides were stable between April – December 2009.

(7) The application of sub-pixel offset techniques to point-like scatterers in rural areas detected a potentially unknown slope failure using TSX Spotlight data.

(8) For the first time, a rotational failure mechanism for the Shuping landslide was inferred, most related to periods of reservoir drawdown. The episodic landslide movements were shown to occur when the reservoir is lowered at a rate exceeding 0.5 m per day, when this lowering has not been preceded by a significant rise in the water level.

Given the assumptions of conventional D-InSAR analyses can be broken by the characteristic features of landslides (i.e. the sharp boundary between stable/active ground, non-linear displacements and the range of temporally-variable velocities), the use of sub-pixel offset time-series techniques is recommended prior to D-InSAR analysis, particularly where CRs are available, since the measured displacement could judge the suitability of more precise and complex techniques.

7.4 Future Research Directions

This independent research has made several original contributions to the field of landslide remote sensing and the results have generated valuable information to help further mitigate the landslide hazard in the Three Gorges region. Limitations of this research have been highlighted, and this section provides suggestions for future analyses in order of priority and impact.

A comprehensive assessment of X- and C-band data was undertaken, although the inclusion of L-band data for further comparisons would boost the evaluation of SAR data for landslide monitoring in the Three Gorges region. Applying the optimal analysis methods found in this study to L-band SAR data (more able to penetrate vegetation) would help determine whether this imaging mode can overcome the limitations found in this study. For D-InSAR analyses, it is hypothesised the resolution and revisit frequency (relative to the TSX Spotlight imagery) would not avoid the spatial displacement gradient constraints. However, the longer wavelength L-band SAR data may help identify more point-like pixels which could generate a higher density of pixel offset measurements.

Given the success of TSX Spotlight imagery for monitoring the Shuping landslide and detecting smaller instabilities within the SAR data frame, continued acquisitions of this data is proposed. Since the TerraSAR-X satellite does not acquire images in a background mode, the data collection has currently ceased for this study area. If remote and near real-time landslide monitoring systems are to be developed, they require the continued

acquisition of high quality data. Despite the current lack of data, SPOT techniques developed in this study demonstrate how the accumulated displacement over this gap in SAR data could still be recovered if image acquisition was restarted. A combination of ascending and descending data may also determine three-dimensional movements for the Shuping landslide and help assess areas previously obscured by SAR image distortions.

For the calculation of sub-pixel offset values, this analysis chose a thorough and *a posteriori* approach which analysed all processed pixels after calculation of the cross-correlations. To reduce processing time and necessary computing power, a recent coseismic study detected and thresholded point-like pixels from a single SAR image before the pixel-offset calculations (Hu *et al.*, 2014b). Determining point-like pixel targets *a priori* would make for an interesting comparison to the high cross-correlation points selected in this study. Application of the SPOT techniques developed in this investigation should also be applied to areas of different land cover to determine whether the cross-correlation threshold of 0.78 can generate a denser coverage of measurements or whether the threshold can be reduced in some cases whilst maintaining the same level of precision.

Future work could also assess whether the ability of the SPOT measurements of large displacements in this study could be used to aid phase unwrapping of interferograms. A reduced phase displacement gradient has previously been obtained by subtracting range offset measurements (Yun *et al.*, 2007). However in the case of retrieving fast and small-scale landslide movements with X-band D-InSAR results, the success might be restricted by the density of SPOT measurements and their precision relative to the wavelength of the SAR sensor.

It would be relatively straightforward to apply D-InSAR time-series techniques to the Kaziwan and Xintan landslides which were found to be stable by the SPOT-CR results of TSX Stripmap data. However the data set is limited to 9 months between April and December 2009 and would still be limited by the constraints on the spatial displacement gradient. Even if more SAR data were available, there is still a risk that episodic and relatively fast landslide movements would not be detected from such analysis.

Finally, the use of Multiple Aperture InSAR (MAI e.g. Bechor and Zebker, 2006) to improve the precision of azimuth-dimension measurements may be attractive to researchers given the rate and orientation of the Shuping landslide. However this was attempted in the course of this investigation and the small scale displacements, coupled with the very high noise level of MAI interferograms in the Three Gorges region, prohibited any useful measurements from being obtained.

This research also has specific implications for the management of landslides within the Three Gorges region. The rate of continued reservoir drawdown between January and July should be carefully considered to minimise movement of landslides. As the reservoir must be lowered to a certain height each year to account for summer rainfall, the drawdown could begin slightly earlier to reduce the required rate of lowering.

A detailed geotechnical investigation of the Shuping landslide is also required. Additional boreholes and geological investigation should improve understanding on the spatial variability of the sliding surface and may provide a better insight into the possibility of any catastrophic failure. The stabilisation of the Kaziwan and Xintan landslide may indicate movements of the Shuping landslide will not be a long-term issue, although it is equally possible other slope deposits might be reactivated.

The episodic and regularity of landslide movements in the months of May – June also promote further investigation. Detailed instrumentation of the Shuping landslide for this two-month period using GNSS receivers, extensometers and subsurface instruments such as piezometers would provide the best opportunity to understand the response of the Shuping landslide to reservoir drawdown and associated groundwater changes.

A database of Global Reservoirs and Dams (GRanD) records all reservoirs > 0.1 km^3 (Lehner *et al.*, 2011) and shows the completion of dams in North America and Northern Europe since 1990 has been limited. Very large reservoirs with storage volumes greater than 1 km^3 are generally located in areas with comparatively low landslide fatalities, except in Asia where a different higher level of hazard is associated with such large construction programmes (Petley, 2013). A wider assessment of slopes bordering reservoirs is recommended, particularly in Asia where high resolution SAR data ($\leq$ 3 m pixel spacing) are available. Similar approaches to this research may help identify reactivated ancient landslide bodies during the construction of dams. To date, there has been insufficient recognition of potential landslide bodies on reservoir slopes, occasionally leading to catastrophic failures such as the famous Vajont disaster.

Overall the integration of spaceborne D-InSAR and SPOT techniques can help assess the stability of slopes over a wider region compared to ground-based techniques. When active landslides are discovered, geotechnical and geomorphological investigations can then be carried out to provide the most comprehensive assessment of current and future landslide behaviour.

Reference List

Abramson, L.W. (2002). *Slope Stability and Stabilization Methods*. New York: Wiley.

Ahmed, R., Siqueira, P., Hensley, S., Chapman, B., & Bergen, K. (2011). A survey of temporal decorrelation from spaceborne L-Band repeat-pass InSAR. *Remote Sensing of Environment, 115*, 2887-2896.

Ailan, C., Xianqi, L., Shaokong, F., & Oda, Y. (2008). Application of surface wave and micro-tremor survey in landslide investigation in the Three Gorges reservoir area. *Landslides and Engineered Slopes. From the Past to the Future, Two Volumes + CD-ROM* (pp. 307-312): CRC Press.

Akbarimehr, M., Motagh, M., & Haghshenas-Haghighi, M. (2013). Slope Stability Assessment of the Sarcheshmeh Landslide, Northeast Iran, Investigated Using InSAR and GPS Observations. *Remote Sensing, 5*, 3681-3700.

Anderson, G., & Richards, K.S. (1987). *Slope Stability: Geotechnical Engineering and Geomorphology*. Chichester: Wiley.

Aryal, K.P. (2006). Slope Stability Evaluations by Limit Equilibrium and Finite Element Methods. In, *Faculty of Engineering Science and Technology*. Trondheim: Norwegian University of Science and Technology.

Askne, J., & Santoro, M. (2005). Multitemporal repeat pass SAR interferometry of boreal forests. *Geoscience and Remote Sensing, IEEE Transactions on, 43*, 1219-1228.

Austin, N.J., Muller, J.P., Gong, L., & Zhang, J. (2013). A regional investigation of urban land-use change for potential landslide hazard assessment in the Three Gorges Reservoir Area, People's Republic of China: Zigui to Wanzhou. *International Journal of Remote Sensing, 34*, 2983-3011.

Australian-Geomechanics-Society (2002). Landslide risk management: concepts and guidelines. *Australian Geomechanics, March*, 50 - 91.

Aysen, A. (2002). *Soil Mechanics: Basic Concepts and Engineering Applications*. The Netherlands: Taylor & Francis.

Baek, Y., Bae, G.J., Kwon, O.I., Jang, S.H., & Koo, H.B. (2008). Sensitivity analysis of shear strength parameters and slope angle in slope stability analysis. In C. Limsiri (Ed.), *Very Soft Organic Clay Applied for Road Embankment: Modelling and Optimisation Approach* (pp. 37 - 42). Delft, Netherlands: Taylor & Francis.

Bai, S., Wang, J., Lu, G., Zhou, P., Hou, S., & Xu, S. (2010). GIS-based logistic regression for landslide susceptibility mapping of the Zhongxian segment in the Three Gorges area, China. *Geomorphology, 115*, 23 - 31.

Bamler, R. (2000). Interferometric stereo radargrammetry: absolute height determination from ERS-ENVISAT interferograms. In, *Geoscience and Remote Sensing Symposium, 2000. Proceedings. IGARSS 2000. IEEE 2000 International* (pp. 742-745 vol.742).

Bamler, R., & Eineder, M. (2005). Accuracy of differential shift estimation by correlation and split-bandwidth interferometry for wideband and delta-k SAR systems. *Geoscience and Remote Sensing Letters, IEEE, 2*, 151-155.

Bamler, R., & Hartl, P. (1998). Synthetic aperture radar interferometry. *Inverse Problems, 14*, R1.

Baran, I., Steward, M.P., Kampes, B.M., Perski, Z., & Lilly, P. (2003). A modification to the Goldstein radar interferogram filter. *IEEE Transactions on Geoscience and Remote Sensing, 41*, 2114 - 2118.

Baran, I., Stewart, M., & Claessens, S. (2005). A new functional model for determining minimum and maximum detectable deformation gradient resolved by satellite radar interferometry. *Geoscience and Remote Sensing, IEEE Transactions on, 43*, 675-682.

Barla, G., Antolini, F., Barla, M., Mensi, E., & Piovano, G. (2010). Monitoring of the Beauregard landslide (Aosta Valley, Italy) using advanced and conventional techniques. *Engineering Geology, 116*, 218-235.

Bechor, N.B.D., & Zebker, H.A. (2006). Measuring two-dimensional movements using a single InSAR pair. *Geophysical Research Letters, 33*, L16311.

Berardino, P., Costantini, M., Franceschetti, G., Iodice, A., Pietranera, L., & Rizzo, V. (2003). Use of differential SAR interferometry in monitoring and modelling large slope instability at Maratea (Basilicata, Italy). *Engineering Geology, 68*, 31-51.

Berardino, P., Fornaro, G., Lanari, R., & Sansosti, E. (2002). A new algorithm for surface deformation monitoring based on small baseline differential SAR interferograms. *Geoscience and Remote Sensing, IEEE Transactions on, 40*, 2375-2383.

Berthier, E., Vadon, H., Baratoux, D., Arnaud, Y., Vincent, C., Feigl, K.L., Rémy, F., & Legrésy, B. (2005). Surface motion of mountain glaciers derived from satellite optical imagery. *Remote Sensing of Environment, 95*, 14-28.

Bianchini, S., Herrera, G., Mateos, R., Notti, D., Garcia, I., Mora, O., & Moretti, S. (2013). Landslide Activity Maps Generation by Means of Persistent Scatterer Interferometry. *Remote Sensing, 5*, 6198-6222.

Bishop, A.W. (1955). The Use of the Slip Circle in the Stability Analysis of Slopes. *Geotechnique, 5*, 7 - 17.

Borla-Tridon, D., Bachmann, M., Schulze, D., Ortega-Mi, Polimeni, M.D., & Martone, M. (2013). TanDEM-X: DEM acquisition in the third year era. In, *5th International Conference on Spacecraft Formation Flying Missions and Technologies (SFFMT)*. Munich, Germany.

Bovenga, F., Nutricato, R., Refice, A., & Wasowski, J. (2006). Application of multi-temporal differential interferometry to slope instability detection in urban/peri-urban areas. *Engineering Geology, 88*, 218-239.

Bovenga, F., Wasowski, J., Nitti, D.O., Nutricato, R., & Chiaradia, M.T. (2012). Using COSMO/SkyMed X-band and ENVISAT C-band SAR interferometry for landslides analysis. *Remote Sensing of Environment, 119*, 272-285.

Bryant, E. (2004). *Natural Hazards*. Cambridge: Cambridge University Press.

Bürgmann, R., Rosen, P.A., & Fielding, E.J. (2000). Synthetic aperture radar interferometry to measure Earth's surface topography and its deformation. *Annual Reviews of Earth and Planetary Science, 28*, 169 - 209.

Calais, E., Dong, L., Wang, M., Shen, Z., & Vergnolle, M. (2006). Continental deformation in Asia from a combined GPS solution. *Geophysical Research Letters, 33*, L24319.

Canuti, P., Casagli, N., Ermini, L., Fanti, R., & Farina, P. (2004). Landslide activity as a geoindicator in Italy: significance and new perspectives from remote sensing. *Environmental Geology, 45*, 907-919.

Cappa, F., Guglielmi, Y., Soukatchoff, V.M., Mudry, J., Bertrand, C., & Charmoille, A. (2004). Hydromechanical modeling of a large moving rock slope inferred from slope levelling coupled to spring long-term hydrochemical monitoring: example of the La Clapière landslide (Southern Alps, France). *Journal of Hydrology, 291*, 67-90.

Carnec, C., Massonnet, D., & King, C. (1996). Two examples of the use of SAR interferometry on displacement fields of small spatial extent. *Geophysical Research Letters, 23*, 3579-3582.

Carpenter, J.R. (1985). STABL5, the Spencer Method of Slices: Final Report. In. Indiana: Joint Highway Research Project Purdue University.

Carter, M., & Bentley, S.P. (1985). The geometry of slip surfaces beneath landslides: predictions from surface measurements. *Canadian Geotechnical Journal, 22*, 234-238.

Cascini, L., Fornaro, G., & Peduto, D. (2010). Advanced low- and full-resolution DInSAR map generation for slow-moving landslide analysis at different scales. *Engineering Geology, 112*, 29 - 42.

Cascini, L., Peduto, D., Pisciotta, G., Arena, L., Ferlisi, S., & Fornaro, G. (2013). The combination of DInSAR and facility damage data for the updating of slow-moving landslide inventory maps at medium scale. *Nat. Hazards Earth Syst. Sci., 13*, 1527-1549.

Casson, B., Delacourt, C., & Allemand, P. (2005). Contribution of multi-temporal remote sensing images to characterize landslide slip surface ‒ Application to the La Clapière landslide (France). *Nat. Hazards Earth Syst. Sci., 5*, 425-437.

Casu, F., Manconi, A., Pepe, A., & Lanari, R. (2011). Deformation Time-Series Generation in Areas Characterized by Large Displacement Dynamics: The SAR Amplitude Pixel-Offset SBAS Technique. *Geoscience and Remote Sensing, IEEE Transactions on, 49*, 2752-2763.

Catani, F., Farina, P., Moretti, S., Nico, G., & Strozzi, T. (2005). On the application of SAR interferometry to geomorphological studies: estimation of landform attributes and mass movements. *Geomorphology, 66*, 119-131.

Chen, D. (1999). Engineering geological problems in the Three Gorges Project on the Yangtze, China. *Engineering Geology, 51*, 183-193.

Chen, J., & Jahn, B.-m. (1998). Crustal evolution of southeastern China: Nd and Sr isotopic evidence. *Tectonophysics, 284*, 101-133.

Chen, L., & Talwani, P. (1998). Reservoir-induced Seismicity in China. *Pure & Applied Geophysics, 153*, 133-149.

Cheng, Y.M., & Lau, C.K. (2008). *Slope Stability Analysis and Stabilization: New Methods and Insight*. Oxford: Taylor & Francis.

Clark, M.K., Schoenbohm, L.M., Royden, L.H., Whipple, K.X., Burchfiel, B.C., Zhang, X., Tang, W., Wang, E., & Chen, L. (2004). Surface uplift, tectonics, and erosion of eastern Tibet from large-scale drainage patterns. *Tectonics, 23*, TC1006.

Clift, P.D. (2006). Controls on the erosion of Cenozoic Asia and the flux of clastic sediment to the ocean. *Earth and Planetary Science Letters, 241*, 571-580.

Cojean, R., & Caï, Y.J. (2011). Analysis and modeling of slope stability in the Three-Gorges Dam reservoir (China) — The case of Huangtupo landslide. *Journal of Mountain Science, 8*, 166-175.

Colesanti, C., Ferretti, A., Prati, C., & Rocca, F. (2003). Monitoring landslides and tectonic motions with the Permanent Scatterers Technique. *Engineering Geology, 68*, 3 - 14.

Colesanti, C., & Wasowski, J. (2006). Investigating landslides with space-borne Synthetic Aperture Radar (SAR) interferometry. *Engineering Geology, 88*, 173-199.

Crosta, G.B., & Agliardi, F. (2003). Failure forecast for large rock slides by surface displacement measurements. *Canadian Geotechnical Journal, 40*, 176-191.

Cruden, D.M. (1991). A simple definition of a landslide. *Bulletin of the International Association of Engineering Geology - Bulletin de l'Association Internationale de Géologie de l'Ingénieur, 43*, 27-29.

Cruden, D.M., & Varnes, D.J. (1996). Landslide types and processes. In A.K. Turner, & R.L. Shuster (Eds.), *Landslides: Investigation and Mitigation* (pp. 36 - 75). Washington DC: Transport Research Board, National Research Council.

Curlander, J.C., & McDonough, R.N. (1991). *Synthetic Aperture Radar*. New York: John Wiley & Sons.

Dai, S.B., & Lu, X.X. (2010). Sediment deposition and erosion during the extreme flood events in the middle and lower reaches of the Yangtze River. *Quaternary International, 226*, 4-11.

de Michele, M., Raucoules, D., de Sigoyer, J., Pubellier, M., & Chamot-Rooke, N. (2010). Three-dimensional surface displacement of the 2008 May 12 Sichuan earthquake (China) derived from Synthetic Aperture Radar: evidence for rupture on a blind thrust. *Geophysical Journal International, 183*, 1097-1103.

Debella-Gilo, M., & Kääb, A. (2011). Sub-pixel precision image matching for measuring surface displacements on mass movements using normalized cross-correlation. *Remote Sensing of Environment, 115*, 130 - 142.

Debella-Gilo, M., & Kääb, A. (2012). Measurement of Surface Displacement and Deformation of Mass Movements Using Least Squares Matching of Repeat High Resolution Satellite and Aerial Images. *Remote Sensing, 4*, 43-67.

Delacourt, C., Allemand, P., Berthier, E., Raucoules, D., Casson, B., Grandjean, P., Pambrun, C., & Varel, E. (2007). Remote-sensing techniques for analysing landslide kinematics: a review. *Bulletin de la Societe Geologique de France, 178*, 89-100.

Delacourt, C., Allemand, P., Casson, B., & Vadon, H. (2004). Velocity field of the "La Clapière" landslide measured by the correlation of aerial and QuickBird satellite images. *Geophysical Research Letters, 31*, L15619.

Delacourt, C., Raucoules, D., Le Mouélic, S., Carnec, C., Feurer, D., Allemand, P., & Cruchet, M. (2009). Observation of a Large Landslide on La Reunion Island Using Differential Sar Interferometry (JERS and Radarsat) and Correlation of Optical (Spot5 and Aerial) Images. *Sensors, 9*, 616-630.

Densmore, A.L., Anderson, R.S., McAdoo, B.G., & Ellis, M.A. (1997). Hillslope Evolution by Bedrock Landslides. *Science, 275*, 369-372.

Densmore, A.L., & Hovius, N. (2000). Topographic fingerprints of bedrock landslides. *Geology, 28*, 371-374.

Dikau, R., Brunsden, D., & Schrott, L. (1996). *Landslide Recognition: Identification, Movement, and Causes*. New York: Wiley.

Dong, S., & Huang, L. (2011). Mapping surface displacement based on D-InSAR technique. In, *Remote Sensing, Environment and Transportation Engineering (RSETE), 2011 International Conference on* (pp. 3259-3262).

Du, J., Yin, K., & Lacasse, S. (2013). Displacement prediction in colluvial landslides, Three Gorges Reservoir, China. *Landslides, 10*, 203-218.

Ducret, G., Doin, M.P., Grandin, R., Lasserre, C., & Guillaso, S. (2014). DEM Corrections Before Unwrapping in a Small Baseline Strategy for InSAR Time Series Analysis. *Geoscience and Remote Sensing Letters, IEEE, 11*, 696-700.

Dzikiti, S., Verreynne, S.J., Stuckens, J., Strever, A., Verstraeten, W.W., Swennen, R., Theron, K.I., & Coppin, P. (2011). Seasonal variation in canopy reflectance and its application to determine the water status and water use by citrus trees in the Western Cape, South Africa. *Agricultural and Forest Meteorology, 151*, 1035-1044.

Eineder, M., Adam, N., Bamler, R., Yague-Martinez, N., & Breit, H. (2009). Spaceborne Spotlight SAR Interferometry With TerraSAR-X. *Geoscience and Remote Sensing, IEEE Transactions on, 47*, 1524-1535.

Elliot, J.R. (2009). Strain accumulation & release on the Tibetan Plateau measured using InSAR. In, *Department of Earth Sciences* (p. 424). Oxford: University of Oxford.

Evans, S.G., Guthrie, R.H., Roberts, N.J., & Bishop, N.F. (2007). The disastrous 17 February 2006 rockslide-debris avalanche on Leyte Island, Philippines: a catastrophic landslide in tropical mountain terrain. *Nat. Hazards Earth Syst. Sci., 7*, 89-101.

Fallourd, R., Fallourd, R., Vernier, F., Yan, Y., Trouve, E., Bolon, P., Nicolas, J.-M., Tupin, F., Harant, O., Gay, M., Vasile, G., Moreau, L., Walpersdorf, A., Cotte, N., & Mugnier, J.-L. (2010). Alpine glacier 3D displacement derived from ascending and descending TerraSAR-X images on Mont-Blanc test site. In, *Synthetic Aperture Radar (EUSAR), 2010 8th European Conference on* (pp. 1-4).

Fan, D., & Li, C. (2008). Timing of the Yangtze initiation draining the Tibetan Plateau throughout to the East China Sea: a review. *Frontiers of Earth Science in China, 2*, 302-313.

Fan, J., HongLi, Z., Pengfei, T., Yi, W., Guo, X., Daqing, G., & Liu, G. (2010). CRInSAR for landslide deformation monitoring: A case in threegorge area. In, *Geoscience and Remote Sensing Symposium (IGARSS), 2010 IEEE International* (pp. 3956-3959).

Farina, P., Colombo, D., Fumagalli, A., Marks, F., & Moretti, S. (2006). Permanent Scatterers for landslide investigations: outcomes from the ESA-SLAM project. *Engineering Geology, 88*, 200-217.

Feng, W., Li, Z., Elliott, J.R., Fukushima, Y., Hoey, T., Singleton, A., Cook, R., & Xu, Z. (2013). The 2011 MW 6.8 Burma earthquake: fault constraints provided by multiple SAR techniques. *Geophysical Journal International, 195*, 650-660.

Ferretti, A., Monti-Guarnieri, M., Prati, C., & Rocca, F. (2007). *InSAR Principles: Guidelines for SAR Interferometry Processing and Interpretation*. Noordwijk: European Space Agency Publications.

Ferretti, A., Prati, C., & Rocca, F. (2001). Permanent scatterers in SAR interferometry. *Geoscience and Remote Sensing, IEEE Transactions on, 39*, 8-20.

Fialko, Y., Simons, M., & Agnew, D. (2001). The complete (3-D) surface displacement field in the epicentral area of the 1999 MW7.1 Hector Mine Earthquake, California, from space geodetic observations. *Geophysical Research Letters, 28*, 3063-3066.

Fielding, E.J., Lundgren, P.R., Taymaz, T., Yolsal-Çevikbilen, S., & Owen, S.E. (2013). Fault-Slip Source Models for the 2011 M 7.1 Van Earthquake in Turkey from SAR Interferometry, Pixel Offset Tracking, GPS, and Seismic Waveform Analysis. *Seismological Research Letters, 84*, 579-593.

Fleming, R.W., & Johnson, A.M. (1994). Landslides in Colluvium. In. Washington: USGS Geological Survey Bulletin.

Fletcher, K. (2005). *Spaceborne Radar Applications in Geology: An Introduction to Imaging Radar, and Application Examples of ERS SAR in Geology and Geomorphology*. ESA Publications Division, ESTEC.

Fourniadis, I.G., & Liu, J.G. (2007). Landslides in the Wushan-Zigui region of the Three Gorges, China. *Quarterly Journal of Engineering Geology and Hydrogeology, 40*, 115 - 122.

Fourniadis, I.G., Liu, J.G., & Mason, P.J. (2007a). Landslide hazard assessment in the Three Gorges area, China, using ASTER imagery: Wushan–Badong. *Geomorphology, 84*, 126-144.

Fourniadis, I.G., Liu, J.G., & Mason, P.J. (2007b). Regional assessment of landslide impact in the Three Gorges area, China, using ASTER data: Wushan-Zigui. *Landslides, 4*, 267-278.

Fruneau, B., Achache, J., & Delacourt, C. (1996). Observation and modelling of the Saint-Étienne-de-Tinée landslide using SAR interferometry. *Tectonophysics, 265*, 181-190.

Fu, W., Guo, H., Tian, Q., & Guo, X. (2010). Landslide monitoring by corner reflectors differential interferometry SAR. *International Journal of Remote Sensing, 31*, 6387-6400.

Fu, Z., Li, Z., Cai, C., Zhao, Y., Shi, Z., Xu, Q., & Wang, X. (2012). Linking soil thickness and plot-scale hydrological processes on the sloping lands in the Three Gorges Area of China: a hydropedological approach. *Hydrological Processes, 26*, 2248-2263.

Fujita, H. (1977). Influence of water level fluctuations in a reservoir on slope stability. *Bulletin of the International Association of Engineering Geology - Bulletin de l'Association Internationale de Géologie de l'Ingénieur, 16*, 170-173.

Funning, G.J., Parsons, B., Wright, T.J., Jackson, J.A., & Fielding, E.J. (2005). Surface displacements and source parameters of the 2003 Bam (Iran) earthquake from Envisat advanced synthetic aperture radar imagery. *Journal of Geophysical Research: Solid Earth, 110*, B09406.

Furuya, M. (2011). SAR Interferometry. In H. Gupta (Ed.), *Encyclopedia of Solid Earth Geophysics* (pp. 1041-1049): Springer Netherlands.

Gance, J., Malet, J.P., Dewez, T., & Travelletti, J. (2014). Target Detection and Tracking of moving objects for characterizing landslide displacements from time-lapse terrestrial optical images. *Engineering Geology, 172*, 26-40.

Gatelli, F., Guamieri, A.M., Parizzi, F., Pasquali, P., Prati, C., & Rocca, F. (1994). The wavenumber shift in SAR interferometry. *Geoscience and Remote Sensing, IEEE Transactions on, 32*, 855-865.

Gelautz, M., Frick, H., Raggam, J., Burgstaller, J., & Leberl, F. (1998). SAR image simulation and analysis of alpine terrain. *ISPRS Journal of Photogrammetry and Remote Sensing, 53*, 17-38.

Giles, A.B., Massom, R.A., & Warner, R.C. (2009). A method for sub-pixel scale feature-tracking using Radarsat images applied to the Mertz Glacier Tongue, East Antarctica. *Remote Sensing of Environment, 113*, 1691-1699.

Glade, T., & Crozier, M.J. (2005). The Nature of Landslide Hazard Impact. *Landslide Hazard and Risk* (pp. 41-74). Chichester: John Wiley & Sons, Ltd.

Gleick, P.H., Palaniappan, M., Morikawa, M., Morrison, J., & Cooley, H. (2013). *The World's Water 2008-2009: The Biennial Report on Freshwater Resources*. Island Press.

Goldstein, R.M., & Werner, C.L. (1998). Radar interferogram filtering for geophysical applications. *Geophysical Research Letters, 25*, 4035-4038.

Grandin, R., Socquet, A., Binet, R., Klinger, Y., Jacques, E., de Chabalier, J.B., King, G.C.P., Lasserre, C., Tait, S., Tapponnier, P., Delorme, A., & Pinzuti, P. (2009). September 2005 Manda Hararo-Dabbahu rifting event, Afar (Ethiopia): Constraints provided by geodetic data. *Journal of Geophysical Research: Solid Earth, 114*, B08404.

Gutiérrez, F., Soldati, M., Audemard, F., & Bălteanu, D. (2010). Recent advances in landslide investigation: Issues and perspectives. *Geomorphology, 124*, 95-101.

Guzzetti, F., Peruccacci, S., Rossi, M., & Stark, C.P. (2007). Rainfall thresholds for the initiation of landslides in central and southern Europe. *Meteorology and Atmospheric Physics, 98*, 239-267.

Hanssen, R.F. (2001). *Radar Interferometry: Data Interpretation and Error Analysis*. Dordrecht: Kluwer Academic Publishers.

Hanssen, R.F. (2005). Satellite radar interferometry for deformation monitoring: a priori assessment of feasibility and accuracy. *International Journal of Applied Earth Observation and Geoinformation, 6*, 253-260.

Haug, T., Kääb, A., & Skvarca, P. (2010). Monitoring ice shelf velocities from repeat MODIS and Landsat data – a method study on the Larsen C ice shelf, Antarctic Peninsula, and 10 other ice shelves around Antarctica. *The Cryosphere, 4*, 161-178.

Hayakawa, Y.S., Oguchi, T., & Lin, Z. (2008). Comparison of new and existing global digital elevation models: ASTER G-DEM and SRTM-3. *Geophysical Research Letters, 35*, L17404.

He, K., Guangming, Y., & Xiangran, L. (2009). The regional distribution regularity of landslides and their effects on the environments in the Three Gorges reservoir region, China. *Environmental Geology, 57*, 1925 - 1931.

He, K., Li, X., Yan, X., & Guo, D. (2008). The landslides in the Three Gorges Reservoir Region, China and the effects of water storage and rain on their stability. *Environmental Geology, 55*, 55-63.

He, K., & Wang, S. (2006). Double-parameter threshold and its formation mechanism of the colluvial landslide: Xintan landslide, China. *Environmental Geology, 49*, 696 - 707.

He, K., Wang, S., Du, W., & Wang, S. (2010). Dynamic features and effects of rainfall on landslides in the Three Gorges Reservoir region, China: using the Xintan landslide and the large Huangya landslide as the examples. *Environmental Earth Sciences, 59*, 1267-1274.

Hendron, A.J., & Patton, F.D. (1987). The vaiont slide — A geotechnical analysis based on new geologic observations of the failure surface. *Engineering Geology, 24*, 475-491.

Herrera, G., Gutiérrez, F., García-Davalillo, J.C., Guerrero, J., Notti, D., Galve, J.P., Fernández-Merodo, J.A., & Cooksley, G. (2013). Multi-sensor advanced DInSAR monitoring of very slow landslides: The Tena Valley case study (Central Spanish Pyrenees). *Remote Sensing of Environment, 128*, 31-43.

Herrera, G., Notti, D., García-Davalillo, J., Mora, O., Cooksley, G., Sánchez, M., Arnaud, A., & Crosetto, M. (2011). Analysis with C- and X-band satellite SAR data of the Portalet landslide area. *Landslides, 8*, 195-206.

Hervás, J., Barredo, J.I., Rosin, P.L., Pasuto, A., Mantovani, F., & Silvano, S. (2003). Monitoring landslides from optical remotely sensed imagery: the case history of Tessina landslide, Italy. *Geomorphology, 54*, 63-75.

Hilley, G.E., Bürgmann, R., Ferretti, A., Novali, F., & Rocca, F. (2004). Dynamics of Slow-Moving Landslides from Permanent Scatterer Analysis. *Science, 304*, 1952-1955.

Hong, Y., Adler, R., & Huffman, G. (2006). Evaluation of the potential of NASA multi-satellite precipitation analysis in global landslide hazard assessment. *Geophysical Research Letters, 33*, L22402.

Hooper, A. (2008). A multi-temporal InSAR method incorporating both persistent scatterer and small baseline approaches. *Geophysical Research Letters, 35*, L16302.

Hooper, A., Segall, P., & Zebker, H. (2007). Persistent scatterer interferometric synthetic aperture radar for crustal deformation analysis, with application to Volcán Alcedo, Galápagos. *Journal of Geophysical Research: Solid Earth, 112*, B07407.

Hooper, A., Zebker, H.A., Segall, P., & Kampes, B.M. (2004). A new method for measureing deformation on volcanoes and other natural terrains using InSAR persistent scatterers. *Geophysical Research Letters, 31.*

Hu, J., Li, Z.W., Ding, X.L., Zhu, J.J., Zhang, L., & Sun, Q. (2012a). 3D coseismic Displacement of 2010 Darfield, New Zealand earthquake estimated from multi-aperture InSAR and D-InSAR measurements. *Journal of Geodesy, 86*, 1029-1041.

Hu, J., Li, Z.W., Ding, X.L., Zhu, J.J., Zhang, L., & Sun, Q. (2014a). Resolving three-dimensional surface displacements from InSAR measurements: A review. *Earth-Science Reviews, 133*, 1-17.

Hu, X., Tang, H., Li, C., & Sun, R. (2012b). Stability of Huangtupo riverside slumping mass II# under water level fluctuation of Three Gorges Reservoir. *Journal of Earth Science, 23*, 326-334.

Hu, X., Wang, T., & Liao, M. (2014b). Measuring Coseismic Displacements With Point-Like Targets Offset Tracking. *Geoscience and Remote Sensing Letters, IEEE, 11*, 283-287.

Hu, X., Zhang, M., Sun, M., Huang, K., & Song, Y. (2013). Deformation characteristics and failure mode of the Zhujiadian landslide in the Three Gorges Reservoir, China. *Bulletin of Engineering Geology and the Environment*, 1-12.

Huang, Z., Law, K.T., Liu, H., & Jiang, T. (2009). The chaotic characteristics of landslide evolution: a case study of Xintan landslide. *Environmental Geology, 56*, 1585 - 1591.

Iglesias, R., Monells, D., Centolanza, G., Mallorqui, J.J., Fabregas, X., & Aguasca, A. (2012). Landslide monitoring with spotlight TerraSAR-X DATA. In, *Geoscience and Remote Sensing Symposium (IGARSS), 2012 IEEE International* (pp. 1298-1301).

Iverson, R.M. (2000). Landslide triggering by rain infiltration. *Water Resources Research, 36*, 1897-1910.

Jia, G.W., Zhan, T.L.T., Chen, Y.M., & Fredlund, D.G. (2009). Performance of a large-scale slope model subjected to rising and lowering water levels. *Engineering Geology, 106*, 92-103.

Jia, Z., Liu, G., Wang, W., & Zhou, Y. (2013). GNSS Investigation in the Early Stage of the Three Gorges Project on the Yangtze River. In F. Bian, Y. Xie, X. Cui, & Y. Zeng (Eds.), *Geo-Informatics in Resource Management and Sustainable Ecosystem* (pp. 389-396): Springer Berlin Heidelberg.

Jian, W., Wang, Z., & Yin, K. (2009). Mechanism of the Anlesi landslide in the Three Gorges Reservoir, China. *Engineering Geology, 108*, 86-95.

Jiang, J., Ehret, D., Xiang, W., Rohn, J., Huang, L., Yan, S., & Bi, R. (2011a). Numerical simulation of Qiaotou Landslide deformation caused by drawdown of the Three Gorges Reservoir, China. *Environmental Earth Sciences, 62*, 411-419.

Jiang, M., Li, Z.W., Ding, X.L., Zhu, J.J., & Feng, G.C. (2011b). Modeling minimum and maximum detectable deformation gradients of interferometric SAR measurements. *International Journal of Applied Earth Observation and Geoinformation, 13*, 766-777.

Jónsson, S., Zebker, H., & Amelung, F. (2005). On trapdoor faulting at Sierra Negra volcano, Galápagos. *Journal of Volcanology and Geothermal Research, 144*, 59-71.

Jónsson, S., Zebker, H., Segall, P., & Amelung, F. (2002). Fault Slip Distribution of the 1999 Mw 7.1 Hector Mine, California, Earthquake, Estimated from Satellite Radar and GPS Measurements. *Bulletin of the Seismological Society of America, 92*, 1377-1389.

Kääb, A. (2002). Monitoring high-mountain terrain deformation from repeated air- and spaceborne optical data: examples using digital aerial imagery and ASTER data. *ISPRS Journal of Photogrammetry and Remote Sensing, 57*, 39-52.

Kalenchuk, K.S., Hutchinson, D.J., & Diederichs, M.S. (2013). Downie Slide: numerical simulation of groundwater fluctuations influencing the behaviour of a massive landslide. *Bulletin of Engineering Geology and the Environment, 72*, 397-412.

Keefer, D.K. (1984). Landslides caused by earthquakes. *Geological Society of America Bulletin, 95*, 406-421.

Keefer, D.K. (2002). Investigating Landslides Caused by Earthquakes – A Historical Review. *Surveys in Geophysics, 23*, 473-510.

Korup, O., Densmore, A.L., & Schlunegger, F. (2010). The role of landslides in mountain range evolution. *Geomorphology, 120*, 77-90.

Kropatsch, W.G., & Strobl, D. (1990). The generation of SAR layover and shadow maps from digital elevation models. *Geoscience and Remote Sensing, IEEE Transactions on, 28*, 98-107.

Lee, E.M., & Jones, D.K.C. (2004). *Landslide Risk Assessment*. London: Thomas Telford.

Lehner, B., Reidy Liermann, C., Revenga, C., Vorosmarty, C., Fekete, B., Crouzet, P., Doll, P., Endejan, M., Frenken, K., Magome, J., Nilsson, C., Robertson, J.C., Rodel, R., Sindorf, N., & Wisser, D. (2011). Global Reservoir and Dam Database, Version 1 (GRanDv1): Dams, Revision 01. In. Palisades, NY: NASA Socioeconomic Data and Applications Center (SEDAC).

Leprince, S., Berthier, E., Ayoub, F., Delacourt, C., & Avouac, J.-P. (2008). Monitoring Earth Surface Dynamics With Optical Imagery. *Eos, Transactions American Geophysical Union, 89*, 1-2.

Leroueil, S., Locat, J., Sève, G., Picarelli, L., & Faure, R.M. (2001). Slopes and Mass Movements. In R.K. Rowe (Ed.), *Geotechnical and Geoenvironmental Engineering Handbook* (pp. 397-428). New York: Springer.

Leroueil, S., Vaunat, J., Picaerlli, L., Locat, J., Lee, H., & Faue, R.M. (1996). Geotechnical characterisation of slope movements. In K. Senneset (Ed.), *7th International Symposium on Landslides* (pp. 53 - 74). Balkeme, Rotterdam.

Lewis, J.P. (1995). Fast normalized cross-correlation. *Vision Interface, 10*, 120 - 123.

Li, D., Yin, K., & Leo, C. (2010). Analysis of Baishuihe landslide influenced by the effects of reservoir water and rainfall. *Environmental Earth Sciences, 60*, 677-687.

Li, J., Xie, S., & Kuang, M. (2001). Geomorphic evolution of the Yangtze Gorges and the time of their formation. *Geomorphology, 41*, 125-135.

Li, P., Shi, C., Li, Z., Muller, J.-P., Drummond, J., Li, X., Li, T., Li, Y., & Liu, J. (2012). Evaluation of ASTER GDEM using GPS benchmarks and SRTM in China. *International Journal of Remote Sensing, 34*, 1744-1771.

Li, Q.S., Li, Z.N., Li, G.Q., Meng, J.F., & Tang, J. (2005). Experimental and numerical seismic investigations of the Three Gorges dam. *Engineering Structures, 27*, 501-513.

Li, X., Muller, J.-P., Chen, F., & Yonghong, Z. (2011a). Measuring displacement field from TerraSAR-X amplitude images by subpixel correlation: an application to the landslide in Shping, Three Gorges Area. *Acta Petrologica Sinica, 27*, 3843 - 3850.

Li, Y. (2012). Three Gorges Dam Set to Displace 100,000. In, *Shanghai Daily*.

Li, Z., Elliott, J.R., Feng, W., Jackson, J.A., Parsons, B.E., & Walters, R.J. (2011b). The 2010 MW 6.8 Yushu (Qinghai, China) earthquake: Constraints provided by InSAR and body wave seismology. *Journal of Geophysical Research: Solid Earth, 116*, B10302.

Liao, M., Tang, J., Wang, T., Balz, T., & Zhang, L. (2012). Landslide monitoring with high-resolution SAR data in the Three Gorges region. *Science China Earth Sciences, 55*, 590-601.

Liao, M., Zhang, L., & Balz, T. (2013). Landslide monitoring with high-resolution TerraSAR-X data in the Three Gorges area. In, *5th TerraSAR-X Science Team Meeting*. DLR Oberpfaffenhofen.

Liu, C., Liu, Y., Wen, M., Li, T., Lian, J., & Qin, S. (2009). Geo-hazard Initiation and Assessment in the Three Gorges Reservoir. In F. Wang, & T. Li (Eds.), *Landslide Disaster Mitigation in Three Gorges Reservoir, China* (pp. 3-40): Springer Berlin Heidelberg.

Liu, J.G., Mason, P.J., Clerici, N., Chen, S., Davis, A., Miao, F., Deng, H., & Liang, L. (2004). Landslide hazard assessment in the Three Gorges area of the Yangtze river using ASTER imagery: Zigui–Badong. *Geomorphology, 61*, 171-187.

Liu, P., Li, Z., Hoey, T., Kincal, C., Zhang, J., Zeng, Q., & Muller, J.-P. (2013). Using advanced InSAR time series techniques to monitor landslide movements in Badong of the Three Gorges region, China. *International Journal of Applied Earth Observation and Geoinformation, 21*, 253-264.

Loo, H. (2006). Reactivation of an old landslide in response to reservoir impoundment and fluctuations. In, *Civil Engineering* (p. 260). Hong Kong: University of Hong Kong.

Lu, N., & Godt, J.W. (2013). *Hillslope Hydrology and Stability*. Cambridge: Cambridge University Press.

Lucieer, A., Jong, S.M.d., & Turner, D. (2014). Mapping landslide displacements using Structure from Motion (SfM) and image correlation of multi-temporal UAV photography. *Progress in Physical Geography, 38*, 97-116.

Luckman, A., Quincey, D., & Bevan, S. (2007). The potential of satellite radar interferometry and feature tracking for monitoring flow rates of Himalayan glaciers. *Remote Sensing of Environment, 111*, 172-181.

Luo, X., Wang, F., Zhang, Z., & Che, A. (2009). Establishing a monitoring network for an impoundment-induced landslide in Three Gorges Reservoir Area, China. *Landslides, 6*, 27-37.

Malet, J.P., Maquaire, O., & Calais, E. (2002). The use of Global Positioning System techniques for the continuous monitoring of landslides: application to the Super-Sauze earthflow (Alpes-de-Haute-Provence, France). *Geomorphology, 43*, 33-54.

Manconi, A., Casu, F., Ardizzone, F., Bonano, M., Cardinali, M., De Luca, C., Gueguen, E., Marchesini, I., Parise, M., Vennari, C., Lanari, R., & Guzzetti, F. (2014). Brief Communication: Rapid mapping of landslide events: the 3 December 2013 Montescaglioso landslide, Italy. *Nat. Hazards Earth Syst. Sci., 14*, 1835-1841.

Mansour, M., Morgenstern, N., & Martin, C.D. (2011). Expected damage from displacement of slow-moving slides. *Landslides, 8*, 117-131.

Martone, M., Rizzoli, P., Bräutigam, B., & Krieger, G. (2013). First 2 years of TanDEM-X mission: Interferometric performance overview. *Radio Science, 48*, 617-627.

Mason, R. (1999). The Three Gorges Dam of the Yangtze River, China: engineering geology in China. *Geology Today, 15*, 30-33.

Massey, C.I., Petley, D.N., & McSaveney, M.J. (2013). Patterns of movement in reactivated landslides. *Engineering Geology, 159*, 1-19.

Massonnet, D., & Feigl, K.L. (1998). Radar interferometry and its application to changes in the Earth's surface. *Reviews of Geophysics, 36*, 441-500.

Massonnet, D., Feigl, K.L., Rossi, M., & Adragna, F. (1994). Radar interferometric mapping of deformation in the year after the Landers earthquake. *Nature, 369*, 227 - 230.

Massonnet, D., Rossi, M., Carmona, C., Adragna, F., Peltzer, G., Feigl, K., & Rabaute, T. (1993a). The displacement field of the Landers earthquake mapped by radar interferometry. *Nature, 364*, 138-142.

Massonnet, D., Rossi, M., Carmona, C., Adragna, F., Peltzer, G., Feigl, K.L., & Rabaute, T. (1993b). The displacement field of the Landers earthquake mapped by radar interferometry. *Nature, 364*, 138 - 142.

McGuire, B., Mason, I.M., Mason, I., & Kilburn, C.R.J. (2002). *Natural Hazards and Environmental Change*. London: Arnold.

Mei, B., Xu, Y., & Zhang, Y. (2013). P- and S-velocity structure beneath the Three Gorges region (central China) from local earthquake tomography. *Geophysical Journal International, 193*, 1035-1049.

Metternicht, G., Hurni, L., & Gogu, R. (2005). Remote sensing of landslides: An analysis of the potential contribution to geo-spatial systems for hazard assessment in mountainous environments. *Remote Sensing of Environment, 98*, 284-303.

Meunier, P., Hovius, N., & Haines, A.J. (2007). Regional patterns of earthquake-triggered landslides and their relation to ground motion. *Geophysical Research Letters, 34*, L20408.

Miao, H., Wang, G., Yin, K., Kamai, T., & Li, Y. (2014). Mechanism of the slow-moving landslides in Jurassic red-strata in the Three Gorges Reservoir, China. *Engineering Geology, 171*, 59-69.

Michel, R., Avouac, J.-P., & Taboury, J. (1999). Measuring ground displacements from SAR amplitude images: Application to the Landers Earthquake. *Geophysical Research Letters, 26*, 875-878.

Michoud, C., Abellán, A., Derron, M.H., & Jaboyedoff, M. (2010). Guidelines for the selection of approrpiate remote sensing technologies for monitoring different types of landslides. In A. Stumpf, N. Kerle, & J.-P. Malet (Eds.), *The Deliverable 4.4 of the European SAFELAND Project.*

Monserrat, O., Moya, J., Luzi, G., Crosetto, M., Gili, J.A., & Corominas, J. (2013). Non-interferometric GB-SAR measurement: application to the Vallcebre landslide (eastern Pyrenees, Spain). *Nat. Hazards Earth Syst. Sci., 13*, 1873-1887.

Nordvik, T., & Nyrnes, E. (2009). Statistical analysis of surface displacements – an example from the Åknes rockslide, western Norway. *Nat. Hazards Earth Syst. Sci., 9*, 713-724.

Notti, D., Davalillo, J.C., Herrera, G., & Mora, O. (2010). Assessment of the performance of X-band satellite radar data for landslide mapping and monitoring: Upper Tena Valley case study. *Nat. Hazards Earth Syst. Sci., 10*, 1865-1875.

Parker, R.N., Densmore, A.L., Rosser, N.J., de Michele, M., Li, Y., Huang, R., Whadcoat, S., & Petley, D.N. (2011). Mass wasting triggered by the 2008 Wenchuan earthquake is greater than orogenic growth. *Nature Geoscience, 4*, 449-452.

Paronuzzi, P., Rigo, E., & Bolla, A. (2013). Influence of filling–drawdown cycles of the Vajont reservoir on Mt. Toc slope stability. *Geomorphology, 191*, 75-93.

Pathier, E., Fielding, E.J., Wright, T.J., Walker, R., Parsons, B.E., & Hensley, S. (2006). Displacement field and slip distribution of the 2005 Kashmir earthquake from SAR imagery. *Geophysical Research Letters, 33*, L20310.

Peduto, D., Cascini, L., & Fornaro, G. (2010). Satellite radar. In V. Tofani, S. Segoni, F. Catani, & N. Casagli (Eds.), *Evaluation report on innovative monitoring and remote sensing methods and future technology* (pp. 42 - 43). Oslo: Norwegian Geotechnical Institute.

Peltzer, G., Crampé, F., & King, G. (1999). Evidence of Nonlinear Elasticity of the Crust from the Mw7.6 Manyi (Tibet) Earthquake. *Science, 286*, 272-276.

Peng, L., Niu, R., Huang, B., Wu, X., Zhao, Y., & Ye, R. (2014). Landslide susceptibility mapping based on rough set theory and support vector machines: A case of the Three Gorges area, China. *Geomorphology, 204*, 287-301.

Perissin, D., & Teng, W. (2012). Repeat-Pass SAR Interferometry With Partially Coherent Targets. *Geoscience and Remote Sensing, IEEE Transactions on, 50*, 271-280.

Perissin, D., & Wang, T. (2011). Time-Series InSAR applications over urban areas in China. *IEEE Journal of Selected Topics in Applied Earth Observations and Remote Sensing, 4*, 92 - 100.

Perski, Z., Liu, G., Wojciechowski, T., Jinhui, F., & Wójcik, A. (2014). Monitoring the Activity of Landslides in the Coastal Zones of Reservoirs with SAR Interferometry. In K. Sassa, P. Canuti, & Y. Yin (Eds.), *Landslide Science for a Safer Geoenvironment* (pp. 331-336): Springer International Publishing.

Petley, D. (2012). Global patterns of loss of life from landslides. *Geology, 40*, 927 - 930.

Petley, D.N. (2013). Global losses from landslides associated with dams and reservoirs. In R. Genevois, & A. Prestininzi (Eds.), *International Conference on Vajont – 1963-2013. Thoughts and analyses after 50 years since the catastrophic landslide* (pp. 63 - 72). Padua, Italy.

Petley, D.N., Mantovani, F., Bulmer, M.H., & Zannoni, A. (2005). The use of surface monitoring data for the interpretation of landslide movement patterns. *Geomorphology, 66*, 133-147.

Petschko, H., Brenning, A., Bell, R., Goetz, J., & Glade, T. (2014). Assessing the quality of landslide susceptibility maps – case study Lower Austria. *Nat. Hazards Earth Syst. Sci., 14*, 95-118.

Pettorelli, N., Vik, J.O., Mysterud, A., Gaillard, J.-M., Tucker, C.J., & Stenseth, N.C. (2005). Using the satellite-derived NDVI to assess ecological responses to environmental change. *Trends in Ecology & Evolution, 20*, 503-510.

Pinyol, N., Alonso, E., Corominas, J., & Moya, J. (2012). Canelles landslide: modelling rapid drawdown and fast potential sliding. *Landslides, 9*, 33-51.

Pipkin, B., Trent, D., Hazlett, R., & Bierman, P. (2010). *Geology and the Environment*. California: Cengage Learning.

Plank, S., Singer, J., Minet, C., & Thuro, K. (2012). Pre-survey suitability evaluation of the differential synthetic aperture radar interferometry method for landslide monitoring. *International Journal of Remote Sensing, 33*, 6623-6637.

Prati, C., Ferretti, A., & Perissin, D. (2010). Recent advances on surface ground deformation measurement by means of repeated space-borne SAR observations. *Journal of Geodynamics, 49*, 161-170.

Qin, H., Wang, S., & Wang, G. (2010). Revival mechanism of Shuping landslide to water level fluctuation in Three Gorges reservoir. In, *International Symposium on Multi-field Coupling Theory of Rock and Soil Media and its Applications*. Chegdu, China: Science Innovation Academic Frontier (online).

Qiu, Y.M., Gao, S., McNaughton, N.J., Groves, D.I., & Ling, W. (2000). First evidence of >3.2 Ga continental crust in the Yangtze craton of south China and its implications for Archean crustal evolution and Phanerozoic tectonics. *Geology, 28*, 11-14.

Quincey, D.J., Lucas, R.M., Richardson, S.D., Glasser, N.F., Hambrey, M.J., & Reynolds, J.M. (2005). Optical remote sensing techniques in high-mountain environments: application to glacial hazards. *Progress in Physical Geography, 29*, 475-505.

Raucoules, D., Carnec, C., Cruchet, M., Delacourt, C., Feurer, D., & Le Mouelic, S. (2003). Identification of landslides in La Reunion Island with JERS-1 and RADARSAT-1 radar interferometry. In ESA (Ed.), *FRINGE*. Frascati, Italy.

Raucoules, D., de Michele, M., Malet, J.P., & Ulrich, P. (2013). Time-variable 3D ground displacements from high-resolution synthetic aperture radar (SAR). application to La Valette landslide (South French Alps). *Remote Sensing of Environment, 139*, 198-204.

Reed, B.C., Brown, J.F., VanderZee, D., Loveland, T.R., Merchant, J.W., & Ohlen, D.O. (1994). Measuring phenological variability from satellite imagery. *Journal of Vegetation Science, 5*, 703-714.

Ren, X.Z., Qin, Y., & Qioa, L.H. (2012). Interferometric properties and processing for spaceborne Spotlight SAR. *Progress in Electromagnetics Research B, 36*, 267 - 281.

Richards, J.A. (2009). *Remote Sensing with Imaging Radar*. Springer.

Richardson, N.J., Densmore, A.L., Seward, D., Wipf, M., & Yong, L. (2010). Did incision of the Three Gorges begin in the Eocene? *Geology, 38*, 551-554.

Rosen, P.A., Hensley, S., Joughin, I.R., Li, F.K., Madsen, S.N., Rodriguez, E., & Goldstein, R.M. (2000). Synthetic aperture radar interferometry. *Proceedings of the IEEE, 88*, 333 - 382.

Rott, H. (2009). Advances in interferometric synthetic aperture radar (InSAR) in earth system science. *Progress in Physical Geography, 33*, 769-791.

Rott, H., & Nagler, T. (2006). The contribution of radar interferometry to the assessment of landslide hazards. *Advances in Space Research, 37*, 710-719.

Rott, H., Scheuchl, B., Siegel, A., & Grasemann, B. (1999). Monitoring very slow slope movements by means of SAR interferometry: A case study from a mass waste above a reservoir in the Ötztal Alps, Austria. *Geophysical Research Letters, 26*, 1629-1632.

SARMAP (2012). SARScape: Technical Description. In, *(pdf)*. Switzerland.

Sassa, K., Picarelli, L., & Yueping, Y. (2009). Monitoring, Prediction and Early Warning. In K. Sassa, & P. Canuti (Eds.), *Landslides – Disaster Risk Reduction* (pp. 351-375): Springer Berlin Heidelberg.

Scaioni, M. (2013). Remote Sensing for Landslide Investigations: From Research into Practice. *Remote Sensing, 5*, 5488-5492.

Scambos, T.A., Dutkiewicz, M.J., Wilson, J.C., & Bindschadler, R.A. (1992). Application of image cross-correlation to the measurement of glacier velocity using satellite image data. *Remote Sensing of Environment, 42*, 177-186.

Schulz, W.H., Lidke, D.J., & Godt, J.W. (2008). Modeling the spatial distribution of landslide-prone colluvium and shallow groundwater on hillslopes of Seattle, WA. *Earth Surface Processes and Landforms, 33*, 123 - 141.

Semenza, E., & Ghirotti, M. (2000). History of the 1963 Vaiont slide: the importance of geological factors. *Bulletin of Engineering Geology and the Environment, 59*, 87-97.

Simons, M., Fialko, Y., & Rivera, L. (2002). Coseismic Deformation from the 1999 Mw 7.1 Hector Mine, California, Earthquake as Inferred from InSAR and GPS Observations. *Bulletin of the Seismological Society of America, 92*, 1390-1402.

Singhroy, V., & Molch, K. (2004). Characterizing and monitoring rockslides from SAR techniques. *Advances in Space Research, 33*, 290-295.

Smith, I. (2006). *Elements of Soil Mechanics*. Oxford: Wiley.

Smith, L.C. (2002). Emerging Applications of Interferometric Synthetic Aperture Radar (InSAR) in Geomorphology and Hydrology. *Annals of the Association of American Geographers, 92*, 385-398.

Spagnolini, U. (1995). 2-D phase unwrapping and instantaneous frequency estimation. *Geoscience and Remote Sensing, IEEE Transactions on, 33*, 579-589.

Squarzoni, C., Delacourt, C., & Allemand, P. (2003). Nine years of spatial and temporal evolution of the La Valette landslide observed by SAR interferometry. *Engineering Geology, 68*, 53-66.

Strozzi, T., Delaloye, R., Kääb, A., Ambrosi, C., Perruchoud, E., & Wegmüller, U. (2010). Combined observations of rock mass movements using satellite SAR interferometry, differential GPS, airborne digital photogrammetry, and airborne photography interpretation. *Journal of Geophysical Research: Earth Surface, 115*, F01014.

Strozzi, T., Farina, P., Corsini, A., Ambrosi, C., Thüring, M., Zilger, J., Wiesmann, A., Wegmüller, U., & Werner, C. (2005). Survey and monitoring of landslide displacements by means of L-band satellite SAR interferometry. *Landslides, 2*, 193-201.

Strozzi, T., Kääb, A., & Frauenfelder, R. (2004). Detecting and quantifying mountain permafrost creep from in situ inventory, space-borne radar interferometry and airborne digital photogrammetry. *International Journal of Remote Sensing, 25*, 2919-2931.

Strozzi, T., Luckman, A., Murray, T., Wegmuller, U., & Werner, C.L. (2002). Glacier motion estimation using SAR offset-tracking procedures. *Geoscience and Remote Sensing, IEEE Transactions on, 40*, 2384-2391.

Strozzi, T., Wegmuller, U., Werner, C.L., Wiesmann, A., & Spreckels, V. (2003). JERS SAR interferometry for land subsidence monitoring. *Geoscience and Remote Sensing, IEEE Transactions on, 41*, 1702-1708.

Stumpf, A., Kerle, N., & Malet, J.-P. (2010). Review of Techniques for Landslide Detection, Fast Characterization, Rapid Mapping and Long-Term Monitoring. In A. Stumpf, N. Kerle, & J.-P. Malet (Eds.), *The Deliverable 4.1 of the European SAFELAND Project.*

Tan, C., Sun, Y., Wang, R., & Hu, D. (1997). Assessment and zonation of regional crustal stability in and around the dam region of the Three Gorges Project on the Yangtze River. *Environmental Geology, 32*, 285-295.

Tantianuparp, P., Shi, X., Zhang, L., Balz, T., & Liao, M. (2013). Characterization of Landslide Deformations in Three Gorges Area Using Multiple InSAR Data Stacks. *Remote Sensing, 5*, 2704-2719.

Thiebes, B. (2012). Theoretical Background. *Landslide Analysis and Early Warning Systems* (pp. 7-84): Springer Berlin Heidelberg.

Tofani, V., Raspini, F., Catani, F., & Casagli, N. (2013). Persistent Scatterer Interferometry (PSI) Technique for Landslide Characterization and Monitoring. *Remote Sensing, 5*, 1045-1065.

Tofani, V., Segoni, S., Catani, F., & Casagli, N. (2010). Evaluation report on innovative monitoring and remote sensing methods and future technology. In V. Tofani, S. Segoni, F. Catani, & N. Casagli (Eds.), *The Deliverable 4.5 of the European SAFELAND Project.*

Tolomei, C., Taramelli, A., Moro, M., Saroli, M., Aringoli, D., & Salvi, S. (2013). Analysis of the deep-seated gravitational slope deformations over Mt. Frascare (Central Italy) with geomorphological assessment and DInSAR approaches. *Geomorphology, 201*, 281-292.

Tomás, R., Li, Z., Liu, P., Singleton, A., Hoey, T., & Cheng, X. (2014). Spatiotemporal characteristics of the Huangtupo landslide in the Three Gorges region (China) constrained by radar interferometry. *Geophysical Journal International.*

Touzi, R., Lopes, A., Bruniquel, J., & Vachon, P.W. (1999). Coherence estimation for SAR imagery. *Geoscience and Remote Sensing, IEEE Transactions on, 37*, 135-149.

Tralli, D.M., Blom, R.G., Zlotnicki, V., Donnellan, A., & Evans, D.L. (2005). Satellite remote sensing of earthquake, volcano, flood, landslide and coastal inundation hazards. *ISPRS Journal of Photogrammetry and Remote Sensing, 59*, 185-198.

Travelletti, J., Delacourt, C., Allemand, P., Malet, J.P., Schmittbuhl, J., Toussaint, R., & Bastard, M. (2012). Correlation of multi-temporal ground-based optical images for

landslide monitoring: Application, potential and limitations. *ISPRS Journal of Photogrammetry and Remote Sensing, 70*, 39-55.

Tullos, D. (2009). Assessing the influence of environmental impact assessments on science and policy: An analysis of the Three Gorges Project. *Journal of Environmental Management, 90, Supplement 3*, S208-S223.

UN-ISDR (Ed.) (2004). *Terminology: Basic Terms of Disaster Risk Reduction*. Geneva: United Nations.

van Asch, T.W.J., Buma, J., & van Beek, L.P.H. (1999). A view on some hydrological triggering systems in landslides. *Geomorphology, 30*, 25-32.

van Asch, T.W.J., Malet, J.P., & Bogaard, T.A. (2009). The effect of groundwater fluctuations on the velocity pattern of slow-moving landslides. *Nat. Hazards Earth Syst. Sci., 9*, 739-749.

van Asch, T.W.J., Van Beek, L.P.H., & Bogaard, T.A. (2007). Problems in predicting the mobility of slow-moving landslides. *Engineering Geology, 91*, 46-55.

Varnes, D.J. (1978). Slope movements: types and processes. In R.L. Schuster, & R.J. Krisek (Eds.), *Landslides Analysis Control* (pp. 11-33): Transport Report Board.

Wang, F.-W., Zhang, Y.-M., Huo, Z.-T., Matsumoto, T., & Huang, B.-L. (2004). The July 14, 2003 Qianjiangping landslide, Three Gorges Reservoir, China. *Landslides, 1*, 157-162.

Wang, F., Wang, G., Sassa, K., Takeuchi, A., Araiba, K., Zhang, Y., & Peng, X. (2005a). Displacement Monitoring and Physical Exploration on the Shuping Landslide Reactivated by Impoundment of the Three Gorges Reservoir, China. In K. Sassa, H. Fukuoka, F. Wang, & G. Wang (Eds.), *Landslides* (pp. 313-319): Springer Berlin Heidelberg.

Wang, F., Yin, Y., Huo, Z., & Wang, G. (2013a). Landsliding Caused by Water Level Variation in China Three Gorges Reservoir. In C. Margottini, P. Canuti, & K. Sassa (Eds.), *Landslide Science and Practice* (pp. 19-26): Springer Berlin Heidelberg.

Wang, F., Yueping, Y., Zhitao, H., Zhang, Y., Wang, G., & Renjie, D. (2013b). Slope deformation caused by water-level variation in the Three Gorges Reservoir, China. In K. Sassa, B. Rouhban, S. Briceno, M. McSaveney, & B. He (Eds.), *Landslides: Global Risk Preparedness* (pp. 227 - 237). Berlin: Springer.

Wang, F., Zhang, Y., Huo, Z., Peng, X., Araiba, K., & Wang, G. (2008a). Movement of the Shuping landslide in the first four years after the initial impoundment of the Three Gorges Dam Reservoir, China. *Landslides, 5*, 321-329.

Wang, F., Zhang, Y., Huo, Z., Peng, X., Wang, S., & Yamasaki, S. (2008b). Mechanism for the rapid motion of the Qianjiangping landslide during reactivation by the first impoundment of the Three Gorges Dam reservoir, China. *Landslides, 5*, 379-386.

Wang, H. (2000). Surface vertical displacements and level plane changes in the front reservoir area caused by filling the Three Gorges Reservoir. *Journal of Geophysical Research: Solid Earth, 105*, 13211-13220.

Wang, H., Harvey, A.M., Xie, S., Kuang, M., & Chen, Z. (2008c). Tributary-junction fans of China's Yangtze Three-Gorges valley: Morphological implications. *Geomorphology, 100*, 131-139.

Wang, H., Hsu, H.T., & Zhu, Y.Z. (2002). Prediction of surface horizontal displacements, and gravity and tilt changes caused by filling the Three Gorges Reservoir. *Journal of Geodesy, 76*, 105-114.

Wang, H.B., Xu, W.Y., Xu, R.C., Jiang, Q.H., & Liu, J.H. (2007). Hazard assessment by 3D stability analysis of landslides due to reservoir impounding. *Landslides, 4*, 381-388.

Wang, Q., Zhang, P.-Z., Freymueller, J.T., Bilham, R., Larson, K.M., Lai, X.a., You, X., Niu, Z., Wu, J., Li, Y., Liu, J., Yang, Z., & Chen, Q. (2001). Present-Day Crustal Deformation in China Constrained by Global Positioning System Measurements. *Science, 294*, 574-577.

Wang, S., Zhang, H., Zhang, Y., & Zheng, J. (2008d). Back analysis of unsaturated parameters and numerical seepage simulation of the Shuping landslide in Three Gorges reservoir area. *Landslides and Engineered Slopes. From the Past to the Future, Two Volumes + CD-ROM* (pp. 985-990): CRC Press.

Wang, T., Perissin, D., Liao, M., & Rocca, F. (2008e). Deformation monitoring by long term D-InSAR analysis in Three Gorges Area. In, *IEEE International Geoscience and Remote Sensing Symposium*. Boston.

Wang, X., & Niu, R. (2009). Spatial Forecast of Landslides in Three Gorges Based On Spatial Data Mining. *Sensors, 9*, 2035-2061.

Wang, Z.Y., Lee, J.H.W., & Cheng, D. (2005b). Impacts of the TGP project on the Yangtze River ecology and management strategies. *International Journal of River Basin Management, 3*, 237-246.

Wangensteen, B., Guðmundsson, Á., Eiken, T., Kääb, A., Farbrot, H., & Etzelmüller, B. (2006). Surface displacements and surface age estimates for creeping slope landforms in Northern and Eastern Iceland using digital photogrammetry. *Geomorphology, 80*, 59-79.

Wasowski, J., & Bovenga, F. (2014). Investigating landslides and unstable slopes with satellite Multi Temporal Interferometry: Current issues and future perspectives. *Engineering Geology, 174*, 103-138.

Wegmuller, U., & Werner, C.L. (1995). SAR interferometric signatures of forest. *Geoscience and Remote Sensing, IEEE Transactions on, 33*, 1153-1161.

Wen-Yen, C., Chih-Tien, W., Chih-Yuan, C., & Jyun-Ru, K. (2012). Mapping Geo-Hazard by Satellite Radar Interferometry. *Proceedings of the IEEE, 100*, 2835-2850.

Wen, B.P., Aydin, A., Duzgoren-Aydin, N.S., Li, Y.R., Chen, H.Y., & Xiao, S.D. (2007). Residual strength of slip zones of large landslides in the Three Gorges area, China. *Engineering Geology, 93*, 82 - 98.

Wright, T.J., Parsons, B.E., & Lu, Z. (2004). Toward mapping surface deformation in three dimensions using InSAR. *Geophysical Research Letters, 31*, L01607.

Wu, S., Shi, L., Wu, R., Tan, C., Hu, D., Mei, Y., & Xu, R. (2001). Zonation of the landslide hazards in the forereservoir region of the Three Gorges Project on the Yangtze River. *Engineering Geology, 59*, 241 - 248.

Wu, X., Niu, R., Ren, F., & Peng, L. (2013). Landslide susceptibility mapping using rough sets and back-propagation neural networks in the Three Gorges, China. *Environmental Earth Sciences, 70*, 1307-1318.

Xia, M., Ren, G., & Ma, X. (2013). Deformation and mechanism of landslide influenced by the effects of reservoir water and rainfall, Three Gorges, China. *Natural Hazards, 68*, 467-482.

Xia, Y. (2008). CR-Based SAR-Interferometry for Landslide Monitoring. In, *Geoscience and Remote Sensing Symposium, 2008. IGARSS 2008. IEEE International* (pp. II-1239-II-1242).

Xia, Y. (2010). Synthetic Aperture Radar Interferometry. In G. Xu (Ed.), *Sciences of Geodesy - I* (pp. 415-474): Springer Berlin Heidelberg.

Xia, Y., Kaufmann, H., & Guo, X.F. (2004). Landslide monitoring in the Three Gorges are using D-InSAR and corner reflectors. *Photogrammetric Engineering & Remote Sensing, 70*, 1167 - 1172.

Xu, X., Tan, Y., & Yang, G. (2013). Environmental impact assessments of the Three Gorges Project in China: Issues and interventions. *Earth-Science Reviews, 124*, 115-125.

Xue, G. (2009). A Study of the 1985 Xintan Landslide in Xiling Gorge, Three Gorges Area, China. In F. Wang, & T. Li (Eds.), *Landslide Disaster Mitigation in Three Gorges Reservoir, China* (pp. 387-409): Springer Berlin Heidelberg.

Xue, G., Xu, F., Wu, Y., & Yu, Y. (2009). Bank Slope Stability Evaluation for the Purpose of Three Gorges Reservoir Dam Construction. In F. Wang, & T. Li (Eds.), *Landslide Disaster Mitigation in Three Gorges Reservoir, China* (pp. 41-86): Springer Berlin Heidelberg.

Yamaguchi, Y., Tanaka, S., Odajima, T., Kamai, T., & Tsuchida, S. (2003). Detection of a landslide movement as geometric misregistration in image matching of SPOT HRV data of two different dates. *International Journal of Remote Sensing, 24*, 3523-3534.

Yang, S., Li, C., & Yokoyama, K. (2006). Elemental compositions and monazite age patterns of core sediments in the Changjiang Delta: Implications for sediment provenance and development history of the Changjiang River. *Earth and Planetary Science Letters, 245*, 762-776.

Yi, L., Zhao, D., & Liu, C. (2012). Preliminary Study of Reservoir-Induced Seismicity in the Three Gorges Reservoir, China. *Seismological Research Letters, 83*, 806-814.

Yin, Y., Wang, H., Gao, Y., & Li, X. (2010a). Real-time monitoring and early warning of landslides at relocated Wushan Town, the Three Gorges Reservoir, China. *Landslides, 7*, 339-349.

Yin, Y., Zheng, W., Liu, Y., Zhang, J., & Li, X. (2010b). Integration of GPS with InSAR to monitoring of the Jiaju landslide in Sichuan, China. *Landslides, 7*, 359-365.

Yoon, Y.T., Eineder, M., Yague-Martinez, N., & Montenbruck, O. (2009). TerraSAR-X Precise Trajectory Estimation and Quality Assessment. *Geoscience and Remote Sensing, IEEE Transactions on, 47*, 1859-1868.

Yuan, X.-z., Zhang, Y.-w., Liu, H., Xiong, S., Li, B., & Deng, W. (2013). The littoral zone in the Three Gorges Reservoir, China: challenges and opportunities. *Environmental Science and Pollution Research, 20*, 7092-7102.

Yun, S.-H., Zebker, H., Segall, P., Hooper, A., & Poland, M. (2007). Interferogram formation in the presence of complex and large deformation. *Geophysical Research Letters, 34*, L12305.

Zebker, H.A., Rosen, P.A., & Hensley, S. (1997). Atmospheric effects in interferometric synthetic aperture radar surface deformation and topographic maps. *Journal of Geophysical Research: Solid Earth, 102*, 7547-7563.

Zebker, H.A., & Villasenor, J. (1992). Decorrelation in interferometric radar echoes. *Geoscience and Remote Sensing, IEEE Transactions on, 30*, 950-959.

Zhang, Q., & Lou, Z. (2011). The environmental changes and mitigation actions in the Three Gorges Reservoir region, China. *Environmental Science & Policy, 14*, 1132-1138.

Zhang, Z., Bai, Z., Mooney, W., Wang, C., Chen, X., Wang, E., Teng, J., & Okaya, N. (2009a). Crustal structure across the Three Gorges area of the Yangtze platform, central China, from seismic refraction/wide angle reflection data. *Tectonophysics*, *475*, 423 - 437.

Zhang, Z., Luo, X., & Wu, J. (2009b). Study on the Possible Failure Mode and Mechanism of the Xietan Landslide When Exposed to Water Level Fluctuation. In F. Wang, & T. Li (Eds.), *Landslide Disaster Mitigation in Three Gorges Reservoir, China* (pp. 375-385): Springer Berlin Heidelberg.

Zheng, Y., & Li, Y. (2009). Study on initial formation time of Three Gorges region in the Yangtze Aquo-System. *Journal of Sichuan Normal University (Natural Science), 2009*, 808 - 811.

Zou, L., Wang, S., & Lai, X. (2013). Creep model for unsaturated soils in sliding zone of Qianjiangping landslide. *Journal of Rock Mechanics and Geotechnical Engineering, 5*, 162-167.

Figure A-1: Installed corner reflectors at the toe of the densely vegetated Shuping landslide. Edge lengths are approximately 1.5 m long.

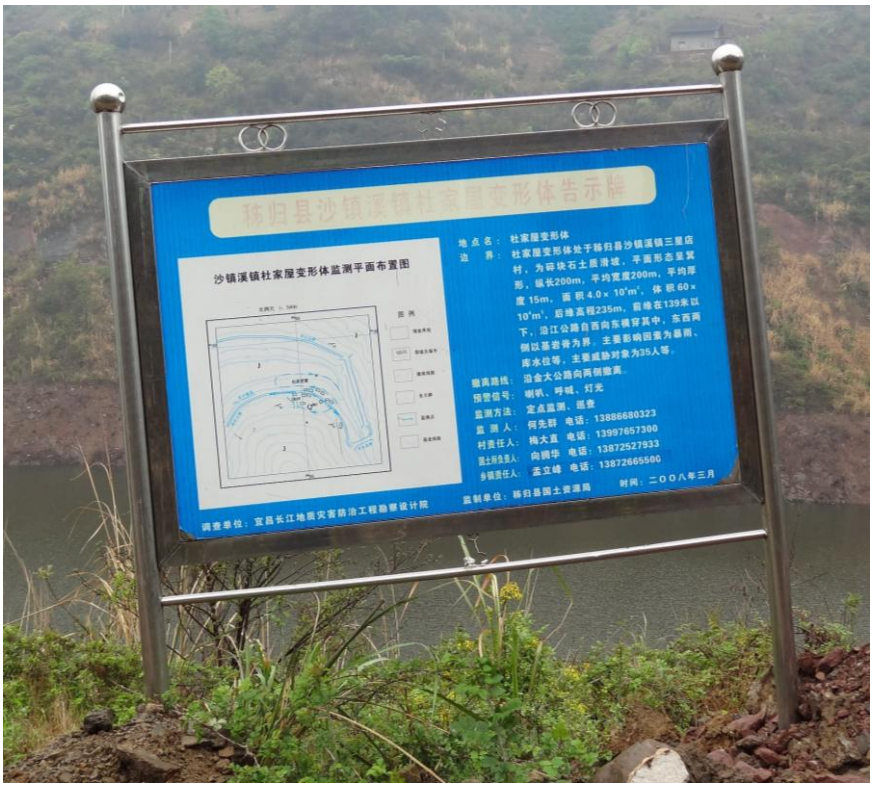

Figure A-2: Landslide warning sign (displaced!) at the site of the Dujiawu landslide.

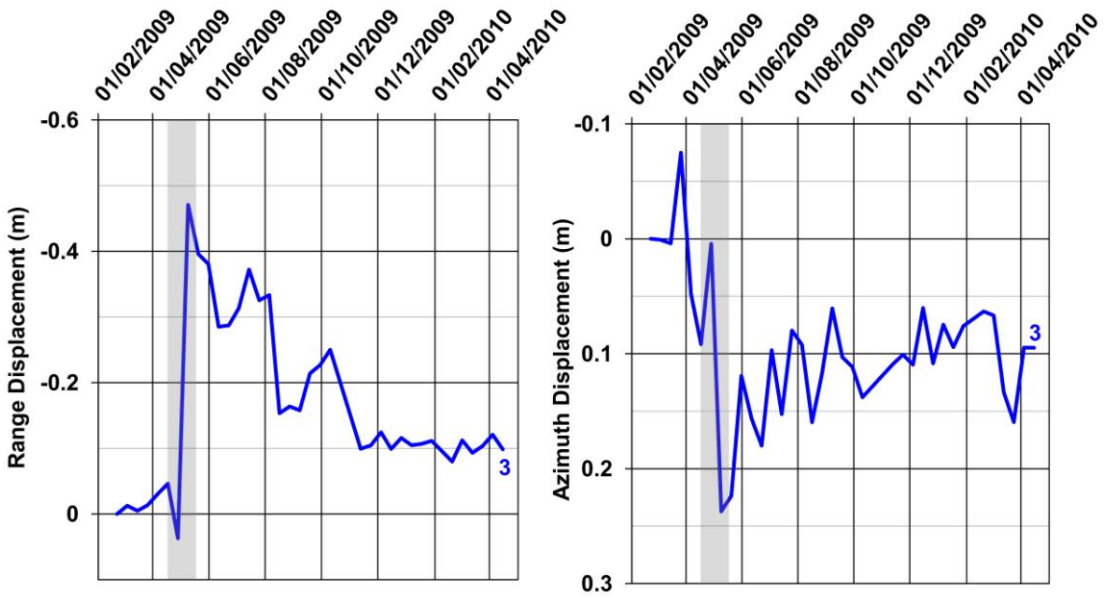

Figure A-3: Offset displacement of Point 3 measured from TSX Spotlight data. The displacement between 28/04/09 and 09/05/09 significantly contrasts with all the other stable points (points 2, 4, 5 & 6) and given this point is assumed to be on stable ground outside the landslide boundary, perhaps some external influence (unrelated to the landslide movement) has caused it to shift. For this reason Point 3 was excluded from all analyses in subsequent results.

Figure A-4: Building damage indicative of land movements and confirmed in communication with residents. Photos were taken on 4th April 2012 and located at 30° 59' 31N 110° 36' 41 E. The longest edge of the yellow notebook is ~0.16 m.

Table A-1: Individual estimates of the vertical (d_U) and horizontal (d_N) components of landslide movement for the numbered corner reflectors shown in Figure 5-5.

Corner Reflector	2009 - 2010		2010 - 2012		2012 – 2013	
	d_U (m)	d_N (m)	d_U (m)	d_N (m)	d_U (m)	d_N (m)
2	0.003	-0.050	0.013	0.032	-0.021	0.012
4	0.006	-0.023	0.008	0.102	0.019	-0.040
5	0.008	0.032	-0.021	0.023	0.048	0.034
6	0.019	-0.023	-0.042	0.017	-0.009	0.038
7	-0.012	0.743	-0.078	0.709	-0.005	0.726
8	0.171	0.761	0.141	0.833	0.049	0.862
9	0.728	0.925	0.618	0.903	0.638	0.794
10	0.722	0.705	0.792	0.732	0.707	0.693
11	0.453	0.316	0.252	0.204	0.212	0.078
12	0.037	0.700	0.014	0.677	0.023	0.742
13	0.111	0.735	0.092	0.682	0.100	0.757
14	0.106	0.809	0.122	0.779	0.101	0.863
15	0.134	0.749	0.129	0.720	0.135	0.764
16	0.263	0.491	0.209	0.520	0.204	0.547
17	0.245	0.640	0.267	1.012	0.239	0.910

Appendix B – First Author *Remote Sensing of Environment* Paper

Remote Sensing of Environment 147 (2014) 133–144

Contents lists available at ScienceDirect

Remote Sensing of Environment

journal homepage: www.elsevier.com/locate/rse

Evaluating sub-pixel offset techniques as an alternative to D-InSAR for monitoring episodic landslide movements in vegetated terrain

A. Singleton [a,*], Z. Li [a,b], T. Hoey [a], J.-P. Muller [c]

[a] School of Geographical and Earth Sciences, University of Glasgow, University Avenue, Glasgow G12 8QQ, UK
[b] School of Civil Engineering and Geosciences, Cassie Building, Newcastle University, Newcastle upon Tyne NE1 7RU, UK
[c] Imaging Group, Mullard Space Science Laboratory, Department of Space and Climate Physics, University College London, Holmbury St. Mary RH5 6NT, UK

ARTICLE INFO

Article history:
Received 1 August 2013
Received in revised form 13 December 2013
Accepted 7 March 2014
Available online 28 March 2014

Keywords:
Synthetic Aperture Radar (SAR)
Differential SAR interferometry (D-InSAR)
SAR sub-pixel offsets
Time-series analysis
TerraSAR-X Spotlight
TerraSAR-X Stripmap
Envisat
Corner reflectors (CR)
Three Gorges region (China)
Slow-moving landslides

ABSTRACT

Spaceborne Synthetic Aperture Radar (SAR) sensors obtain regular and frequent radar images from which ground motion can be precisely detected using a variety of different techniques. The ability to measure slope displacements remotely over large regions can have many uses, although the limitations of the most commonplace technique, differential InSAR (D-InSAR), must be considered prior to interpreting the final results. One such limitation is the assumption that different rates of movement over a given distance cannot exceed a threshold value, dependent upon the pixel spacing of the SAR images and the radar wavelength. Characteristic features of landslides (i.e. the sharp boundary between stable/active ground and the range of temporally-variable velocities) can exhibit high spatial displacement gradients, breaking a fundamental assumption for reliable D-InSAR analysis. Areas of low coherence are also known to hinder the exploitation of InSAR data. This study assesses the capability of TerraSAR-X Spotlight, TerraSAR-X Stripmap and Envisat Stripmap images for monitoring the slow-moving Shuping landslide in the densely vegetated Three Gorges region, China. In this case study, the episodic nature of movement is shown to exceed the measurable limit for regular D-InSAR analysis even for the highest resolution 11-day TSX Spotlight interferograms. A Sub-Pixel Offset Time-series technique applied to corner reflectors (SPOT-CR) using only the SAR amplitude information is applied as a robust method of resolving time-varying displacements, with verifiable offset measurements presented from TSX Spotlight and TSX Stripmap imagery. Care should be exercised when measuring potentially episodic landslide movements in densely vegetated areas such as the Three Gorges region and corner reflectors are shown to be highly useful for SPOT techniques even when the assumptions for valid D-InSAR analysis are broken. Finally the capability to derive two-dimensional movements from sub-pixel offsets (in range and along-track directions) can be used to derive estimates of the vertical and northwards movements to help infer the landslide failure mechanism.

1. Introduction

Satellite radar imagery has been recognised as a powerful tool for measuring surface motions over large regions and offers the capability to remotely monitor unstable slopes (Rott, Scheuchl, Siegel, & Grasemann, 1999; Tofani, Segoni, Catani, & Casagli, 2010). In the best cases of landslide management, Early Warning Systems (EWS) have been developed and employed to minimise harm and loss. The nature of EWS and the landslide risk is strongly dependent upon landslide type, which is often classified by the initial mechanism of motion and the associated velocity (Cruden & Varnes, 1996). Whilst rapid landslides are the most dangerous, deep and slow landslides are capable of destroying buildings and infrastructure particularly on reactivated ancient landslide deposits (Sassa, Picarelli, & Yueping, 2009).

A well-developed EWS should include various elements such as understanding the local knowledge of risks, communicating timely and reliable warnings, and building local capacity to respond to warnings (UN-ISDR, 2004). However, one other technical component involves monitoring the hazard(s) which requires: (i) detection; (ii) rapid mapping; (iii) characterisation; and, (iv) long-term monitoring of landslides (Tofani et al., 2010). The generic benefits of using remote sensing data are well known, and a sub-report from the European SAFELAND Project (Stumpf, Kerle, & Malet, 2010) compares the merits of numerous remote sensing techniques for monitoring different types of landslides. Airborne LiDAR surveys can provide useful data in terms of spatial resolution, precision and the capacity to measure a variety of displacement rates, although the cost and logistics required for regular repeat acquisitions are barriers for its routine use. Synthetic Aperture Radar (SAR) images from the most recent generation of SAR

* Corresponding author.
E-mail addresses: a.singleton.1@research.gla.ac.uk (A. Singleton), zhenhong.li@newcastle.ac.uk (Z. Li).

http://dx.doi.org/10.1016/j.rse.2014.03.003

satellite sensors (e.g. TerraSAR-X and COSMO SkyMed) can acquire regular data (up to every 4 days), over regional areas (e.g. 10–1000 km^2), at a high resolution (up to 1 m ground resolution) and in the case of slow-moving landslides (i.e. several metres per year; Cruden & Varnes, 1996), can meet the four requirements of landslide monitoring mentioned above. Whilst the repeat interval may not be short enough to provide timely warnings to vulnerable populations, it is possible to detect individual landslide accelerations over large regions and then direct monitoring equipment to areas at risk. The ability to make numerous point measurements of displacement over the landslide body can not only identify and map the actively deforming slopes (significantly reducing uncertainty in landslide inventory maps; e.g. Cascini, Fornaro, & Peduto, 2010), but also help to characterise the landslide mechanism (Tofani, Raspini, Catani, & Casagli, 2013). Further interpretations of landslide processes can then be inferred when comparing a time-series of displacement with potential triggering factors such as rainfall, seismicity and site-specific factors such as fluctuating reservoir water-levels (e.g. Tolomei et al., 2013). Finally, historic landslide movements can be measured from SAR satellite imagery using archived data scenes.

Whilst differential InSAR (D-InSAR) analysis is capable of mapping and measuring landslide movements, a major limitation is dense vegetation which can lead to rapid decorrelation between SAR acquisitions even for the highest resolution TSX Spotlight image mode with a revisit time of 11-days. Episodic and spatially variable landslide movements can also lead to decorrelation between SAR acquisitions when the spatial displacement gradient is exceeded. Determining the cause of decorrelation is often difficult and whilst time-series InSAR techniques have been developed to identify slowly decorrelating pixels in vegetated areas (e.g. Hooper, 2008; Hooper, Segall, & Zebker, 2007), resolving episodic and time-varying displacements remains a difficult task.

In this paper, Sub-Pixel Offset Time-series techniques applied to corner reflectors (SPOT-CR) using frequently acquired SAR images from a variety of sensors are quantitatively evaluated and compared for landslide monitoring. The measured landslide displacements are then used to help judge the suitability of using more precise D-InSAR time-series techniques in situations where assumptions of conventional D-InSAR analyses can be broken by the characteristic features of landslides (i.e. the sharp boundary between stable/active ground, the non-linear nature of the displacements and the range of temporally-variable velocities). The benefits and limitations of SPOT-CR techniques are assessed for studying landslides on densely vegetated slopes and their ability to monitor spatially large 2-dimensional movements using the installed corner reflectors is shown to infer a possible failure mechanism of the Shuping landslide within the Three Gorges region, China.

2. Investigating landslides using SAR observations

D-InSAR has been employed to monitor the slow motion of many landslides and compared to (typically sparse) GPS point measurements (e.g. Akbarimehr, Motagh, & Haghshenas-Haghighi, 2013; Wen-Yen, Chih-Tien, Chih-Yuan, & Jyun-Ru, 2012), D-InSAR techniques are especially useful for providing spatially continuous coverage of surface displacement which can help define the boundaries of active landslides (Yin, Zheng, Liu, Zhang, & Li, 2010). Rott et al. (1999) used D-InSAR to examine a slow moving landslide (up to 4 cm/yr) in the Austrian Alps highlighting the inter-annual variability of displacements, and the limitations of D-InSAR techniques for landslide monitoring were proposed for the first time. Over the last decade, the number of InSAR applications to landslide studies has grown significantly following initial studies (e.g. Berardino et al., 2003; Fruneau, Achache, & Delacourt, 1996; Strozzi et al., 2005), with comprehensive overviews of interferometric SAR (InSAR) techniques for landslide studies presented by Colesanti and Wasowski (2006) and Rott and Nagler (2006) for sensors such as Envisat/ASAR and RADARSAT. However, it should be noted these reviews pre-date the launch of the most recent commercial SAR sensors. Rott (2009) provides a slightly updated summary with reference to the TerraSAR-X and COSMO SkyMed satellites.

Despite the advantages of D-InSAR methods these continue to have limitations that should always be considered, such as geometric decorrelation, temporal decorrelation, atmospheric artefacts, scale constraints, a limit on the spatial displacement gradient, geometric distortions and a 1-dimensional Line-of-Sight (LOS) measurement sensitivity (Colesanti & Wasowski, 2006) and assumptions of linearity in the displacement process. A range of techniques have been developed to help minimise some of these effects (e.g. time-series analysis to estimate various phase components; Berardino, Fornaro, Lanari, & Sansosti, 2002; Ferretti, Prati, & Rocca, 2001, using external data to reduce atmospheric path delays; Foster et al., 2013; Li, Fielding, Cross, & Muller, 2006; Li, Muller, Cross, & Fielding, 2005; Onn & Zebker, 2006), although fundamental theoretical constraints still exist. It has been suggested that the inherent limitations of SAR data, coupled with the complexity of landslides, may be insufficiently appreciated which results in the misrepresentation of landslide measurements (Peduto, Cascini, & Fornaro, 2010). Consequently, end-users can lack confidence in these remotely-sensed results unless verified with ground data (thereby negating some of the benefits of using remotely collected data).

To illustrate a potential problem with D-InSAR analysis, consider the loss of coherence which often occurs between two time-adjacent SAR acquisitions in a densely vegetated region. This might be wrongly interpreted to result from temporal decorrelation when the real reason was a landslide movement exceeding the spatial displacement gradient. Subsequently, any D-InSAR time-series technique spanning this fast event would erroneously underestimate the landslide displacement. Such a scenario is shown to occur in the Three Gorges and motivates this research to find a complimentary technique to extract verifiable landslide measurements from SAR images.

A range offset map from SAR pixel offset methods contains the same information as a differential interferogram (Yun, Zebker, Segall, Hooper, & Poland, 2007) and being less restricted by the assumption of a low spatial displacement gradient, provides a useful comparison with InSAR results. Past studies using SAR pixel offset methods have been dominated by co-seismic and glacial applications, due to the widespread decorrelation in conventional interferograms from high deformation gradients across ruptured faults or rapidly changing ice surfaces. As such, accurate fault traces have been revealed using pixel offset techniques (e.g. Funning, Parsons, Wright, Jackson, & Fielding, 2005; Jónsson et al., 2002; Li, Elliott, et al., 2011; Michel, Avouac, & Taboury, 1999) along with the capability to remotely measure glacier/rock glacier flow (e.g. Haug, Kääb, & Skvarca, 2010; Quincey et al., 2005; Scambos, Dutkiewicz, Wilson, & Bindschadler, 1992).

To date, only a small number of studies have used pixel offset techniques for monitoring slope movements, the majority using optical imagery from airborne and spaceborne platforms (Debella-Gilo & Kääb, 2011; Delacourt, Allemand, Casson, & Vadon, 2004; Kääb, 2002; Leprince, Berthier, Ayoub, Delacourt, & Avouac, 2008; Wangensteen et al., 2006; Yamaguchi, Tanaka, Odajima, Kamai, & Tsuchida, 2003). The sensitivities of normalised cross-correlation were considered by Delacourt et al. (2004) and Debella-Gilo and Kääb (2011) which include: (i) noise in the images; (ii) rotation/shearing between the images to be correlated; and (iii) the relationship between the pixel size and the precision of measurements. However, optical images can only be used to assess purely horizontal movements (north–south and east–west directions) without consideration of the vertical component. A sub-pixel offset technique was first applied to (TerraSAR-X Spotlight) SAR data by Li, Muller, et al. (2011) with promising results for monitoring the Shuping landslide, although only 4 sets of measurements were shown in the paper (corresponding to 4 offset pairs). This study attempts to recover landslide movements from

TerraSAR-X data with a temporal resolution of up to every 11 days over a time period of 15 months.

3. Landslides in the Three Gorges region

Landslides, mainly deep and slow-moving, are the most frequent and widespread geohazard in the Three Gorges region, predominantly caused by high slope gradients, lithological susceptibilities, heavy summer rainfall and human activities (Liu et al., 2004). Over the last decade, the construction of the Three Gorges project (TGP) has created a 600 km long reservoir with a bi-annually fluctuating water level (range ≈ 25 m) which has been shown to reactivate ancient landslides (Wang, Zhang, et al., 2008). The Three Gorges were formed by incision along narrow fault zones of massive limestone mountains interbedded with siltstone, shale and mudstone (Wang, Harvey, et al., 2008), although between the gorges the lithologies are much less resistant. Dominated by weathered mudstones, these inter-gorge areas favour river bank erosion, terrain dissection and the development of slow-moving slope failures (Liu et al., 2004).

This study focuses on the Shuping landslide located towards the eastern end of the Three Gorges (Fig. 1), the toe of which is connected to the Yangtze River. The Shuping landslide was selected as a case study and regular SAR data were commissioned in three different image modes over the landslide over the same time period. These data allow robust comparisons between data modes and the application of D-InSAR or sub-pixel offset techniques. The landslide is densely vegetated with orange trees, representative of the majority of hillslopes in the Three Gorges region, which makes the application of D-InSAR techniques very difficult. The north facing landslide orientation also makes it insensitive to LOS measurements. Independent of this study, corner reflectors have been installed over the landslide which aid the analysis of SAR data.

Previous studies that have monitored the Shuping landslide using D-InSAR techniques have yielded highly varied results. Fu, Guo, Tian, and Guo (2010) used 12 corner reflectors installed over the landslide to obtain a single measurement of displacement between September 2005 and March 2006 using Envisat data. Good agreement with GPS measurements was reported, although this result did not cover the months of April–June where the fastest movements are normally observed (and when the assumptions for reliable D-InSAR analysis are most likely to be broken).

Extensometer measurements over the time period of September 2005 and June 2007 show minimal displacements until around May–June 2007 when there is a rapid increase of ~0.4 m in the accumulated movements up to June 2007 (Wang et al., 2013). Whilst recognising the different vectors of measurement sensitivity, this contradicts the results of Xia (2010) who used the same 12 corner reflectors to calculate a time-series of displacement over the same time period, presenting very linear rates of downwards movement for all points.

This landslide has been divided into eastern and western parts with the eastern block (also known as Block 1) shown to be most active (Wang, Zhang, et al., 2008). The motion of Block 1 has been recorded primarily using extensometers from 2004 until 2010 (Wang, Zhang, et al., 2008; Wang et al., 2013) and these results display high spatial variability along with a stepped behaviour in time. Particularly using the longest record of movement, from August 2004 until May 2010, the periods of greatest movement have been suggested to relate to the drawdown of the Three Gorges Reservoir (Wang, Zhang, et al., 2008). Liao, Tang, Wang, Balz, and Zhang (2012) used Persistent Scatterer (PS) interferometry with TerraSAR-X Stripmap data to show movements up and down in the LOS direction in the order of ±5 mm between February 2008 and January 2010 which is unusual given that these measurements are an order of magnitude lower than the extensometer data. The highly non-linear velocity trend revealed by in-situ measurements and the disparities between previous D-InSAR studies prompts further analysis of the Shuping landslide using SAR data.

4. Methods

4.1. Data

The availability of 36 commissioned TerraSAR-X (TSX) Spotlight SAR images, 23 TSX Stripmap images as well as 17 Envisat Stripmap images all covering the same Shuping landslide (and significantly overlapping in time; see Fig. 1 and Supplementary material Table S1), also enables comparison of D-InSAR and SPOT-CR techniques which both aim to remotely monitor the landslide without the use of ground data. All results presented below were produced using the SARscape® software package (SARMAP, 2012), which includes an interferometry module capable of processing the above image modes along with an amplitude tracking tool for calculating sub-pixel offsets.

4.2. Maximum spatial displacement gradients and coherence analysis

One major limitation of D-InSAR techniques is their inability to measure high spatial gradients of rapid deformation. To observe

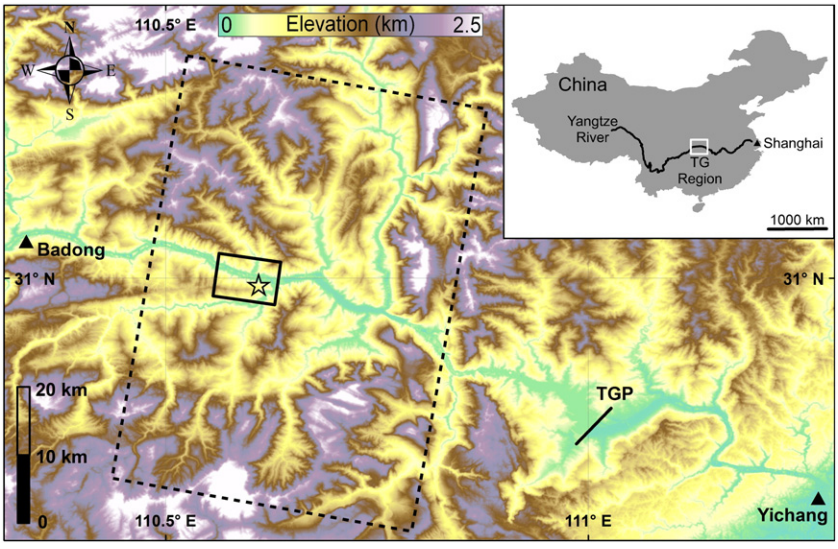

Fig. 1. Elevation of the eastern Three Gorges (TG) region. The star indicates the site of the Shuping landslide, ca. 45 km upstream of the Three Gorges Project (TGP). TSX Spotlight data coverage is shown by the solid box and TSX Stripmap data coverage is given by the dashed box. Envisat data covers the whole map.

interferometric fringes without ambiguity, the maximum displacement between two neighbouring pixels in a wrapped interferogram must not exceed λ / 2 (Massonnet & Feigl, 1998), with wavelengths (λ) typically in the order of ~30–300 mm. However, from the viewpoint of phase unwrapping, the maximum displacement gradient should be less than 0.5 fringes per pixel (Jiang, Li, Ding, Zhu & Feng, 2011; Spagnolini, 1995) making the limit of displacement between neighbouring pixels λ / 4. As such, D-InSAR has most commonly been applied to deformation phenomena measureable within these limits, such as very slow moving landslides, city subsidence, volcanoes and far-field earthquake deformation patterns. This theoretical limit does not consider noise in the radar observations caused by decorrelation effects (Zebker, Rosen, & Hensley, 1997) and hence reduces the maximum realistic measureable displacement gradient (Baran, Stewart, & Claessens, 2005; Jiang et al., 2011). It is therefore practically impossible to derive measurements of fast-moving phenomena with sharp boundaries between stable and moving areas such as glaciers, co-seismic deformation near faults and landslides moving beyond a threshold limit. The capability of D-InSAR to measure such movements is primarily determined by the pixel spacing and the wavelength of the SAR sensor.

The limits on the spatial displacement gradient are the theoretical maxima when the radar observations are unaffected by noise. Decorrelation between SAR acquisitions can be a major problem in the use of D-InSAR techniques particularly in densely vegetated regions (Ahmed, Siqueira, Hensley, Chapman, & Bergen, 2011) such as the Three Gorges. To assess the decorrelation effects, interferometric coherence was analysed for all three image modes. Differential interferograms were generated with a multi-look factor of 2 applied in both range and azimuth, and the topographic phase component was removed using the ASTER GDEM v2, a product of METI and NASA, with a RMSE of 12.1 m compared to 121 GPS benchmarks in the Three Gorges area (Li et al., 2012). To measure the interferometric coherence, a sample estimate using a 9 × 9 window was employed for an area of 5 km^2 adjacent to but excluding the landslide body, from which a mean coherence could be obtained. Seasonal patterns were assessed by plotting the mean coherence for every 11-day (TSX) or 35-day (Envisat) pair over time. Effects of the perpendicular baselines were considered by plotting the mean coherence for the same pairs with respect to the baseline and to assess the temporal decorrelation, the mean coherence for all pairs with a baseline less than 25 m (TSX data) or 50 m (Envisat data) was plotted with respect to the time interval between image acquisitions (Fig. 2). For the generation of the final interferograms, a spectral shift filter accounting for the difference in incidence angles between master and slave images (Gatelli et al., 1994) was applied, along with a Doppler filter to remove the non-overlapping azimuth spectra between the master and slave images.

4.3. Sub-pixel offset techniques

Although less precise than conventional InSAR methods, pixel offset techniques using SAR amplitude images can overcome the D-InSAR limitation on the spatial displacement gradient and are far more robust (not requiring phase unwrapping, not strongly limited to regions of high coherence and significantly less affected by atmospheric water vapour due to an independence on the use of phase values). Additionally, pixel offset data can provide complimentary information since conventional interferograms are only sensitive to displacements in the sensor's LOS direction (Michel et al., 1999). Using just two images acquired at different times, displacement vectors can be measured in the sensor look direction (range) as well as the satellite flight (along-track, or 'azimuth') direction. The 2-dimensional measurements are obtained by measuring the row and column offsets between the two acquisitions at defined intervals in range/azimuth in order to generate sufficient coverage of offset measurements (Pathier et al., 2006).

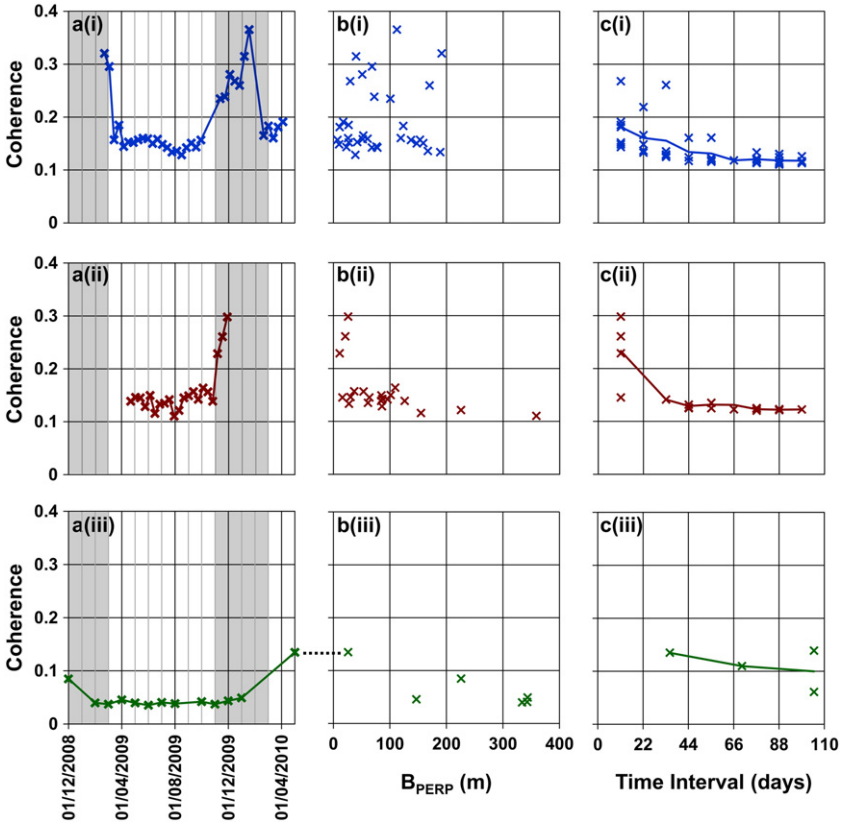

Fig. 2. (a) Coherence of temporally-adjacent SAR images showing highest values between November and February each year. (b) Coherence of 11-day (TSX) or 35-day (Envisat) interferograms plotted against perpendicular baseline showing no significant patterns. (c) Coherence of interferograms with respect to time interval showing a decline by ~30 days. (i) TSX Spotlight data (ii) TSX Stripmap data (iii) Envisat data.

SPOT-CR techniques are capable of measuring more spatially variable movements than D-InSAR although the results from pixel offset methods are highly dependent upon the various processing parameters (notably the cross-correlation window size and oversampling factor) which should be carefully tuned with regard to the scale of the deformation feature(s) and the pixel size of the SAR images (Bechor & Zebker, 2006; Yun et al., 2007). Consequently, the size of the moving window should be large enough to maximise the signal-to-noise ratio whilst minimising the spatial velocity gradient. The search area size must also be large enough to include the fastest moving distance whilst minimising the computational cost of the process (Debella-Gilo & Kääb, 2011). Following an approach outlined by Yun et al. (2007), the cumulative distribution for an area of 2 km^2 (adjacent to the landslide site and assumed to be stable) was analysed with a combination of different parameters. Visual inspection from these tests provides a heuristic way of tuning the moving window size and the oversampling parameters, considering the data characteristics and the phenomenon under study. However, contrary to Yun et al. (2007), no piecewise linear fit was used to exclude any offset value since valid landslide offsets would be concentrated in one tail of the distribution when considering the stable ground also within the offset map.

Prior to generating the sub-pixel offset measurements, SAR images were aligned using a simple translational shift based on the orbital data and the digital elevation model. A standard normalised cross-correlation procedure based on the optimal window size and oversampling factor was then applied without any filtering in any part of the processing, and the final offset values used to generate the time-series curves were taken as the mean from a small window of 10 × 10 pixels at various locations around the landslide. The same window position in rows/columns was used to extract measurements from every subsequent slave image for the time-series.

5. Results and analyses

5.1. Maximum spatial displacement gradients and coherence analysis

For the three different image modes employed in this study, the spatial displacement gradients were considered. Table 1 displays the displacement gradients for an interferogram produced at the original SLC resolution and when considering a small multi-look factor of two. The pixel size controls the maximum measurable displacement and, even for the highest resolution TSX Spotlight imagery, it would not be possible to measure a difference in the displacement between image acquisitions of more than 0.12 m (or 0.06 m after multi-looking) over a distance of 10 m. Despite the slightly longer wavelength of Envisat data, the greater pixel size is a significant disadvantage for measuring spatially variable movements over short distances.

The results of the coherence analysis are presented in Fig. 2. The coherence between temporally-adjacent SAR images over the time period of available acquisitions for all image modes (Fig. 2: left hand column) is low throughout the 1.5 years, although a consistent seasonal pattern is shown for the TSX imagery whereby coherence increases between November and February each year. Given the sensitivity of radar backscatter to the dielectric effects of changing the surface moisture content (Smith, 2002), the seasonal coherence pattern could be attributable to the heavy summer rainfall after comparing the coherence trends with the mean monthly rainfall values for the winter (~19 mm/month for November–February) and the rest of the year (~100 mm/month for March–October). The seasonality in coherence and rainfall may also be interrelated with the dense orange trees in the area since the canopy reflectance can change significantly over the year even if the orange trees are evergreen (Dzikiti et al., 2011).

Despite its shorter wavelength, the TSX data display higher coherence than the Envisat data due to its higher resolution and shorter repeat interval. Coherence for each 11-day (TSX) or 35-day (Envisat) interferogram with respect to the perpendicular baseline (Fig. 2: middle column) shows no definitive trend over the relatively short range of baselines (up to 400 m), and the coherence values > 0.2 are from interferograms created in the dry winter period. The right hand column of Fig. 2 shows coherence for all interferograms with a baseline of less than 25 m (TSX) or 50 m (Envisat) in relation to the time-interval between acquisitions. A relatively fast fall in coherence is seen with the TSX data until the interval exceeds ~33 days where it remains at a constant non-zero level. This constant value is considered to represent the natural bias in estimating the coherence correlation magnitude (Touzi, Lopes, Bruniquel, & Vachon, 1999). The almost complete loss of coherence beyond 33 days also explains why no significant seasonal coherence pattern is observed from the Envisat data. The low coherence throughout the time period suggests that the maximum measurable spatial displacement gradient is below the theoretical values presented in Table 1.

Table 1
Displacement gradients (m/m) for original resolution interferograms and for interferograms with a small multi-look factor of 2. The data used in these calculations are shown in the Supplementary material (Table S1). Multiply these values by the distance between two points to calculate the maximum detectable difference in the rates of displacement.

Sensor/image mode	Displacement gradient (DG)	DG after multi-looking (using a small factor of 2)
TerraSAR-X/Spotlight	0.01177	0.00589
TerraSAR-X/Stripmap	0.00394	0.00197
Envisat ASAR/Stripmap	0.00070	0.00035

5.2. D-InSAR analysis

To remotely monitor landslides with high precision, the optimal approach would use high coherence interferograms with minimal geometric distortions which cover the whole time period. Given that the shortest time intervals gave the best coherence, every 11-day TSX Spotlight pair was processed using a Goldstein filter (Goldstein & Werner, 1998) prior to geocoding. Fig. 3 shows three of these (wrapped) interferograms for adjacent 11-day intervals. The landslide boundary is indicated by the sharp colour changes as shown by the black line, and this boundary is consistent over the 33-day period (3 × 11-day interferograms).

Assuming a purely translational failure mechanism parallel to the slope surface, sliding velocities can be projected into the downslope sliding direction (e.g. Hilley, Bürgmann, Ferretti, Novali, & Rocca, 2004) although using a scaling factor impacts on the precision of measurements (Colesanti & Wasowski, 2006). The SAR geometry is typically incapable of measuring translational movements on ascending or descending orbits for slope aspects close to 0° and 180° (Cascini et al., 2010) and for Envisat ascending data a scaling factor threshold of 3.3 was used to select suitable 'projectable' PS points (Cascini et al., 2013). Projection of the TSX Spotlight D-InSAR data in Fig. 3 was not undertaken primarily due to the high scaling factor (9.8 for the north-facing Shuping landslide).

In Fig. 3 an increase in the fringe rate can also be observed from left to right, which relates to an increase in the landslide movement over each interval. However, Fig. 3b and c shows a loss of coherence particularly towards the head of the landslide that is most likely due to the displacements exceeding the maximum measurable limit of 0.00589 m/m (see Table 1). The sole use of these TSX Spotlight images (or lower resolution X-band or C-band SAR images) for any D-InSAR time-series analysis would subsequently underestimate landslide displacement and a technique is required to verify whether this coherence is lost due to the fast landslide movement or other factors.

5.3. Sub-pixel offset observations

Over a completely stable area, the offset value should be randomly distributed around a mean of zero, although with small moving window

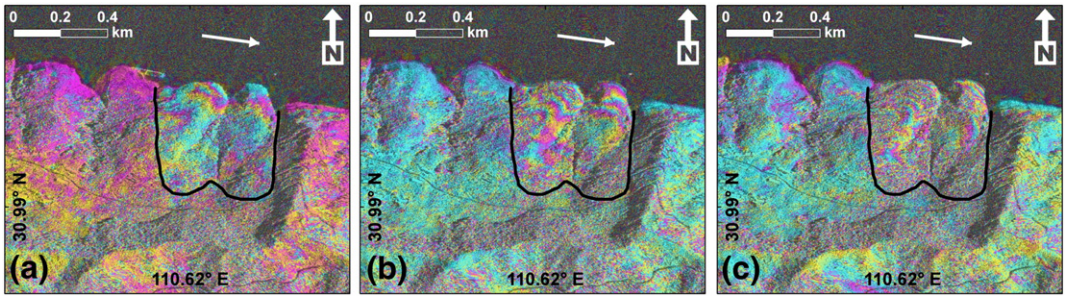

Fig. 3. Wrapped, 11-day TSX Spotlight interferograms covering the time periods: (a) 09/05/09–20/05/09; (b) 20/05/09–31/05/09; and (c) 31/05/09–11/06/09. Colour cycles represent modulo-2π phase changes and therefore each cycle represents ~0.016 m of displacement in the radar Line-of-Sight (LOS) direction. Assuming the main landslide movement is northwards (downslope towards the river), the LOS direction is perpendicular to the landslide direction and must be most sensitive to vertical surface changes, shown by the unit vector defining the look direction of the TSX Spotlight imagery $u = [d_E\ d_N\ d_U] = [-0.68\ 0.12\ -0.72]$ (positive up, left-handed coordinate system). This shows only around 12% of possible north–south displacement is recorded by TSX Spotlight D-InSAR data. The white arrow shows the flow direction of the Yangtze River.

sizes and no oversampling, the distribution of values is determined by the size of the moving window (Fig. 4) due to spurious correlation. As the oversampling factor increases for the small window sizes, the range of possible offset values increases to eradicate the step-like behaviour of the cumulative distribution, but the linear trend shows no concentration around zero. For a window size of 32 × 32 pixels, ~75% of the offset values are between ±0.5 pixel units and the oversampling factor was increased until no observable improvement is seen (an oversampling factor of 16 is identical to an oversampling factor of 24). As the window size and oversampling factors are increased, the results improve but the processing time should also be considered. For example, doubling the window size from 32 × 32 pixels to 64 × 64 pixels increases the processing time for each offset pair from 01:41 h to nearly 05:37 h (detailed processing timings shown in Supplementary material Table S2). Given the associated times for generating one offset measurement using different parameters, the final selection of a 32 × 32 pixel window size and an oversampling factor of 16 was deemed preferable.

Following the processing of the first offset pair, the correlation values associated with each offset measurement (Fig. 5) show that points with very high correlations (>0.9) are distributed across the landslide in positions which correspond to the corner reflector locations. Given the significant contrast in the radar backscatter between the corner reflectors and the natural terrain, these points result in a very high cross correlation value when they are within the total area covered by the moving window used in the calculation. Following the numbering scheme displayed on the right of Fig. 5, it is clear that most are within the landslide boundary, although a number of points are situated outside the landslide on ground that is assumed to be stable which can then help identify the potential noise level of the offset measurements.

5.4. Results of Sub-Pixel Offset Time-series techniques applied to corner reflectors (SPOT-CR)

A final step in the processing strategy considered how to generate a time-series of measurements. The two simplest approaches are to: (i) use the same master image with subsequent slave images; and, (ii) process every 11-day offset pair to generate a cumulative time-

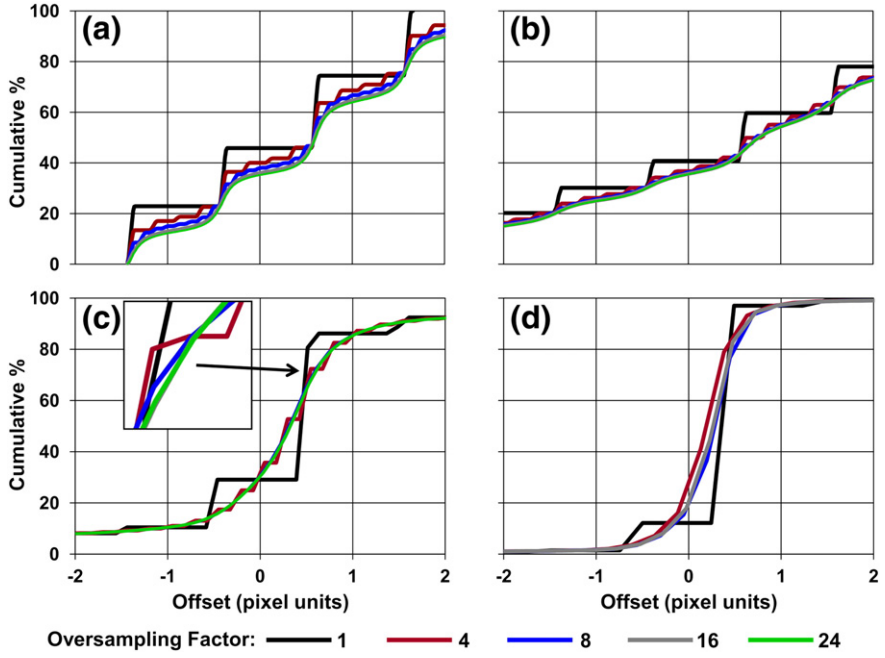

Fig. 4. Cumulative percentage of TSX Spotlight sub-pixel offset values in the azimuth direction over a stable area of ground (1.75 km^2) adjacent to the landslide. This is plotted for different pixel-oversampling factors and also different cross-correlation window sizes: (a) 4 × 4, (b) 8 × 8, (c) 32 × 32, and (d) 64 × 64. A window size of 16 × 16 was also assessed (Supplementary material Fig. S1). The final parameter set used a window size of 32 × 32 since this results in >80% of the area being characterised with values around zero. A larger window size increases precision but the processing time is significantly longer (see Supplementary material Table S2). An oversampling factor of 16 was chosen, above which no improvement is observed as shown by the inset of Fig. 4c.

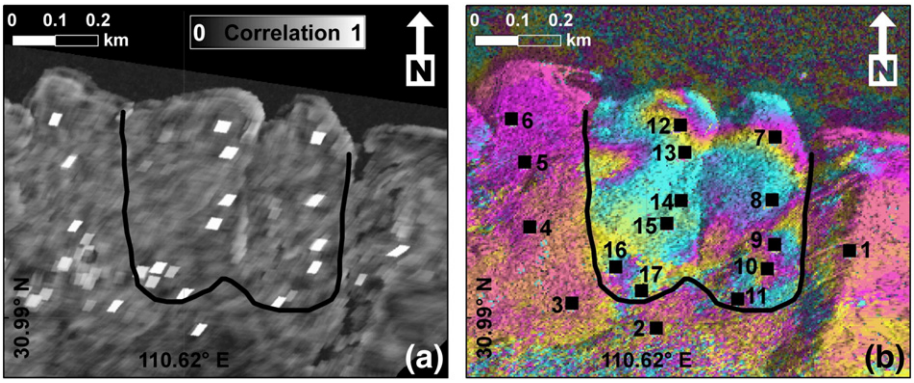

Fig. 5. (a) The value of peak correlation used for the TSX Spotlight offset measurements (11-day pair, 21st Feb–4th Mar 2009, showing the minimum temporal decorrelation). The high correlations (the white areas) are caused by a high-contrast feature (mostly corner reflectors) within the cross-correlation window. The same features are observed for the TSX Stripmap offset measurements. (b) The numbering of corner reflectors used to extract time-series of displacement in Fig. 7(a–d), overlain on an interferogram showing the landslide boundary (11-day pair, 9th May–20th May 2009). Point 1 is outside the landslide and used as the reference for all other points. Points 2–6 are also outside the landslide boundary. Points 7–11 ascend up the east part of the landslide. Points 12–17 ascend up the west part of the landslide. Point 3 was excluded from analysis after results suggested it had unnaturally shifted (see Supplementary material Fig. S4).

series of displacement. The first of these possibilities is preferred since the temporal decorrelation from the corner reflector points is believed to be very small, and this strategy ensures that errors in each offset measurement is independent from the results of previous image pairs. For example using time-adjacent pairs, the first measurement would be the result of just one offset pair whereas the last measurement would be calculated as the sum of all previous offset measurements. An alternative to both the above strategies is to create a small-baseline (SBAS) network of offset pairs, similar to that proposed by Casu, Manconi, Pepe, and Lanari (2011). Using Envisat data, Casu et al. (2011) attempted to reduce the perpendicular baselines of the offset pairs which influenced the amount of reliable measurements generated. When considering the TSX data used here, no significant dependence upon the perpendicular baseline is observed (Fig. 6) most likely due to the consistently short perpendicular baseline values which never exceed 300 m. Additionally, no significant decay in the amount of reliable pixels is observed over time and so the benefit of inverting a SBAS network of offset maps to generate a time-series of displacement is limited. The simplest approach ((i) above) of using one constant master image for all the offset pairs therefore meets the requirements of this investigation.

The offset time-series graphs from TSX Spotlight and Stripmap data (Fig. 7) show a significant step in landslide movement in both the range and azimuth directions towards the end of May and the start of June. Movements of more than 0.1 m recorded towards the head of the landslide over an 11-day period further explain the loss of coherence from the interferograms presented in Fig. 3. Additionally, considering the curves related to the points outside the landslide boundary, it is noted that the noise in the azimuth direction measurements exceeds that in the range direction, a result that is assumed to be caused by the larger azimuth pixel spacing. Additionally, the variability in subsequent offset values from the Stripmap data is greater than the Spotlight data which is another likely consequence of the larger pixel spacing.

Considering the topographical location of the corner reflectors, a strong association is found between elevation and the range displacement. Displacement in the LOS (which includes a vertical component of movement) is up to ten times greater towards the head of the landslide which may reflect the failure mechanism. No such topographic dependence is shown in the azimuth offset results. These patterns in both range and azimuth are very consistent between the Spotlight and Stripmap data and given the independence of the datasets, the duplicate measurements over the same time period validate the results without the requirement for ground data. Confidence in the SPOT-CR results is boosted by a qualitative comparison to extensometer data over the same time period (Wang et al., 2013). The maximum step-like displacement of ~0.5 m occurred in May 2009 before stabilising for the remainder of the year. Despite this extensometer measurement being taken at the eastern boundary of the landslide, the magnitude and timing of movements recorded by the extensometer closely follow the results presented here. Additionally, the magnitude and

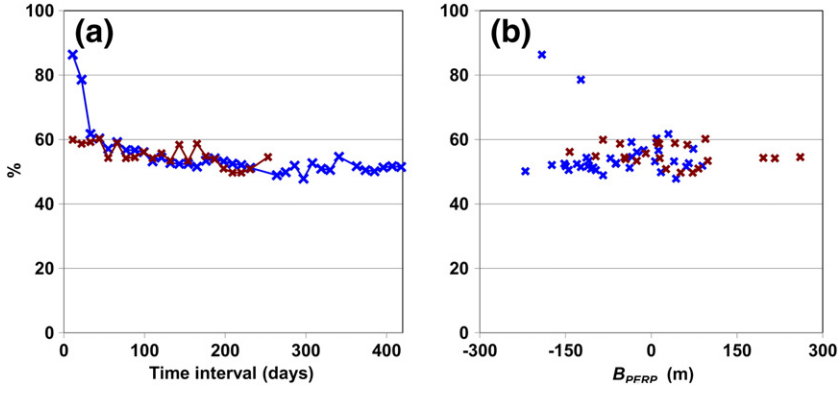

Fig. 6. Percentage of pixels with a correlation above an arbitrary value of 0.25 with respect to (a) the time interval between master and slave image and (b) the perpendicular baseline. This is shown for both the TSX Spotlight offsets (blue) and TSX Stripmap offsets (red). No obvious deterioration is seen with respect to increasing perpendicular baselines which contrasts the pattern shown by Envisat data in Casu et al. (2011), most likely due to the far smaller range in perpendicular baselines of the TSX data.

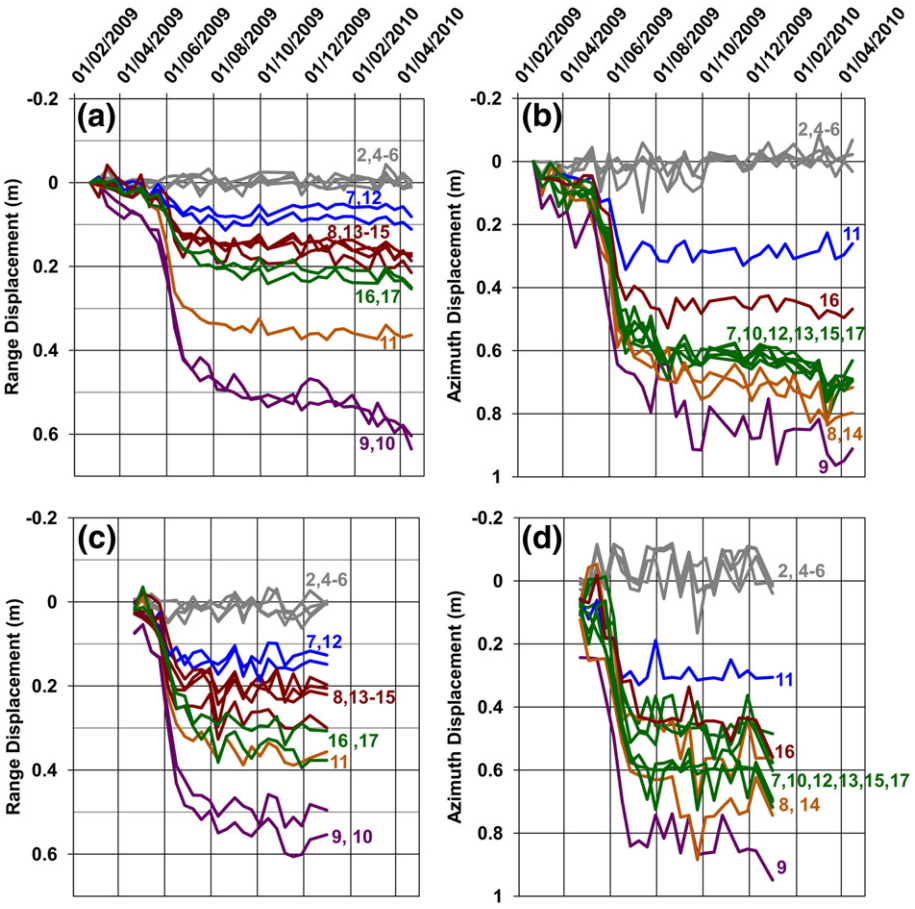

Fig. 7. Offset displacement of the corner reflectors. (a–b) Range and azimuth offsets measured from TSX Spotlight data. (c–d) Range and azimuth offsets measured from TSX Stripmap data. The positive scale is away from the sensor in range dimension and the reverse along-track direction (i.e. predominantly northwards) in azimuth dimension.

linearity of repeated GPS measurements closely follow the range offset results for the GPS survey period August 2009–April 2010 (Liao, Zhang, & Balz, 2013).

5.5. Accuracy assessment of SPOT-CR results

An assessment of the offset errors is undertaken using two independent offset pairs significantly overlapping in time. The offsets were measured between the first and penultimate available image, and compared to offsets between the second and last image (~9 months for TSX Spotlight and ~5 months for TSX Stripmap data). Since using these data to assess errors assumes that the displacements in these two time periods are equal, the two master images were chosen at the start of August since this is when the landslide velocity had significantly reduced. The differences between offset measurements from these overlapping pairs for both the TSX Spotlight and TSX Stripmap imagery are shown in Table 2. Using the corner reflector points to generate the offset measurements, the RMS errors are all less than 0.038 m and 0.071 m in the range and azimuth directions, respectively. The errors are significantly lower for the TSX Spotlight imagery than for the Stripmap imagery, and the errors are also consistently lower for the range offsets than for the azimuth offsets. In all cases, both range and azimuth error values are an order of magnitude lower than the total accumulated landslide displacement.

To assess offset errors from the natural terrain, areas of land adjacent to the corner reflector points were used to carry out the same analysis. Table 2 shows that the RMS errors for the two offset pairs from natural terrain are at least 20 times higher than from the corner reflector points and are the same order of magnitude as the recorded landslide movements, which therefore suggests natural terrain areas of dense vegetation are not optimal for generating reliable offset measurements in the Three Gorges region. Regardless of the displacement magnitude, corner reflectors remain beneficial for generating precise, 2-dimensional sub-pixel offset measurements only using the SAR amplitude data. Envisat data failed to produce successful offset results given its significantly larger pixel spacing covering the relatively small landslide area. A far greater contrast in the ground terrain backscatter, much faster ground movements or consistent movements over a larger area would all increase

Table 2
Comparison between two independent offset calculations from two image pairs significantly overlapping in time (the first two images in August were used as the two master images, with the last two available images used as the respective slave images). This can help assess the errors between different SAR image modes and also between the offsets calculated from corner reflectors and densely vegetated terrain (directly adjacent to the corner reflector points).

	Range offsets		Azimuth offsets	
Sensor/image mode	Mean difference (m)	RMS error (m)	Mean difference (m)	RMS error (m)
TSX Spotlight (corner reflectors)	0.008	0.011	0.055	0.060
TSX Stripmap (corner reflectors)	0.040	0.038	0.059	0.071
TSX Spotlight (vegetated terrain)	0.574	0.912	1.146	1.478
TSX Stripmap (vegetated terrain)	1.198	1.394	3.044	3.979

the likelihood of obtaining reliable SPOT results from natural terrain in all image modes.

6. Discussion

The movements of the Shuping landslide in May–June 2009, revealed by the SPOT-CR results, demonstrate how the spatial displacement gradient assumption is broken and invalidates long-term D-InSAR analyses. It would be impossible to accurately unwrap any interferogram which spanned this movement episode (without the use of in-situ data) and this issue can perhaps explain the variety of D-InSAR measurements of the Shuping landslide outlined in Section 3. Certainly this time-period should not be analysed using D-InSAR time-series analyses since an even sparser network of measurements (relative to the original interferograms) generated from any form of persistent scatterer interferometry would be less able to resolve such spatially variable measurements.

The SPOT-CR technique is robust when applied to corner reflectors, although it is limited by the rate of movement in relation to the pixel spacing of the SAR data, size of the search window used in the cross-correlation calculation and any significant change in the surface reflectance between image acquisitions. With the use of highly contrasting ground features (i.e. installed corner reflectors in this case), verifiable offset measurements were generated from TSX Spotlight and TSX Stripmap data. When such point-like targets exist over a landslide, it would be beneficial to run SPOT-CR analysis for a stack of SAR images prior to any D-InSAR analysis to assess if any movements exceed the spatial displacement gradient.

Identified as an ancient landslide (Wang, Zhang, et al., 2008), the Shuping landslide is underlain by sandy mudstones and muddy sandstones of the Triassic Badong Formation, a unit within which many landslides are concentrated (Wen, Wang, Wang, & Zhang, 2004). This landslide has been divided into two parts: eastern and western blocks with a combined width of about 600 m. A borehole towards the lower part of Block-1 (eastern) indicated the surface of the rupture zone was at a depth of 65 and 75 m, a zone where numerous slickensides were evident (Wang et al., 2005).

Whilst the rates of displacement are different over the landslide body, the timing of faster and slower episodes (Fig. 7) is very consistent which suggests the same causal factors are affecting the whole landslide. Another capability of sub-pixel offset measurements is the ability to estimate the displacement vectors from the range and azimuth directions to resolve the purely northwards (d_N) and vertical (d_U) components of displacement (Fialko, Simons, & Agnew, 2001). This derivation assumes that landslide movement in the east–west direction (d_E) is zero which is a relatively safe assumption given the orientation of the Shuping landslide with respect to the SAR sensor:

$$\begin{aligned} d_{\text{RANGE}} &= [-0.68 \quad 0.12 \quad -0.72][d_E \quad d_N \quad d_U]^T \\ d_{\text{AZIMUTH}} &= [-0.17 \quad 0.98 \quad 0][d_E \quad d_N \quad d_U]^T \\ d_E &= 0 \end{aligned}.$$

By solving this system of equations, Fig. 8 shows the estimated accumulated vertical and horizontal components of displacement for the Shuping landslide between 21st Feb 2009 and 15th April 2010. A clear topographic trend is visible for the vertical measurements with the total accumulated displacement increasing with elevation. The head of the landslide moved downwards at least 25 times more than the toe of the landslide. The northwards displacement data does not show this trend, but has the greatest movements towards the middle and toe of the landslide. A rotational failure mechanism along a curved plane would be consistent with these 2-dimensional movements and is proposed as a first-order interpretation of the data.

Additionally, the period of most rapid displacement around May–June 2009 corresponds to the annual lowering of the Three Gorges Reservoir (Fig. 9) which accommodates the heavy summer rainfall and helps prevent flooding downstream. The faster the rate of change in the reservoir level, the longer the water table levels take to adjust. When the water-level is lowered, drainage of the landslide lags the reservoir drop which results in high hydraulic gradients and favours slope instability (Shimei, Huawei, Yeming, & Jun, 2008). The biggest displacements appear to correspond to the greatest rates of reservoir lowering, whilst periods of slower reservoir lowering do not lead to an increased propensity of slope failure. However, both the managed and natural changes in the reservoir water-level are related to the seasonal variations in rainfall, so an analysis of landslide movement in relation to both factors is required to fully understand the mechanisms of movement for the Shuping landslide. Corroboration from the analysis of other nearby landslide sites is a subsequent stage of this work.

7. Conclusions

Recognising that landslides often exhibit non-linear and complex displacement patterns, this paper assesses the capability of various SAR image modes (TSX Spotlight, TSX Stripmap and Envisat data) to reliably identify, map, monitor and characterise landslide movement using D-InSAR and a Sub-Pixel Offset Time-series technique applied to corner reflectors (SPOT-CR). The Shuping landslide within the densely vegetated Three Gorges region (China) is used to test these methods on account of the data availability from numerous SAR image modes

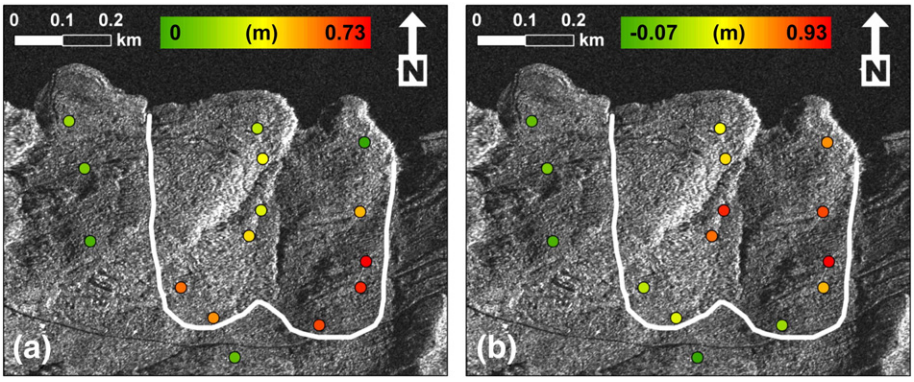

Fig. 8. Using the azimuth and range offset corner reflector measurements (calculated from the first and last TSX Spotlight images), the displacement vectors can be decomposed to calculate the total accumulated vertical (a) and (b) northwards displacement between 21st Feb 2009 and 15th April 2010. The exact values can be found in Supplementary material (Table S3).

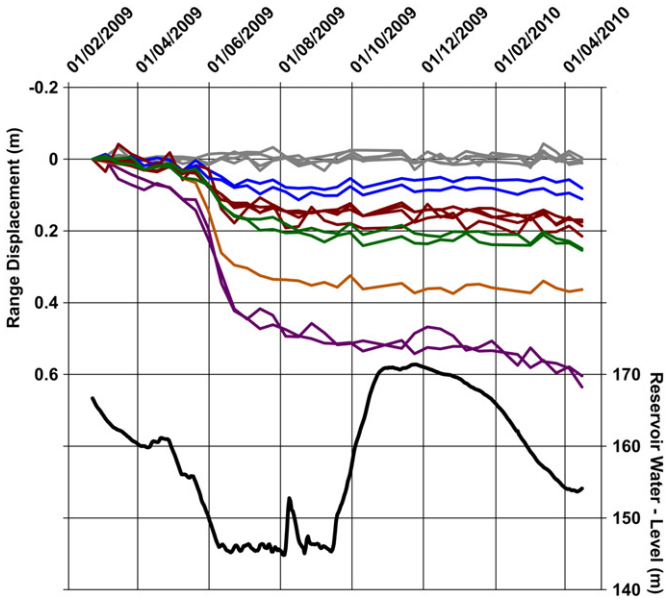

Fig. 9. Range displacement from TSX Spotlight in relation to the water-level changes of the Three Gorges Reservoir.

and the network of corner reflectors installed in and around the landslide body.

D-InSAR measurements can be successfully used to detect movements of the Shuping landslide, although there are significant limitations that prohibit long term D-InSAR monitoring using single-pair and time-series techniques. Interferometric coherence in the Three Gorges region is always low due to the density of vegetation and the limited satellite revisit times, but there are seasonal signals (Fig. 2) most likely caused by consistent annual variations in rainfall and soil moisture. Particularly for TSX imaging modes, it is found that the coherence is highest between November and February each year when rainfall and vegetation coverage is at a minimum.

Despite the problems of low coherence, landslides can be reliably identified and mapped using high resolution D-InSAR measurements providing the movement does not exceed the spatial displacement gradient. However, episodic and faster landslide movements can exceed the displacement gradient (most likely around landslide boundaries) due to the potentially high contrast in displacement rates between stable and moving land (Fig. 3). High displacement gradients identified for the Shuping landslide invalidate the use of D-InSAR time-series approaches for the data stacks from all three SAR image modes used in this study.

Subsequently, a Sub-Pixel Offset Time-series approach applied to corner reflectors is used as a robust method to resolve time-varying landslide displacements. A quantitative, heuristic approach shows how the distribution of offset values for a stable reference area close to the landslide can help reduce the likelihood of spurious correlation and after considering the pixel spacing of SAR data as well as the expected movement of the phenomenon under study, enables suitable sub-pixel offset parameters to be selected (Fig. 4). Additionally the same initial master image is chosen to calculate the displacement time-series from subsequent slave images in order to avoid the propagation of errors associated with an accumulative time-series curve from time-adjacent image pairs. Given the small range in TSX perpendicular baselines (Fig. 6), the use of a small baseline approach for generating time-series displacement curves was not pursued.

Offset measurements from corner reflectors are shown to generate verifiable cross-correlations when located amongst dense vegetation (Fig. 5) and Table 2 shows the errors associated with the corner reflector offsets from TSX data are at least an order of magnitude lower than the landslide displacements. It is also clear that higher resolution SAR data reduces the offset errors.

From the final SPOT-CR analysis, it is clear that large, episodic movements are responsible for a loss of interferometric coherence and the range offset displacement in May 2009 towards the head of the Shuping landslide (Fig. 7) is shown to exceed the displacement gradient measurable by D-InSAR. Assuming the E–W component of displacement is zero, the range and azimuth offsets can be decomposed into estimates of the vertical and horizontal measurements (Fig. 8) to help infer a rotational component of the Shuping landslide and differences between the eastern and western sides of the landslide imply the movements are highly variable and not moving in a uniform manner. Finally, the main episodes of landslide movement appear to occur at the same time as the rapid drawdown of the Three Gorges Reservoir in May/June 2009 (Fig. 9).

This study has considered one landslide in a specific type of terrain. Landslides with different surface features, orientated differently with respect to the SAR sensor and with different movement behaviours, may require different forms of analysis. Areas with less vegetation (either with more buildings or bare rock) which move at slower rates may be more successfully monitored using D-InSAR time series techniques. Larger landslides with displacements spread over a bigger area or moving less episodically would also be more suited for D-InSAR time series analysis. SPOT techniques should achieve better results for landslides with more contrasting surface features (natural or man-made) or where the movement is greater with respect to the SAR image pixel size, up to the point when movement induces significant change in the Earth's surface (and therefore change in the radar backscatter). The application of SPOT techniques to more landslide sites using different SAR data types should be the focus of future studies, and the use of time-adjacent (or small baseline) pairs may be optimal for extracting time-series data from areas of lower correlation. Independent verification of the SAR-derived displacements for the CRs should also be conducted once such data becomes available along with comparing the observed displacement patterns of the Shuping landslide to potential causal factors such as rainfall, groundwater and reservoir water-levels.

Acknowledgements

This work is supported by an EPSRC Industrial Studentship to AS (EP/P505534/1). Part of this work was supported by the Natural Environment Research Council (NERC) through the National Centre for Earth Observation (NCEO), of which the Centre for the Observation and Modelling of Earthquakes, Volcanoes and Tectonics (COMET+) is part. The Envisat images were supplied through the ESA–MOST Dragon 2 Cooperation Programme (ID: 5343). The TSX Spotlight and Stripmap images were supplied through DLR project (ID: GEO0112). We are very grateful to Xiao Cheng for the MET rainfall data from Badong as well as Prof. Simon Wheeler from the University of Glasgow for discussions on the landslide mechanism.

Appendix A. Supplementary data

Supplementary data to this article can be found online at http://dx.doi.org/10.1016/j.rse.2014.03.003.

References

Ahmed, R., Siqueira, P., Hensley, S., Chapman, B., & Bergen, K. (2011). A survey of temporal decorrelation from spaceborne L-band repeat-pass InSAR. *Remote Sensing of Environment, 115*, 2887–2896.

Akbarimehr, M., Motagh, M., & Haghshenas-Haghighi, M. (2013). Slope stability assessment of the Sarcheshmeh landslide, northeast Iran, investigated using InSAR and GPS observations. *Remote Sensing, 5*, 3681–3700.

Baran, I., Stewart, M., & Claessens, S. (2005). A new functional model for determining minimum and maximum detectable deformation gradient resolved by satellite

radar interferometry. *IEEE Transactions on Geoscience and Remote Sensing*, *43*, 675–682.
Bechor, N.B.D., & Zebker, H. A. (2006). Measuring two-dimensional movements using a single InSAR pair. *Geophysical Research Letters*, *33*, L16311.
Berardino, P., Costantini, M., Franceschetti, G., Iodice, A., Pietranera, L., & Rizzo, V. (2003). Use of differential SAR interferometry in monitoring and modelling large slope instability at Maratea (Basilicata, Italy). *Engineering Geology*, *68*, 31–51.
Berardino, P., Fornaro, G., Lanari, R., & Sansosti, E. (2002). A new algorithm for surface deformation monitoring based on small baseline differential SAR interferograms. *IEEE Transactions on Geoscience and Remote Sensing*, *40*, 2375–2383.
Cascini, L., Fornaro, G., & Peduto, D. (2010). Advanced low- and full-resolution DInSAR map generation for slow-moving landslide analysis at different scales. *Engineering Geology*, *112*, 29–42.
Cascini, L., Peduto, D., Pisciotta, G., Arena, L., Ferlisi, S., & Fornaro, G. (2013). The combination of DInSAR and facility damage data for the updating of slow-moving landslide inventory maps at medium scale. *Natural Hazards and Earth System Sciences*, *13*, 1527–1549.
Casu, F., Manconi, A., Pepe, A., & Lanari, R. (2011). Deformation time-series generation in areas characterized by large displacement dynamics: The SAR amplitude pixel-offset SBAS technique. *IEEE Transactions on Geoscience and Remote Sensing*, *49*, 2752–2763.
Colesanti, C., & Wasowski, J. (2006). Investigating landslides with space-borne Synthetic Aperture Radar (SAR) interferometry. *Engineering Geology*, *88*, 173–199.
Cruden, D.M., & Varnes, D. J. (1996). Landslide types and processes. In A. K. Turner, & R. L. Shuster (Eds.), *Landslides: Investigation and mitigation* (pp. 36–75). Washington, DC: Transport Research Board, National Research Council.
Debella-Gilo, M., & Kääb, A. (2011). Sub-pixel precision image matching for measuring surface displacements on mass movements using normalized cross-correlation. *Remote Sensing of Environment*, *115*, 130–142.
Delacourt, C., Allemand, P., Casson, B., & Vadon, H. (2004). Velocity field of the "La Clapière" landslide measured by the correlation of aerial and QuickBird satellite images. *Geophysical Research Letters*, *31*, L15619.
Dzikiti, S., Verreynne, S. J., Stuckens, J., Strever, A., Verstraeten, W. W., Swennen, R., et al. (2011). Seasonal variation in canopy reflectance and its application to determine the water status and water use by citrus trees in the Western Cape, South Africa. *Agricultural and Forest Meteorology*, *151*, 1035–1044.
Ferretti, A., Prati, C., & Rocca, F. (2001). Permanent scatterers in SAR interferometry. *IEEE Transactions on Geoscience and Remote Sensing*, *39*, 8–20.
Fialko, Y., Simons, M., & Agnew, D. (2001). The complete (3-D) surface displacement field in the epicentral area of the 1999 Mw 7.1 Hector Mine earthquake, California, from space geodetic observations. *Geophysical Research Letters*, *28*, 3063–3066.
Foster, J., Kealy, J., Cherubini, T., Businger, S., Lu, Z., & Murphy, M. (2013). The utility of atmospheric analyses for the mitigation of artifacts in InSAR. *Journal of Geophysical Research — Solid Earth*, *118*, 748–758.
Fruneau, B., Achache, J., & Delacourt, C. (1996). Observation and modelling of the Saint-Étienne-de-Tinée landslide using SAR interferometry. *Tectonophysics*, *265*, 181–190.
Fu, W., Guo, H., Tian, Q., & Guo, X. (2010). Landslide monitoring by corner reflectors differential interferometry SAR. *International Journal of Remote Sensing*, *31*, 6387–6400.
Funning, G. J., Parsons, B., Wright, T. J., Jackson, J. A., & Fielding, E. J. (2005). Surface displacements and source parameters of the 2003 Bam (Iran) earthquake from Envisat advanced Synthetic Aperture Radar imagery. *Journal of Geophysical Research — Solid Earth*, *110*, B09406.
Gatelli, F., Guamieri, A.M., Parizzi, F., Pasquali, P., Prati, C., & Rocca, F. (1994). The wavenumber shift in SAR interferometry. *IEEE Transactions on Geoscience and Remote Sensing*, *32*, 855–865.
Goldstein, R. M., & Werner, C. L. (1998). Radar interferogram filtering for geophysical applications. *Geophysical Research Letters*, *25*, 4035–4038.
Haug, T., Kääb, A., & Skvarca, P. (2010). Monitoring ice shelf velocities from repeat MODIS and Landsat data — A method study on the Larsen C ice shelf, Antarctic Peninsula, and 10 other ice shelves around Antarctica. *The Cryosphere*, *4*, 161–178.
Hilley, G. E., Bürgmann, R., Ferretti, A., Novali, F., & Rocca, F. (2004). Dynamics of slow-moving landslides from permanent scatterer analysis. *Science*, *304*, 1952–1955.
Hooper, A. (2008). A multi-temporal InSAR method incorporating both persistent scatterer and small baseline approaches. *Geophysical Research Letters*, *35*, L16302.
Hooper, A., Segall, P., & Zebker, H. (2007). Persistent scatterer interferometric Synthetic Aperture Radar for crustal deformation analysis, with application to Volcán Alcedo, Galápagos. *Journal of Geophysical Research — Solid Earth*, *112*, B07407.
Jiang, M., Li, Z. W., Ding, X. L., Zhu, J. J., & Feng, G. C, (2011). Modeling minimum and maximum detectable deformation gradients of interferometric SAR measurements. *International Journal of Applied Earth Observation and Geoinformation*, *13*(5), 766–777.
Jónsson, S., Zebker, H., Segall, P., & Amelung, F. (2002). Fault slip distribution of the 1999 Mw 7.1 Hector Mine, California, earthquake, estimated from satellite radar and GPS measurements. *Bulletin of the Seismological Society of America*, *92*, 1377–1389.
Kääb, A. (2002). Monitoring high-mountain terrain deformation from repeated air- and spaceborne optical data: Examples using digital aerial imagery and ASTER data. *ISPRS Journal of Photogrammetry and Remote Sensing*, *57*, 39–52.
Leprince, S., Berthier, E., Ayoub, F., Delacourt, C., & Avouac, J. -P. (2008). Monitoring earth surface dynamics with optical imagery. *Eos, Transactions American Geophysical Union*, *89*, 1–2.
Li, Z., Elliott, J. R., Feng, W., Jackson, J. A., Parsons, B. E., & Walters, R. J. (2011). The 2010 MW 6.8 Yushu (Qinghai, China) earthquake: Constraints provided by InSAR and body wave seismology. *Journal of Geophysical Research — Solid Earth*, *116*, B10302.
Li, Z., Fielding, E. J., Cross, P., & Muller, J. -P. (2006). Interferometric Synthetic Aperture Radar atmospheric correction: GPS topography-dependent turbulence model. *Journal of Geophysical Research — Solid Earth*, *111*, B02404.
Li, X., Muller, J. -P., Chen, F., & Yonghong, Z. (2011). Measuring displacement field from TerraSAR-X amplitude images by subpixel correlation: An application to the landslide in Shuping, Three Gorges area. *Acta Petrologica Sinica*, *27*, 3843–3850.
Li, Z., Muller, J. -P., Cross, P., & Fielding, E. J. (2005). Interferometric Synthetic Aperture Radar (InSAR) atmospheric correction: GPS, moderate resolution imaging spectroradiometer (MODIS), and InSAR integration. *Journal of Geophysical Research — Solid Earth*, *110*, B03410.
Li, P., Shi, C., Li, Z., Muller, J. -P., Drummond, J., Li, X., et al. (2012). Evaluation of ASTER GDEM using GPS benchmarks and SRTM in China. *International Journal of Remote Sensing*, *34*, 1744–1771.
Liao, M., Tang, J., Wang, T., Balz, T., & Zhang, L. (2012). Landslide monitoring with high-resolution SAR data in the Three Gorges region. *Science China Earth Sciences*, *55*, 590–601.
Liao, M., Zhang, L., & Balz, T. (2013). Landslide monitoring with high-resolution TerraSAR-X data in the Three Gorges area. *5th TerraSAR-X Science Team Meeting. DLR Oberpfaffenhofen*.
Liu, J. G., Mason, P. J., Clerici, N., Chen, S., Davis, A., Miao, F., et al. (2004). Landslide hazard assessment in the Three Gorges area of the Yangtze River using ASTER imagery: Zigui–Badong. *Geomorphology*, *61*, 171–187.
Massonnet, D., & Feigl, K. L. (1998). Radar interferometry and its application to changes in the Earth's surface. *Reviews of Geophysics*, *36*, 441–500.
Michel, R., Avouac, J. -P., & Taboury, J. (1999). Measuring ground displacements from SAR amplitude images: Application to the Landers Earthquake. *Geophysical Research Letters*, *26*, 875–878.
Onn, F., & Zebker, H. A. (2006). Correction for interferometric Synthetic Aperture Radar atmospheric phase artifacts using time series of zenith wet delay observations from a GPS network. *Journal of Geophysical Research — Solid Earth*, *111*.
Pathier, E., Fielding, E. J., Wright, T. J., Walker, R., Parsons, B. E., & Hensley, S. (2006). Displacement field and slip distribution of the 2005 Kashmir earthquake from SAR imagery. *Geophysical Research Letters*, *33*, L20310.
Peduto, D., Cascini, L., & Fornaro, G. (2010). Satellite radar. In V. Tofani, S. Segoni, F. Catani, & N. Casagli (Eds.), *Evaluation report on innovative monitoring and remote sensing methods and future technology* (pp. 42–43). Oslo: Norwegian Geotechnical Institute.
Quincey, D. J., Lucas, R. M., Richardson, S. D., Glasser, N. F., Hambrey, M. J., & Reynolds, J. M. (2005). Optical remote sensing techniques in high-mountain environments: Application to glacial hazards. *Progress in Physical Geography*, *29*, 475–505.
Rott, H. (2009). Advances in interferometric Synthetic Aperture Radar (InSAR) in earth system science. *Progress in Physical Geography*, *33*, 769–791.
Rott, H., & Nagler, T. (2006). The contribution of radar interferometry to the assessment of landslide hazards. *Advances in Space Research*, *37*, 710–719.
Rott, H., Scheuchl, B., Siegel, A., & Grasemann, B. (1999). Monitoring very slow slope movements by means of SAR interferometry: A case study from a mass waste above a reservoir in the Ötztal Alps, Austria. *Geophysical Research Letters*, *26*, 1629–1632.
SARMAP (2012). *SARScape: Technical description*. Switzerland: SARMAP.
Sassa, K., Picarelli, L., & Yueping, Y. (2009). Monitoring, prediction and early warning. In K. Sassa, & P. Canuti (Eds.), *Landslides — Disaster risk reduction* (pp. 351–375). Berlin, Heidelberg: Springer.
Scambos, T. A., Dutkiewicz, M. J., Wilson, J. C., & Bindschadler, R. A. (1992). Application of image cross-correlation to the measurement of glacier velocity using satellite image data. *Remote Sensing of Environment*, *42*, 177–186.
Shimei, W., Huawei, Z., Yeming, Z., & Jun, Z. (2008). *Back analysis of unsaturated parameters and numerical seepage simulation of the Shuping landslide in Three Gorges Reservoir area.* Landslides and engineered slopes. From the past to the future, two volumes + CD-ROM. CRC Press, 985–990.
Smith, L. C. (2002). Emerging applications of interferometric Synthetic Aperture Radar (InSAR) in geomorphology and hydrology. *Annals of the Association of American Geographers*, *92*, 385–398.
Spagnolini, U. (1995). 2-D phase unwrapping and instantaneous frequency estimation. *IEEE Transactions on Geoscience and Remote Sensing*, *33*, 579–589.
Strozzi, T., Farina, P., Corsini, A., Ambrosi, C., Thüring, M., Zilger, J., et al. (2005). Survey and monitoring of landslide displacements by means of L-band satellite SAR interferometry. *Landslides*, *2*, 193–201.
Stumpf, A., Kerle, N., & Malet, J. -P. (2010). Guidelines for the selection of appropriate remote sensing technologies for monitoring different types of landslides. In A. Stumpf, N. Kerle, & J. -P. Malet (Eds.), *The Deliverable 4.4 of the European SAFELAND Project*.
Tofani, V., Raspini, F., Catani, F., & Casagli, N. (2013). Persistent scatterer interferometry (PSI) technique for landslide characterization and monitoring. *Remote Sensing*, *5*, 1045–1065.
Tofani, V., Segoni, S., Catani, F., & Casagli, N. (2010). Evaluation report on innovative monitoring and remote sensing methods and future technology. In V. Tofani, S. Segoni, F. Catani, & N. Casagli (Eds.), *The Deliverable 4.5 of the European SAFELAND Project*.
Tolomei, C., Taramelli, A., Moro, M., Saroli, M., Aringoli, D., & Salvi, S. (2013). Analysis of the deep-seated gravitational slope deformations over Mt. Frascare (Central Italy) with geomorphological assessment and DInSAR approaches. *Geomorphology*, *201*, 281–292.
Touzi, R., Lopes, A., Bruniquel, J., & Vachon, P. W. (1999). Coherence estimation for SAR imagery. *IEEE Transactions on Geoscience and Remote Sensing*, *37*, 135–149.
UN-ISDR (Ed.). (2004). *Terminology: Basic terms of disaster risk reduction*. Geneva: United Nations.
Wang, H., Harvey, A.M., Xie, S., Kuang, M., & Chen, Z. (2008). Tributary-junction fans of China's Yangtze Three-Gorges Valley: Morphological implications. *Geomorphology*, *100*, 131–139.
Wang, F., Wang, G., Sassa, K., Takeuchi, A., Araiba, K., Zhang, Y., et al. (2005). Displacement monitoring and physical exploration on the Shuping landslide reactivated by impoundment of the Three Gorges Reservoir, China. In K. Sassa, H. Fukuoka, F. Wang, & G. Wang (Eds.), *Landslides* (pp. 313–319). Berlin, Heidelberg: Springer.

Wang, F., Yueping, Y., Zhitao, H., Zhang, Y., Wang, G., & Renjie, D. (2013). Slope deformation caused by water-level variation in the Three Gorges Reservoir, China. In K. Sassa, B. Rouhban, S. Briceno, M. McSaveney, & B. He (Eds.), *Landslides: Global risk preparedness* (pp. 227–237). Berlin: Springer.

Wang, F., Zhang, Y., Huo, Z., Peng, X., Araiba, K., & Wang, G. (2008). Movement of the Shuping landslide in the first four years after the initial impoundment of the Three Gorges Dam Reservoir, China. *Landslides*, *5*, 321–329.

Wangensteen, B., Guðmundsson, Á., Eiken, T., Kääb, A., Farbrot, H., & Etzelmüller, B. (2006). Surface displacements and surface age estimates for creeping slope landforms in northern and eastern Iceland using digital photogrammetry. *Geomorphology*, *80*, 59–79.

Wen, B., Wang, S., Wang, E., & Zhang, J. (2004). Characteristics of rapid giant landslides in China. *Landslides*, *1*, 247–261.

Wen-Yen, C., Chih-Tien, W., Chih-Yuan, C., & Jyun-Ru, K. (2012). Mapping geo-hazard by satellite radar interferometry. *Proceedings of the IEEE*, *100*, 2835–2850.

Xia, Y. (2010). Synthetic Aperture Radar interferometry. In G. Xu (Ed.), *Sciences of geodesy (1)* (pp. 415–473). Berlin: Springer.

Yamaguchi, Y., Tanaka, S., Odajima, T., Kamai, T., & Tsuchida, S. (2003). Detection of a landslide movement as geometric misregistration in image matching of SPOT HRV data of two different dates. *International Journal of Remote Sensing*, *24*, 3523–3534.

Yin, Y., Zheng, W., Liu, Y., Zhang, J., & Li, X. (2010). Integration of GPS with InSAR to monitoring of the Jiaju landslide in Sichuan, China. *Landslides*, *7*, 359–365.

Yun, S. -H., Zebker, H., Segall, P., Hooper, A., & Poland, M. (2007). Interferogram formation in the presence of complex and large deformation. *Geophysical Research Letters*, *34*, L12305.

Zebker, H. A., Rosen, P. A., & Hensley, S. (1997). Atmospheric effects in interferometric Synthetic Aperture Radar surface deformation and topographic maps. *Journal of Geophysical Research — Solid Earth*, *102*, 7547–7563.

Appendix C – Co-Author *Geophysical Journal International* Paper

Geophysical Journal International

Geophys. J. Int. (2014) **197,** 213–232
Advance Access publication 2014 February 21

doi: 10.1093/gji/ggu017

Spatiotemporal characteristics of the Huangtupo landslide in the Three Gorges region (China) constrained by radar interferometry

R. Tomás,[1,2] Z. Li,[2] P. Liu,[2,3] A. Singleton,[2] T. Hoey[2] and X. Cheng[4]

[1]*Departamento de Ingeniería Civil, Escuela Politécnica Superior, Universidad de Alicante, P.O. Box* 99, *E*-03080 *Alicante, Spain. E-mail: roberto.tomas@ua.es*
[2]*School of Geographical and Earth Sciences, University of Glasgow, Glasgow G*12 8*QQ, UK*
[3]*Shenzhen Key Laboratory of Spatial Information Smart Sensing and Services, Shenzhen University, Shenzhen* 518060*, China*
[4]*College of Global Change and Earth System Science, Beijing Normal University, Beijing* 100875*, China*

Accepted 2014 January 16. Received 2014 January 15; in original form 2013 July 11

SUMMARY

The Huangtupo landslide is one of the largest in the Three Gorges region, China. The county-seat town of Badong, located on the south shore between the Xiling and Wu gorges of the Yangtze River, was moved to this unstable slope prior to the construction of the Three Gorges Project, since the new Three Gorges reservoir completely submerged the location of the old city. The instability of the slope is affecting the new town by causing residential safety problems. The Huangtupo landslide provides scientists an opportunity to understand landslide response to fluctuating river water level and heavy rainfall episodes, which is essential to decide upon appropriate remediation measures. Interferometric Synthetic Aperture Radar (InSAR) techniques provide a very useful tool for the study of superficial and spatially variable displacement phenomena. In this paper, three sets of radar data have been processed to investigate the Huangtupo landslide. Results show that maximum displacements are affecting the northwest zone of the slope corresponding to Riverside slumping mass I#. The other main landslide bodies (i.e. Riverside slumping mass II#, Substation landslide and Garden Spot landslide) exhibit a stable behaviour in agreement with *in situ* data, although some active areas have been recognized in the foot of the Substation landslide and Garden Spot landslide. InSAR has allowed us to study the kinematic behaviour of the landslide and to identify its active boundaries. Furthermore, the analysis of the InSAR displacement time-series has helped recognize the different displacement patterns on the slope and their relationships with various triggering factors. For those persistent scatterers, which exhibit long-term displacements, they can be decomposed into a creep model (controlled by geological conditions) and a superimposed recoverable term (dependent on external factors), which appears closely correlated with reservoir water level changes close to the river's edge. These results, combined with *in situ* data, provide a comprehensive analysis of the Huangtupo landslide, which is essential for its management.

Key words: Time series analysis; Spatial analysis; Radar interferometry; Geomorphology; Creep and deformation.

1 INTRODUCTION

The Three Gorges (TG) Dam, located along the Yangtze River in Central China (Fig. 1), has become one of the most important hydraulic projects in the world. The dam is 175 m high and 2335 m long, and the reservoir has a capacity of 3.93×10^{10} m^3 and covers an area of 1084 km^2. In addition to its size, the TG Dam is the largest power plant in the world and has caused the displacement of more people than any other hydraulic project (Jackson & Sleigh 2000; Suo *et al.* 2012). The aim of the project was to generate hydropower, reduce the potential of floods downstream and increase the Yangtze River's upstream shipping capacity. The project also had a significant socioeconomic impact, such as the relocation of over 1.3 million people (Jackson & Sleigh 2000; Jiazhu 2002). Since the first impoundment of the reservoir in 2003 June and even during prior relocation tasks, there were significant environmental impacts (e.g. induced seismicity, trapping of sediments and nutrients behind dams that promotes downstream erosion, river system fragmentation that causes multilevel effects throughout the aquatic ecosystem) including landslides (Tullos 2009). Slope instabilities are the most common natural hazard associated with the TG project. Over 2000 unstable areas, mostly triggered by rain and water storage, have

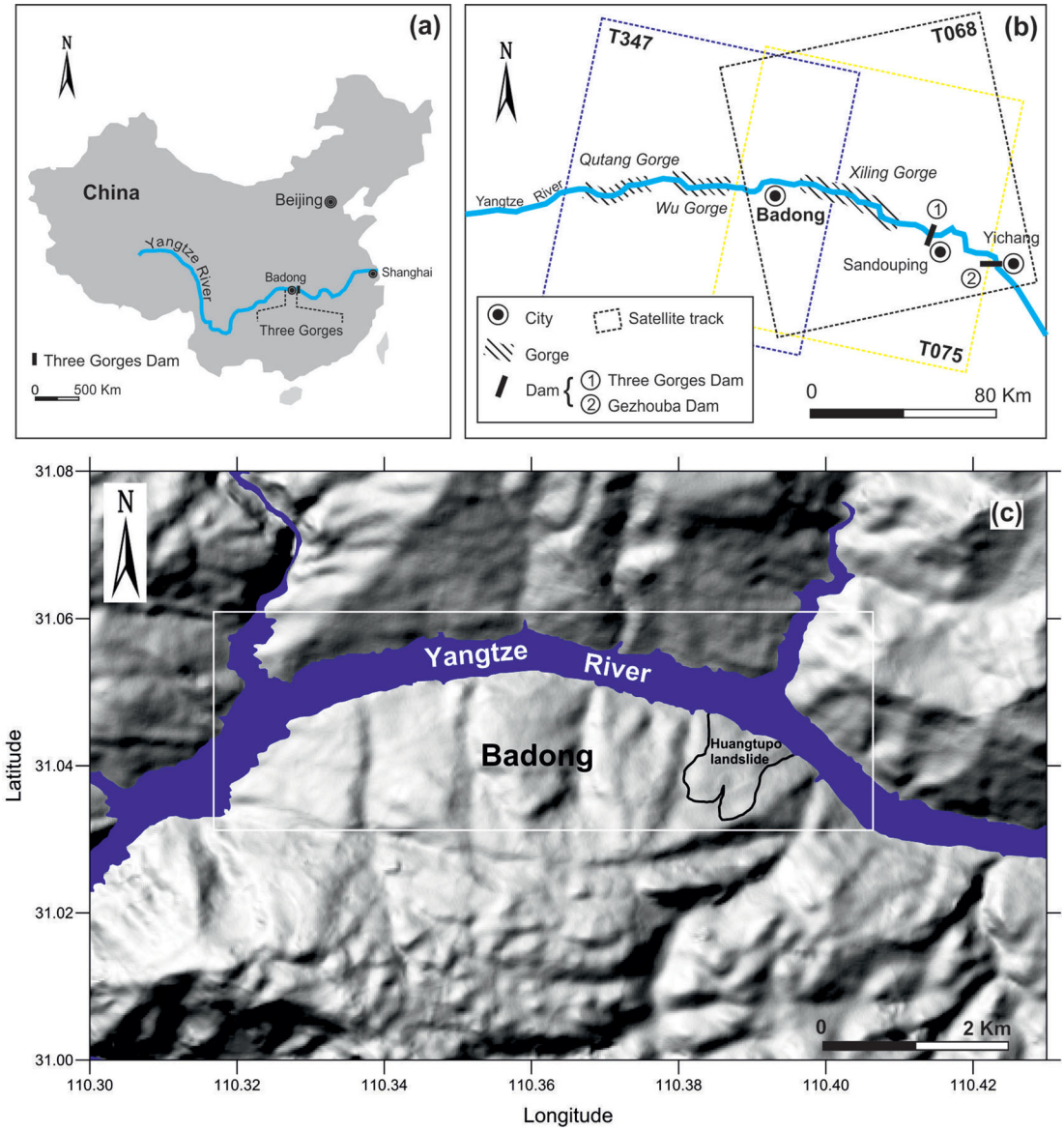

Figure 1. Location of (a) the study area, (b) the Badong County and the coverage of Envisat tracks T068, T075 and T347 and (c) the Huangtupo landslide. The white box in (c) corresponds to the spatial coverage of the InSAR processing, presented below. The boundary of the landslide plotted in (c) is based on Xie (2009).

been identified in the TG region (Liu *et al.* 2004; He *et al.* 2008); some of them in a state of active displacement.

The Huangtupo slope is one of the largest landslides with problems related to the residential safety of inhabitants in the reservoir area of the TG Project (Deng *et al.* 2000). This slope is located on the southern shore of the transition between the Xiling and Wu gorges of the Yangtze River in Badong County (Hubei Province, China; Fig. 1). The town of Badong was moved from its original location to a site overlying the Huangtupo landslide in 1982 because of the construction of the Gezhouba Dam. During the construction of the new town, many complex environmental and geological issues were discovered and two main interpretations of the landslide were presented (Wu *et al.* 2006): (i) there are two isolated ancient slide bodies in the new town site; (ii) the entirety of Huangtupo is a large superficial layer from an ancient slide body. More recently, Xie (2009) and Hu *et al.* (2012a,b) stated that the landslide composed of multiple slumps recognizing more than 10 different slide bodies (4 main bodies and 12 minor shallow landslides).

In 1995 June and October, after the city was partially relocated over the Huangtupo slope, reactivation of the main slide body led to two shallow landslides (Sandaogou and Erdaogou landslides; see location in Fig. 2) on the surface of the Huangtupo complex deep-seated landslide, causing nine injuries and five fatalities (Deng *et al.* 2000; Wu *et al.* 2006; Deng & Wang 2009). Tang *et al.* (2009) and Deng *et al.* (2000) attributed the occurrence of the Erdaogou landslide to the loading of solid waste and wastewater at the back of the landslide and attributed the triggering of the Sandaogou landslide to rainfall and the fluctuation of the Yangtze River water level. As a result, in 2002 the authorities permanently started to evacuate inhabitants from the Huangtupo slope and built a reinforced concrete retaining wall at the toe of the Huangtupo slope with the aim of reducing the risk of movements and preventing new shallow landslides caused by the reactivation of the main bodies which could affect inhabitants.

Rainfall and reservoir water level changes, especially rapid drawdown, are important triggering factors of landslides in the TG region

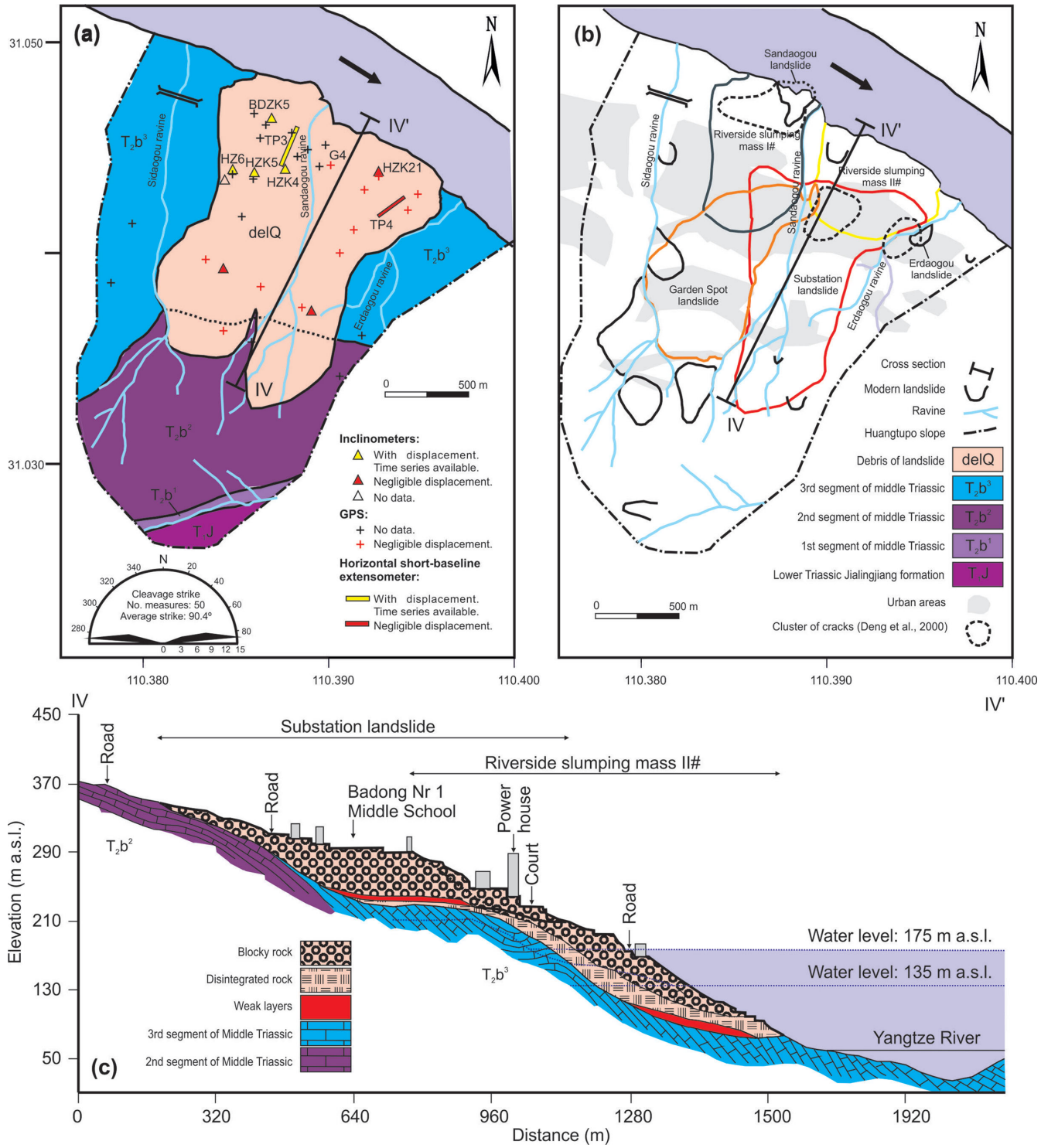

Figure 2. (a) Geological sketch and displacement monitoring network, (b) landslides mapping and (c) cross-section of the Huangtupo slope (adapted from Tang *et al.* 2009; Xie 2009; Chai *et al.* 2013).

(He *et al.* 2008). Therefore, their influence on the Huangtupo slope movement must be assessed to provide a complete understanding of the landslide and its evolution, which is essential for landslide management.

In the last two decades, Interferometric Synthetic Aperture Radar (InSAR) has become a powerful tool for studying landslides, capable of generating wide-area maps of ground surface displacements with millimetre precision and complementing regional scale investigations (Massonnet & Feigl 1998; Metternicht *et al.* 2005; Colesanti & Wasowski 2006). Many successful examples of InSAR applications to landslide studies can be found in the literature (e.g. Fruneau *et al.* 1996; Singhroy *et al.* 1998; Colesanti *et al.* 2003; Squarzoni *et al.* 2003; Tarchi *et al.* 2003a,b; Catani *et al.* 2005; Strozzi *et al.* 2005; Herrera *et al.* 2011; Bovenga *et al.* 2012; Zhao *et al.* 2012;

Herrera *et al.* 2013), with some of them focused on the monitoring of landslides in the TG region (Wang *et al.* 2008; Liao *et al.* 2012; Liu *et al.* 2013).

In this paper, we use a small baseline subset of interferograms processed using the Stanford Method for Persistent Scatterers (StaMPS; Hooper 2008) to assess the spatiotemporal patterns of surface movement and the active boundaries of the large complex Huangtupo landslide. Moreover, the temporal relationships of displacements with rainfall and reservoir water level changes are analysed after being validated with comparisons to *in situ* data. Combination of InSAR and geological data sets provides a whole new spatial and temporal insight of the Huangtupo landslide.

The paper is organized as follows: Section 2 describes the geological setting of the study area, Section 3 details the InSAR processing strategy and time-series validation, Section 4 analyses the Huangtupo landslide surface displacement data set obtained from InSAR, Section 5 discusses the long- and short-term trends from the InSAR data and Section 6 presents the main conclusions.

2 GEOLOGICAL DESCRIPTION OF THE STUDY AREA

The Huangtupo landslide is located on the southern shore of the Yangtze River, 66 km upstream from the TG Dam and about 1 km upstream from the old city of Badong. The slide body extends up to 600 m from 50 m a.s.l. (the foot of the landslide is submerged) and has a slope of about 20° that increases towards the east. Two flat areas can be recognized at an elevation of 285–310 and 430–455 m a.s.l., respectively (Deng & Wang 2009, Deng *et al.* 2000). The whole landslide body is cut by three 1000–2000 m long ravines, up to 50 m deep (Xie 2009) where rock substratum and some sliding zones can be recognized (Fig. 2). From a structural point of view the slope is placed over the south flank of the Guandukou syncline (Deng *et al.* 2000; Deng & Wang 2009). The rock basement bedding dips downhill with a variable dip angle that reduces towards the fold axis. The rock mass is also affected by an east–west cleavage direction (see rose diagram in Fig. 2) related to the fold. The upper portion of the rock mass belongs to the middle Triassic rock basement and is composed of purplish red pelite alternating with pelitic siltstone in T_2b^2 unit and grey pelitic limestone in T_2b^3 unit in the upper and middle-lower part of the slope, respectively (Fig. 2). The landslide body is mostly covered by loose debris (delQ) of variable thickness up to 92 m (Fig. 2). The upper and the lower part of the debris deposits are composed of loose purplish-red and pelitic limestone debris, respectively, that originated from the degradation and sliding of the original rock mass. Some disorganized grey pelitic limestone (T_2b^3) blocks are recognizable in the pelitic limestone debris. These blocks present different orientations than the original substratum indicating that they have been transported during landslide events (Deng *et al.* 2000; Deng & Wang 2009).

Deng *et al.* (2000) stated that the Huangtupo landslide originated more than 10^5 yr BP from a succession of complex deep gravitational processes affecting the south flank of the Guandukou syncline which were initiated by river incision. They also stated that nowadays, the ancient Huangtupo landslide is stable as a whole due to the partial cementation of the deep original sliding zones, and the possibility of the whole landslide failing is very low because the main body has been divided into different sliding bodies by the deep ravines. As a consequence, current geological conditions are only favourable for the development of partial failure across other weak zones instead of reactivating the entire Huangtupo landslide.

3 HUANGTUPO LANDSLIDE FEATURES AND AVAILABLE DATA

The Huangtupo landslide is a complex deep-seated landslide formed by the superposition of several slumps (Jiang *et al.* 2007; Chen *et al.* 2008; Xie 2009; Hu *et al.* 2012a,b; Chai *et al.* 2013), which cover a total area of 1.358×10^6 m^2 mobilizing a volume of 6.934×10^7 m^3. Four main slumping bodies can be recognized in the slope (Fig. 2): Riverside slumping mass I#, Riverside slumping mass II#, Garden Spot landslide and Substation landslide.

Riverside slumping mass I# is located at the northwest side of the slope between Sidaogou and Sandaogou ravines and has its toe under the water level of the Yangtze River. Riverside slumping mass II# is placed between Sandaogou and Erdaogou ravines, northeast of the slope, and also has its toe submerged under the river water level. Garden Spot landslide is boot shaped and located southwest of the slope and with a front edge covering the upper part of Riverside slumping mass I#. The fourth slumping mass is the Substation landslide that is located northeast of the slope and partially placed over Riverside slumping mass II#. Several more recent smaller landslides can also be recognized in the slope (Fig. 2; Jiang *et al.* 2007; Chen *et al.* 2008; Xie 2009; Hu *et al.* 2012a,b). The main characteristics of the landslides are summarized in Table 1.

Deng *et al.* (2000) recognized three main fracture clusters in the Huangtupo slope. The first and second clusters of surface cracks were found in the vicinity of Erdaogou and Sandaogou landslides, respectively (Fig. 2b), predominantly trending northwest–southeast. These two clusters of cracks were probably caused by the preceding/subsequent deformations associated to the shallow landslides in 1995. The strike of the cracks of the third clustering is also predominantly northwest–southeast. It was located in the centre of the urban area of Huangtupo, just in the vicinity of the Sandagou ravine. Numerous crack clusters can still be recognized in this area (Fig. 3), which consist of opened (more than 5 cm), slipped (even more than 5 cm) and long (even longer than 100 m) fractures with a predominant NW–SE orientation that is perpendicular to the slope dip direction.

Table 1. Main characteristics of the Huangtupo landslide (based on Xie 2009; Hu *et al.* 2012a,b).

Landslide (see location in Fig. 2)	Elevation (m a.s.l.)	Mean dimensions, length–width (m)	Mean thickness (minimum and maximum) (m)	Area $\times 10^4$ (m^2)	Volume $\times 10^7$ (m^3)
Slumping Mass I#	∼70–300	∼770–500	69.4 (60–80)	32.5	2.2555
Slumping Mass II#	∼50–270	∼ 400–500	61.1 (35–92)	32.0	1.9921
Garden Spot	∼220–520	∼1100–220*	30.0 (20–82)	32.6	1.3529
Substation	∼160–600	∼1200–440**	35.0 (20–58)	38.1	1.3335

*The width increases up to 530 m downhill.
**The width increases up to 860 m downhill.

Figure 3. Cracks in Badong caused by the Huangtupo landslide. Note that north arrows, which approximately indicate the downhill direction, have been shown in the pictures.

The Huangtupo landslide has been intensely monitored by Chinese authorities using ground-based techniques, including GPS, borehole inclinometers, horizontal short-baseline extensometers and groundwater level monitoring (Jiang *et al.* 2007; Xie 2009; Hu *et al.* 2012a,b; Fig. 2a). This monitoring network has been operational since 2003 and provides more than 40 000 observations each year. Unfortunately, the monitoring data are confidential and only few published displacement data available in the scientific literature have been used in this work for validating DInSAR data (Fig. 2). Ground water time-series between 2003 and 2006 from different monitoring wells are also available, indicating that the groundwater level for the rear edge of the slope is clearly controlled by rainfall while the front edge of talus is controlled by the reservoir water level. Ground-based displacement monitoring data reveal that only Riverside Slumping mass I# is clearly active while Riverside Slumping mass II#, Garden Spot landslide and Substation landslide displacements are not significant (Jiang 2005; Jiang *et al.* 2007; Xie 2009; Hu *et al.* 2012a,b). These *in situ* monitoring data also revealed that Riverside slumping mass I# shows an almost identical pattern of displacement at the surface and at depth (at the sliding surface; Xie 2009), which indicates that the landslide exhibits a predominantly translational behaviour over a sliding surface composed of clay and gravel soil (Chai *et al.* 2013). Wen & Chen (2007) and Chai *et al.* (2013) studied the properties of the multiple incompetent layers existing in the Huangtupo slope, stating that they are mainly composed of illite, chlorite, quartz and calcite. These authors also observed that active chemical and physical interactions between the pre-existing weak zones and groundwater resulted in shear strength reduction of the weak zones causing them to become slip zones of the landslide.

4 SAR INTERFEROMETRY PROCESSING AND TIME-SERIES ANALYSIS

InSAR is a remote sensing technique which uses two or more complex SAR images acquired by satellites for the generation of interferograms that represent the differences in the range changes (i.e. phase) in the radar line of sight (LOS). This phase change can be expressed as the sum of several terms: topographical term, ground surface displacements, atmospheric artefacts, orbital errors and other noises (Hanssen 2001). Various InSAR techniques can be used to separate the displacement phase term from other terms (e.g. Ferretti *et al.* 2001; Berardino *et al.* 2002; Hooper *et al.* 2007). In this study, ground movements were obtained using a small baseline subset of interferograms with the StaMPS technique. A detailed description of the technique can be found in Hooper (2008) but a summary is included here for completeness.

4.1 Small baseline InSAR

Our processing is based on a small baseline subset approach (Berardino *et al.* 2002). This uses interferograms with small spatial and temporal baselines and reduced Doppler centroid frequency differences. These are respectively defined as the physical separation between the two satellite acquisition positions perpendicular to the LOS, the separation in time and the difference between the Doppler centroids of acquisition pairs. Minimizing these components helps minimize spatial and temporal decorrelation and topographic errors (Hooper 2008). StaMPS selects the slowly decorrelating filtered phase (SDFP) pixels (i.e. pixels whose phase hardly decorrelates over short time intervals) from small baseline interferograms to maintain coherence over a long time interval (Just & Bamler 1994; Hooper 2008). Because SDFP phase stability can be estimated using the amplitude difference dispersion, an initial threshold is set to select a high number of points. This set of candidate pixels is then refined to generate the final set of SDFP pixels using the algorithm set out in Hooper *et al.* (2007).

The refinement process aims to assess the phase stability of the initial candidate pixels, selecting those where the noise is small enough not to completely mask deformation signals. Phase changes due to deformation, atmospheric delay differences, satellite orbit inaccuracies and look angle error are dominant relative to the noise term (which is mainly related to scattering, thermal noise and coregistration error). Assuming that the deformation signals under investigation, variations in atmospheric delay and satellite orbit inaccuracies are spatially correlated, it allows these terms to be estimated through the use of an adaptive bandpass filter, which adjusts to any phase gradient present in the data (Hooper *et al.* 2007). This filter is combined with a lowpass filter with a cut-off wavelength of 800 m, which is not only the recommended distance thought to be spatially correlated for the phase values according to Hooper *et al.* (2007), but also has limited impacts on localized landslide movements. The look angle errors are estimated for each pixel with its perpendicular baselines. Removing these terms from the original wrapped phase (from flattened and topographically corrected interferograms) provides an estimate for the noise term, which can then be used to weight the contribution of each pixel to its reestimation via an iterative process that stops when the noise term drops below a specified value (0.005). After the robust process of SDFP selection and correcting for spatially uncorrelated look angle errors, the remaining step estimates the integer cycle ambiguities from the wrapped phase of SDFP pixels using the 3-D statistical-cost network-flow algorithm for phase unwrapping (SNAPHU; Hooper & Zebker 2007). The unwrapped interferograms are finally inverted using a least-squares method to obtain the time-series of phase change of SDFP pixels. From these values, long-wavelength atmospheric effects and orbit error are estimated from the SDFP pixels using a best-fit plane.

4.2 Data set and processing details

The SAR data set analysed in this study consists of 41 Envisat ASAR images collected between 2003 August and 2010 July from descending track 075 (T075), 31 images collected between 2004 January and 2010 April from descending track 347 (T347) and 13 images collected between 2008 December and 2010 March from ascending track 068 (T068; see a detailed list of the used images in the Supporting Information). We extracted a 2.5 × 8 km area for processing that corresponds to Badong. This selection of interferograms has been restricted to those interferograms with spatial and temporal baselines smaller than 1070 m and 1500 d. In addition, only those interferograms with a mean coherence greater than 0.4 are selected for time-series analysis. The topographic phase contribution was removed using the Shuttle Radar Topography Mission (SRTM) 3-arcsecond (∼90 m) spacing digital elevation model (DEM) that has the voids filled with other data sources (Jarvis *et al.* 2008). The amplitude dispersion index threshold was set at 0.6 as this was the highest threshold (and therefore generates the largest set of candidate pixels) above which the numerically simulated interference between a set of Gaussian scatterers has been shown to result in high levels of decorrelation (Hooper 2008). Atmospheric signals are present in most (if not all) of interferograms in the study area and can be estimated using spatial and time filtering in StaMPS, assuming atmospheric signals are correlated in space and uncorrelated in time. However, in cases where the deformation and atmospheric signals follow similar patterns, the removal of an estimated atmospheric error term can cause problems in the estimation of deformation signals (Peltier *et al.* 2010). Therefore, in this study, a simple best-fit plane was estimated for each unwrapped interferogram to account for orbit errors and long-wavelength atmospheric effects since the area of study is small (∼2.5 × 8.0 km). For the two descending tracks, the greatest consistency between the deformation results was achieved when a best-fit plane was applied to account for atmospheric effects, rather than using time-series atmospheric filtering.

For validation, comparisons between the two adjacent descending tracks in their overlapping area were used due to their similar incidence and azimuth angles, and since both cover a long time interval from 2004 and 2010. An rms estimate can be derived from the displacement differences between the estimated displacement values from T347 and the interpolated displacement values for T075 (at the same acquisition dates of T347) for every pixel. For many different pixels, the rms values are much smaller than the magnitude of deformation, which suggests the displacement time-series are consistent between the two tracks. Pixels between T075 and T347 with time-series rms differences below 3, 5 and 10 mm, account for 16, 64 and 95 per cent of the total common pixels, respectively. 57 per cent of the common pixels have a mean velocity difference of less than 1 mm yr^{-1} (over the whole processed area). This suggests that the displacement time-series and velocities in our study are reliable and it is worth noting the differences within the landslide boundary are all <2.5 mm yr^{-1}.

4.3 Results

Fig. 4 shows the results for the three tracks over the Badong area. Although the area is partially vegetated, 22, 25 and 24 persistent scatterers per square kilometre were detected for tracks T068, T075 and T347, respectively. The Huangtupo landslide exhibits a higher concentration of SDFP pixels with an average density of 60 SDFP pixels per square kilometre due to its urbanized areas and a high population density (Gao & Yin 2014). The Huangtupo landslide also exhibits high displacement rates with an average velocity of up to 15.6 mm yr^{-1} in the LOS direction.

The standard deviations of the mean velocity at each pixel were calculated using a bootstrapping method (Efron & Tibshirani 1986) in StaMPS. The standard deviations of the mean velocity at each coherent pixel provide an estimation of the precision of the mean velocity. This statistic increases when the precision of the mean velocity is low and/or when the persistent scatterer exhibits a non-linear behaviour. The average standard deviation of the mean velocities per point computed for the study area is 2.9, 0.4 and 0.7 mm yr^{-1},

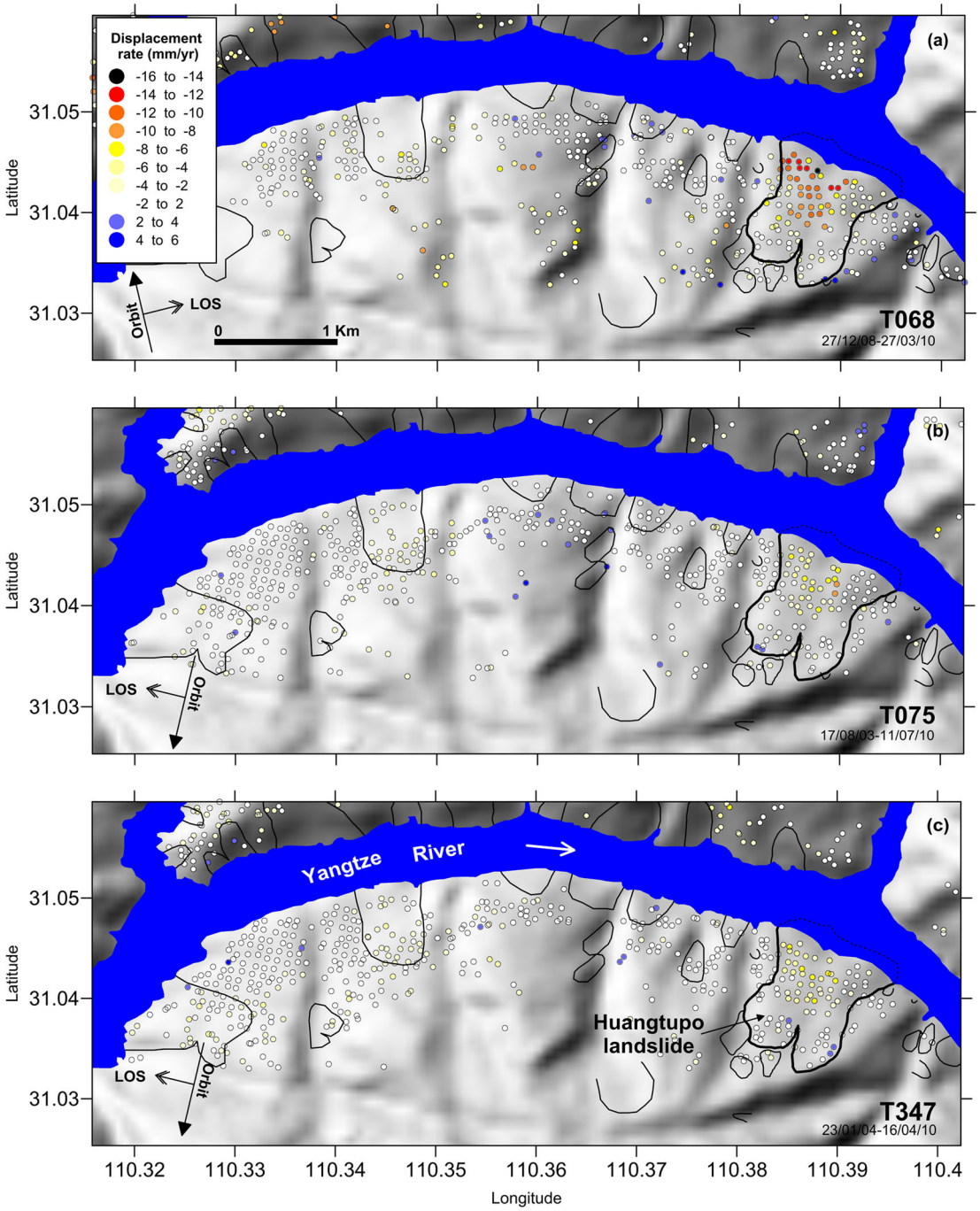

Figure 4. Mean LOS displacement rates derived from different tracks: (a) Track T068 (ascending); (b) track T075 (descending) and (c) track T347 (descending). The plotted landslide boundaries are based on the works of Cojean & Caï (2011) and Chai *et al.* (2013). The background is a shaded relief map derived from the SRTM DEM.

reaching maximum values of 7.1, 0.8 and 0.8 mm yr^{-1} in the Huangtupo landslide for the T068, T075 and T347, respectively. The standard deviations of the mean velocity per pixel for track T068 exhibits some pixels located on the northwest sector of the processed area with standard deviation values up to 7.1 mm yr^{-1}. This variability in T068 can be caused by the short data period (15 months) and a limited number of SAR images (13 images) used in the InSAR time-series analysis. The coefficient of variation (CV), defined as the ratio of the standard deviations to the mean velocities, has been also computed in order to estimate the robustness of the processing results. The computed CV values vary from 0 to 0.4 for the 7.3, 51.7 and 47.3 per cent of the SDFP pixels of the tracks T068, T075 and T347. CV values have been found to be especially robust for tracks T075 and T347, mainly due to the longer time coverage than for track T068, providing a better estimation of mean velocity and a lower standard deviation.

To interpret the displacement signals in the next sections, the different viewing geometries of the ascending and descending tracks have to be taken into account. Track 068 has an ascending orbit and a LOS oriented towards the northeast (N76.7°E) while tracks T075 and T347 have descending orbits and the LOS oriented towards the northwest (N283.3°E). Taking into account the predominant

strike of the Huangtupo slope (N100–110°E), the ascending track LOS means that the vertical and horizontal components of landslide movements are additive, where the descending LOS has them partially cancelling each other out being more sensitive to vertical displacements. Therefore, the T068 LOS mean displacement rates in the Huangtupo landslide are far greater than those in tracks T075 and 347 (Fig. 4).

4.4 InSAR data versus *in situ* monitoring information

In this section, InSAR data are compared with available ground-based information. For this purpose, the nearest SDFP pixels to the instrumental ground monitoring point have been selected. Also, displacement rates between +2 and −2 mm yr^{-1} and accumulated deformations between +5 and −5 mm have been considered to be stable (motionless) since they are in the level of the sensitivity of the technique (Herrera *et al.* 2009; Prati *et al.* 2010; Ferretti *et al.* 2011).

As mentioned in Section 3, although the Huangtupo displacement monitoring network includes GPS, inclinometers and horizontal short-baseline extensometers (see location in Fig. 5) only few published displacement monitoring data are available for the Huangtupo landslide. InSAR time-series from the two longer InSAR time-series (i.e. tracks T075 and T347) have been compared with inclinometers (BDZK5, HZ6, HZK4 and HZK5) and horizontal short-baseline extensometers (TP3) data-series from Riverside Slumping Mass I#, projecting ground data along the satellite LOS (Fig. 6) considering the geometry of the satellite system and the type of ground-based data (Colesanti & Wasowski 2006; Farina *et al.* 2006; Tofani *et al.* 2013). Note that comparisons are possible because deep displacement measurements (i.e. the ones provided by inclinometers and horizontal short-baseline extensometers) and surface displacements (i.e. those provided by GPS) are consistent (Jiang 2005; Jiang *et al.* 2007; Chen *et al.* 2008; Xie 2009). As shown in Fig. 6, InSAR data are consistent with inclinometers and horizontal short-baseline extensometers since all of them exhibit a similar deformation trend with a similar displacement rate (i.e. the slope of the displacement plot). The agreement between InSAR and ground-based time-series shown in Fig. 6 has been evaluated through their respective displacement rates projected along the LOS (v_{LOS}) for Slumping Mass I#. InSAR displacement rates have been computed by means of a linear least-square fitting for the same time period for which ground monitoring data are available, and then both velocities have been compared. Note that as a minimum, five points from the InSAR time-series have been considered in order to avoid local temporal changes. The comparison from these data shows a mean difference of 2.2 ± 2.5 mm yr^{-1} and a maximum difference of 6.4 mm yr^{-1} for T075. Note that if we do not consider the outlier value corresponding to PS295 for the statistic, the mean difference reduces to 1.1 ± 0.9 mm yr^{-1}. For T347, the mean and maximum differences are 1.0 ± 0.4 and 1.6 mm yr^{-1}. These differences are similar to those computed by other authors (Colesanti *et al.* 2003; Ferretti *et al.* 2011).

Ground-based data from the monitoring network placed on Riverside Slumping Mass II# (Fig. 5), consisting of one inclinometer HZK21, six GPS stations and one horizontal short-baseline extensometer (TP3; Jiang *et al.* 2007), have been also used for validating InSAR results. Inclinometer HZK21, placed on Riverside Slumping Mass II# (Fig. 5) did not show any obvious displacement in 2006 (Jiang *et al.* 2007; Xie 2009). The nearest selected SDFP pixel (PS260 and PS263 in Fig. 5) shows accumulated displacements for this year of 1.4 and 3.7 mm and a displacement rate for the whole processing time period of −0.4 and +1.7 mm yr^{-1} for tracks T075 and T347, respectively. Taking into account that these values are below the sensitivity of the technique we can assume that they are stable in agreement with *in situ* data. GPS station, G4, also placed on Riverside Slumping Mass II# (Fig. 5), exhibited an accumulated displacement of 12.9 mm (5.1 mm along LOS) in 2005 and no obvious displacement in 2006 (Xie 2009; Hu *et al.* 2012a). The nearest persistent scatterer from track T075 (PS 270 in Fig. 5) shows 6.1 mm of displacement for 2006, which is slightly higher than that provided by GPS projected along LOS. Note that there is no persistent scatterer near G4 in track T347 and as a consequence no comparison was performed. Other GPS stations placed on Riverside Slumping Mass II# (see location in Fig. 5) are stable in agreement with the information represented in Fig. 5 (Xie 2009; Hu *et al.* 2012a). The horizontal short-baseline extensometer TP4 (Fig. 5) shows a displacement of 3.0 mm (1.2 mm along LOS) in 2005 and no obvious displacements afterwards (Xie 2009; Hu *et al.* 2012a). The nearest persistent scatterers from tracks T075 and T347 provide −0.57 (PS179) and 0.2 (PS200) mm of displacement for 2005 and practically zero displacement from 2005 to the end of the displacement time-series in agreement with instrumental data. Thus, the monitoring results show that the slumping mass II# was basically stable with no obvious deformation from 2003 to 2006.

Xie (2009) also stated that GPS (see location of GPS stations in Fig. 5) showed great fluctuations in amplitude and irregularity in direction while inclinometers showed non-obvious deformation at depth for Substation and Garden Spot landslides. InSAR-derived results provide mean LOS displacement rates of −4.7 ± 4.3, −2.2 ± 2.9 and −2.2 ± 2.7 mm yr^{-1} for tracks T068, T075 and T347, respectively, on Substation landslide and −5.2 ± 4.2, −2.4 ± 2.9 and −1.9 ± 2.3 mm yr^{-1} for tracks T068, T075 and T347, respectively, on Garden Spot landslide (Fig. 5). Note that most of the activity of Garden Spot and Substation landslides is located in their foot, coinciding with the overlapping area among them and Riverside Slumping Mass I#. However, these two landslides exhibit a general stability in agreement with *in situ* monitoring data (Xie 2009). Note that the displacement rate derived from track T068 differs from those obtained from tracks T075 and T347. This can be mainly due to the smaller number of images and the shorter time span that can under- or overestimate the linear component of the processing which provides the displacement rate as well as considering a different LOS direction relative to the landslide movements.

5 DISPLACEMENT PATTERNS OF THE HUANGTUPO LANDSLIDE

In this section, we analyse the InSAR-derived surface displacements for the Huangtupo landslide. Different InSAR products are used in the analysis: displacement rates (mean velocities), cumulative displacements and displacement time-series measurements.

5.1 2-D velocity of the Huangtupo landslide

Fig. 5 shows the LOS mean velocity maps for all the three tracks. Descending and ascending tracks have different incidence and azimuth angles and, as a result, they can be used to recover 2-D or 3-D displacement patterns. In the case of the Huangtupo landslide, 3-D displacement and/or velocities cannot be recovered due to the similarity in the T075 and T347 satellite geometries, but 2-D (south–north and vertical velocities) can be obtained assuming the absence

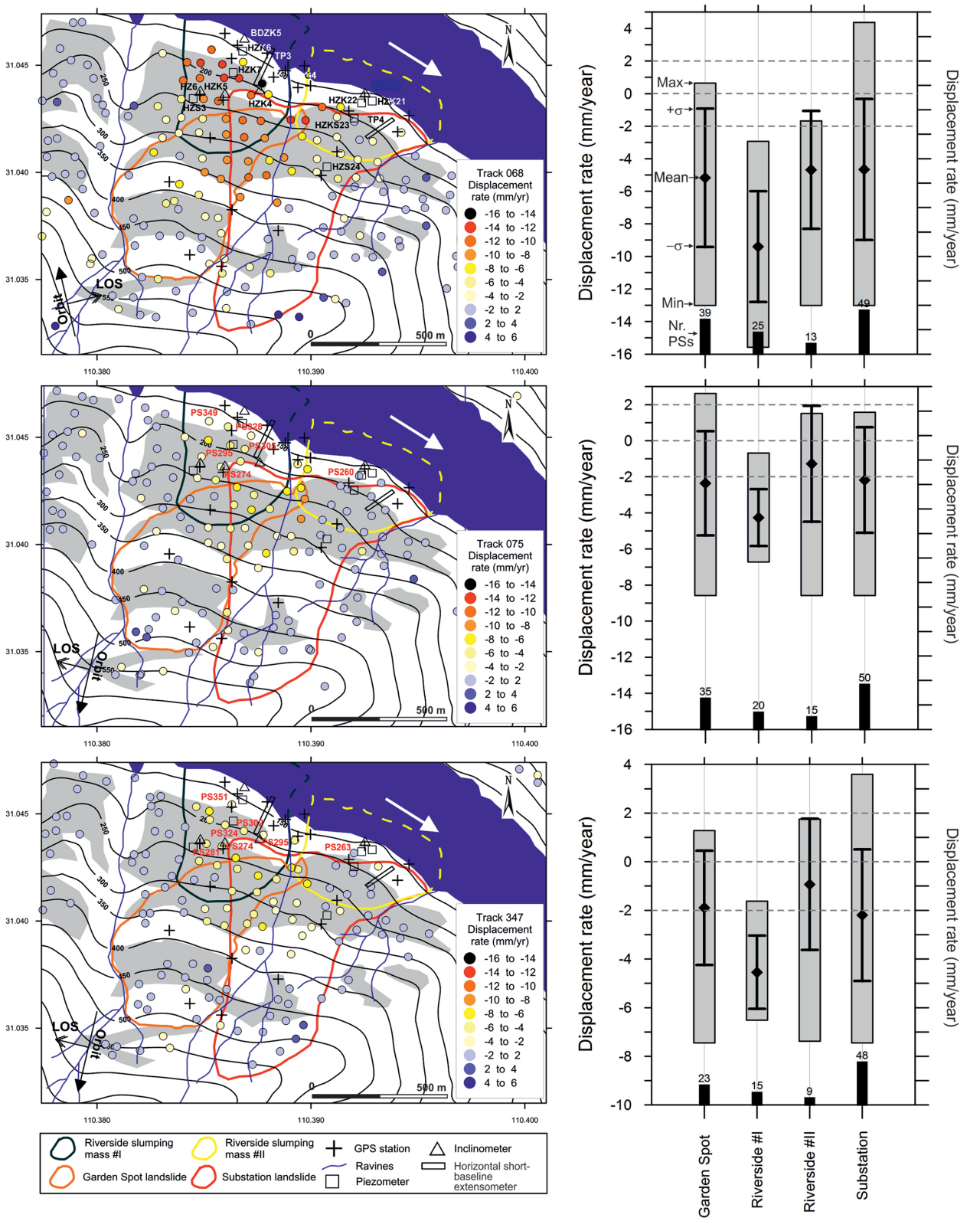

Figure 5. Mean LOS displacement rate map (left) and statistic (right) for the three tracks. Landslide zonation is based on Xie (2009) and Hu *et al.* (2012a,b). Grey shading of the maps delineates the main urban areas. Mean, mean LOS displacement rate of the landslide; Max, maximum displacement rate; Min, minimum displacement rate; σ, standard deviation.

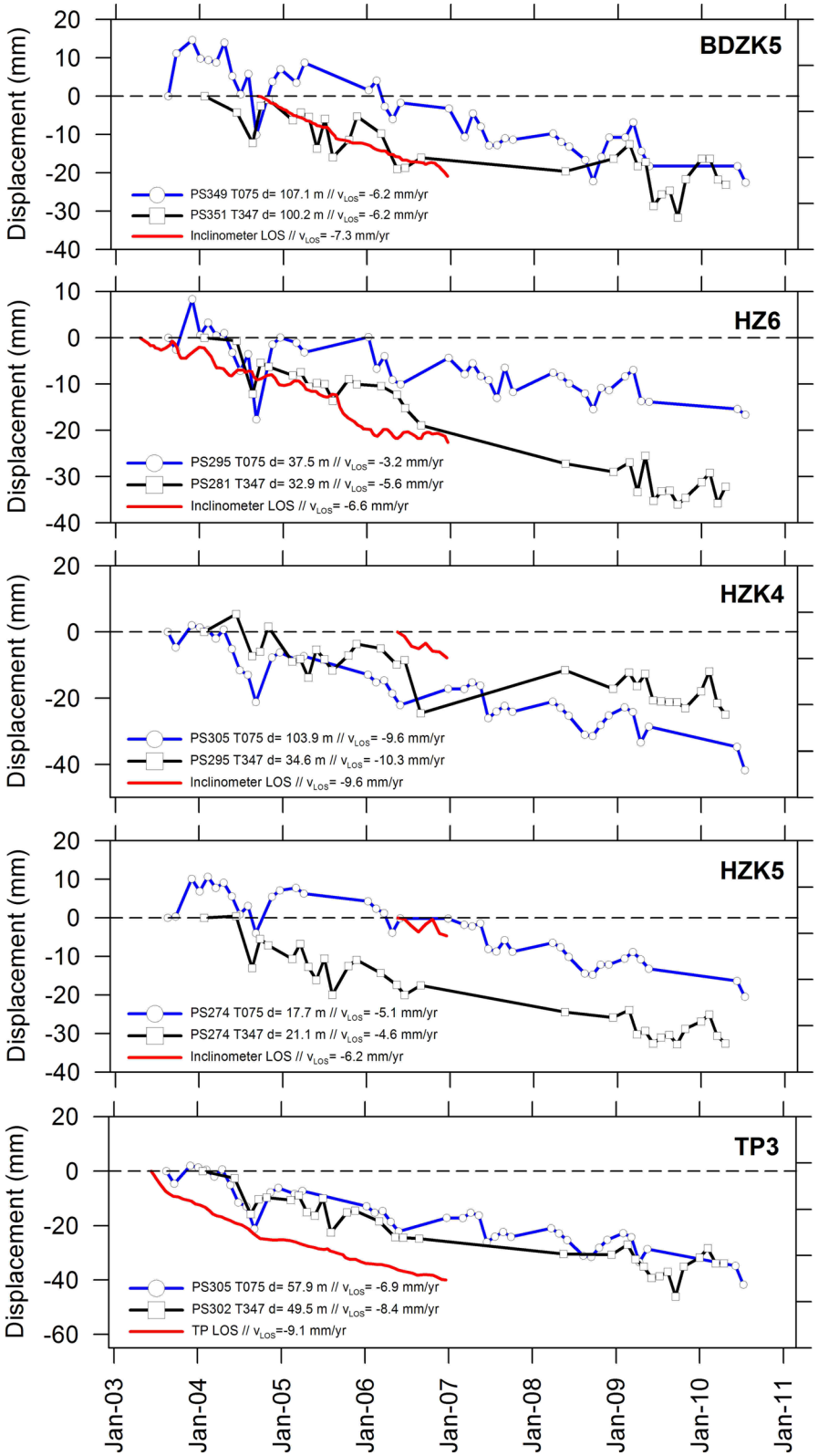

Figure 6. Comparisons of available InSAR time-series and ground-based data from Riverside Slumping Mass I# projected in the LOS direction. See location of selected SDFP pixels, inclinometers and horizontal short-baseline extensometers in Fig. 5. v_{LOS} is the displacement rate computed by means of a linear least-square fitting for the time interval for which ground data are available. d is the minimum distance between the nearest PS used for comparing the time-series and the ground-based monitoring point.

of a displacement component in the east–west direction by means of next expression (Liu *et al.* 2013):

$$V = B \cdot LOS, \tag{1}$$

where V is the 2-D velocity field matrix, LOS is InSAR LOS velocity matrix and B is:

$$B = (A^T \cdot A)^{-1} \cdot A^T, \tag{2}$$

where A is the coefficient matrix of the satellite geometry (dependent on the incidence angles) and T and $()^{-1}$ represent matrix transpose and inversion, respectively.

This assumption seems to agree with the slope aspect and field observations that show a predominant southwest–northeast displacement field on the Huangtupo landslide with negligible east–west displacements. Note that GPS data show azimuth directions of 9–108° for Riverside Slumping Mass I# and 16–48° for Riverside Slumping Mass II#, while the horizontal short-baseline extensometer TP3 show a 20–45° displacement azimuth (Xie 2009) in agreement with the adopted assumption. The resulting 2-D displacement rates in vertical and south–north directions are shown in Figs 7(a) and (b).

It is clear in Figs 5 and 7(a) that the highest displacements are concentrated between Sidaogou and Sandaogou ravines from the riverside to an elevation below 350 m a.s.l., coinciding with the location of the Riverside Slumping Mass I# and the foot of the Garden Spot landslides. Note that displacements in the foot of this landslide are greater than those of the middle and head areas and the displacement of the central axial part is significantly greater than the traction area on both flanks in agreement with inclinometers and GPS stations (Xie 2009). The maximum computed total velocity of the landslide, considering the two components of the displacement (south–north and vertical), is 17.2 mm yr^{-1}. This velocity corresponds to 'Very slow' landslides (IGUS/WGL 1995) although most of the SDFP pixels located on the sliding body exhibit 'Extremely slow' (IGUS/WGL 1995) total velocities. Maximum vertical and north–south displacements measured in the Huangtupo slope exhibit displacement rates up to −14.3 and +12.8 mm yr^{-1}, respectively. The upper part of the slope that corresponds to the landslide head shows a lower activity with maximum displacement rates of −2.7 and +4.1 mm yr^{-1} for the vertical and south–north displacement components.

5.2 Long-term displacements

Reservoir water level changes, mainly rapid drawdowns, have an important impact on the stability of the slopes located along their shores, acting as triggering factors of landslides (He *et al.* 2008). Water level in the TG reservoir has drastically increased from 65 to 175 m a.s.l. in the last decade. The first reservoir water level rise started on 2003 June 1, and the reservoir water level reached 135 m on 2003 June 15 (Stage 1, Fig. 8). On 2006 October 27, the water level of the reservoir increased to 156 m a.s.l. (Stage 2) and in 2008 November rose to 175 m a.s.l. (Stage 3, Fig. 8). This increase in reservoir water level from 2003 June is affected by seasonal fluctuations (Fig. 8) that have major impacts on the stability of slopes. These seasonal fluctuations correspond with amplitudes over 5, 10 and 25 m for the first, second and third stages, respectively.

In this paper, long-term displacement refers to net displacements during the period from 2003 to 2009 while short-term displacement is used for referring to the interannual displacement evolution of

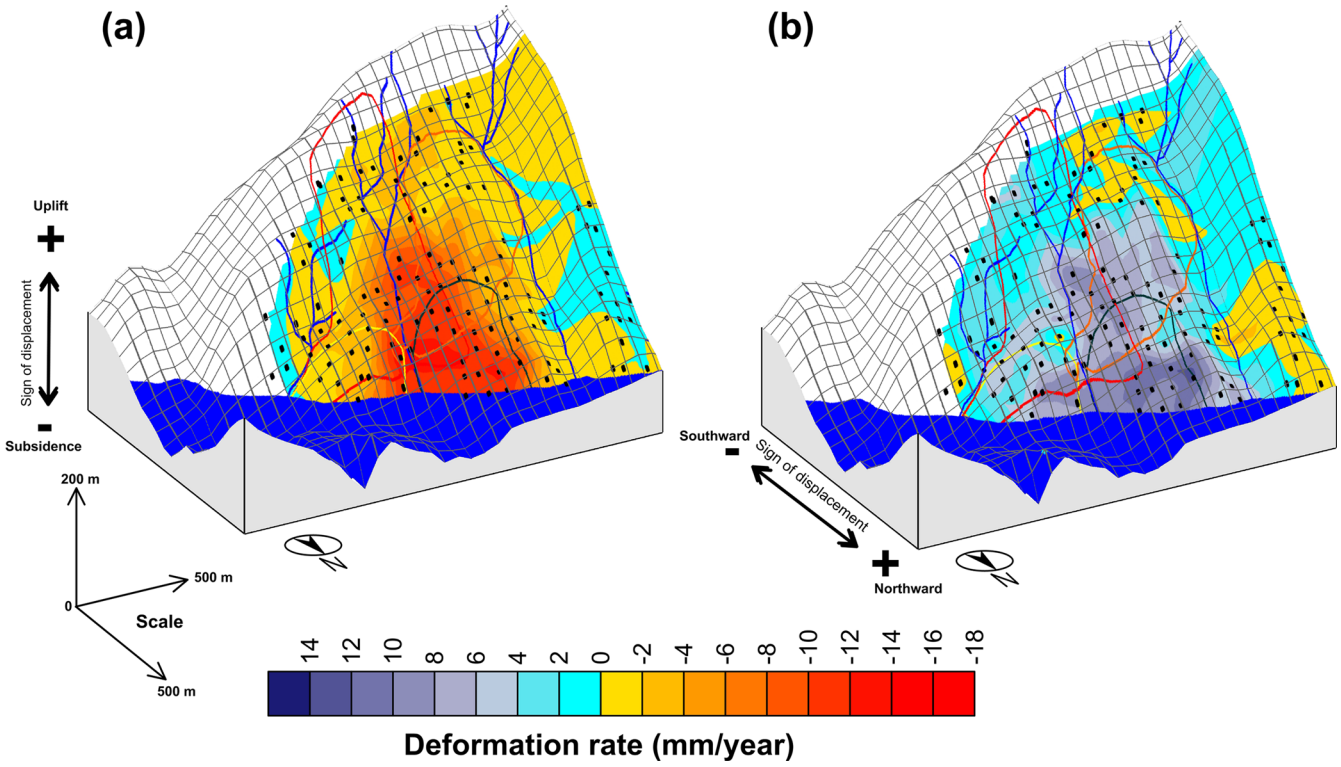

Figure 7. Vertical (a) and south–north (b) interpolated displacement components maps of the Huangtupo landslide. Black dots indicate the location of SDFP pixels where displacement information is available and the thick black curve delineates the four main landslides boundaries. Note: Negative displacement rates represent subsidence in (a) while positive values in (b) indicate horizontal displacements towards the river. As a consequence, negative and positive displacement rates of vertical (a) and horizontal (b) components indicates that landslides towards the river in both vertical and horizontal components. The information is superposed on the SRTM topography.

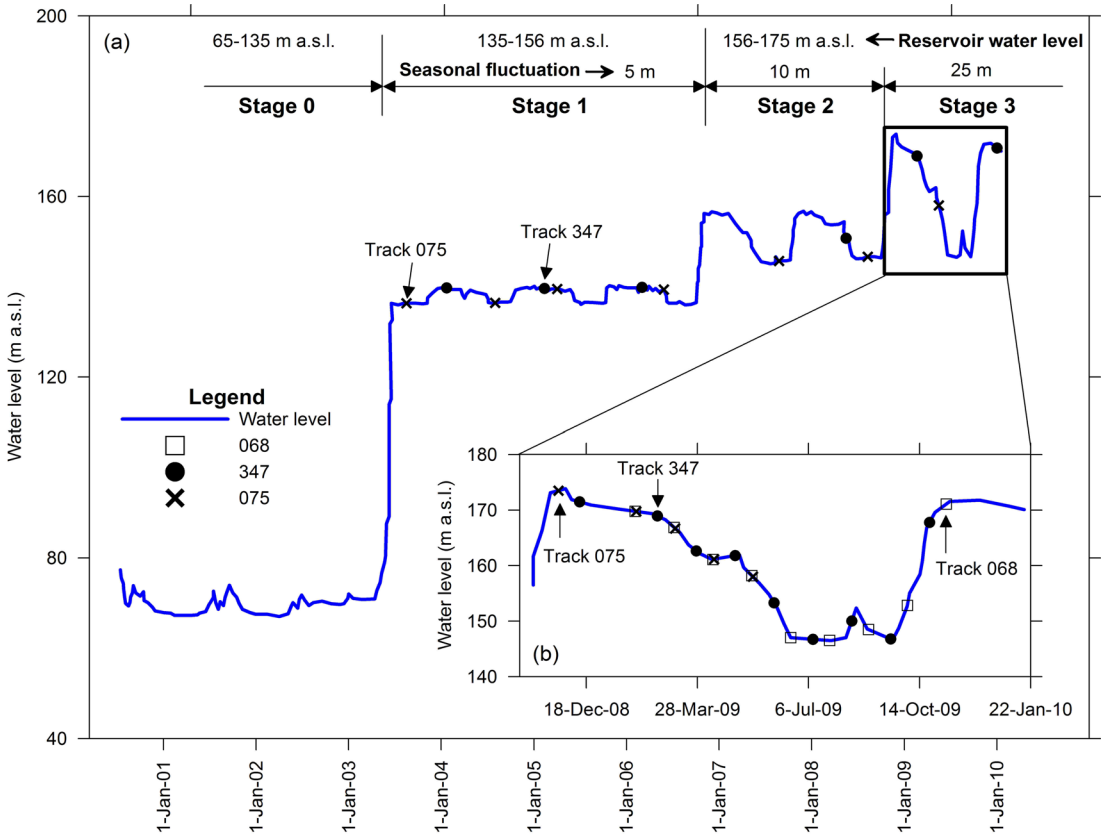

Figure 8. Images selected for (a) long-term and (b) short-term spatial analysis of the Huangtupo landslide marked on with water level fluctuations of the Yangtze River (blue line). Note that the images selected from InSAR processing time-series are represented using squares, circles and crosses for tracks T068, T347 and T075.

the Huangtupo landslide related to seasonal reservoir water level changes. In this section, the long-term displacement evolution of the Huangtupo landslide is analysed. Since Envisat ASAR images are only available for the study area since 2003 August, after the first impoundment had occurred, displacements related with the first impoundment cannot be measured using Envisat.

Fig. 9 shows the temporal evolution of mean displacements for Riverside Slumping Mass I# and II#, Garden Spot landslide and Substation landslide. Note that the mean time-series shown in Fig. 9 have been computed averaging all displacement values from all SDFP pixels contained in the contour area defined by the different landslides (Figs 2 and 5) and thus in the overlapping areas of different landslides the pixels are considered for the computation of the time-series from both landslides. Reservoir water level fluctuations (blue line) and a 10-d average of rainfall (grey bars) have also been plotted in the figures. It can be seen that the long-term behaviour is slightly different for the different parts of the slope. Riverside Slumping Mass I# exhibits a general negative deformation trend for the long-term period with lower superimposed oscillations related with the seasonal reservoir water level changes (Fig. 9). As it can be easily recognized, Riverside Slumping Mass I# time-series exhibit a downhill (mainly detected by T068 which is more sensitive to both vertical and N–S horizontal displacements) and vertical displacement (mainly detected by tracks T075 and T347 which are insensitive to N–S displacement horizontal components due to the parallel relative orientation of their LOS azimuth (N283.3°E) to the NW–SE slope strike). Furthermore, a clear acceleration of the landslide is recognizable during reservoir water level lowering in agreement with the numerical models performed on the landslide by different authors (Bin *et al.* 2007; Cojean & Caï 2011; Hu *et al.* 2012a,b; Jin *et al.* 2012). It should be noted in Fig. 9 that we have included the displacement rates for Riverside Slumping Mass I# and II# associated with the ascending and descending branches of the different reservoir water level cycles (WLC). The displacement rates have been computed after a linear fitting to the points from the displacement time-series associated to the considered branch from each WLC. Riverside Slumping Mass II# shows a general stable behaviour with seasonal displacements also related with river water level fluctuations (Fig. 9). These periodic displacements are mainly correlated with reservoir water level increasing when water level falls and being totally or partially recovered when the level recovers (Fig. 9).

Substation and Garden Spot landslides exhibit a quite stable kinematic behaviour, although some displacements are detected on the landslide foot areas which overlays Riverside Slumping Mass I# (Figs 5 and 9). Note that these two landslides mainly show a clear stable long-term behaviour only with seasonal displacement patterns associated with rainfall at elevations higher than 350–400 m a.s.l., which cause displacement acceleration episodes (interpreted as uplift phenomena caused by soil expansion due to soil effective stress reduction caused by pore pressure changes) when water infiltration from rainfall begins (Fig. 9). The general long-term behaviour of the upper part of the slope (crown) presents a more stable component and a low amplitude seasonal displacement superposed to the general trend (Fig. 9). These displacements seem also to be related with rainfall, suffering low seasonal vertical displacement oscillations during the wet and dry seasons, respectively. Note that seasonal correlations observed on Huangtupo's non-creeping areas

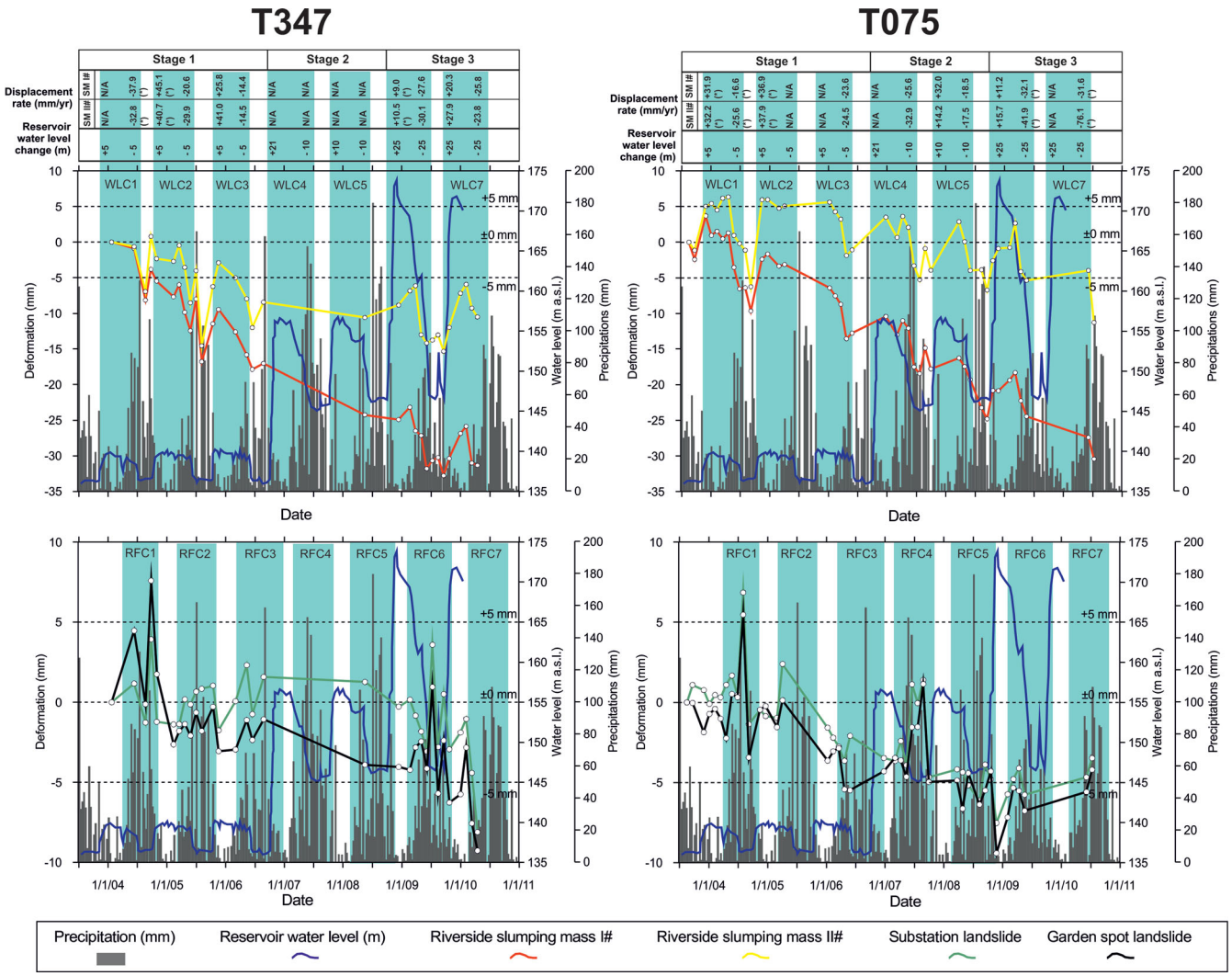

Figure 9. Mean LOS displacement time-series of the different slumping masses from the Huangtupo landslide: Riverside Slumping Mass I# and II#, Substation landslide and Garden Spot landslide for tracks T075 and T347. Shadowed areas delimitate reservoir water level cycles (WLC) and rainfall cycles (RFC). Note that the displacement rates values marked with an asterisk have been computed only using two points from the time-series. SMI#, Riverside Slumping Mass I#; SMII#, Riverside Slumping Mass II#.

among soil displacements, reservoir water level and rainfall have been also observed for other zones from the study area off the Huangtupo landslide affected by the same triggering factors. These observations are in agreement with Xie (2009) and Jiang *et al.* (2007) who pointed out that the water table shows that the groundwater of the foot of the Huangtupo slope varies with the water level of the Yangtze River almost simultaneously but fluctuations barely influence the water table of the middle or upper part of the Huangtupo slope while in the middle and back part of the Huangtupo slope displacements are mainly influenced by precipitation with a lag of about 10 d (Jiang *et al.* 2007; Xie 2009) as InSAR data show (Fig. 9).

So, it can be concluded that only Riverside Slumping Mass I# and Substation and Garden Spot feet areas overlaying Slumping Mass I# are clearly active and their seasonal behaviour depends on the distance to the riverside, being conditioned by Yangtze River water level in the foreside areas and by rainfall in the middle and upper zones. These effects will be discussed in greater details in Section 6.

Fig. 10 shows the interpolated accumulated displacements measured along the radar LOS over the Huangtupo area for tracks T075 and T347, considering a spacing in both directions equal to 25 m and using the kriging method. Track T068 only covers the period between 2008 December and 2010 March and thus does not provide long-term information. Areas without SDFP pixels have been masked (grey shadow). Using the time-series of data, it would be possible to build interpolated displacement maps overlaid to the 3-D topographical surface for each SAR acquisition to investigate the long-term behaviour of the landslide. In this case, we have generated the interpolated displacement maps at approximately yearly intervals. As it can be seen in Fig. 10, the spatial distribution of LOS displacements for T075 and T347 presents a similar shape with a clear concentration of displacement in the nearby western areas of Sandaogou.

This landsliding area mainly corresponds to Riverside Slumping Mass I#. Other small areas of displacement are recognized along the Huangtupo landslide although a clear pattern cannot be established for them and/or have not been measured by both tracks. The main landsliding area seems to be quite similar from 2006 for both tracks although new small areas of instability are recognized mainly in the foot zone.

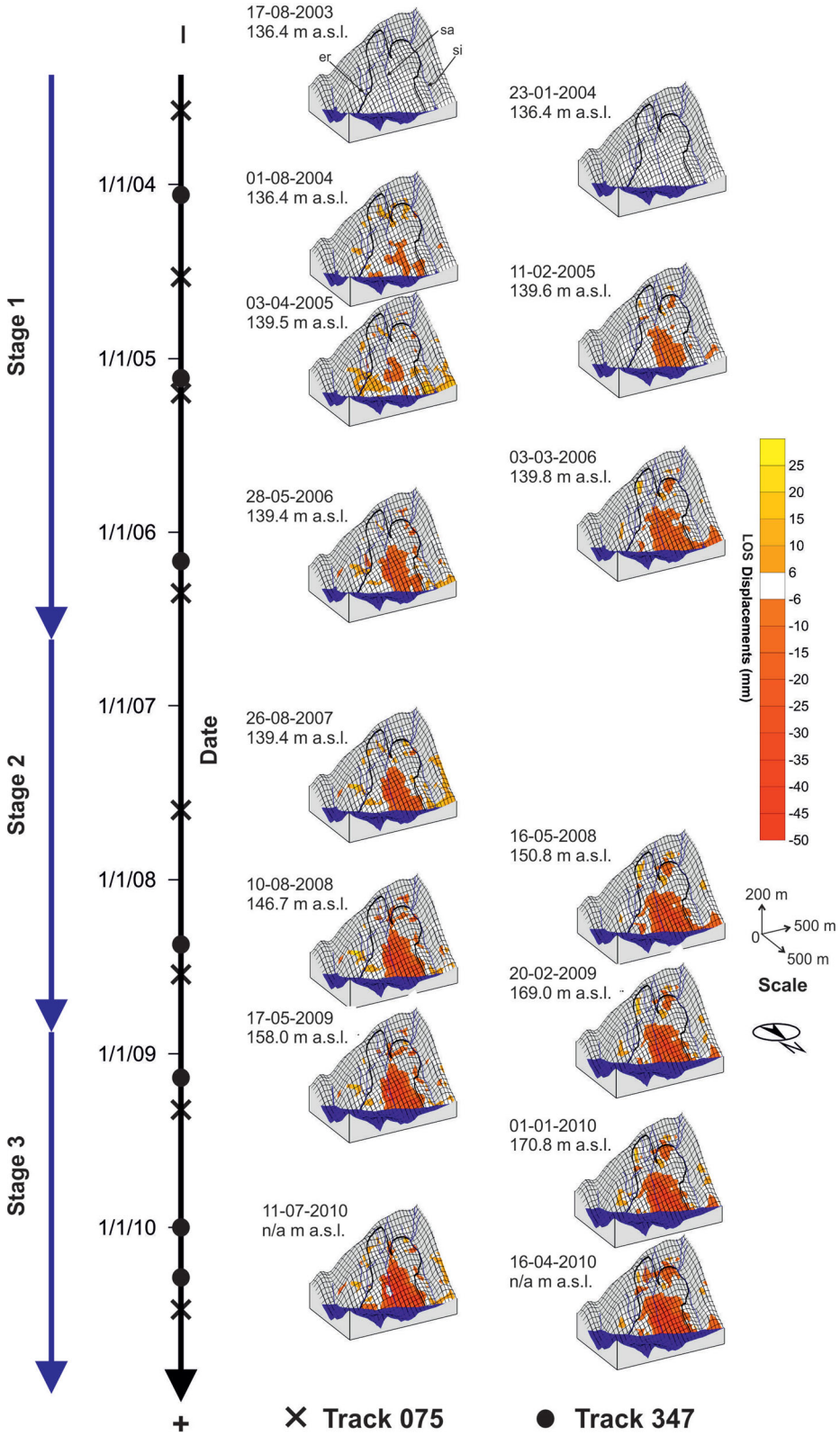

Figure 10. Long-term LOS displacements measured from tracks T075 and T347. Note that symbols plotted in black axis shows image acquisition dates and blue axis indicates the different reservoir water level stages shown in Fig. 8. Temporal distribution of the used images and the reservoir water level evolution corresponding to the different stages are also shown in Fig. 8(a). n/a, non-available data; sa, Sandaogou ravine; si, Sidaogou ravine; er, Erdaogou ravine.

5.3 Short-term displacements

Short-term displacements are considered in this paper as displacements related with (interannual) seasonal changes. For the analysis of short-term displacements, the period between 2008 December and 2010 April, has been analysed when the water level declined by over 25 m (Stage 3 in Fig. 8). He *et al.* (2008) stated that the high oscillations of reservoir water level in Stage 3 (Fig. 8) can cause landslides.

Fig. 11 shows the interpolated, cumulative LOS displacements of the Huangtupo landslide for 2008–2009 period for tracks T068, T075 and T347. Using the whole data time-series, interpolated displacement maps overlaid to the 3-D topographical surface for each SAR acquisition have been generated at approximately monthly (35 d) intervals as shown in Fig. 11 (see Fig. 8 for SAR image locations) to study the short-term behaviour of the landslide. Tracks T068 and T347 cover the whole temporal seasonal cycle with nine images in total, while track T075 only covers the water decrease section with four images.

Due to the different azimuth angles of ascending and descending tracks, their displacement patterns are not identical. However, for all the three tracks the maximum displacements seems to be concentrated in the lower part of the Huangtupo slope coinciding with the nearby area of the wetting–drying zone affected by reservoir water level changes during the water lowering period (Fig. 11). Moreover, although limited SAR acquisitions were collected for tracks T068 and T347 during the period that water descended (Fig. 8b), the displacement shape seems to change, being the displacements mainly concentrated in the west areas of the Sandaogou ravine affecting upper bounds (Fig. 11). Fig. 9 shows that the lower part of the slope exhibits a close relationship between water level change in the reservoir and the displacement evolution for the cyclical changes. Although a general displacement tendency can be recognized (high displacement rate for Riverside Slumping Mass I# and stability for the rest of the slope), minor periodic displacements above ± 20 mm amplitude clearly correlated with reservoir water level changes are superimposed to this trend (Fig. 9). However, the deformation behaviour of the upper part of the slope does not exhibit any correlation with reservoir water level changes from 350 to 400 m a.s.l. elevation. Nevertheless, seasonal displacements above ± 10 mm superposed to the general trend of the slope movement seem to exhibit a slight correlation with the available rainfall time-series (Fig. 9) in this area. These observations confirm that the lower zones of the landslide are affected by the seasonal reservoir water level changes while the top area exhibits an independent behaviour on these short-period oscillations (Jiang *et al.* 2007; Xie 2009).

6 DISCUSSION

It is well known that water (including both rainfall and reservoir water level changes) has several effects on landslides: (i) physical and chemical interactions between the slip zones' materials and groundwater result in shear strength reduction of the weak zones (Wen & Chen 2007; He *et al.* 2008); (ii) increased water gradient and seepage force of landslide mass during reservoir water level rise (Jiang *et al.* 2011); (iii) the reduction of effective stresses on landslide mass causes consolidation processes (Jiang *et al.* 2011). Many published works have discussed the above-mentioned effects on landslides (e.g. Iverson 2000; Bin *et al.* 2007; He *et al.* 2008; Cojean & Caï 2011; Jiang *et al.* 2011; Hu *et al.* 2012a,b; Jin *et al.* 2012).

In this study, our InSAR results suggest that the Huangtupo slope exhibits predominantly downward movements for Riverside Slumping Mass I# (Fig. 7) whose activity can be classified as 'Very slow' to 'Extremely slow' (IGUS/WGL 1995) and relatively general stability for the rest of the landslide.

InSAR results (Figs 5 and 9–11) also confirm that the lower part of the Huangtupo slope is more sensitive to Yangtze River hydraulic effects while the water table in the middle and back part is mainly influenced by precipitation. This fact is in agreement with other works (Jiang *et al.* 2007; Xie 2009) which show that groundwater of the front part of the Huangtupo slope varies with the water level of Yangtze River almost simultaneously, while water fluctuations barely influence the water table of the middle or upper part of the slope located at elevations higher than 350–400 m a.s.l., which is mainly influenced by precipitation.

Riverside Slumping Mass II# shows a quite long-term stable behaviour, although seasonal displacements associated with river water level can clearly be recognized in the InSAR time-series (Fig. 9). The top area of the Huangtupo slope (upper part of Garden Spot and Substation landslides and the slope crown) also exhibits a stable long-term behaviour with a superposed deformational seasonal cycle. Nevertheless, the seasonal displacements of these areas are not correlated with reservoir water level changes but are linked with rainfall (Fig. 9). This fact was observed by Jiang *et al.* (2007) and Xie (2009) considering the piezometric level time-series of several wells located in the slope.

Riverside Slumping Mass I# exhibits a general long-term displacement trend with annual displacements. These seasonal displacements, which are closely related with reservoir water level changes (Fig. 9) may be caused by consolidation–expansion geotechnical processes of the soils from the slope subjected to effective stress increase–reduction. This process can be derived from the effective stress change due to soil watering and dewatering produced by the phreatic level variation along the slope as a result of reservoir water level changes (Bin *et al.* 2007; Jiang *et al.* 2011). Note that the amplitude of the seasonal displacements affecting the foot of the slope is higher for Stage 3 (reservoir water level varying from 135 to 175 m a.s.l.) and the relation with reservoir water level is also clearer for this period with higher seasonal reservoir water level variations (Fig. 9). This fact probably happens because the soil thickness affected by the soil effective stress changes due to groundwater level variations is higher towards the middle part of the landslide (Xie 2009) only affected by the highest river water level changes.

Fig. 12 shows the overlapped mean time-series from tracks T347 and T075 and different triggering factors (rainfall, reservoir water level and groundwater piezometric level) for 2003–2007 period. From this figure it can be seen that for this period the groundwater level was slightly related with the reservoir water level near the river (i.e. the lower part of the Riverside Slumping Masses I# and II#) acting as a triggering factor of displacements (Figs 12a and b). However, for higher elevations (Figs 12c and d), groundwater level is mainly related with rainfall and as a consequence, reservoir water level has a limited influence on the displacement patterns. Note that the rainfall time-series and the corresponding groundwater levels are more variable and irregular. However, correlation between displacements (which are only available at a frequency of 35 d or more) and rainfall (available every 10 d) can be observed and higher displacements are recognized during rainy periods in which groundwater levels rise (Figs 12c and d).

The kinematic behaviour of Riverside Slumping Mass I# can be expressed as the addition of general displacement trend controlled

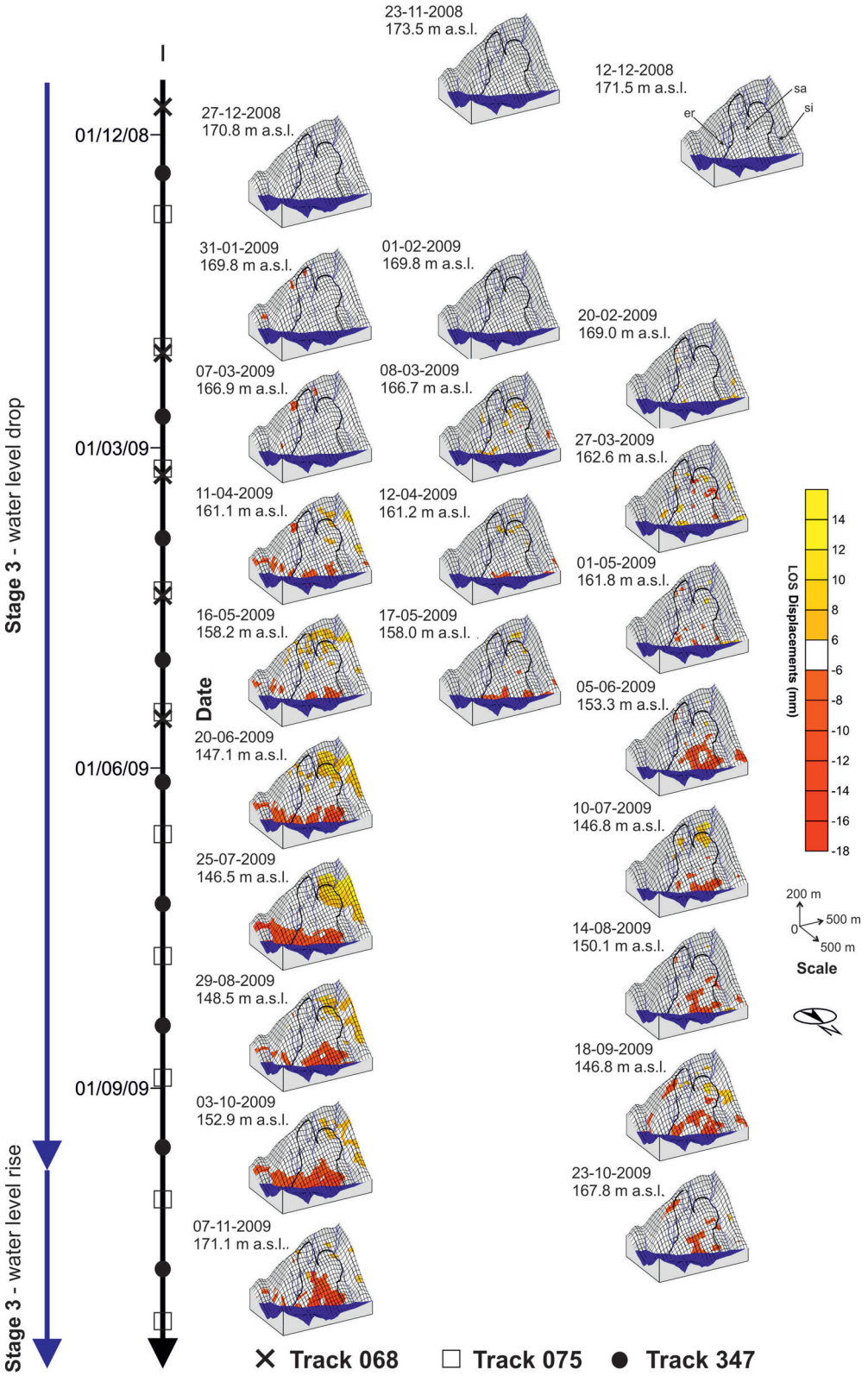

Figure 11. Short-term LOS displacements measured from tracks T068, T075 and T347. Note that symbols plotted in black axis shows image acquisition dates and blue axis indicates the different reservoir water level stages shown in Fig. 8. Temporal distribution of used images and the reservoir water level evolution corresponding to the different stages are also shown in Fig. 8(b). sa, Sandaogou ravine; si, Sidaogou ravine; er, Erdaogou ravine.

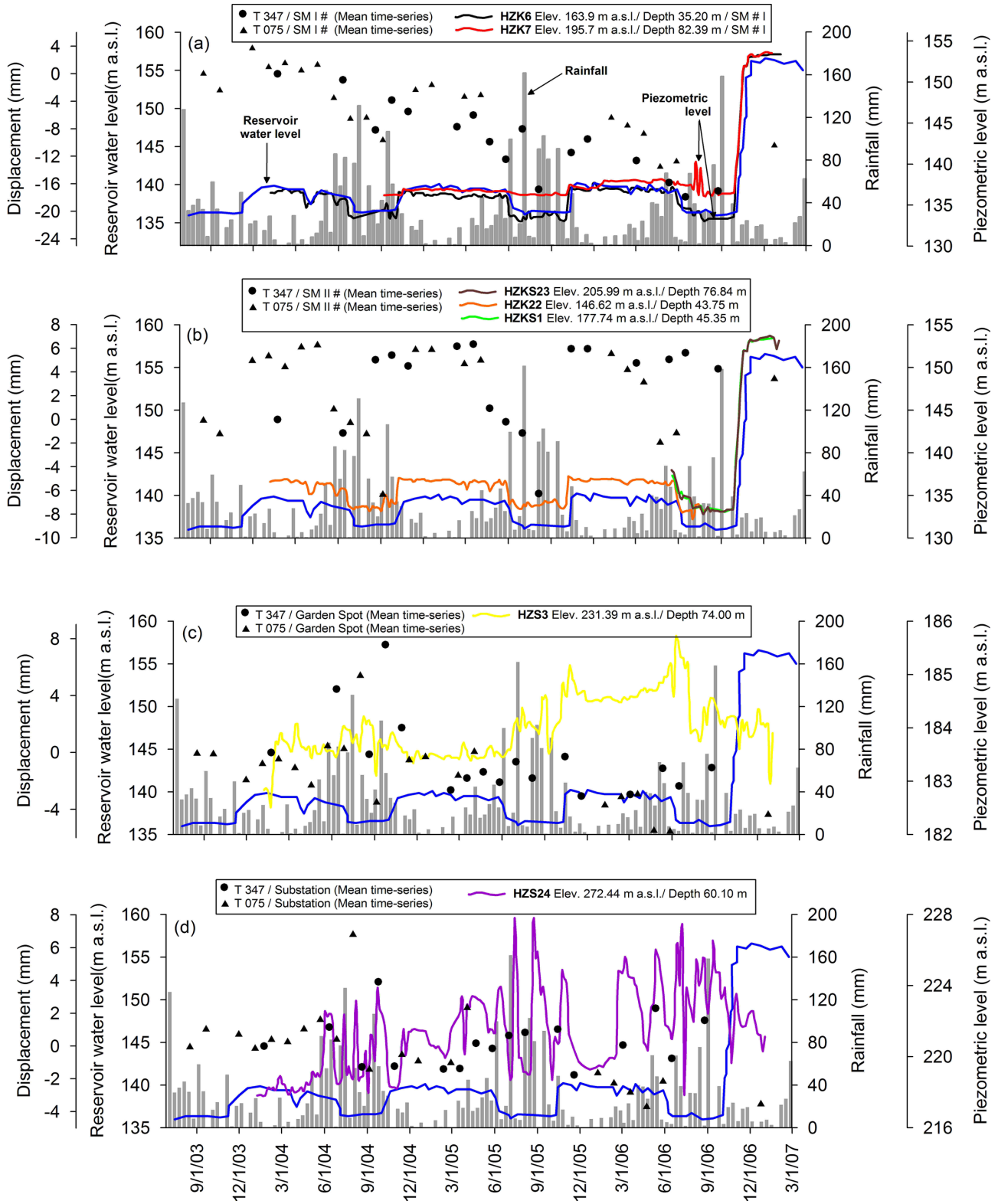

Figure 12. Mean InSAR time-series from tracks T347 (circles) and T075 (triangles) overlapped to the different triggering factors for 2003–2007 period: rainfall (bars), reservoir water level (blue line) and groundwater piezometric level (different colours). Elev., elevation of the borehole; Depth, depth of the borehole. See Fig. 5 for piezometers location.

by geological conditions and a seasonal displacement dependent on external factors which fluctuate in the short term (Du *et al.* 2012). Since several authors pointed out that Huangtupo long-term deep displacements correspond to creep phenomena (Deng *et al.* 2000; Bing *et al.* 2008; Chen *et al.* 2008; Song *et al.* 2009; Xie 2009; Chai *et al.* 2013) a rheological model is adopted for reproducing displacement behaviour. Bing *et al.* (2008) tested undisturbed soil samples from Huangtupo slip band concluding that creep behaviour

of the Huangtupo landslide can be explained by means of a Burgers' creep model. Consequently, in this work, a generalized Kelvin material with a superimposed Maxwell viscoelastic (Burgers' material) has been fitted using a least-square method to the displacement time-series and the non-linear component has been computed as the residuals (Pytharouli & Stiros 2010):

$$\delta = A\left(1 - \mathrm{e}^{-\frac{t}{B}}\right) + K \cdot t + C, \tag{3}$$

where δ is the LOS displacement, A, B, K and C are constants and t is the time.

The original InSAR time-series, the fitted creep model (eq. 3) and the residuals of different selected SDFP pixels from Riverside Slumping Mass I# are plotted in Fig. 13. The fitted models provide correlation coefficients (r) varying from 0.75 to 0.95. Although there exist some time gaps in the time-series, residuals exhibit a correlation with reservoir water level changes mainly recognizable for Stages 2 and 3 (Fig. 8) when the reservoir water level increased from 135 to 156 m a.s.l. and 156 to 175 m a.s.l. Note that for the two tracks, some displacement peaks related with rainfall seem to be overlapped to the main displacement trend caused by reservoir water level changes.

It can be concluded that the Huangtupo slope appears to exhibit a continuous and irrecoverable downward gravitational displacement rate for Riverside Slumping Mass I#, not correlated with reservoir water level changes that can be defined as a creep deformation. This deformation is accompanied by minor elastic and recoverable seasonal displacement closely linked with reservoir water level variations and to a lesser extent with rainfall. These seasonal displacements also affect the rest of the slope being mainly related with river water level and rainfall episodes in the lower and upper part of the slope, respectively, in agreement with groundwater data derived from monitored wells (Xie 2009).

7 CONCLUSIONS

In this paper, three tracks of Envisat ASAR images have been employed to investigate the Huangtupo slope, one of the most active landslides in the TG region. Ascending and descending images have been used to retrieve north–south and vertical displacements and time-series displacements given a good density of persistent scatterers in the Huangtupo slope and its surrounding areas due to its dense urbanization. The reliability of InSAR results has been shown through the cross-validation of adjacent tracks and the comparisons with ground-based data (GPS, horizontal short-baseline extensometers and inclinometers).

Once InSAR data have been validated, the spatial and temporal displacement data have been analysed. These results show that the whole slope is affected by seasonal displacements related with

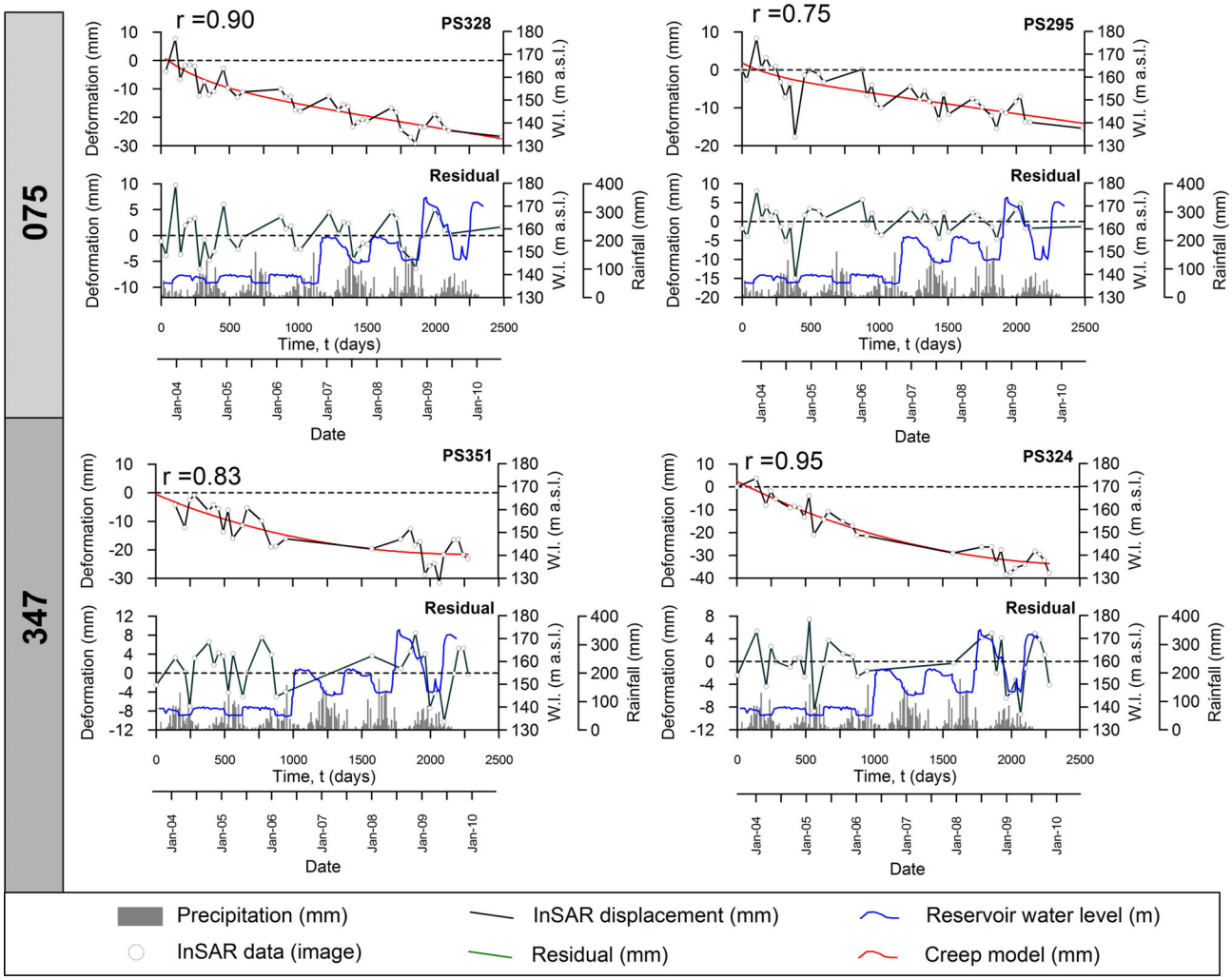

Figure 13. Total LOS displacement time-series of four selected SDFP pixels (black line) and fitted creep models (red line). The residuals (green line) have been also represented jointly with river water level and rainfall. See Fig. 5 for the distribution of SDFP pixels.

rainfall in the upper part and Yangtze River water level fluctuations in the lower part. Furthermore, a general long-term displacement is recognized in the northwest area of the slope corresponding to Riverside Slumping Mass I#. The measured velocity along the radar LOS on this landslide indicates that it is a 'Very slow' landslide (IGUS/WGL 1995) although most of the SDFP pixels located on the sliding body exhibit 'Extremely slow' (IGUS/WGL 1995) total velocities. The dynamics of the Riverside Slumping Mass I# landslide has been successfully explained by the means of a gravitational creep deformation, only controlled by geological conditions, with superposed minor vertical displacement oscillations related to consolidation–expansion processes caused by ground water changes induced by the river fluctuations. The rest of the slope (i.e. Riverside Slumping Mass II#, Substation and Garden Spot landslides) exhibits a stable behaviour with only minor seasonal displacements related with river water level and rainfall in the lower and upper areas of the slope, respectively. Note that the amplitude of the referred seasonal deformations affecting the foot of the slope is higher for reservoir water level varying from 135 to 175 m a.s.l. (Stage 3) and the relation with water level is clearer for this period of higher seasonal water level variations and for those areas placed under 350–400 m a.s.l.

To summarize, InSAR data have helped understand the kinematic behaviour of the landslide complementing ground monitoring measurements and identifying the active boundaries and monitoring its activities. Furthermore, the analysis of the displacement time-series has helped recognize the different displacement patterns on the slope and their relationships with various triggering factors. Finally, displacements on active areas (i.e. Riverside Slumping Mass I#) have been explained as the addition of seasonal elastic and inelastic creep displacements. This work highlights the feasibility to use InSAR and *in situ* data for investigating landslides. Furthermore, the use of satellite images with a higher resolution (e.g. TerraSAR-X or COSMO SkyMED) and longer ground monitoring data time-series in the future, will provide a more detailed understanding of the landslide that is essential for its management and decision making.

ACKNOWLEDGEMENTS

R. Tomás is supported by a Generalitat Valenciana fellowship BEST-2011/225, P. Liu by a China Scholarship Council (CSC) scholarship and A. Singleton by an EPSRC Industry scholarship. Part of this work is supported by the Natural Environmental Research Council (NERC) through the GAS project (Ref: NE/H001085/1), by a China National Natural Science Foundation of China (NSFC) project (No. 41074005) and by the Spanish Government under project TEC2011-28201-C02. The ENVISAT images were supplied through the ESA-MOST Dragon 2 Cooperation Program (ID: 5343). We thank JPL/Caltech for the use of ROI_PAC, TU-Delft for DORIS and Andy Hooper for StaMPS/MTI in our data processing and analysis.

REFERENCES

Berardino, P., Fornaro, G., Lanari, R. & Sansosti, E., 2002. A new algorithm for surface deformation monitoring based on small baseline differential SAR interferograms, *IEEE Trans. Geosci. Remote Sens.,* **40,** 2375–2383.

Bin, W., Huiming, T., Jiebin, Z., Wei, X. & Jun, L., 2007. Deformation and failure mechanisms of reservoir landslide considering fluid-solid coupling effect, *Chinese J. Rock Mech. Eng.,* **26,** 4484–4489.

Bing, W., Jie-Bin, Z., Hui-Ming, T.G. & Wei, X., 2008. Study on creep behavior of slip band soil of Huangtupo landslide, *J. Yangtze River Sci. Res. Inst.,* **25,** 49–52.

Bovenga, F., Wasowski, J., Nitti, D.O., Nutricato, R. & Chiaradia, M.T., 2012. Using COSMO/SkyMed X-band and ENVISAT C-band SAR interferometry for landslides analysis, *Remote Sens. Environ.,* **119,** 272–285.

Catani, F., Farina, P., Moretti, S., Nico, G. & Strozzi, T., 2005. On the application of SAR interferometry to geomorphological studies: estimation of landform attributes and mass movements, *Geomorphology,* **66,** 119–131.

Chai, B., Yin, K., Du, J. & Xiao, L., 2013. Correlation between incompetent beds and slope deformation at Badong town in the Three Gorges reservoir, China, *Environment. Earth Sci.,* **69**, 209–223.

Chen, S., Chen, G.-J. & Xu, G.-L., 2008. Mechanism of geological processes of formation and deformation of the Huangtupo landslide, *Earth Sci. J. China Univ. Geosci.,* **33,** 411–415.

Cojean, R. & Caï, Y., 2011. Analysis and modeling of slope stability in the Three-Gorges Dam reservoir (China)—the case of Huangtupo landslide, *J. Mountain Sci.,* **8,** 166–175.

Colesanti, C. & Wasowski, J., 2006. Investigating landslides with space-borne Synthetic Aperture Radar (SAR) interferometry, *Eng. Geol.,* **88,** 173–199.

Colesanti, C., Ferretti, A., Prati, C. & Rocca, F., 2003. Monitoring landslides and tectonic motions with the Permanent Scatterers Technique, *Eng. Geol.,* **68,** 3–14.

Deng, Q. & Wang, X., 2009. Mass rock creep and landsliding on the Huangtupo slope in the reservoir area of the Three Gorges Project, Yangtze River, China, in *Landslide Disaster Mitigation in Three Gorges Reservoir, China,* pp. 353–374, eds. Wang, F. & Li, T., Springer-Verlag.

Deng, Q.L., Zhu, Z.Y., Cui, Z.Q. & Wang, X.P., 2000. Mass rock creep and landsliding on the Huangtupo slope in the reservoir area of the Three Gorges Project, Yangtze River, China, *Eng. Geol.,* **58,** 67–83.

Du, J., Yin, K. & Lacasse, S., 2012. Displacement prediction in colluvial landslides, Three Gorges Reservoir, China, *Landslides,* **10**, 203–218.

Efron, B. & Tibshirani, R., 1986. Bootstrap Methods for Standard Errors, Confidence Intervals, and Other Measures of Statistical Accuracy, *Stat. Sci.,* **1,** 54–75.

Farina, P., Colombo, D., Fumagalli, A., Marks, F. & Moretti, S., 2006. Permanent scatterers for landslide investigations: outcomes from the ESA-SLAM project, *Eng. Geol.,* **88,** 200–217.

Ferretti, A., Prati, C. & Rocca, F., 2001. Permanent scatterers in SAR interferometry, *IEEE Transactions on Geoscience and Remote Sensing,* **39,** 8–20.

Ferretti, A., Tamburini, A., Novali, F., Fumagalli, A., Falorni, G. & Rucci, A., 2011. Impact of high resolution radar imagery on reservoir monitoring, *Energy Procedia,* **4,** 3465–3471.

Fruneau, B., Achache, J. & Delacourt, C., 1996. Observation and modelling of the Saint-Étienne-de-Tinée landslide using SAR interferometry, *Tectonophysics,* **265,** 181–190.

Gao, H.-x. & Yin, K.-I., 2014. Study on spatial prediction and time forecast of landslide, *Nat. Hazards,* **70**(3), 1735–1748.

Hanssen, R.F., 2001. *Radar Interferometry. Data Interpretation and Error Analysis,* Vol. **2,** Springer-Verlag.

He, K., Li, X., Yan, X. & Guo, D., 2008. The landslides in the Three Gorges Reservoir Region, China and the effects of water storage and rain on their stability, *Environment. Geol.,* **55,** 55–63.

Herrera, G. *et al.*, 2009. Validation and comparison of Advanced Differential Interferometry Techniques: Murcia metropolitan area case study, *ISPRS J. Photogram. Remote Sens.,* **64,** 501–512.

Herrera, G., Notti, D., García-Davalillo, J., Mora, O., Cooksley, G., Sánchez, M., Arnaud, A. & Crosetto, M., 2011. Analysis with C- and X-band satellite SAR data of the Portalet landslide area, *Landslides,* **8,** 195–206.

Herrera, G., Gutiérrez, F., García-Davalillo, J.C., Guerrero, J., Notti, D., Galve, J.P., Fernández-Merodo, J.A. & Cooksley, G., 2013. Multi-sensor advanced DInSAR monitoring of very slow landslides: the Tena Valley case study (Central Spanish Pyrenees), *Remote Sens. Environ.,* **128,** 31–43.

Hooper, A., 2008. A multi-temporal InSAR method incorporating both persistent scatterer and small baseline approaches, *Geophys. Res. Lett.,* **35,** doi:10.1029/2008gl034654.

Hooper, A., Segall, P. & Zebker, H., 2007. Persistent scatterer interferometric synthetic aperture radar for crustal deformation analysis, with application to Volcán Alcedo, Galápagos, *J. geophys. Res.: Solid Earth,* **112,** doi:10.1029/2006jb004763.

Hooper, A. & Zebker, H.A., 2007. Phase unwrapping in three dimensions with application to InSAR time series, *J. Opt. Soc. Am. A,* **24,** 2737–2747.

Hu, X., Tang, H., Li, C. & Sun, R., 2012a. Stability of Huangtupo riverside slumping mass II# under water level fluctuation of Three Gorges Reservoir, *J. Earth Sci.,* **23,** 326–334.

Hu, X.L., Tang, H.M., Li, C.D. & Sun, R.X., 2012b. Stability of Huangtupo I# landslide under Three Gorges reservoir operation, *Appl. Mech. Materials*, **8**, 170–173.

IGUS/WGL, 1995. A suggested method for describing the rate of movement of a landslide, *Bull. Intl. Assoc. Eng. Geol.,* **52,** 75–78.

Iverson, R.M., 2000. Landslide triggering by rain infiltration, *Water Resour. Res.,* **36,** 1897–1910.

Jackson, S. & Sleigh, A., 2000. Resettlement for China's Three Gorges Dam: socio-economic impact and institutional tensions, *Communist Post-Communist Studies,* **33,** 223–241.

Jarvis, A., Reuter, H.I., Nelson, A. & Guevara, E., 2008. Hole-filled SRTM for the globe Version 4. Available from the CGIAR-CSI SRTM 90m Database. Available at: http://srtm.csi.cgiar.org/, last accessed 5 February 2014.

Jiang, H.-B., 2005. Approach on the control plan for deformation in depth of Huangtupo Landslide, Badong County in Hubei Province, *Zhongguo Dizhizaihai Yu Fangzhi Xuebao,* **16,** 53–60.

Jiang, J., Ehret, D., Xiang, W., Rohn, J., Huang, L., Yan, S. & Bi, R., 2011. Numerical simulation of Qiaotou Landslide deformation caused by drawdown of the Three Gorges Reservoir, China, *Environment. Earth Sci.,* **62,** 411–419.

Jiang, W.-P., Huang, B.-Z. & Ouyang, H., 2007. The monitoring technological method of landslide in Huangtupo, *Resour. Environ. Eng.,* **21,** 575–578.

Jiazhu, W., 2002. Three Gorges Project: the largest water conservancy project in the world, *Public Admin. Dev.,* **22,** 369–375.

Jin, Y., Wen-xing, J., Hu-feng, Y. & Jiu-long, Z., 2012. Dynamic variation rule of phreatic line in Huangtupo landslide in the Three Gorges Reservoir Area, *Rock Soil Mech,* **5**, 853–858.

Just, D. & Bamler, R., 1994. Phase statistics of interferograms with applications to synthetic aperture radar, *Appl. Opt.,* **33,** 4361–4368.

Liao, M., Tang, J., Wang, T., Baltz, T. & Zhang, L., 2012. Landslide monitoring with high-resolution SAR data in the Three Gorges region, *Sci. China, Earth Sci.,* **55,** 590–601.

Liu, J.G., Mason, P.J., Clerici, N., Chen, S., Davis, A., Miao, F., Deng, H. & Liang, L., 2004. Landslide hazard assessment in the Three Gorges area of the Yangtze river using ASTER imagery: Zigui-Badong, *Geomorphology,* **61,** 171–187.

Liu, P., Li, Z., Hoey, T., Kincal, C., Zhang, J., Zeng, Q. & Muller, J.-P., 2013. Using advanced InSAR time series techniques to monitor landslide movements in Badong of the Three Gorges region, China, *Intl. J. Appl. Earth Obs. Geoinformat.,* **21,** 253–264.

Massonnet, D. & Feigl, K.L., 1998. Radar interferometry and its application to changes in the Earth's surface, *Rev. Geophys.,* **36,** 441–500.

Metternicht, G., Hurni, L. & Gogu, R., 2005. Remote sensing of landslides: an analysis of the potential contribution to geo-spatial systems for hazard assessment in mountainous environments, *Remote Sens. Environ.,* **98,** 284–303.

Peltier, A., Bianchi, M., Kaminski, E., Komorowski, J.C., Rucci, A. & Staudacher, T., 2010. PSInSAR as a new tool to monitor pre-eruptive volcano ground deformation: validation using GPS measurements on Piton de la Fournaise, *Geophys. Res. Lett.,* **37,** doi:10.1029/2010GL043846.

Prati, C., Ferretti, A. & Perissin, D., 2010. Recent advances on surface ground deformation measurement by means of repeated space-borne SAR observations, *J. Geodyn.,* **49,** 161–170.

Pytharouli, S.I. & Stiros, S.I., 2010. Kinematics and rheology of a major landslide based on signal analysis, *Géotechnique,* **60,** 207–222.

Singhroy, V., Mattar, K.E. & Gray, A.L., 1998. Landslide characterisation in Canada using interferometric SAR and combined SAR and TM images, *Adv. Space Res.,* **21,** 465–476.

Song, C., Guang-li, X., Guo-jin, C. & Xue-ting, W., 2009. Research on engineering geology characteristics of soil in sliding zone of Huangtupo landslide in Three Gorges Reservoir area, *Rock Soil Mech.,* **30,** 3048–3052.

Squarzoni, C., Delacourt, C. & Allemand, P., 2003. Nine years of spatial and temporal evolution of the La Valette landslide observed by SAR interferometry, *Eng. Geol.,* **68,** 53–66.

Strozzi, T. *et al.*, 2005. Survey and monitoring of landslide displacements by means of L-band satellite SAR interferometry, *Landslides,* **2,** 193–201.

Suo, L., Niu, X. & Xie, H., 2012. 6.07—the Three Gorges Project in China, in *Comprehensive Renewable Energy,* pp. 179–226, ed. Sayigh, A., Elsevier.

Tang, H., Hu, X., Deng, Q. & Xiong, C., 2009. Research on the characteristics and slope deformation regularity of the badong formation in the Three Gorges reservoir area, in *Landslide Disaster Mitigation in Three Gorges Reservoir, China*, pp. 87–113, eds. Wang, F. & Li, T., Springer-Verlag.

Tarchi, D., Casagli, N., Fanti, R., Leva, D.D., Luzi, G., Pasuto, A., Pieraccini, M. & Silvano, S., 2003a. Landslide monitoring by using ground-based SAR interferometry: an example of application to the Tessina landslide in Italy, *Eng. Geol.,* **68,** 15–30.

Tarchi, D., Casagli, N., Moretti, S., Leva, D. & Sieber, A.J., 2003b. Monitoring landslide displacements by using ground-based synthetic aperture radar interferometry: application to the Ruinon landslide in the Italian Alps, *J. geophys. Res.: Solid Earth,* **108**, doi:10.1029/2002jb002204.

Tofani, V., Raspini, F., Catani, F. & Casagli, N., 2013. Persistent scatterer interferometry (PSI) technique for landslide characterization and monitoring, *Remote Sens.,* **5,** 1045–1065.

Tullos, D., 2009. Assessing the influence of environmental impact assessments on science and policy: an analysis of the Three Gorges Project, *J. Environment. Manage.,* **90**(Suppl. 3), S208–S223.

Wang, T., Perissin, D., Mingsheng, L. & Rocca, F., 2008. Deformation monitoring by long term D-InSAR analysis in Three Gorges area, China, in *Proceedings of the Geoscience and Remote Sensing Symposium, 2008. IGARSS 2008,* IEEE International, pp. IV-5–IV-8.

Wen, B. & Chen, H., 2007. Mineral compositions and elements concentrations as indicators for the role of groundwater in the development of landslide slip zones: a case study of large-scale landslides in the Three Gorges area in China, *Earth Sci. Frontiers,* **14,** 98–106.

Wu, X., Yu, Q., He, M., Zhao, X. & Zhang, L., 2006. Slide mechanisms of a giant ancient slide body at Huangtupo, Badong County in the Three Gorges Reservior area, in *IAEG2006,* p. 8, eds Culshaw, M.G., Reeves, H.J., Jefferson, I. & Spink, T.W., The Geological Society of London.

Xie, L., 2009. Complex geological characteristics and mechanism and control technical of landsliding of Huangtupo at Three Gorges Reservoir, *PhD thesis*, Wuhan University of Technology, Wuhan.

Zhao, C., Lu, Z., Zhang, Q. & de la Fuente, J., 2012. Large-area landslide detection and monitoring with ALOS/PALSAR imagery data over Northern California and Southern Oregon, USA, *Remote Sens. Environ.,* **124,** 348–359.

SUPPORTING INFORMATION

Additional Supporting Information may be found in the online version of this article:

Table S1. List of Envisat ASAR images used in the processing. Master image is in bold (http://gji.oxfordjournals.org//lookup/supp1/doi:10.1093/gji/ggu017/-/DC1).

Please note: Oxford University Press are not responsible for the content or functionality of any supporting materials supplied by the authors. Any queries (other than missing material) should be directed to the corresponding author for the article.